A multimodal nanopipette-based imaging and analytical platform for exploring brain communication

Martina Papa

INSTITUT POLYTECHNIQUE DE PARIS

NNT : 2024IPPAX049

Thèse de doctorat

A multimodal nanopipette-based imaging and analytical platform for exploring brain communication

Thèse de doctorat de l'Institut Polytechnique de Paris
Préparée à École Polytechnique

École doctorale n°626 : Ecole Doctorale de l'Institut Polytechnique de Paris (ED IP Paris)
Spécialité de doctorat: Chimie

Thèse présentée et soutenue à Palaiseau, le 26.03.2024, par

Martina Papa

Composition du Jury :

Antigoni Alexandrou Research Director, École Polytechnique	Président du Jury
Robert Lazenby Assistant Professor, Florida State University	Rapporteur
Binoy Paulose Nadappuram Assistant Professor, University of Strathclyde	Rapporteur
Frédéric Lemaitre Professor, ENS University PSL	Examinateur
Luisa Ciobanu Research Director, CEA/ NeuroSpin	Examinatrice
Aleix Güell Assistant Professor, École Polytechnique	Directeur de thèse
Jean-Pierre Mothet Research Director, ENS Paris-Saclay	Co-Directeur de thèse

To Mom and Dad,
my roots and shelter.

And to Thibaut,
the small light in each of my days.

Institut Polytechnique de Paris
91120 Palaiseau, France

Table of Contents

Institut Polytechnique de Paris
91120 Palaiseau, France

Institut Polytechnique de Paris
91120 Palaiseau, France

Acknowledgements

I would like to start by acknowledging the fundamental contributions that my supervisors had during this PhD journey. I will always be thankful to Dr. Aleix Güell for having provided me the opportunity to live this experience. His supervision has been fundamental to navigate the complex topic of this PhD, as well as to help me to go out of my comfort zone. I also would like to thank Dr. Jean-Pierre Mothet, for having been a teacher and a point of reference during these years. I have really appreciated all our discussions, and most importantly I have been inspired by his mentorship.

In addition, I would like to thank Dr. François Treussart, for having dedicated his time to my project, and for having always been available to discuss with me. A precious help also came from Prof. Loredano Pollegioni, who provided us with the enzyme used in this work as well as important suggestions about the work.

This PhD would have not been possible, without the help of several other people. Dr. Funes Hernando taught me the basis of this project during my first year and he later became of great help in moments of difficulties. Dr. Mucientes has taught me a lot about SICM and has always encouraged me. Finally, when at the end of my third year I found myself to deal with a new subject, I could have not asked for better help than the one Dr. De Oliveira Souza provided me. She taught me a lot, and really made me feel comfortable working in LuMIn laboratory.

A proverb says that "you need a village to grow a kid". I learned that "you need a lab to grow a PhD student". Actually, in my case, I needed two labs. Therefore, I would like to thank all the people from the LPICM and LuMIn laboratories. In particular, it is very important for me to thank Dr. Yvan Bonnassieux for his continuous encouragement and support during this adventure, and Dr. Jean-Charles Vanel, for having carefully looked after me. I am very grateful for having met them.

Moreover, I would like to thank Dr. Christian Murga and Shenming Wang for their support in the chemistry lab, and Dr. Zhao, for having followed and supported my work for three long years. I would also like to thank Brigitte Potier for having helped me during my work in LuMIn.

A particular thank also goes to LOB laboratory, for having allowed me to use their L2 room, and having provided me with all the support I needed.

Together with them, I would like to extend my thanks to the full LPICM and LuMIn laboratory, for having provided hints and points of reflection to improve my work.

If scientific support has been important, the personal one has been my real asset. Therefore, thanks … to Guili, for having laughed and cried with me; to Daniel, for his patience; to Marta, for having faced RER B with me; to Monalisa, for our chats about novels and life; to Juhna, for his

Institut Polytechnique de Paris
91120 Palaiseau, France

kindness; to Aymeric, Weixi, Inass, and Alexandre, for our days together in the office; to Aram, Sami, Issoufou, Camilla, Andrea, Hindia, Michel, Xinlei, and Deyan, for the time together.
Thanks to Louis and Lucy, here in Paris, and the Famille Dirand, for having taken care of me, as well as thanks to my "Parisian" friends: Chiara, Laura, Nina, Antonio, Fanny, Victoria, Francesca, and Benjamin.

Finally, all my efforts are dedicated to some people that, spread around the world, have been my support system in these three long years. Most importantly, thanks to my best friends: Francesca, Emilia, Chicca, Andrea, Edoardo, Beatrice, Silvia, and Marco, because thanks to them I never feel lonely.
I would like to conclude thanking my family, Matteo, Mamma and Papa'. Without you, nothing of this would be worthy. And Thibaut: during the last three years, you have been my most precious resource.

This project was sponsored by the ERC Starting Grant 716641-AQUARAMAN and the ANR French Research Agency ANR-10-LABX-035-BrainSICM.

Institut Polytechnique de Paris
91120 Palaiseau, France

List of abbreviations

- aCSF: artificial cerebrospinal fluid
- AD: Alzheimer's disease
- AFM: Atomic force microscopy
- AMPARs: α-amino-3-hydroxy-5-methyl-4-isoxazole propionic acid receptors
- BSA: Bovine serum albumin
- CA: Chronoamperometry
- CE: Capillary electrophoresis
- CNS: Central nervous system
- CV: Cyclic voltammetry
- CVD: Chemical vapor deposition
- D-AAs: D-amino acids
- DAAO: D-amino acid oxidase
- DG: Dentate gyrus
- DMEM: Dulbecco's modified eagle medium
- EFM: Electric force microscopy
- EMEM: Eagle's minimal essential medium
- FAD: Flavin adenine dinucleotide
- FIB: Focused ion beam
- FRET: Fluorescence resonance energy transfer
- FSCV: Fast-scan cyclic voltammetry
- GABA: Gamma-aminobutyric acid
- GC: Gas chromatography
- GluOx: Glutamate oxidase
- GOx: Glucose oxidase
- GPCRs: G-protein-coupled receptors
- H.a.r: Hopping approach rate
- HPICM: Hopping probe ion conductance microscopy
- HPLC: High performance liquid chromatography
- HRP: Horseradish peroxidase
- H.r.r.: Hopping retract rate
- i_{DC}: DC current

Institut Polytechnique de Paris
91120 Palaiseau, France

- iPSC: Induced pluripotent stem cells
- iGluRs: Ionotropic glutamate receptors
- LOD: Limit of detection
- L.s.r.: Lateral scan rate
- MDCK: Madin Darby Canine kidney (cells)
- MFM: Magnetic force microscopy
- mGluRs: Metabotropic glutamate receptors
- MS: Mass spectrometry
- NMDARs: N-methyl D-aspartate receptors
- NTs: Neurotransmitters
- O-DNS: Ortho-dianisidine
- PBS: Phosphate-buffered saline
- PC12: Adrenal phaeochromocytoma cell line
- PEGDE: Polyethylene glycol diglycidyl ether
- PPD: Polyphenylenediamine
- QRCE: Quasi-reference counter electrode
- SAW: Surface acoustic wave
- SCaM: Scanning capacitance microscopy
- SECM: Scanning electrochemical microscopy
- SEM: Scanning electron microscopy
- sem: standard error of mean
- SERS: Surface-enhanced Raman spectroscopy
- SFM: Scanning force microscopy
- SICM: Scanning ion conductance microscopy
- SNOM: Scanning near-field optical microscopy
- SPM: Scanning probe microscopy
- SR: Serine racemase
- $SR^{-/-}$: Serine racemase knock-out mice
- SthM: Scanning thermal microscopy
- STM: Scanning tunneling microscopy
- TLE: Temporal lobe epilepsy
- WT: Wild type (mouse)

Institut Polytechnique de Paris
91120 Palaiseau, France

List of figures

Institut Polytechnique de Paris
91120 Palaiseau, France

Institut Polytechnique de Paris
91120 Palaiseau, France

Chapter 1. Introduction and state-of-the-art

1.1 Introduction

1.1.1 Brain Communication: Synapses and NMDA receptors

The brain is a highly intricate and complex organ, serving as the central hub for coordinating vital functions within living organisms. Together with the spinal cord, it forms the central nervous system (CNS). By integrating and computing all sensory inputs, our memory, and our thoughts, and by controlling our movements, the CNS enables us to adapt to our environment at every millisecond of our life and therefore shapes individual identities and experiences.

The fundamental building units of this organ are specialized cells called neurons. Brain activity is generated by a complex and precise chemical communication interplay inside neural assemblies[1] that takes place at specialized structure called synapses.[2, 3] Recent literature indicate that this synaptic communication is modulated by the neuroglial cells.[4]

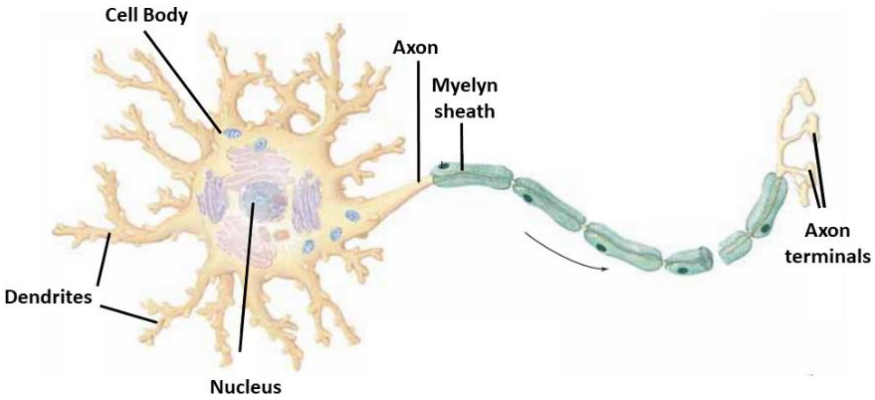

Figure 1. Schematic representation of a neuron.
Neurons are highly polarized cells characterized by a cell body, and the presence of dendrites and the axon with nerve terminals where neurotransmitters are released for information transmission to other cells. The figure is modified from *Martini et al.*[4]

Regardless of their specific function, all neurons types share the same structural morphology, schematically represented in *figure 1*. They feature a central cell body, also known as soma, housing the nucleus, along with lateral processes known as dendrites, relatively short yet highly intricate structures, essential for conveying information from the external environment of the cell to the soma. Additionally, the neurons exhibit an elongated process called axon, serving for transmitting electrical information away from the cell. The myelin sheath, depicted in green in *figure 1*, consists of phospholipid layers that envelop the axons of some neurons, insulating them electrically. These sheaths are segmented by gaps referred to as Ranvier nodes, which serve as crucial sites for the efficient transmission of information along the neuron.[4]

Institut Polytechnique de Paris
91120 Palaiseau, France

Information transmission between neurons occurs through electrical impulses. In its resting state, a neuron maintains a polarized state, with a more negative charge on the inside compared to the outside of the membrane, due to ionic distribution. Thus, neurons have negative membrane potential ~-70 mV, depending on their type and their maturation state. When stimulated, the membrane depolarizes, leading to an action potential, which involves an influx of Na^+ ions, making the trans-membrane potential more positive. Subsequently, the cell membrane becomes highly permeable to K^+ ions which exit the cell, restoring a more positive charge outside. The electrical information then reaches the synapses, which are nanoscopic gaps between cells, where specialized chemical messengers called neurotransmitters (NTs) are secreted from the presynaptic neurons by a calcium dependent vesicular mechanism and reach the postsynaptic one.[5] Here, they bind to specific proteins called neuroreceptors on the cell's membrane, provoking the generation of a new electrical impulse that proceeds through the second cell in a chain of information transfer. A representative illustration of a synapses can be observed in *figure 2*.[4] Neurons and their partners (i.e. glia cells) use a plethora of messenger molecules like amino acids (glutamate, GABA), catecholamines (dopamine, serotonin), and gasotransmitters (NO, CO, H_2S) to enable brain computation and cognitive functions.[6] Converging evidence from preclinical and clinical studies indicate that many if not all disorders that affect our society, like Alzheimer's disease (AD), epilepsies or schizophrenia, are caused by a malfunction of synapses.[7] Therefore, synapses are common targets for pharmacological interventions aiming to rebalance synaptic activity by focusing on specific brain NTs systems.

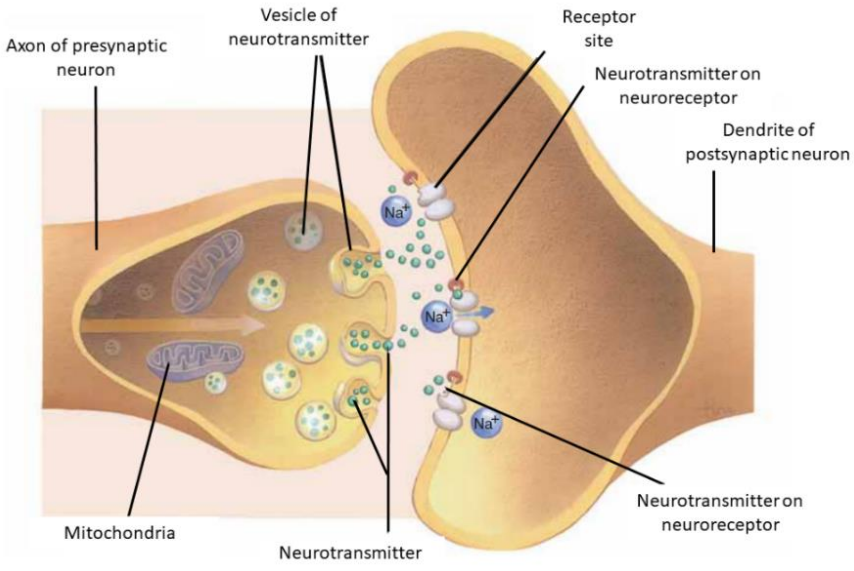

Figure 2. Schematic representation of a chemical synapse.
The information flow travels from presynaptic to postsynaptic terminal (indicated by the arrow). Once action potential reaches the nerve terminal, depolarization, NTs stored in synaptic vesicles in the nerve terminal are released in the synaptic cleft and then binds to specific receptors present on the postsynaptic dendrites. The figure is modified from *Martini et al*.[4]

Institut Polytechnique de Paris
91120 Palaiseau, France

Besides serving as metabolic intermediates and as building units for protein synthesis, amino acids can also act as neuroinformative molecules. In this realm, our attention is particularly drawn to the glutamatergic system of neurotransmission that plays a pivotal role in the CNS, facilitating excitatory synaptic transmission and contributing to numerous physiological processes, as memory formation and learning, as well as pathological conditions.[8, 9]

Once released in the synaptic cleft, glutamate binds to specific receptors. Glutamate receptors are classified into two major types: ionotropic glutamate receptors (iGluRs) and metabotropic glutamate receptors (mGluRs). iGluRs mediate fast synaptic transmission by allowing the flow of cations across the neuronal membrane upon glutamate binding. This rapid excitatory signaling underlines critical processes such as learning and memory. The iGluRs family comprises the N-methyl D-aspartate (NMDA), the α-amino-3-hydroxy-5-methyl-4-isoxazole propionic acid (AMPA) receptors, and the Kainate receptors.[10] In contrast, mGluRs (mGluR1-8) are G-protein-coupled receptors (GPCR) that act through intracellular signaling pathways, modulating neuronal excitability and synaptic plasticity and are associated with more prolonged stimuli.[11] *Figure 3* shows the classification of glutamate receptors.

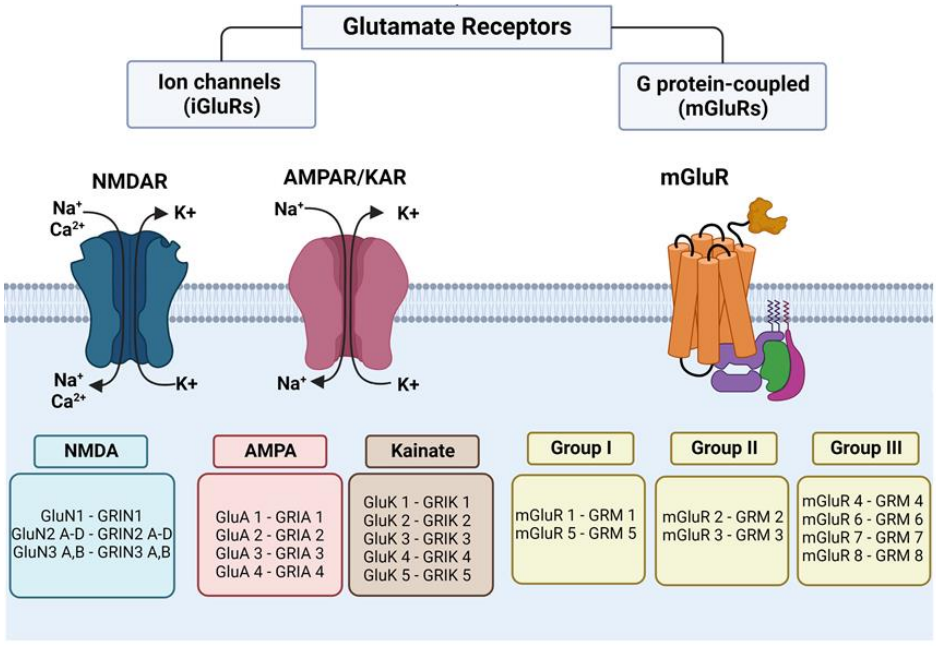

Figure 3. Classification of glutamate receptors.
iGluRs, on the left, can be classified in NMDA, AMPA, and Kainate receptors. mGluRs are shown on the right. The figure is modified from *Garcia Gaytan et al.*[12]

1.1.2 The NMDA receptors

In this thesis, we will focus on the NMDARs. NMDARs exhibit widespread distribution in the mammalian CNS and play a crucial role in synaptic transmission, synaptic plasticity, and higher cognitive functions, with their impact extending to physiological processes like the regulation of

Institut Polytechnique de Paris
91120 Palaiseau, France

blood pressure and respiration.[13] They operate as ion channels, facilitating the passage of Ca^{2+}, Na^{+}, and K^{+} ions across neuronal cell membranes upon glutamate NTs binding.[11]

The activation of canonical NMDARs is a precisely regulated process that necessitates a specific set of conditions for activation, with a critical role played by the co-agonists, glycine and D-serine.[14] In addition to their ligand-binding dependence, NMDARs exhibit voltage sensitivity. Indeed, unlike other receptors, NMDARs require not only glutamate binding but also coincident depolarization of the postsynaptic membrane to remove the magnesium ions (Mg^{2+}) that typically block their ion channel under resting condition (-70 mV).[15] In addition, the activity of NMDARs is influenced positively or negatively by many others effectors (H^{+}, Zn^{2+}, polyamines) which bind at different sites of the four domains, NTD (N-terminal domain), ABS (agonist binding site), TMD (trans-membrane domain), and CTD (C-terminal domain), of the receptor, as shown in *figure 4a*.[16]

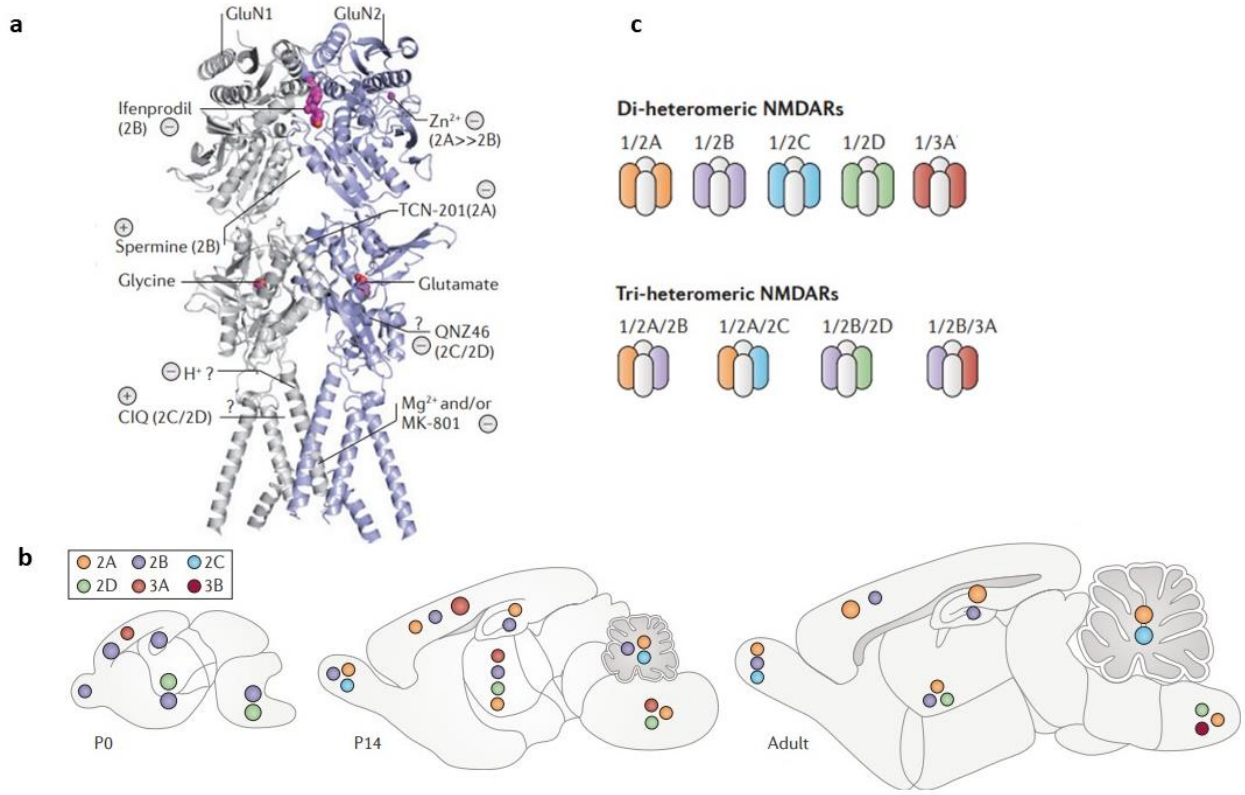

Figure 4. NMDARs structure and subunits composition.
A model of NMDARs, showing binding sites for several molecules modulating its activity. b) The developmental profile of GluN subunit expression in the mouse brain at day of birth (P0), 2 weeks following birth (P14) and in the adult stage. c) of various types of di-heteromeric and tri-heteromeric NMDARs subunit compositions. Figure modified from *Paoletti et al*.[14]

Structurally, NMDARs are synaptic protein complexes assembled as tetramers, comprising different subunits, the association of which enables the expression of a large repertoire of receptors with different pharmacological and biophysical properties. NMDARs subunits come in three primary types: GluN1, GluN2, and GluN3.[14] Eight potential isoforms of the GluN1 subunit derive from alternative splicing of a single gene.[17] The GluN1 subunit is indispensable for the receptor's

fundamental function, housing the binding site for the co-agonist, which is mandatory for NMDARs activation. This is reflected by GluN1 large expression in all brain areas and during all life. In contrast, there are four distinct GluN2 subunits: GluN2A, B, C, and D. GluN2A subunits are associated with faster channel opening and closing, whereas GluN2B and GluN2C/D subunits exhibit slower kinetics. In addition to contribute to the receptors' diverse functional characteristics the GluN2s show diverse regional distribution during development and in the adult brain, as summarized in *figure 4b*. For example, there is a developmental switch from GluN2B to GluN2A during postnatal development.[18] GluN2C expression increases after birth but is limited to cerebellum while GluN2D, which is abundant during embryogenesis and fetal life, declines to traces after birth. Additionally, GluN3A and GluN3B were also recently identified,[19] extending the molecular catalog and the number of possible arrangements. GluN3A is only marginally expressed during the two first post-natal weeks of development, while GluN3B is only expressed in some deep nuclei of the brain. Canonical diheteromeric or triheteromeric NMDARs consist in the association of two GluN1 subunits with two GluN2 or a mix of GluN2/GluN3 subunits, as shown schematically in *figure 4c*.[18]
Of note, GluN1-GluN3 diheteromeric NMDARs are not gated by glutamate (which only bind to GluN2 subunits) and are adopting only glycine and/or D-serine as agonists.[20]

A comprehensive understanding of the intricacies of NMDARs activation and modulation is essential due to their multifaceted role in neural functioning. Malfunction (due to gain or loss of function, or caused by default in expression) of NMDARs is detrimental for synapses and circuits formation and dynamics, and for this reason is implicated in a large spectrum of neurological and psychiatric disorders, including AD, schizophrenia, Parkinson's disease, Huntington's disease, and mood disorders.[21] A particular emphasis has been placed on unravelling the significance of co-agonists, such as glycine and D-serine, in modulating NMDAR function. D-serine, in particular, has attracted substantial attention as a co-agonist, yet many of the mechanisms governing its contribution to NMDARs regulation remain enigmatic.

1.1.3 D-serine: known facts and open questions

As seen in section 1.1.2, canonical GluN1-GluN2 NMDARs possess a dual-lock mechanism, requiring the concurrent binding of two molecules – the neurotransmitter glutamate and a co-agonist in addition to a specific membrane depolarization for activation.

From the beginning, glycine has been recognized as the endogenous co-agonist of NMDARs, as elucidated by breakthrough studies in the late 1980s. Notably, in 1987, *Johnson* and *Ascher* demonstrated the potentiation of NMDARs activity through the addition of minute quantities of glycine.[22] The term of co-agonist was given later when *Kleckner* and *Dingledine* reported that glycine,

on one side, and glutamate/NMDA, on other side, bind to different subunits of the receptor.[23] During that period, the existence of D-amino acids (D-AAs) in mammals was emerging but not widely accepted. Indeed, all amino acids with the exception of glycine have a chiral carbon and can exist in their L- and D-forms. However, according to the long-cherished dogma of homochirality of life, D-AAs were thought to only occur within microorganisms[24] as constituents of bacterial cell walls. Therefore, D-AAs were considered to be non-natural chemicals in higher organisms like mammals. However, in 1992, *Hashimoto et al.* identified the presence of D-AAs, in particular D-serine, in the brain.[25]

The hypothesis proposing D-serine as a potential NMDARs co-agonist originated from converging observations indicating the co-localization of D-serine distribution and NMDARs in the brain. In 1995, *Snyder* and colleagues charted the cellular and regional positioning of D-serine in a rat brain, affirming its alignment with NMDARs locations.[26] These findings, coupled with the observation of low glycine levels in areas with a high presence of NMDARs, led them to suggest that D-serine is the primary co-agonist for NMDARs in the observed brain regions.[27]

Direct evidence was first reported in 2000, when the same team, using a biochemical and electrophysiological approach, demonstrated that the depletion of D-serine present in the brain, through the use of selective enzyme scavengers, considerably impaired NMDARs-mediated synaptic currents, therefore that D-serine is the right co-agonist for synaptic NMDARs, contrary to the initial belief that glycine fulfilled this role.[28] Additionally, the identification of a specific enzyme, serine racemase (SR), localized in the same cells as D-serine and responsible for converting L-serine to D-serine, had finally elucidated the source of the molecule.[29] On the other side, it was suggested that D-serine would be catabolized by D-amino acid oxidase (DAAO), a peroxisomal enzyme.[30] Consequently, D-serine gained official recognition as a NMDARs ligand as being metabolized by neural cells.

Nowadays, it is largely accepted that both glycine and D-serine can act as co-agonists for NMDARs to which they bind with the same relative affinity.[31] They engage in an intricate cross-talk, wherein their roles as NMDARs modulators are preferentially emphasized over the other depending on several factors such as developmental stage, cell location, region of the brain, and the compositions of NMDARs subunits.[31, 32, 33] Research over the last 25 years have uncover that D-serine is at the core of complex signaling pathway involving different cell types (neurons and glia), transporters and different mode of release. Initially it was believed that D-serine is exclusively produced in astrocytes through the racemization of L-serine by SR. L-serine is obtained from the breakdown of glucose, that is the brain's primary energy source and is derived from the blood, as schematically represented in *figure 5*. Nevertheless, subsequent studies revealed that astrocytes may not be the exclusive source

Institut Polytechnique de Paris
91120 Palaiseau, France

of D-serine production. In 2006, *Kartvelishvily et al.* reported for the first time that D-serine and SR were present in neurons and not glia.[34] Thus, the authors suggested that neurons rather than glial cells as initially thought are a major source of D-serine to modulate NMDARs activity. However, a notable question persisted regarding the absence of L-serine in neurons, challenging the understanding of D-serine production. The D-serine shuttle hypothesis[35] proposes that L-serine, originating in astrocytes, is transported into neurons through specific transporters. Within neurons, it is used for D-serine production, then shuttled back to astrocytes, where it is stored and released. Despite ongoing inquiries into the D-serine shuttle hypothesis, uncertainties remain regarding whether astrocytic or neuronal D-serine regulates neuron communication.[36] A study from 2006 indicated that the dominance of astrocytic or neuronal D-serine production varies during development, each playing distinct roles.[37] The collective evidence of D-serine production by neurons in both *in vitro* and *in vivo* scenarios has given rise to a new model proposing a bidirectional flow of D-serine between neurons and astrocytes, with both contributing to the activation of NMDA receptors.

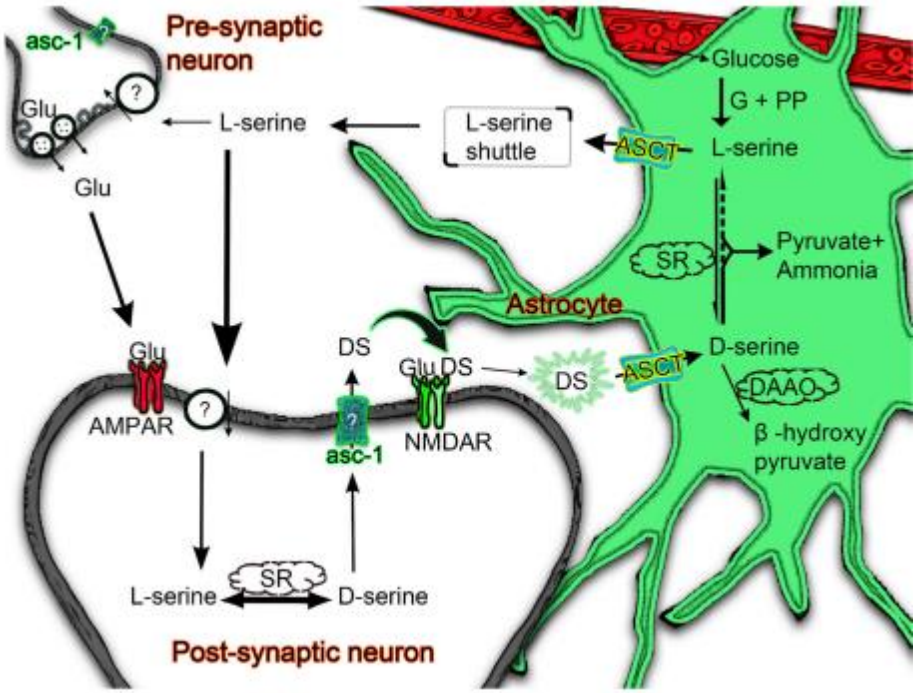

Figure 5. Mechanisms controlling the availability of D-serine at synapses.
L-serine is synthesized in astrocytes from glucose. ASC transporters on astrocytic membranes assist in transferring L-serine into neurons, through specific neuronal L-serine transporters. Within neurons, L-serine is transformed into D-serine by SR and then released through asc-1 transporters. D-serine, upon release, collaborates with glutamate to regulate neuronal communication via NMDARs. D-serine is cleared from the synaptic cleft through a process involving astrocytic ASC transporters. Inside astrocytes, D-serine can be broken by DAAO. Alternatively, astrocytic D-serine can undergo α,β- elimination to produce pyruvate and ammonia, catalyzed by SR. The picture is taken from *Krishnan et al.*[38]

The regulation of D-serine production and release in astrocytes and neurons is a multifaceted process involving various proteins and sub-mechanisms. Notably, the activation of AMPA receptors on the astrocyte membrane stimulates the release of astrocytic D-serine. This leads to the binding of specific

Institut Polytechnique de Paris
91120 Palaiseau, France

proteins to SR, resulting in its activation and a subsequent increase in D-serine production.[39, 40] In addition, the activation of AMPARs induces a rise in astrocytes intracellular Ca^{2+} concentration, leading to the release of D-serine from small intracellular vesicles. A study from 2005, in fact, highlighted the involvement of vesicular storage and confirmed vesicular exocytosis mechanism for D-serine release from astrocytes[26] and subsequent investigations about this process further supported this hypothesis.[41] Regarding the release of D-serine from neurons, it has been revealed that it differs in nature from astrocytic release and does not involve vesicular exocytosis.[41] Instead, neuronal release of D-serine would mainly relies on the alanine-serine-cysteine (Asc-1) exchanger, expressed at the membrane of presynaptic neurons. Asc-1 primarily mediates the efflux of D-serine and glycine through the hetero-exchange with other neutral amino acids.[42] But many questions remain unanswered regarding notably the direction of operation modality in situ.[43, 44] Researchers have also extensively delved into the clearance mechanism of D-serine, identifying several transporters located at both glial cells and neurons such as alanine serine cysteine transporter 1 (ASCT1) and transporter 2 (ASCT2).[45] Once D-serine is re-uptaken by cells, its degradation can occur through various mechanisms. One such mechanism involves the DAAO enzyme. However, DAAO is not uniformly abundant in all brain regions, necessitating consideration of alternative D-serine degradation mechanisms in specific areas.[46] *Figure 5*, summarizes the proposed mechanisms in which D-serine is involved.

D-serine, as a regulator of NMDARs activity, plays crucial physiological roles, particularly in synaptogenesis, synaptic plasticity and in higher cognitive function such memory formation.[47, 48] Beyond its physiological roles, preclinical and clinical studies indicate that alterations in the metabolism of D-serine which cause aberrant levels are consistently linked to several pathological conditions including neurological diseases (amyotrophic lateral sclerosis, chronic pain, epilepsies), neurodegenerative diseases (AD, Parkinson disease) or psychiatric disorders (schizophrenia, depression) (*Figure 6).* For these reasons, the D-AA is viewed as a reliable biomarker and a promising drug target.[49] The intricate regulatory mechanisms of D-serine, together with its role in severe disorders, have prompted the research community to prioritize precise measurements of D-serine levels. The following section will delve into traditional methods for D-serine analytical detection and explore how these approaches can be surpassed by more efficient technologies.

Institut Polytechnique de Paris
91120 Palaiseau, France

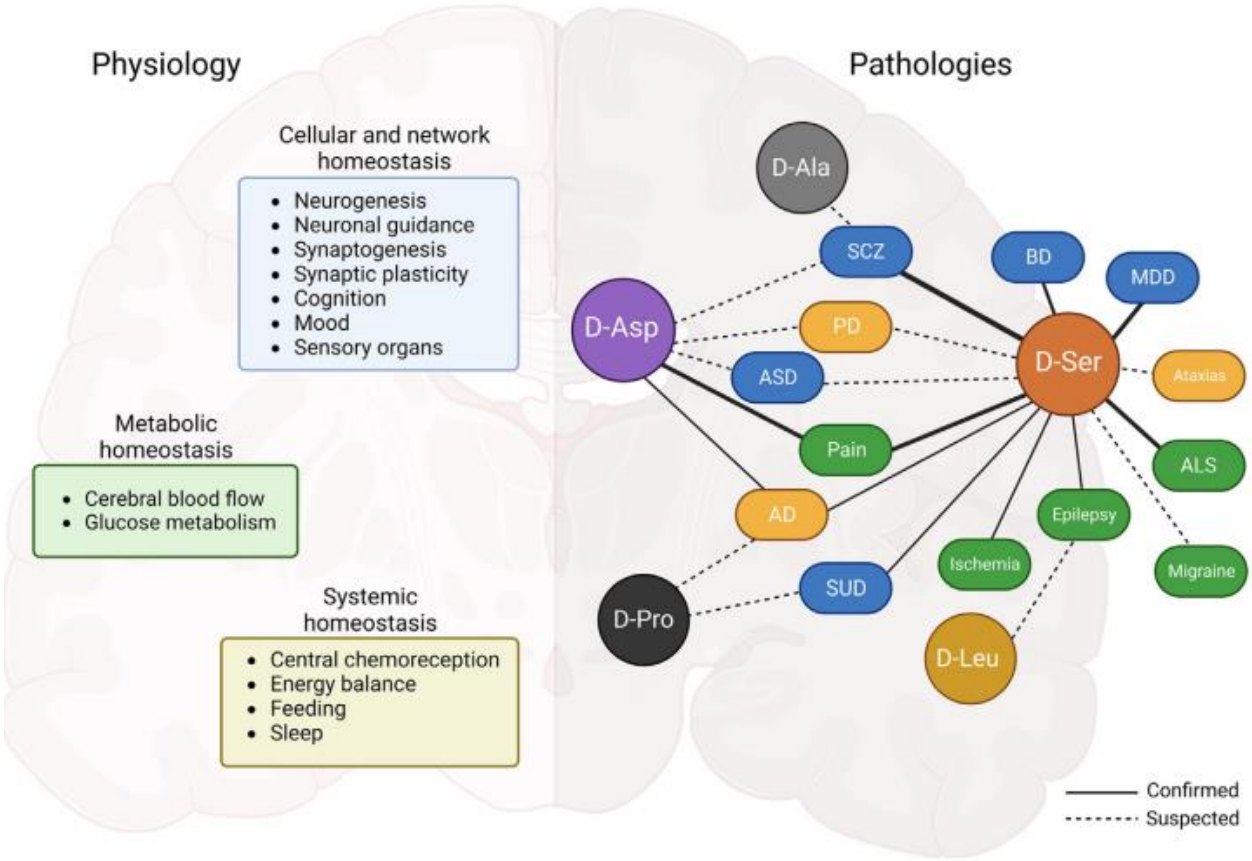

Figure 6. Roles of D-amino acids in physiology and pathologies.
On the left, relations with physiological processes are described. On the right, role of D-amino acids in pathologies is illustrated. Dotted connection are indicating suspected link between the D-amino acids and the pathologies. Abbreviations stand for: AD, Alzheimer's disease; ALS, amyotrophic lateral sclerosis; ASD, autism spectrum disorders; BD, bipolar disorder; MDD, major depressive disorders; PD, Parkinson's disease; SCZ, schizophrenia; SUD, substance use disorder.[49]

1.1.4 Techniques for measuring D-serine

Detection of D-serine in the brain presents a significant challenge due to its low concentrations (extracellular level of 1-10 µM in physiological conditions).[50] Therefore sensitive and specific detection methods are needed. Various analytical techniques have been employed for the detection of D-serine along with other D-amino acids, including chromatography-based methods, capillary electrophoresis (CE), mass spectrometry (MS), antibody-based methods, and biosensors, each offering distinct advantages and limitations.

1.1.4.1 Chiral analytical methods

Chiral analytical methods encompass a series of techniques used for distinguishing and analyzing molecules based on their chirality, a property stemming from their asymmetrical spatial arrangement. Chiral molecules exist in two distinct forms known as enantiomers (e.g. D-serine and L-serine), which are non-superimposable mirror images of each other, and that often manifest distinct properties. The

objective of chiral analytical methods is to facilitate the separation, detection, and quantification of these enantiomers.

Chromatography-based methods have been extensively utilized for the detection and quantification of D-serine in various biological samples. Between chromatography-based techniques, high-performance liquid chromatography (HPLC) has found widespread use. HPLC is a technique used to separate, identify, and quantify the chemical components of a mixture, like as being present in any biological sample. The basic unit of a HPLC experiment is a chromatographic column in which the biological sample to analyze is passing through, transported by a mobile phase, pumped at high pressure. The column contains the stationary phase, made of adsorbent material, typically a granular material composed of solid particles. Each chemical component of the sample to be analysed interacts differently with the stationary phase, resulting in different migration rates then enabling their separation. At the exit of the column, the components are sensed by a specific detector, which can be a UV detector, fluorescence detector, or mass spectrometry detector. The results of the analysis are depicted in a chromatogram.[51, 52] In the early 1990s, *Hashimoto et al.*, employed HPLC to identify D-serine in different regions of rodent brain, observing age-related variations.[25] Similarly, in 1995, *Matsui et al.* used HPLC to investigate the effects of free D-serine and glycine on NMDARs. The study found that the extracellular concentration of D-serine in the rodent frontal cortex was sufficient to saturate the glycine site on the receptors, suggesting a crucial modulatory role for D-serine in this brain region.[53] In addition, in 1997, *Hamase et al.* combined HPLC with fluorescence detection to analyze D-amino acids content in rat brains, affirming the presence of D-serine in various brain regions and revealing gender-associated differences in D-amino acids content in specific brain regions.[54]

Another chromatography technique that has been utilized in the context of D-serine measurement in the brain is gas chromatography (GC). In gas chromatography, the mobile phase is a gas carrier, in which the sample is injected after vaporization. As in liquid chromatography, the mobile phase transports the sample in the column, and interacts with the stationary phase, prompting the separation of individual components based on their affinity with the stationary phase.[55] In 1995, *Goodnough* and colleagues integrated GC with mass spectrometry, developing a swift procedure for separating and quantifying D-serine and L-serine from a rat brain.[56]

Capillary electrophoresis (CE) is another method of choice that has been introduced early in 2004 to detect and measure D-amino acids. CE involves the separation of charged molecules within a narrow capillary, under the influence of an electric field. As for chromatographic techniques, CE can be coupled to UV or fluorescencedetectors.[57] *Zhao* and colleagues demonstrated the efficacy of CE for the detection of D-serine in a rat brain by combining CE with fluorescence detection.[58]

Institut Polytechnique de Paris
91120 Palaiseau, France

Moreover, CE combined with laser-induced fluorescence (LIF) and mass spectrometry (MS) has also been used for measuring the D-serine content of synaptic vesicles.[41]

MS is the third technique extensively utilized for D-serine measurements. In a typical MS experiment, the sample undergoes ionization and the charged ions are then propelled through a magnetic field, causing them to separate based on their mass-to-charge ratio. The resulting data is collected by a specialized electron multiplier, generating a mass spectrum that provides valuable insights into the molecular structure and abundance of the components present in the sample. However, MS alone is not able to distinguish between enantiomers. Therefore, MS has to be coupled with complementary techniques such as chromatography or CE in order to detect enantiomers in biological samples.[59] Several examples of the use of MS for D-serine detection can be found in literature. Following the already mentioned study conducted by *Hashimoto et al.* in 1992,[25] subsequent investigations have demonstrated the efficacy of MS coupled with LC for quantifying D-serine in various biological matrices, including mouse brain,[60] plasma, and other tissues.[61] Additionally, the integration of MS with chiral microchip electrophoresis has been used for appreciating D-serine uptake and release processes in PC12 cells.[62]

The three methods described so far can be used offline but have been also applied to online detection of D-amino acids when coupled to *in vivo* microdialysis. In microdialysis, a thin and flexible probe (0.5-2 mm diameter) is inserted into the tissue of interest. The probe comprises a semi-permeable membrane through which small molecules can diffuse. Connected to a perfusion system, the probe continuously delivers a physiological solution, called the perfusate, through the membrane. As the perfusate flows, it exchanges molecules with the surrounding extracellular fluid. The semi-permeable membrane acts as a molecular filter, permitting only molecules within a specific size range to pass through. Detection methods such as chromatography, CE, or MS are then employed to quantify specific molecule concentrations.[63] For example, *Ciriaks et al.* used CE together with microdialysis for the online detection of D-serine in the rat striatum.[64, 65] Similarly, *O' Brien et al.* also utilized CE combined with microdialysis to detect the release of D-serine from an intact retina.[66]

All these three analytical techniques discussed so far offer high sensitivity and reproducibility. In addition, they allow simultaneous measurements of different chemicals, enabling multiplex analysis in a biological matrix. However, they come with limitations. These methods fall in achieving real-time localization of molecules of interest, posing a challenge for functional studies of these molecules in the brain. Additionally, they require costly instrumentation and involve intricate chemical procedures for derivatizing molecules to make them readable. Moreover, when used in combination with microdialysis, these techniques face constraints due to the size of the implanted probes used for sample collection, limiting spatial resolution in observing small and narrow brain

areas. The implantation process may also cause tissue lesions, potentially impacting physiological processes and observations. Moreover, even in the case of microdialysis it is not possible to sample faster than minutes.

1.1.4.2 Antibodies-based methods

Alternatively, since the inception of interest in D-serine, various antibody-based immunolabelling methods on fixed tissues have also been used. In 1995, *Schell et al.* developed stereoselective antibodies to precisely map D-serine in the rodent brain, combining immunohistochemistry with optical microscopy. Their approach facilitated the observation of D-serine's complementary localization to DAAO in different brain regions.[27] Two years later, the same group utilized the same technique to demonstrate that D-serine is present in a specific type of astrocytes in the telencephalon near NMDARs, suggesting its role as an endogenous ligand for these receptors in these observed brain areas.[67] Using a selective antibody for D-serine, *Williams* and colleagues have reported that D-serine present in glial cells is confined within vesicle-like compartments which has been further confirmed by two studies.[68, 41] While these antibody-based techniques for D-serine identification have the advantage of offering more precise localization of D-serine in biological preparation with subcellular resolution, they are limited in that they cannot be employed for measurements of living tissues and lack real-time capability. In addition, they are time consuming.

1.1.4.3 Biosensors

In recent years, biosensors have garnered increasing significance for D-serine analysis, allowing for rapid, stable, and sensitive detection during seconds or milliseconds time-scale events. Several types of biosensors have been developed, including optical fluorescence-based[69] and electrochemical-based sensors.[70, 71] The following section will describe these two types of sensors, including also an example of a surface acoustic wave (SAW) biosensor.[72]

Of particular interest in the context of this thesis are electrochemical enzyme-based sensors. This type of sensors has a great versatility, as they can be implanted *in vivo* and are also applicable for *in vitro* analyses. Most of these systems involve specially shaped microelectrodes whose surfaces are functionalized with D-serine sensitive enzymes (DAAO, D-serine dehydratase, etc).[70, 71] Notably, the potential for miniaturization of sensor design is advantageous, enabling the analysis at cellular or subcellular domains to gain better understanding of the mechanisms in which D-serine is involved.

Before describing the state-of-the-art on this topic, the following section will provide deeper insights into the main components, typologies, and working principles of biosensors with a particular

focus on NTs detection. Additionally, we will review the development of biosensors for D-serine detection, offering a summarizing overview.

1.2 Biosensors

1.2.1 Biosensors: definitions, classification, and applications

According to IUPAC recommendation (1999) a biosensor can be defined as *an integrated receptor-transducer device which is capable of providing selective quantitative or semi-quantitative analytical information using a biological recognition element.*[73] A biosensor is therefore an analytical integrated device that transforms a physicochemical parameter of some kind within a biological system, as a molecular species concentration, into a measurable electrical or optical signal. Each biosensor is composed by three parts, schematically represented in *figure 7.*

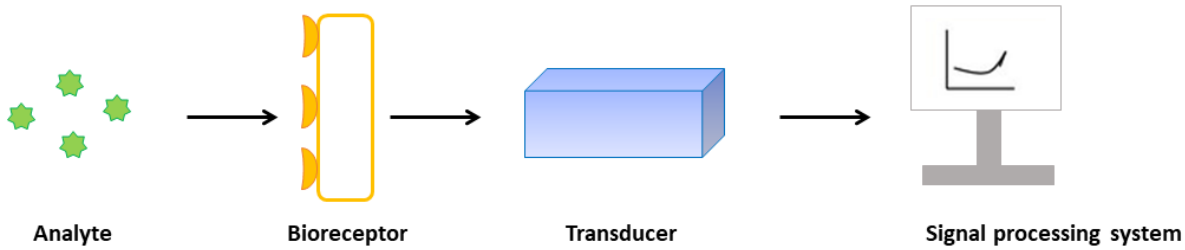

Figure 7. Components of the biosensor

The analyte is detected by the bioreceptor. The information is then transformed, by the transducer, in a measurable and quantifiable signal that can then be processed.[74, 75, 76]

The receptor functions as the molecular entity for sensing and it earns a chemical sensor the designation of "biosensor" due to its biological origin. It reacts specifically with the analyte triggering a mechanism that produces a quantitative or semi-quantitative input for the transducer. It is commonly immobilized or in close proximity to the transducing system, responsible for converting the biological mechanism response into an electrical signal that can be measured and processed.[73, 74, 75, 76]

There are two possible classifications for biosensor. The first one is based on the nature of the bioreceptor. The schematic represented in *figure 8* can help in the following explanation.[77]

Institut Polytechnique de Paris
91120 Palaiseau, France

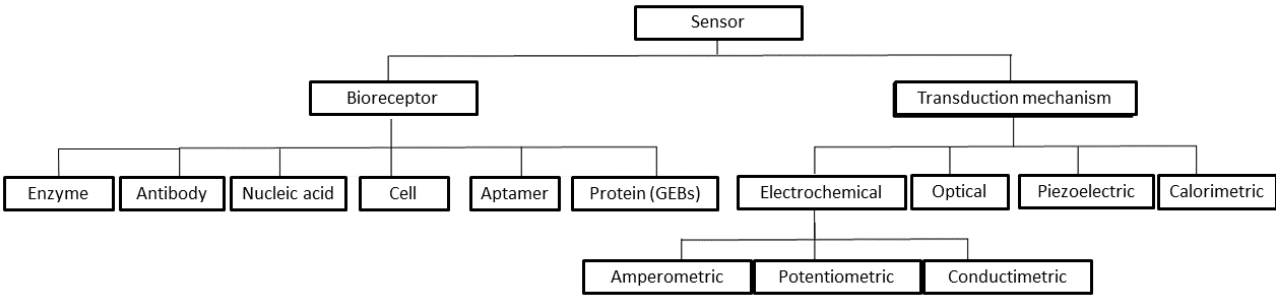

Figure 8. Classification of different types of biosensors.
Classification is based on the nature of the bioreceptor or on the transduction system.

Based on the biological signaling mechanism, biosensors can be divided in six main categories (*figure 8*).

1. Enzyme-based biosensors use enzymes as bioreceptors, that specifically recognize the target and catalyze their transformation.[78]
2. Immunosensors use antibodies as bioreceptors and their working principle is based on the ability of the antibody to specifically bind to its antigen.[79]
3. Nucleic Acids-based biosensors use DNA strands as receptors, based on their ability to recognize the complementary strand to form a stable hydrogen bond between nucleic acids.[80]
4. Cell-based sensors use living cells as bioreceptors and exploit the cell ability to detect the intracellular and extracellular microenvironment conditions variations.[81]
5. Biomimetic sensors are artificial/synthetic and often based on the use of aptamers that are synthetic strands of nucleic acids designed to recognize specific amino acids, peptides, or proteins.[82, 83]
6. Genetically encoded biosensors (GEBs) are molecular tools that utilize genetically engineered proteins as receptors to detect and quantify specific biological molecules. These biosensors enable real-time tracking of signaling activities in live cells, providing valuable insights into the dynamic of biological processes.[84, 85]

Alternatively, based on the type of transduction mechanisms used, we can classify biosensors in four other main groups.[77]

1. Electrochemical biosensors use an electrochemical transduction element and they work based on the measurement of an oxidation/reduction current that is proportional to the analyte's concentration. Electrochemical biosensors are quick, simple, inexpensive, sensitive and easy to use. The type of the electrochemical changes, allows for further characterization, as follows.[86]

1a. Amperometric biosensors are based on the measurement of a current that derives from an oxido-reduction reaction of an electrochemically active species whose concentration depends on the analyte to detect.[87]

1b. In potentiometric biosensors, the recognition event leads to a potential accumulation on an indicator electrode with respect to a reference electrode (e.g. Ag/AgCl), while the current is null or negligible. This voltage variation is proportional to the concentration of the substrate according to Nernst equation.[88]

1c. In conductometric biosensors, the information is obtained from the electrolyte conductivity, due to the ionic species in solution, that varies as a result of the biorecognition event.[89]

2. Optical biosensors exploit the interaction between light and bio-molecules to detect target substances based on optical properties as absorption, fluorescence, or refractive index, resulting from binding interactions between target biomolecules and receptors.[90, 91]
3. Piezoelectric-based biosensor are advanced devices that utilize the piezoelectric effect when variations in vibration or resonance frequency are caused by binding events, allowing for highly sensitive and precise detection.[92]
4. Calorimetric-based biosensors detect the heat released or absorbed when targeted molecules bind to recognition elements on the sensor surface and provide highly sensitive and accurate information about the target substances.[74]

The applications of biosensors today span across vastly different fields, as food industry,[93, 94, 95] sustainable agriculture,[96, 97, 98] and bio-terrorism risk mitigation.[99] Nevertheless, the primary domain for the utilization of biosensors is the field of medicine, where biosensors have revolutionized healthcare by enabling precise and rapid diagnosis and monitoring of various medical conditions, affirming their central role in improving human health and well-being.

The evolution of biosensors application in life-science traces back to the groundbreaking development of the Clark electrode in 1956, enabling real-time measurements of oxygen levels in biological systems.[100] This invention found applications in various medical domains, such as monitoring oxygen availability during hypothermia and low blood flow conditions,[101] or blood oxygen tension during whole total body perfusion.[102] Most importantly, it laid the foundation for the first glucose biosensor, created by Clark and Lyons in 1962.[103] This biosensor utilized enzyme-based electrochemical sensing, based on Glucose Oxidase (GOx), to measure glucose concentrations.[103] Over time, the technology has evolved from a niche concept to an industrialized and user-friendly

Institut Polytechnique de Paris
91120 Palaiseau, France

solution, significantly enhancing point-of-care management for individuals with diabetes and improving their ability to monitor their blood glucose level effectively.[75]

Nowadays, in clinical diagnosis, biosensors are used for the identification and quantification of biomarkers, extending well beyond the scope of monitoring glucose levels and encompassing an array of analytes, like cholesterol[104] and various proteins. Biosensors, for example, play a crucial role in cancer detection by detecting biomarkers like nucleic acids, proteins and hormones. These devices utilize recognition molecules, such as antibodies, attached to transducers tailored for specific targets. In this context, electrochemical, optical, and piezoelectric transducers are commonly employed, with recent advancements in nanomaterials enhancing sensitivity and stability.[105] Alternatively, nucleic acids-based biosensors utilize selective sequence matching and electrochemical/optical transduction methods. Biosensors also find crucial applications in detecting infectious diseases and have been employed for detecting viruses like HPV, dengue, and hepatitis.[106, 107] as well as bacterial diseases like tuberculosis, leprosy,[108 , 109] and meningitis.[110]

In addition, biosensors have evolved into integral components of wearable technology and their application extends to diverse types of users, supporting telemedicine through the remote transmission of physiological data.[111, 112] Moreover, biosensors are crucial tools for drug screening[113] and play a pivotal role in investigating cellular and molecular functions, expanding our understanding of health and disease. Specifically, within neuroscience, biosensors enable precise measurements of NTs and other brain molecules, facilitating research on neurodegenerative diseases, mental disorders and the intricacies of brain function.[114]

1.2.2 Biosensors for neurotransmitters detection

Biosensors have emerged as preferred tools for tracking NTs levels due to their real-time monitoring capabilities, eliminating the time and cost associated with traditional techniques.[115] Essential requirements for biosensors in NTs detection include high sensitivity, biocompatibility and functionality in the detection environment, along with the imperative need for sensor miniaturization. Compact biosensors, crucial for *in vivo* studies, enable precise placement near the release site of NTs, improving spatial measurement resolution and minimizing tissue damage. Their reduced size facilitates rapid response to fluctuations in NTs concentrations, ensuring precise detection even at low concentrations. In addition, miniaturized biosensors can be easily integrated into micro-devices, enhancing their versatility for a wide range of research and clinical applications.[116]

The field of NTs detection using biosensors sees the predominance of electrochemical sensors due to their high sensitivity, real-time monitoring capabilities, minimal sample preparation required,

fast response time, *in vivo* suitability, cost-effectiveness, and potential for miniaturization.[114] This review primarily focuses on electrochemical biosensors due to their dominance and to the thesis' thematic focus.

Electrochemical sensors for NTs detection fall into two main categories: non-enzymatic and enzymatic biosensors. Non-enzymatic biosensors can detect intrinsically electroactive NTs (e.g., dopamine, epinephrine, serotonin) using appropriates electrodes and electrochemical techniques. For non-electroactive NTs (e.g., GABA, acetylcholine, glutamate), their detection involves electrode functionalization with material like transition metal oxides, conducting polymers, carbon materials, and nanoparticles facilitating electron transfer between the analyte and the transducer.[117] On the other hand, enzymatic biosensors provide enhanced sensitivity, selectivity, and signal amplification. Therefore, despite the long-term stability of non-enzymatic electrochemical sensor, enzyme-based electrochemical biosensors are widely employed.[115]

Classic electrodes often use noble metals like gold (Au), silver (Ag), and platinum (Pt) due to their excellent conductivity and efficient electron transfer kinetics. Nevertheless, also carbon-based electrodes are widely employed.[118] Moreover, novel materials such as conductive polymers have emerged as alternatives since they offer mechanical flexibility and optical transparency.[119] Other types of transducers are electrode arrays[120] and transistors.[121] Finally, the incorporation of nanomaterials as transduction elements in electrochemical sensors enhances detection efficiency with improved sensitivity and selectivity.[122]

Micro- and nano-electrodes are utilized for NTs detection in the brain, employing various electrochemical techniques. The most commonly used methods include chronoamperometry (CA), cyclic voltammetry (CV) and fast scan cyclic voltammetry (FSCV).[123, 124] (Each technique has distinct advantages and disadvantages. In CV, the potential is swept between two values, producing a unique voltammogram for each molecule, characterized by oxidation and reduction peaks. However, due to the scan rates of hundreds of mV/s, CV is not suitable for tracking sun-second NT dynamics, resulting in limited temporal resolution. CA, with its fast response time due to small electrode size, offers excellent temporal resolution but lacks selectivity. It records faradaic currents in response to an applied potential, which may result in reactions of multiple molecules simultaneously. FSCV addresses the need for both selectivity and temporal resolution. In FSCV, the potential is rapidly swept between a holding potential and a switching potential at scan rates 10 to 100 times higher than conventional CV (300-400 V/s), allowing scan durations on the order of milliseconds. This enables real-time monitoring of NT dynamics. Repeated scans generate multiple voltammograms, with peaks indicating the presence of specific molecules of interest. FSCV is typically performed using carbon fiber microelectrodes (CFMEs) due to their small size,

biocompatibility, ad low time constant, which facilitates rapid signal stabilization. Advancements in FSCV include incorporating nanomaterials or conductive polymers into electrodes structure to enhance sensitivity and selectivity. However, due to high scan rates, FSCV is characterized by substantial background currents, necessitating background subtraction to accurately interpret faradaic signals. Consequently, FSCV is a differential technique better suited for detecting discrete variations in NT levels rather than basal levels. In summary, the choice of electrochemical techniques should be based on the specific goals of the study, considering the balance between temporal resolution and sensitivity required.[124, 125]

Biosensors have been used for *in vivo* application, as well as for analysis of group of tissue samples or group of cells.[126, 127] However, to investigate single cells or subcellular details, nanobiosensors are needed. Nanosensors rely on nanoelectrodes, defined as solid electrodes with at least one dimension measuring below 1 µm. Nanoelectrodes function by discerning faradaic currents generated from the redox reactions of analytes like electroactive NTs. Alternatively, their surface may be functionalized, for instance, by means of enzymatic modifications, to facilitate the electrochemical detection of non-reactive NTs.[128] Their miniaturized geometry enables precise analysis within confined volumes and precise placement in proximity of regions of interest in the cells. In addition, nanosensensors can be introduced within cells, thus allowing intracellular analysis while minimizing invasiveness.

Many nanobiosensors for NTs detection are based on carbon nanofibers. These electrodes can be modified in geometry to achieve structures such as disk-shaped nanoelectrodes, sensitive to processes occurring at the very tip. Alternatively, carbon nanowires can be sharpened into nanoelectrodes through an etching process, thereby enabling their insertion into highly confined areas of interest. In 1996, *Zhang* and colleagues employed ion beam etching to create conical nanoelectrodes with diameters ranging from 50 to 500 nm and detect low concentrations of dopamine and serotonin.[129] Similarly, *Cheng* and colleagues utilized carbon fibers fused to the tip of a glass capillary for detecting the release of dopamine from PC12 cells, with the nanoelectrodes positioned in close proximity to the release sites.[130] *Li* and colleagues also reported the use of carbon nanoelectrodes for insertion into the narrow space between a neuron soma and a neuron varicosity, facilitating the detection of vesicular neurotransmitter releases.[131] In addition platinum, gold, and silver nanowires have also been utilized to craft nanoelectrodes with dimensions as small as 1 nm.
Alternatively, nanopipette-based carbon nanoelectrodes have also found wide application. One method for fabricating such probes exploits the pyrolytic decomposition of carbon precursor gases inside a tapered glass capillary. This process generated small disk-shaped electrodes, with their size depending on the initial opening of the pipette tip.[132] Carbon nanoelectrodes of this type, have already

been used for intracellular measurements.[133] An alternative approach involves the application of chemical vapor deposition (CVD).[134] Nanoelectrodes of this type also find extensive utility also in combination with scanning probe microscopy techniques and their sensing applications will be the described in section 1.3.4. Alternative techniques have also found their place in this field. For instance, the attachment of a carbon nanotube to a tungsten tip resulted in the creation of the smallest nanoneedle electrode ever used to detect dopamine. Furthermore, subsequent immobilization of glutamate oxidase (GluOx) on this probe also allowed glutamate detection.[135] Similarly, production of nanoelectrodes by modification of tungsten and niobium nanowires with carbon nanospikes for the detection of various NTs was also reported.[136]

Electrochemical sensors, while prominent in detecting NTs in the brain, are not the sole biosensor category employed for this purpose. Optical sensors have become increasingly important in the detection of NTs, complementing the traditional use of electrochemical sensors. Optical sensors offer distinct advantages, including superior temporal and spatial resolution, making them valuable tools for studying NTs dynamics in the brain.[85]

Non-genetically encoded optical sensors, such as carbon quantum dots and fluorescent carbon nanotubes, have shown promise in NTs detection. For instance, carbon quantum dots have been used in the development of electrochemical biosensors for the determination of depression-related NTs, demonstrating their potential in this field.[137] Additionally, fluorescent carbon nanotube-based sensors have been engineered to detect NTs such as dopamine and norepinephrine, with high sensitivity and selectivity.[138] However, it is essential to consider the limitations of optical biosensors (non-genetically encoded). While these sensors provide less invasive detection methods, they require precise delivery to target area and may not be applicable to specific cell types, posing challenges for their widespread application.[85]

Genetically encoded biosensors have emerged as an alternative to electrochemical methods and classical optical biosensors for the analysis of NTs, particularly suited for long-term studies of NTs dynamics in the brain.[85, 139] These biosensors are designed around two key components: a ligand-binding protein and a fluorescent domain. The fluorescent domain consists of a pair of fluorescent proteins for Fluorescence Resonance Energy Transfer (FRET)-based sensors or a single fluorescent protein. The operational principle of these biosensors relies on the conformational change induced by the binding of the target analyte to the ligand-binding protein, resulting in a variation in the fluorescent signal of the fluorescent domain.[85] Genetically encoded biosensors are designed through a sophisticated molecular engineering process integrating them into the genome of cells. This process involves the creation of DNA constructs, where the genes responsible for the ligand-binding protein and the fluorescent domain are combined. These engineered genes are then introduced into the cell

of interest, using techniques such as transfection or viral transduction. Once inside the cells, the genetic code instructs the cell itself to produce the biosensor. The output of genetically encoded biosensors, manifested as a variation in the recorded fluorescent signal, necessitates their use in conjunction with optical techniques capable of detecting fluorescence. These techniques encompass fiber photometry, multi-photon imaging, wide-field epifluorescence imaging, and super resolution (SR) imaging. The selection of a specific technique is contingent upon the experiment's requirements, considering the disparities in final spatial and temporal resolution and instrument complexity.[85] For instance, fluorescent sensors such as as iGluSnFR, dLight, and iSeroSnFR have been developed to detect respectively glutamate, dopamine or serotonin with single-neuron precision, shedding light on the spatiotemporal regulation of signaling networks.[84, 140] Furthermore, these fluorescent sensors, since they can be genetically encoded, offer unprecedented cell-type resolution. Additionally, FRET-based sensors have been successfully used to monitor steady-state levels of NTs, changes in response to external supply, and flux across membranes in living cells.[141] Genetically encoded sensors offer versatility for both *in vitro* and *in vivo* experiments, enabling the analysis of neurotransmitters (NTs) across various tissue types. Their internalization within cells allows continuous monitoring of NT dynamics directly in the cellular environment, supporting long-term and real-time observations. However, the engineering of these sensors is a complex and time-consuming process, demanding technical expertise in molecular biology for engineering variants with optimized optical features. In addition, genetic vectorization of these fluorescent sensors into a specific cell-type, or membrane compartments is not always feasible, limiting their use.[142] Furthermore, these fluorescent biosensors are derived from green fluorescent protein (GFP) which fluorescence is sensitive to pH variations and in all cases they also show cross-reactivity with other molecules. For example, the iAChSnFR sensor responds to both acetylcholine (Ach) and its precursor choline.[143]

1.2.3 Biosensors for D-serine detection

This section will provide an overview of the biosensors developed, over the past two decades, for the detection of D-serine, primarily focusing on electrochemical biosensors. Within this category, the role of enzymatic amperometric biosensors based on D-amino acids oxidase (DAAO) will be emphasized. due to their significance and alignment with the thematic focus of this thesis. Nonetheless, as we explore these enzyme-based sensors, we will also briefly touch upon other types of biosensors used for D-serine detection, including acoustic and optical sensors.

Excluding any mention of commercial biosensors, as they are no longer available, the introduction of electrochemical enzymatic biosensor for D-serine detection in the brain can be tracked back to 2008. In this first development, driven by the need for real-time localized measurements of

D-serine at single-cell level, *Pernot et al.* engineered a micrometric sensor designed specifically for detecting the neurotransmitter. The sensor's operation relied on a two-step enzymatic reaction involving the highly sensitive and selective enzyme DAAO, derived from *Rhodotorula Gracilis* (*Rg*DAAO). DAAO is a flavoenzyme responsible for converting D-amino acids into their corresponding α-ketoacids (in the case of D-serine, it produces hydroxypyruvate) while simultaneously generating equimolar quantities of hydrogen peroxide. During this process, Flavin adenine dinucleotide (FAD), a coenzyme associated with DAAO, undergoes reduction as it accepts electrons from D-serine, transforming into $FADH_2$. The H_2O_2 generated is subsequently oxidized at the surface of a platinum electrode, which is connected to an amplifier. The reaction is described in *equation 1*.

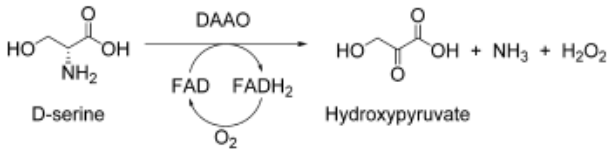

$$H_2O_2 \xrightarrow{Pt\ (500\ mV)} 2H^+ + O_2 + 2e^- \qquad \textit{(eq. 1)}$$

The resulting oxidation current is directly proportional to the concentration of D-serine present in the microenvironment surrounding the biosensor.[70] The sensor's structure is crafted by covalently immobilizing DAAO onto a micro-cylinder-shaped platinum microelectrode (25 µm diameter, 150 µm length), through glutaraldehyde crosslinking.

When designing a microsensor for detecting biomolecules within intricate matrices, such as the brain, it is imperative to prevent interaction with interfering molecules whose signals could affect the accuracy of the final results. In the case of D-serine detection, the presence of other electroactive compounds like ascorbic acid or monoamines in the brain, which share the same electrochemical potential window as hydrogen peroxide, must be taken into account. To mitigate the risk of non-specific adsorption onto the platinum electrode's surface, a semipermeable membrane of poly-phenylenediamine (PPD) is deposited on the electrode before immobilizing the enzyme. The semipermeable membrane operates on the principle of size-exclusion, effectively blocking larger interfering molecules while still permitting hydrogen peroxide to diffuse through and reach the platinum electrode. The resultant sensor reaches a limit of detection (LOD) of 16 nM and exhibits a specific sensitivity of 89 µA/mMcm^2. These sensors have been surgically implanted into the frontal cortex of anesthetized rats and have proven capable of detecting applied concentrations of D-serine, as it crosses the blood-brain barrier after injection, thus demonstrating their suitability for *in vivo* detection. It is worth noting that these electrodes are also sensitive to other D-amino acids that may

Institut Polytechnique de Paris
91120 Palaiseau, France

be present in the brain, notably D-alanine, for which DAAO exhibits even higher activity compared to D-serine. However, this sensitivity to D-alanine does not significantly affect the sensor's practical use. This is because D-serine remains the most prevalent D-amino acid in the central nervous system, and the concentration of D-alanine appears to be quite low in comparison.[70]

Following the same principle, two years later, similar sensors for D-serine detection were developed by *Zain et al.* These biosensors featured both cylindrical and disk-shaped electrodes constructed from 125 µm diameter platinum wires, coated with Nafion and PPD. Mammalian DAAO, derived from porcine kidney, was immobilized on the electrode surface. The resultant sensor demonstrated a specific sensitivity of 61 µA/mMcm^2 and exhibited a LOD of 20 nM.[144] The slightly lower sensitivity of this sensor can be attributed to the use of the mammalian enzyme version, which previous studies had characterized as less effective.[70] Similarly, another D-serine electrochemical sensor was developed using sol-gel immobilization of DAAO. This method allows the entrapment of the enzyme within a robust porous bilayer around the surfaces of cylindrical electrodes of various sizes. The resulting specific sensitivity (200 µA/mMcm^2) surpasses that of previous sensors due to the entrapment technique. However, it should be noted that this increase in sensitivity comes at the expenses of long term stability.[145]

Exploring alternative immobilization methods, *Vasylieva* and colleagues, in 2011, investigated the use of polyethylene glycol (PEGDE) for immobilizing enzymes on biosensors, including DAAO. The resulting cylindrical microsensors (25 µm diameter, 100 µm length) exhibited a sensitivity to D-serine comparable to that observed in previous studies and achieved a LOD of 0.8 nM.[146]

Traditionally, the use of cylindrical microsensors allowed to work with probes of dimension equal to or larger than single cells. This often leads to challenges in individuating the precise source location of the detected signal. In order to achieve more accurate spatial targeting, *Polcari* and colleagues made a significant improvement, in 2014, by developing a disk-shaped microsensor based on 25-µm diameter platinum wire. The enhanced sensitivity of these disk-shaped microsensors (276 µA/mMcm^2) is largely attributed to the geometry as well as the higher activity of the enzyme employed. In fact, disk-shaped microelectrodes are characterized by a spherical diffusion profile, and therefore higher current densities, leading to increased specific sensitivity (µA/mMcm^2). These sensors were effectively employed *in vivo*, measuring the chemically-induced release of endogenous D-serine in the brain of Xenopus laevis tadpoles.[71] Subsequent refinements and modifications of these electrodes included the optimization of the permselective PPD. In particular, it was observed that increasing the number of CV cycles used for the electro-polymerization of the PPD layer on the platinum surface leads to thicker polymeric coverage, better rejecting interferences. The optimal

deposition protocol was therefore established for suitable selectivity, while still maintaining good response time, that tends to increase when using a higher number of CV cycles. These electrodes were then employed for scanning electrochemical microscopy (SECM) measurements to map D-serine release from an artificial model system. The potential of these sensors as scanning probes, providing high spatial and temporal resolution, holds promises for investigating the primary site and mechanisms of release of D-serine, a subject that still carries many uncertainties.[147]

In the following years, ongoing advancements led to further improvements and modifications of these electrodes.[148] A miniaturized version of this micro-disk sensor was introduced in 2021 by *Moussa et al.* The sensor, based on a 10 µm diameter platinum wire, facilitates easier implantation, minimized tissue damage, and offer the potential for single-cell interrogation. Although the sensor is significantly smaller than its predecessors, its specific sensitivity remains comparable to earlier models. These sensors have been used *ex vivo,* for observing daily fluctuations in D-serine levels, and *in vivo*, enabling measurements within the brain of living tadpoles.[149]

A similar concept has been applied in the development of ceramic-based microelectrode self-referencing arrays for D-serine detection, designed for implantation into the brain of moving rats. The arrays consist of a pair of sensing electrodes, where DAAO is immobilized, along with a pair of reference electrodes. The reference electrodes serve the purpose of detecting signals related to background noise and interfering molecules that are subtracted from the sensor signals, allowing for a more accurate assessment of D-serine levels.[150]

Nevertheless, DAAO-based electrochemical biosensors are not the only types of sensors available for D-serine detection. Staying within the domain of electrochemical biosensors, several alternative approaches can be found in literature.[151, 152]

Non-electrochemical biosensors for D-serine detection are relatively less common, yet some notable examples exist. In 2016, a surface acoustic wave (SAW) biosensor was developed. This SAW biosensor operated by via an inactivated form of the enzyme *Saccharomyces Cerevisiae* D-serine Dehydratase. The modified enzyme, immobilized on the sensor substrate, binds to D-serine without converting it into pyruvate and, by closely monitoring the changes in acoustic wave properties, such as direction and velocity of propagation, this method allows for the detection of micromolar concentrations of D-serine with exceptional selectivity.[72]

Moreover, several attempts have been done to develop optical methods for sensing D-serine. For example, *Mothet et al.*, in 2005, used a highly sensitive bioassay to monitor extracellular D-serine content in cultured astrocytes. In particular, they used DAAO and HRP combined with luminol to probe levels of D-serine via luminescence variations, detected with a photomultiplier tube. Nevertheless, this method could only be used in cell culture and was not suitable for providing local

Institut Polytechnique de Paris
91120 Palaiseau, France

information about D-serine content.[26] In 2012, the enzyme *Saccharomyces Cerevisiae* D-serine Dehydratase was employed in the creation of an optical sensor for D-serine. In this approach, a nitrocellulose strip was coated with a solution of fluorescent dye, and affixed to a fluorescence cuvette filled with a solution of the enzyme. The introduction of D-serine in the cuvette caused a modification in the absorption spectrum, resulting in a change in the fluorescence intensity of the label.[153] In 2021, a computationally designed (FRET)-based optical biosensor was also engineered, starting from a D-alanine-specific solute-binding protein (SBP). Using two-photon excitation fluorescence for detection, the sensor has been tested in acute hippocampal rat brain slices, showcasing its response to exogenously applied D-serine. Moreover, its ability to respond to extracellular changes in D-serine levels in living animals has also been demonstrated.[69]

Nanosensors also found applications in combination with scanning probe microscopy (SPM) technique. In the context if this PhD work, one particular SPM technique, scanning ion conductance microscopy (SICM), has been utilized, as will be elucidated in the following sections. For this reason, section 1.3 will describe the principles and applications of SICM, starting from a more general introduction about SPM techniques.

1.3 Scanning Ion Conductance Microscopy

1.3.1 Scanning Probe Microscopy techniques

SICM is a SPM technique, a category encompassing a series of methods for surface topography and properties analysis. SPM involves scanning a probe across a specimen's surface to gather information, enabling the reconstruction of a detailed spatial map of the examined sample. Due to their capability for high-resolution visualization at the nanoscale down to atomic structures, SPM techniques are invaluable imaging tools across various scientific domains, including material science, nanotechnology, and biology.

The origin of SPM techniques traces back to 1981 with the development of Scanning Tunneling Microscopy (STM), recognized with a Nobel Prize in 1986 for its inventors, G. Binnig and H. Rohrer.[154] STM utilizes a sharp conducting tip to sense conductive surface based on the principle of quantum tunneling. When the tip approaches the analyzed surface and a bias is applied, electrons tunnel through the vacuum in between them. The resulting current, dependent on tip position, applied voltage, and local density of states, is monitored while the tip scans the surface, allowing the construction of a map. Modern STMs can operate in ambient environments, providing atomic-scale images of surfaces and broadening the technique's applicability.[155]

STM laid the groundwork for various SPM techniques, including Atomic Force Microscopy (AFM) in 1985.[156] AFM employs a cantilever with a tip at its extremity as a scanning probe, providing information by physically touching and sensing the surface, whether conductive or insulating. As the probe scans, the contact between the tip and the sample causes the deflection of the cantilever, proportionally to the sample's height. Detection of this deflection involves reflected lasers and a position-sensitive detector. AFM belongs to the broader category of Scanning Force Microscopy (SFM), that are based on sensing forces between a sharp tip and a surface while raster scanning the tip. SFMs can be classified by the nature of the forces utilized for signal generation.[157] Unlike AFM, non-contact forces are employed in SFM techniques like Electric Force Microscopy (EFM), utilizing electrostatic forces, or Magnetic Force Microscopy (MFM), measuring magnetostatic forces.[158] Various approaches derived from STM or AFM have been developed for scientific or industrial purposes, leading to a broad classification of SPM techniques, which now includes sub-techniques like Scanning Near-Field Optical Microscopy (SNOM)[159] and Scanning Thermal Microscopy (SThM).[160] SNOM involves scanning a fine optical fiber near a sample surface to use near-field effects for signal reconstruction, [159] while SThM utilizes a thermocouple junction at the tip of a metal probe to detect temperature variations on a sample.[160] Additionally, Scanning Capacitance Microscopy (SCaM) maps variations in dielectric properties by observing capacitance changes as a fine electrode scans a sample.[161] Scanning Electrochemical Microscopy (SECM) employs an ultra-microelectrode to probe local electrochemical behavior by measuring faradaic currents as a function of tip position, providing topographical imaging and reactivity information.[162]

SPM techniques have found application in the analysis of biological samples,[163] exemplified by AFM which, when extended to a liquid environment,[164] enables the examination of cell topography while immersed in physiological solutions. AFM has been employed in studying dynamic living systems, including migrating and dividing cells,[165] conformation changes of proteins,[166] and elastic properties of biological tissues.[167] Nevertheless, the contact-nature of the forces applied in AFM for topographical information on living soft samples imposes limitations. In contrast, Scanning Ion Conductance Microscopy (SICM) is employed for non-contact topographical mapping of biological specimens, as will be elucidated in the subsequent sections.

1.3.2 SICM Principle and imaging modes

SICM entails the scanning of a glass or quartz pipette across the surface of the target specimen to acquire relevant information to reconstruct a detailed spatial map of the sample under examination. In the subsequent sections, the working principles, primary modes of operation, and applications of SICM will be illustrated, shedding light on its significance in the analysis of biological samples.

Principle. The Scanning ion Conductance Microscopy (SICM) was developed by *Hansma et al.* (published in 1989), describing a scanning probe microscope able to image the topography of non-conductive samples immersed in an electrolyte containing solution.[168] SICM utilizes a glass pipette, filled with an electrolyte solution, as scanning probe, which is systematically moved over the sample for imaging. Illustrated in *figure 9a,* the working principle relies on the generation of an ionic current when a DC (direct current) potential *V* is applied between an electrode within the pipette (P_E) and another in the bulk solution (C_E). As the probe scans the sample surface, the current i_{DC} is continuously monitored and it exhibits a decrement when the distance (*d*) between the probe and the sample diminishes. This is due to the physical presence of the sample's surface that hinders the flow of ions towards the pipette's opening, increasing the local resistance of the overall circuit. In particular, the relation between i_{DC} and the voltage *V* can be expressed through different equations, modelling the influence of the geometrical characteristics of the probe and the resistive elements of the system on the measured current. In particular, Nitz model,[169] is characterized by ease of implementation and good agreement with experimental data. It is based on the computation of the total resistance between the pipette and the electrode, R_{tot}, as a sum of two resistances: R_p, resistance of the pipette, and R_z, access resistance, as shown in *equation 2a.* The pipette resistance, R_p, is due to the geometry of the probe and the conductivity of the electrolyte, and can be computed as shown in *equation 2b*, where r_i is the radius of the tip opening, r_e is the radius of the tip base, h is the tip length, and k is the conductivity of the electrolyte. The access resistance, R_z, is due to the conductivity of the electrolyte in solution and the gap between the tip and the interface. It can be calculated according to *equation 2c*, where r_o is the outer radius of the tip opening, and d is the tip-to-sample distance. The relation between i_{DC} (d) and *V* can therefore be computed as shown in *equation 2d*, where the bulk current, i_∞ is defined as $\frac{V}{R_p}$.

$$R_{tot} = R_p + R_z \quad \textit{(eq. 2a)}, \qquad R_p = \frac{h}{k*\pi*ri*re} \quad \textit{(eq. 2b)}, \qquad R_z = \frac{{}^3\!/_2 * ln\,(ro/ri)}{k*\pi*d} \quad \textit{(eq. 2c)},$$

$$i_{DC}(d) = \frac{V}{R_p+R_z} \approx i_\infty \left(1 + \frac{{}^3\!/_2\, ln(ro/ri)*ri*re}{h*d}\right)^{-1} \quad \text{with } i_\infty = \frac{V}{R_p}. \quad \textit{(eq. 2d)}$$

The current decrement, indicative of the reduced ion flow space, occurs before any physical contact is established, enabling non-contact detection of the surface presence. During lateral scanning, a feedback mechanisms aims to keep the tip-to-sample distance constant by utilizing piezo-actuators that adjust the probe position and trace the underlying surface's topography.[168]

Institut Polytechnique de Paris
91120 Palaiseau, France

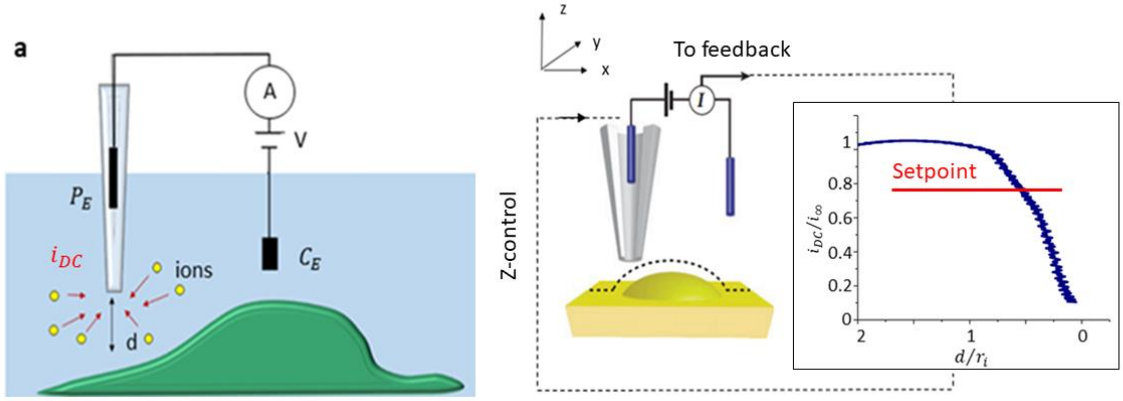

Figure 9. SICM working principle in DC mode
a) schematic representation of the working principle of the scanning ion conductance microscopy technique. b) Figure modified from *Chen et al.*[170] During raster scanning, the probe is vertically positioned using a stepper motor or piezoelectric positioner. As the scan proceeds, i_{DC} is continuously monitored. The vertical movement of the probe stops when the current reaches a predetermined value corresponding to a desired distance between the tip and the sample surface. Throughout the scan, this current value is maintained constant by feedback mechanism, ensuring a stable tip-to-sample distance. Any deviations from this setpoint are detected as changes in current, leading to adjustments to the vertical position of the probe to maintain the desired distance.

In *figure 9b*, an approach curve is depicted, illustrating the trend of the measured ionic current, normalized to the current bulk value I_∞, as a function of the distance d between the probe and the sample, normalized to the internal radius of the probe (r_i). Notably, as the probe is in the bulk solution far from the sample surface, the ionic current remains relatively constant and equal to the bulk value. As the pipette vertically approaches the surface, a sudden decrement in the current i_{DC} occurs when the tip-to-sample distance d becomes comparable to the radius r_i of the probe. This abrupt change in current serves as the basis for the feedback mechanism of SICM, elucidated in further detail in the schematic presented in *figure 9b*.

At the initiation of the raster scan, the probe undergoes a controlled vertical approach facilitated by a stepper-motor or piezoelectric positioner, concurrently with continuous monitoring of the i_{DC}. The vertical advancement of the pipette stops in the proximity of the surface of the sample when the current reaches a specific chosen value, corresponding to a desired tip-to-sample distance, as previously determined by the approach curve. This particular i_{DC} value is therefore established as a setpoint and maintained constant throughout the mapping experiment by the feedback mechanism, ensuring a constant and stable tip-to-sample distance. To achieve this, while the probe is laterally displaced along the XY direction during the raster scan, i_{DC} is continuously measured, being any deviations from the setpoint understood as physical approach or distancing of the tip from the sample. This difference between i_{DC} and the setpoint is processed by the feedback to trigger the piezo actuators to adjust and counterbalance these variations in vertical position.

SICM has demonstrated remarkable applicability in the imaging of soft biological materials, due to its truly non-contact interaction with the sample. This minimal invasiveness, permits the

Institut Polytechnique de Paris
91120 Palaiseau, France

analysis of biological surfaces and interfaces in liquid solutions without compromising their integrity and enables observations in a more realistic and unaltered state, compared to other techniques suitable for the characterization of the topography of biological specimes.[171, 172]

For example, another method is Scanning Electron Microscopy (SEM), which can also provide high-resolution imaging of biological samples. Comparative studies on images obtained with SICM and SEM for various fixed cell types indicate that SICM achieves imaging quality comparable to SEM.[173] Nevertheless, unlike conventional SEM, SICM operates in a wet environment, enabling the investigation of dynamically changing samples without the need for cell fixation. SEM, on the other hand, requires cells to be rendered conductive, leading to morphological shrinkage and alterations compared to their natural state.[173] However, it is important to acknowledge the existence of advanced SEM variants, such as environmental SEM (ESEM),[174] which facilitate the imaging of biological samples in a wet environment and a more natural state than standard SEM.

Within the domain of scanning probe microscopy methodologies, Atomic Force Microscopy (AFM) has also been extensively employed for mapping cellular topographies. Numerous comparative investigations between AFM and SICM have been reported. In a study conducted in 2011, *Rheinlaender et al.* employed both SICM and AFM to assess their capabilities to map fixed human fibroblasts.[171] The overall topography of the entire cell was distinctly observable with both methodologies. However, AFM exhibited a reduction in both height and width dimensions of the sample in comparison to SICM. This discrepancy can be attributed to the inherent feedback mechanism of AFM, which involves the application of forces between the cantilever and the cell that lead to cell indentation and cause cell deformation. Furthermore, AFM was also associated with lateral deformation of the sample, discernible in consecutive scans. Additionally, AFM exhibited limitations in mapping weakly attached details, as the tip had a tendency to displace them. Conversely, SICM demonstrated superior capabilities in mapping such features. Similar observations were extended to micrometric lateral processes and cellular details, with SICM exhibiting enhanced resolution.[171] These distinctions were further highlighted in studies involving non-fixed living cells, such as the work by *Seifert et al.* in 2015 on epithelial A6 cells and Mouse Embryonic Fibroblasts. Their findings confirmed those observed in fixed cells and underscored the notion that, in AFM, lateral resolution is significantly influenced by the elastic properties of the examined cell.[172] Despite the suitability of SICM for delineating cellular surface topography, AFM was employed to reveal elements of the cytoskeleton, due to its capacity to sense details beneath the surface.[171]

Modulated modes. SICM operating in DC mode can experience drifts or localized changes in the measured current that can lead to topographical artifacts or the damage of the probe and sample.

Consequently, to mitigate this challenge, the evolution of new imaging modes, specifically modulated modes, has been introduced.

In 2001, *Shevchuk et al.* proposed a new SICM mode by introducing a modulation of the tip-to-sample distance. Thanks to this modulated mode, it was possible to image contracting myocytes, an extreme example of cells undergoing rapid changes in volume (around 4 µm in 200 ms), with a spatial resolution ranging from 10 nm to several micrometers and with milliseconds temporal resolution.[175] In this modulated mode, in addition to the constant voltage applied between the electrodes, a small oscillation is applied to the piezo controlling the displacement of the pipette in the z-direction, inducing a small vertical movement of the probe (10-20% of the tip's opening size). This oscillation leads to an alternating current (AC) component in the measured ionic current, that is extracted with a Lock-in Amplifier, as illustrated in *figure 10a*, utilizing as reference signal the same frequency as the probe's vibrational frequency. *Figure 10b* illustrates a comparison between the two signals, DC and AC, during an approach curve. As seen, the AC component value of the current becomes significant when the tip-to-sample distance reaches values comparable to the pipette's size. Compared to DC mode, where even slight variations in current can render feedback difficult or impossible, AC mode can handle substantial variations in i_{DC} (e.g. partial tip clogging or changes in ionic strength) due to a minor impact on AC (around 1-2 % of observed DC variations).[175] This characteristic allows for the execution of complex biological experiments.

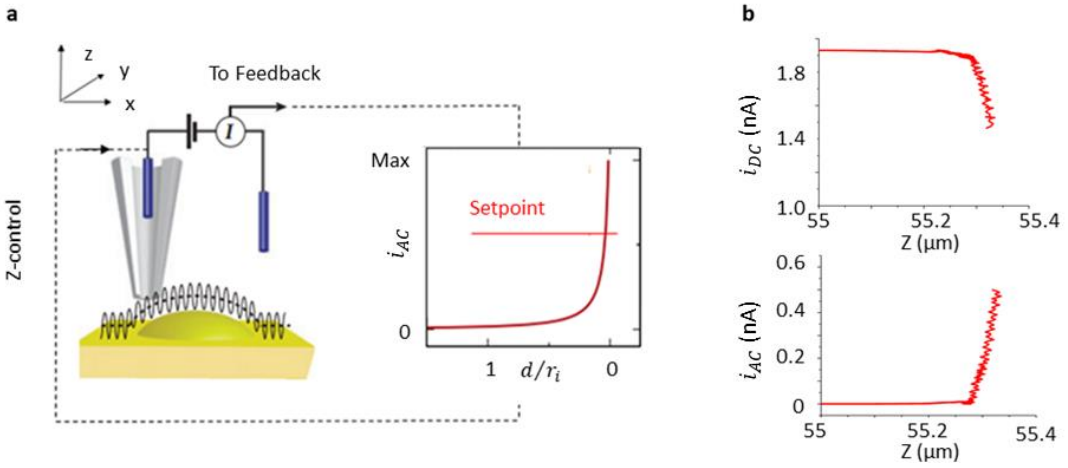

Figure 10. AC modulated mode.
a) Schematic of the feedback mechanisms in the AC modulated mode. Modified from Chen et al.[170] b) Comparison between the DC and AC approach curves.

Compared to AC, DC feedback has a less steep current- tip-to-sample distance dependence, risking probe crashes and necessitating larger distances for imaging. AC feedback's steeper dependence allows operation at smaller distances, even a few nanometers, enhancing spatial resolution by minimizing the risk of crashes and optimizing sensitivity.[176]

Institut Polytechnique de Paris
91120 Palaiseau, France

The adoption of AC modulated mode does not signify the abandonment of DC current recording. When operating in AC mode, the simultaneous recording of i_{DC} offers additional valuable information that might not be discernible solely with the topographical mapping. This is exemplified by samples in where variations in i_{DC} (not repeated in AC) cannot be attributed to topographical changes but to localized alterations in electrical potential due to the activation of ion channels or other specific membrane components, providing insights that contribute to a more comprehensive understanding of the sample under investigation.[176]

A distance modulation of the probe can induce convective movements of the fluid around the pipette's tip, potentially impacting the microenvironment under observation. Addressing this concern, in 2014, *Unwin et al.* proposed a novel modulated SICM mode based on applying a small (10 mV) oscillating bias between the QRCEs.[177] The resulting i_{DC} is sent to a Lock-In amplifier to extract the magnitude and phase of its AC component. Either the amplitude or the phase can serve as a feedback signal for the vertical positioning of the tip due to their dependence on the tip-to-sample distance. Furthermore, if the bias oscillation is centered around a 0 V DC value, no net current flux is produced, minimizing issues such as polarization of the QRCEs or perturbation of the electrolyte concentration around the probe. Additionally, electro-osmotic movements of the fluid inside the pipette are minimized.

Hopping imaging mode. Up to this point, we have delineated the conventional method for scanning the probe atop the sample, involving a raster movement in the XY direction after vertically approached the sample. Specifically, we have described a constant distance mode wherein at the initiation of the scan, the probe is vertically approached to the sample's surface and stops in proximity of the sample, in accordance with the defined setpoint (whether based on the DC or AC current). During the subsequent raster scan of the probe on the sample, the feedback mechanism ensures the maintenance of the current at the predetermined threshold, as represented in the schematic of *figure 11a.* However, this method clashes to map protruding samples such as living cells with heights up to 10 µm, posing a risk of the pipette colliding with the sample during the lateral movement. This collision can lead to deformation of the samples, introduction of imaging artifacts, or even breakage of the probe, particularly when dealing with hard samples. To address this concern, in 2009, *Novak et al.* introduced Hopping Probe Ion Conductance Microscopy (HIPCM), a subtype of SICM that differs solely in the method of performing the vertical movement of the probe.[178]

Institut Polytechnique de Paris
91120 Palaiseau, France

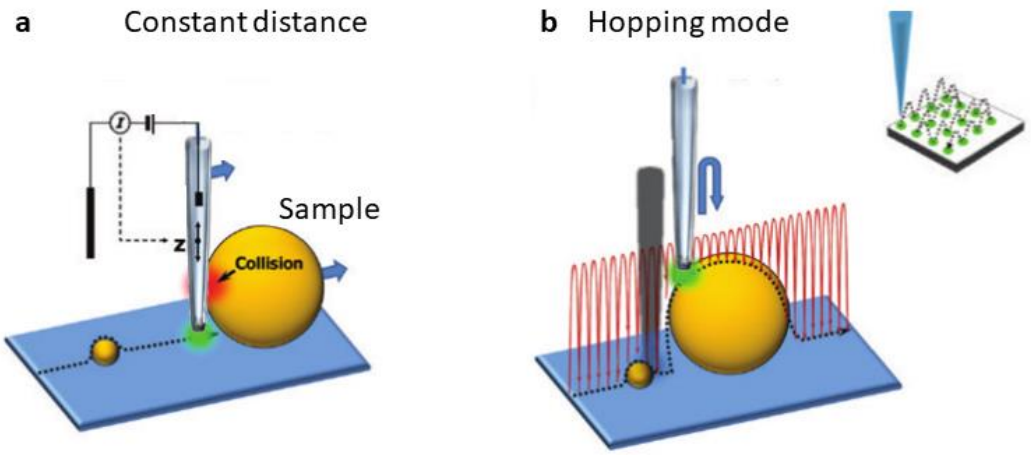

Figure 11. Movements of the probe in different imaging modes.
a) Schematic representing the vertical movement of the probe when operating in constant distance imaging mode, leading to the risk of lateral collision with convoluted samples. b) Schematic representing the vertical movement of the probe when operating in hopping imaging mode. Figures are taken from Novak et al.[178]

Within HIPCM, the probe is scanned over the sample as a series of "hops", as shown in *figure 11b*.[178] More in detail, the probe starts each imaging point from a position higher than the roughness of the structures under measurement, where the current corresponds to a bulk value. Subsequently, the probe is vertically approached to the surface until a predefined setpoint value (DC or AC) is reached, at which point the probe stops and sets the value of the sample height. The pipette is then retracted by a user-defined distance, moves laterally to the subsequent imaging point and initiates another approach.[178] Alternatively, instead of a lateral movement of the probe, the sample itself can be shifted beneath the probe, achieving the same effect.[179] It is worth noting that the XY resolution of the resultant topographical map is determined by the number of pixels, in this case set by the distance the probe traverses between successive approaches, or hops. A notable drawback of HPICM, compared to standard SICM, lies in the increased scan time due to the multiple withdrawals, lateral movements, and subsequent re-approaches of the probe for each imaging point. To mitigate mapping time, the withdrawal distance can be adjusted to position the pipette just above the roughness of the specific area, as predefined by a prior low-resolution scan. This adaptive approach demonstrated a 70% reduction in the time required to map the full topography of a hippocampal neuron.[178]

1.3.3 SICM Imaging of living neurons

It wasn't until 1997 that the first instance of SICM imaging of living cells emerged. In their study, *Korchev et al.* successfully obtained topographical maps of highly convoluted surfaces and delicate cellular structures while keeping the cells viable and active.[180] Remarkably, they demonstrated the capability to track entire cell movements and small-scale cellular dynamics without the need for any specimen preparation prior to measurement.[181] In recent years, there have been important

developments in using SICM to study neurons, offering multiple insights into their morphology. In 2002, *Mann et al.* employed pulse-mode SICM to achieve the first high-resolution images of a single rat neuron with a lateral resolution of 500 nm. This method allowed detailed mapping of complex neuronal structures that may pose challenges due to the non-tight adhesion of the lateral processes.[182] In 2009, *Novak* and colleagues, to further address the challenges encountered in mapping intricate structures within neural networks, used HIPCM to acquire topographical maps of hippocampal rat neurons, revealing fine details with impressive 20 nm resolution. The images captured synaptic buttons (50-60 nm structures) and thin filaments forming neuronal network connections, highlighted by the white arrows in *figure 12a*.[178] In the same year, *Happel et al.* conducted long-term observations of neuronal cells. Through repetitive and non-damaging scans, they monitored the shape variations of a cell for several hours. Moreover, they tracked the process of connection formation between two nerve cells achieving nansoscale resolution, as depicted in *figure 12b*.[183] To record cellular movement, *Gesper et al.*, in 2015, observed the migration of a mouse neuron from the dorsal root ganglion, revealing migration speed of 20 µm/h, accompanied by variations in the neuron's morphology.[184] Another instance of monitoring intriguing morphological variations involves the observation of PC12 cells differentiation by *Yang* and colleagues. Correlating SICM imaging with patch-clamp electrophysiological measurements, they compared morphological variations with increased electrical excitability. *Figure 12c* illustrates their series of observation at days 0, 3, 6, and 9 post Nerve Growth Factor treatment. Notably, the SICM topographical maps reveal progressive neurite outgrowth, increased cellular volume, and decreasing roughness as differentiation progresses.[185] Similarly, time-lapse images of morphological changes during apoptosis of rat cortical neurons were also investigated via SICM.[186]

In 2016, *Shevchuk et al.* showcased the versatility of SICM imaging by introducing an innovative angular approach. They connected the pipette to a patch-clamp micro-positioner, incorporating an angular tilt relative to the sample plane, thus enabling suitable optical illumination, overcoming the obstruction caused by the vertical positioning of the tip. They demonstrated significant potential in revealing the topography of lateral side areas of rat hippocampal neurons, typically inaccessible with standard SICM.[187]

To investigate topographical variations associated with Parkinson's disease, *Wong Su et al.* utilized SICM on SH-SY5Y cells, commonly used in neurological disorders studies, and examined the impact of alpha-synuclein (α-syn) addition. They obtained a topographical map at a spatial resolution of 30 nm and the image revealed pore formations in the cellular membrane with diameters ranging from 100 nm to a few micrometers. Additionally, the in-situ addition of α-syn induced further morphological variations.[188]

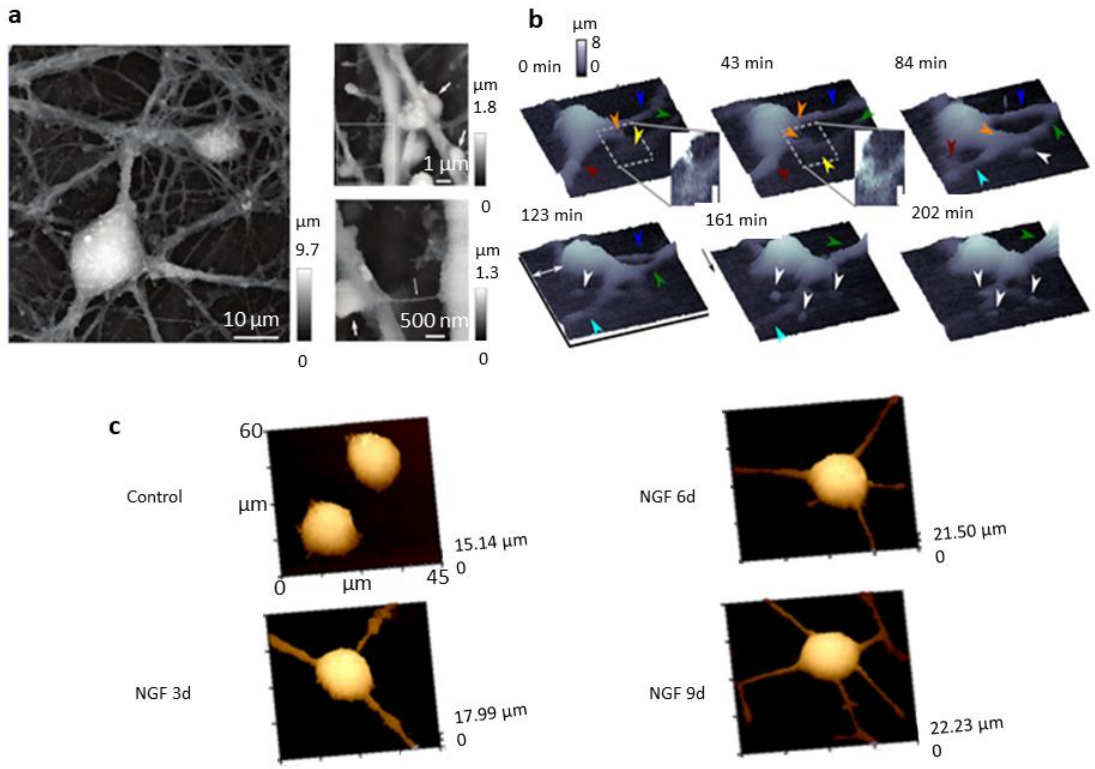

Figure 12. SICM imaging of living neurons.
a) SICM imaging of a network of hippocampal rat neurons. White arrows indicate thin filaments and synaptic butons.[178] b) Set of SICM images of a living neurons, conducted during more than 3 hours.[183] c) SICM images picturing the differentiation process of PC12 cells.[185]

1.3.4 SICM as a multifunctional technique

The utility of SICM probes, specifically monobarrel non-conducting nanopipettes, extends beyond their high-resolution imaging capabilities. The precise mapping of cellular structures has facilitated the use of SICM images as guides for accurately positioning pipettes in defined locations, enabling various types of local measurements.

Mechanical Stimulation. In 2007, *Sanchez et al.* employed SICM to investigate mechanosensitive ion channels on the surface of a dorsal root ganglion sensory neuron, whose function had long remained unclear due to the lack of suitable non-invasive stimulation technique. Through SICM, the researchers could precisely position the probe over the area of interest, enabling non-contact stimulation by applying a controlled pressure jet without causing damage to cellular structures.[189] Similarly, using SICM for mechanical stimulation of cells, *Pellegrino et al.* investigated the role of SICM imaging in directing the growth of neuronal cones in leech neurons, whose imaging is challenging due to their high mobility and fragility. SICM proved to be suitable for acquiring

topographical information, and the researchers observed how the imaging process itself, specifically the interaction between the probe and the sample, influenced the growth modeling when operated at an appropriate distance. According to the chosen scanning direction, researchers could guide the formation of connections between different cells that persisted for several hours, indicating their non-temporary nature. An example of connection creation is illustrated in *figure 13a.*[190, 191]

Mechanical properties measurements. SICM can be used to determine local stiffness by observing the variation of the slope of the approach curves in close proximity of the cell surface and by measuring the decrement of ionic current at different setpoints, as a result of the application of a pressure by the tip on the cell surface.[192, 193] Alternatively, the determination of the local cellular stiffness is based on the recording of the vertical movement of the pipette that, connected to a feedback mechanism that keeps the tip-to-sample distance constant, follows the indentation of the cell surface provoked by the application of an external pressure.[194] AD is characterized by the formation of ß-amyloids aggregates on the neuronal membrane, linked to the reorganization of the cytoskeleton and resulting in variations in the cell's mechanical properties. *Kolmogorov et al.* employed SICM to associate topographical information with stiffness measurements on SH-SY5Y cell membranes. Upon application of ß-amyloids, a disruption of the membrane structure was observed, accompanied by the formation of anomalous surface structures, as depicted in *figure 13b*, and an increase in the Young modulus across the entire cell. Conversely, in the regions where these structures formed, the Young modulus was locally decreased.[195] Disruption of neurotransmission, such as that induced by excitotoxicity and hyper activation of NMDA and AMPA receptors, is knows to lead to deviations from natural mechanical characteristics and cytoskeleton reorganization. Again, Kolgomorov et al. showed how SICM could locally deliver controlled amounts of glutamate at dendrites and soma locations and subsequently observed variations in hippocampal neuron morphology and Young's modulus. The results showed an increase in the cell's volume and a rapid decrease in Young's modulus, as illustrated in figure 13c , demonstrating the powerful capability of the technique in establishing correlations between chemical stimulation and variations in mechanical characteristics.[196]

Institut Polytechnique de Paris
91120 Palaiseau, France

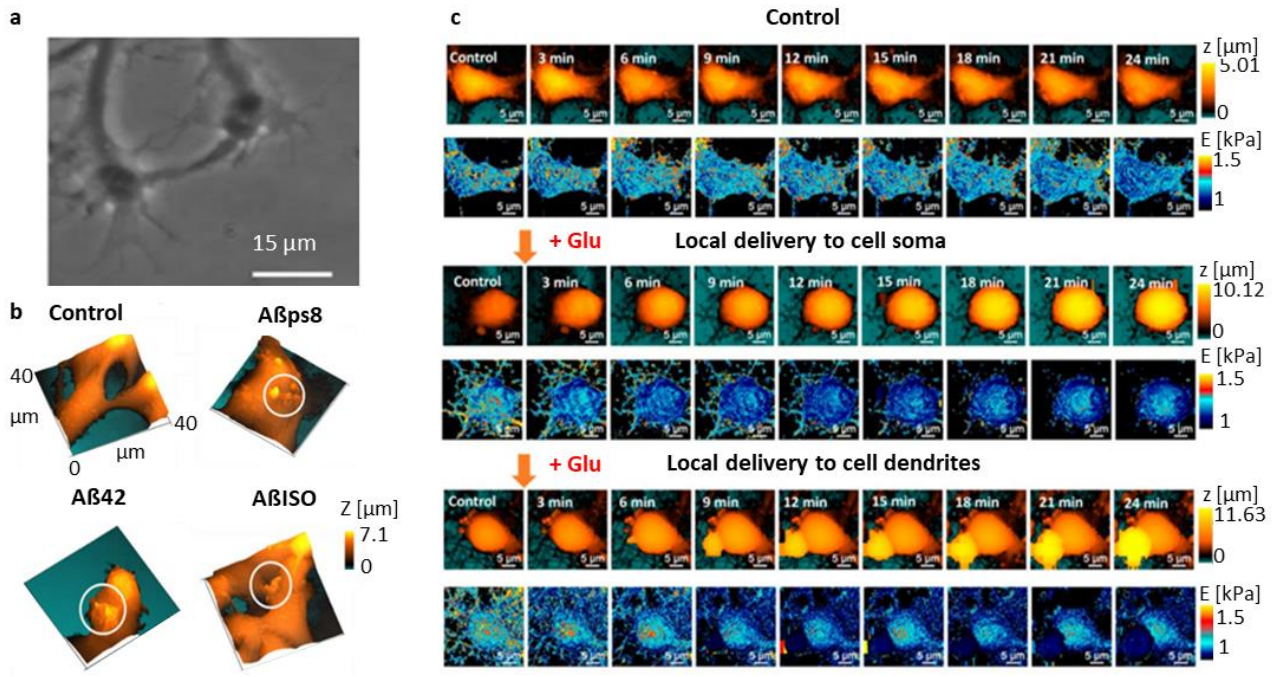

Figure 13. SICM as a multifunctional technique.
a) Optical image of the connection created between two neurons using SICM to redirect neuronal growth cones.[190] b) SICM topographical map showing the formation of novel structures after the treatment with different types of ß-amyloids.[195] c) Topographical variations and mechanical properties variations after local glutamate administration at soma and dendrites of neurons.[147]

Delivery and uptake at single cell level. Nanopipettes also serve, in single-cell analysis, the functions of aspiration and delivery. *Actis et al.* demonstrated the non-disruptive retrieval of genetic material from living cells using SICM nanopipettes, based on the principle of electrowetting. This technology, when integrated with SICM, enables precise probe localization for accessing specific areas of interest. The extracted material can undergo characterization through complementary techniques.[197] A similar non-invasive approach, employing double-barreled probes, has been employed for extracting DNA, proteins, nucleic acids, and mitochondria from living cells, allowing simultaneous acquisition of topographical information.[23] Nanopipettes also play a role in delivering specific molecules at the single-cell level. For instance, *Bruckbauer et al.*, in 2007, integrated nanopipettes into a SICM system for voltage-controlled, precise delivery of fluorescent molecules to cell membranes, facilitating studies on glycoprotein diffusion on different domains of boar spermatozoa cells.[198]

SICM combined with other techniques. Combining nanopipette-based delivery systems with SICM imaging demonstrates enhanced capabilities. *Takahashi et al.* illustrated this by using a double-barrel pipette for simultaneous topographical SICM mapping and electrochemical activity measurements on PC12 cells. The functionalized barrel allowed the use of the pipette as SECM probe, enabling the detection of electroactive species, while the unmodified barrel was utilized for precise positioning, as

Institut Polytechnique de Paris
91120 Palaiseau, France

SICM mode.[132] Additionally, in 2017, SICM and SECM measurements have also been combined to study cellular uptake.[199]

SICM has also been coupled with the patch-clamp technique, that is an electrophysiological method employed in neurobiology and cell biology for studying individual cell electrical activity. In a study from 2000, *Korchev et al.* employed the label-free SICM technique to detect single ATP-controlled K^+ ion channels on the plasma membrane of living cardiomyocytes. This innovative approach combined patch-clamp with topographical imaging, utilizing a K^+ filled nanopipette for mapping and controlled local cell stimulation, while a separate patch-clamp pipette simultaneously detected electrical activity. The correlation of topographical maps with pixel-by-pixel electrical current information allowed for the localization of K^+ channels on the cell membrane.[200]

SICM has also been effectively combined with optical techniques, as demonstrated in a study by *Korchev* and colleagues, proposing a SICM-SNOM approach that provided near-field optical images of living cardiomyocytes. This hybrid technique utilized a micro-fiber as a light source within a laterally coated aluminum SICM probe, for precise control of the probe-to-sample distance, crucial for obtaining SNOM information in the proximity of the sample.[201] In addition, in other studies, the modification of glass nanopipettes' external surfaces with nanoparticles facilitates applications in Surface-Enhanced Raman Spectroscopy (SERS) intracellular measurements, that have been used to detect intracellular environment variations on HeLa cells, after insertion in the cytoplasm.[202] In a recent advancement, silver nanoparticles decorated nanopipettes, were used for simultaneous cellular topographical imaging, Young modulus estimation, and intracellular SERS measurements.[203]

Sensing. Label-free sensing at single-cell level, both intracellular and extracellular, is feasible thanks to the minimally invasive structure of the nanopipette. In the realm of sensing, nanopipettes have initially been employed for surface charge mapping, providing crucial insights into the distribution of charged species on cellular membranes.[204, 205] In addition, modification of nanopipettes has paved the way for the development of diverse types of sensors.

For example, the development of nanopipette pH sensors has been driven by its relevance in biological applications. In 2019, high-resolution label-free 3D mapping of extracellular pH in single living cells was achieved using a dual-barrel nanopipette sensor, using a zwitterionic membrane. The pH detection, coupled with SICM's potential for precise positioning and 3D mapping, allowed monitoring dynamic variation of pH cancerous cells, revealing heterogeneous distribution.[206] Other approaches for the modification of nanopipettes for pH sensing included external decoration with gold nanoparticles that, combined with SERS technology, can be used to analyze intracellular pH in HeLa cells in response to variation in external pH.[207]

Nanopipettes-based sensing can also detect naturally electroactive entities within cells, as NTs like dopamine. In 2014, *Actis et al.* created nanopipette-based platinized disk-shaped nanoelectrodes for detecting oxygen consumption in a mouse hippocampal brain slice, highlighting high free radicals' concentration in cancerous melanoma cells.[133] In 2018, redox metabolism at the subcellular level was investigated using nanopipette-based sensors with ultra-small 30 nm openings functionalized with G-quadruplex (G4) DNAzyme. These modified pipettes penetrated cells and enabled the monitoring at high-spatial resolution of reactive oxygen species (ROS) production and oxidative stress, in continuous and in 3D, across various cell types.[208]

Sensitive and selective sensors for specific molecules like DNA have also been produced, by modifying nanopipettes with dendrimers.[209] ATP has also been sensed through nanopipette sensors, such as a dual-barrel nanopipette in which a poly-pyrrole Field Effect Transistor (FET)-based nanosensor functionalized with the enzyme hexokinase, was constructed. The sensor allowed for the detection of ATP and pH changes in clusters of melanoma cells.[210] Another molecule of interest at single-cell level is glucose and researchers have modified the inner walls of a nanopipette with GOx to enable the detection of intracellular glucose levels. This sensor, integrated into a SICM system, accurately positioned the nanopipette for probing and insertion. This approach revealed cancerous cells expressing reproducible and reliable increases in glucose levels compared to healthy cells.[211]
Taking into account the potentialities of nanopipettes functionalization for sensing purposes, we will now describe the objective of my PhD work.

1.4 Objectives

Recalling what said in section 1.1 of this chapter, it becomes evident that unraveling the mechanisms ruling NMDARs functions, and notably the roles of D-serine, holds paramount significance, since they are related to physiological processes and pathological conditions. Notably, due to the numerous evidences linking NMDARs with neurological disorders lacking effective treatment, there exists an urgent need to develop suitable techniques for microscopic and nanoscopic online measurements methods for D-serine. Electrochemical biosensors are a method of choice for studying NTs concentrations in both *in vivo* and *in vitro* studies without the need to introduce genetic modifications to the biological preparations. This preference stems from their high sensitivity and selectivity, rapid response, user-friendly operation, and potential for miniaturization. These qualities surpass those of traditional analytical measurement techniques (section 1.1.2.1) which, despite their analytical capabilities, lack temporal and spatial resolution. Notably, enzyme-based electrochemical sensors have already been utilized to detect D-serine in the brain.[70, 147, 149] This is the context of my PhD project.

Specifically, my work encompasses two main objectives:

1) To apply electrochemical enzyme-based micro-sensors[70, 71, 149] to explore the role of D-serine in brain slice model of epilepsy. Briefly, the operational principle of these sensors, illustrated schematically in *figure 14*, involves modifying a platinum microelectrode surface with the enzyme *Rg*DAAO. These sensors also incorporate a polymeric layer of PPD, depicted in red in *figure 14a*, to enhance the final sensor selectivity. The degradation of D-serine, depicted in *figure 14b*, generates stoichiometric amounts of hydrogen peroxide. By applying a suitable voltage bias to the platinum electrode, hydrogen peroxide oxidizes on the platinum surface, leading to a measurable current signal proportional to the original amount of D-serine.

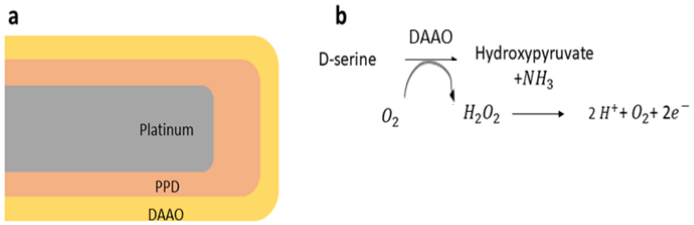

Figure 14. Principle of D-serine sensor.
a) Schematic representation of a micron-sized biosensor for D-serine detection: a platinum wire is coated with a layer of PPD and one of *Rg*DAAO; b) Reaction allowing D-serine detection at the micro-biosensor.

2) Because micro-sensors are unsuitable for analyzing individual cells, or nanodomains and synapses, I next envision the development of the first nano-biosensors for D-serine detection. I propose developing an analytical tool based on SICM. In my approach, nanopipettes will be employed as probes for measuring D-serine levels with sub-micron resolution, by means of a sensor integrated on the tip of the probe itself. To be able to combine imaging and sensing capabilities, I utilize double-barrel nanopipettes. One of the barrels will be functionalized by embedding a nanosensor in it, while the other will remain untouched for SICM topographical mapping and position control. Ideally, the fusion of SICM imaging capabilities with advancements in tip engineering will become a valuable tool, enabling the measurement of NMDARs co-agonist concentrations in a network of mature neuros, concurrently providing the topography of the synapses where the molecule is active.

Institut Polytechnique de Paris
91120 Palaiseau, France

Chapter 2. Micro-sensors for D-serine detection

2.1 Introduction

This chapter will describe the development and application of micrometric sensors designed for detecting D-serine. These sensors rely on the immobilization of the enzyme *Rg*DAAO onto a platinum electrode.[70, 149, 212]

This chapter will be divided in two parts. The first part will describe the process of fabrication and characterization of the sensors for D-serine detection.

The second part will describe an application of these sensors to measure D-serine levels in biological samples.

2.2 Micro-sensors fabrication and characterization

2.2.1 Materials and methods

Electrode structure fabrication and cleaning. To fabricate the structure of the micro-sensors, 25 µm diameter platinum wire characterized by 99.9% purity (WR-000113, Goodfellow) were linked to a copper wire (0.3 mm diameter) using electro-conductive silver paint (RS Components), and this assembly was carefully inserted into a tapered glass capillary (B120-69-10, Sutter Instruments). The capillary was pulled using a laser puller (P2000, Sutter) to achieve a tapered apex that was cut to enlarge its opening. The apex of the tip was sealed with epoxy resin to expose only the platinum to the external environment and the resin underwent curing beneath a UV lamp (wavelength λ 254 nm, CAMAG) for 30 minutes. This step of the functionalization prevents the solution to leak into the glass structure during measurement. In addition, this allows to control constant exposure of the platinum length to the solution, for functionalization and testing, by immersing the electrode structure at least until the sealing point. Subsequently, the platinum wire was cut with a scalpel to the desired exposed length of 1 mm, resulting in the formation of a micro-cylinder structure. Nevertheless, the cutting process is performed manually. Therefore, before providing the length of each sensor, the micro-electrodes were inspected via an optical microscope. A connector pin was introduced to ensure proper electrical contact during measurements. The tip of the final structure was immersed in a solution containing 0.5 M KOH (Sigma Aldrich) in MilliQ water (18.2 MΩcm at 25 ℃) for 20 minutes. This step was followed by 20-minutes immersion in ethanol, to clean the exposed platinum from any impurities originating from the fabrication process. *Figure 15* describes the process of fabrication of the micro-sensors structure.

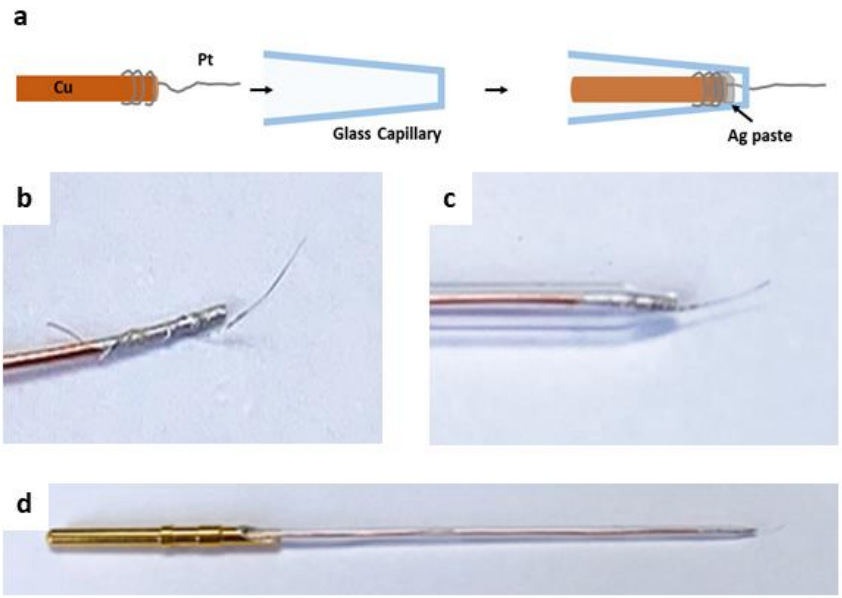

Figure 15. Steps of the micro-sensor structure fabrication.
a) Schematic representation of the phases for micro-sensor structure fabrication. b) connection of a 25 µm diameter platinum wire to a thicker copper wire, c) insertion of the copper-platinum wire in a glass capillary, d) connection of the back part of the sensor with a metallic pin.

Microelectrode functionalization. For functionalization of the sensor, a layer of PPD (Sigma Aldrich) was electro-polymerized onto the platinum surface by immersing the electrodes in a solution of 0.01 M PBS containing 100 mM PPD. Employing a potentiostat (1010B, Gamry Instruments), the electrode's potential was swept between -0.1 V and 1 V for 5 CV cycles against an Ag/AgCl reference electrode, at a scanning rate of 100 mV/s. The experimental setup consisted of a 3-electrodes configuration, with a platinum wire serving as the counter electrode. Following the deposition of PPD, the removal of unbound monomer was accomplished by applying 5 CV cycles between -0.1 and 0.5 V vs Ag/AgCl at a scan rate of 100 mV/s while immersing the electrodes in PBS.[212] The 0.1 M PBS is composed of 137 mM NaCl, 2.7 mM KCl, 10 mM Na_2HPO_4, and 1.8 mM KH_2PO_4 in MilliQ water. The 0.01 M PBS was prepared by diluting the 0.1 M PBS in MilliQ water. All chemicals were purchased from Sigma Aldrich. The Pt-PPD electrode underwent further functionalization by immobilizing *Rg*DAAO, kindly provided by the Protein Factory 2.0 Laboratory of Universita' dell Insubria (Varese, Italy). The enzyme, supplied at a concentration of 54 mg/ml, along with 27 mg/ml of Bovine Serum Albumin (BSA) in PBS (pH 7.4) containing 1% (v/v) glycerol, was immobilized by dipping the electrode in the enzyme solution for 30 seconds, repeated 4 times, with a drying interval of 4 minutes between each immersion. Subsequently, the biosensor was placed in a desiccator containing 10 ml of 50% (v/v) glutaraldehyde solution (Sigma Aldrich) for 15 minutes for PPD-DAAO crosslinking.

Storage. Between fabrication and utilization, the sensors were stored in a sealed box at -20°C.

Detection of hydrogen peroxide. The characterization of micro-electrodes for hydrogen peroxide detection utilized the potentiostat and the 3-electrodes configuration established for the PPD deposition. CA pulses at 0.5 V vs Ag/AgCl, lasting 10 seconds, were applied while the platinum part of the micro-electrodes were completely immersed in PBS solution enriched with an increasing concentration of H_2O_2 (Sigma Aldrich), ranging from 100 nM o 10 mM, according to a protocol similar to the one used by *Pernot et al*. for D-serine sensing calibration.[70] The measurements, for each concentration, were replicated 3 times. *Figure 16* shows, for example, current trends recorded during the application of 3 CA pulses in PBS, in black, and in PBS enriched with 1 mM H_2O_2, in red. In order to obtain the calibration curve, the last 2 seconds of the PBS current trends, indicated by the grey shaded region, were averaged over time and the mean between them was calculated. The resulting value was taken as background signal $I_{background}$. Similarly, for each of the concentration, the same mean value was also calculated in the time interval indicated by the red shaded region, for the concentration of 1 mM, and corrected by subtracting $I_{background}$. To obtain the calibration curves, the values of $I-I_{background}$ were then plotted as a function of the concentration. In all the calibration curves, the error bars reported represent standard deviation calculated on three measurements.

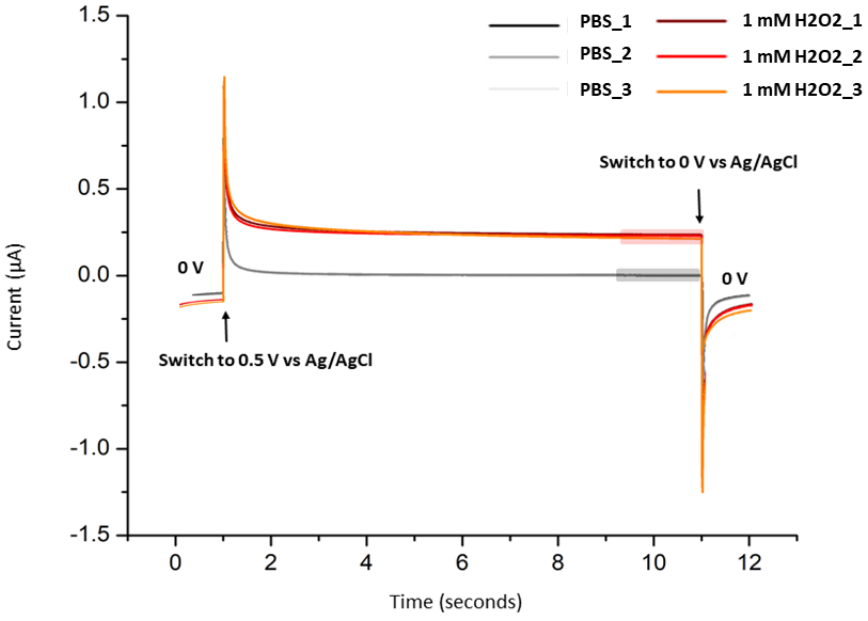

Figure 16. Construction of the calibration curve.

PPD characterization. For determining interferences, currents were measured before and after the application of the PPD. CA pulses at 0.5 V vs Ag/AgCl lasting 10 seconds were applied to the micro-electrodes while immersing them completely in PBS or in solution of PBS enriched with 20 µM serotonin (5-HT) (Sigma Aldrich) and/or 5 mM L-ascorbic acid (Sigma Aldrich). Every measurement was repeated 3 times. To quantify the rejection of interferences, each PPD deposition condition (N=1,

3, 5, or 8) was evaluated with a different micro-electrode (approximate length of 1 mm). For each of the micro-electrodes, the average current during the last 2 seconds of the CA recording was calculated for the bare platinum electrode, and taken as a reference, after subtracting the background value recorded in PBS. After the deposition of PPD, the same average value was calculated again, and the percentile decrement with respect to the reference current was evaluated. Similarly, for evaluating the decrement in the sensitivity to hydrogen peroxide, a calibration curve was obtained for each bare platinum micro-electrode and the sensitivity was computed and taken as a reference. After the deposition of PPD, according to the different CV cycles number, the calibration curve was repeated and the new sensitivity was computed. The percentile decrement was calculated with respect to the reference values. SEM images of Pt-PPD electrodes were obtained using a voltage of 2kV and 5uA of current.

Protein activity determination. An assay was executed using a coupled system that involved Horse Radish Peroxidase (HRP) and the chromogenic substrate ortho-dianisidine (o-DNS). In this process, HRP undertakes the reduction of hydrogen peroxide, a byproduct formed in the reaction between *Rg*DAAO and D-amino acid, simultaneously oxidizing o-DNS and resulting in the distinctive formation of a red color. The rate of color development is directly proportional to the enzymatic activity of *Rg*DAAO present in the sample. The assay was performed by preparing a reaction mixture consisting of 75 mM NaPPi at pH 8.5, 25 mM D-alanine in 100 mM pyrophosphate buffer solution, 0.32 mg/ml of o-DNS in water, and 4 µg/ml of HRP in water. All the chemicals were purchased from Sigma Aldrich. To initiate the reaction, the enzyme was added to the mixture. The color variation was systematically monitored spectrophotometrically (Cary 60 UV-Vis, Agilent Technologies) for a defined time duration (6 minutes). Quantification of the enzymatic activity of *RgD*AAO was achieved by measuring the change in absorbance at the wavelength of 440 nm.

Micro-sensors characterization for the detection of D-serine and D-alanine. Utilizing the same instrumentation and electrochemical configuration as previously described, CA pulses at 0.5 V vs Ag/AgCl, lasting for 10 seconds, were applied while the platinum part of the micro-electrodes was completely submerged in oxygen saturated PBS or artificial cerebral spinal fluid (aCSF) solution enriched with increasing amounts of D-serine (Sigma Aldrich) or D-alanine (Sigma Aldrich), spanning from 100 nM to 10 mM. The aCSF is composed by 124 mM NaCl, 3.5 mM KCl, 1.5 mM $MgSO_4$, 2.5 mM $CaCl_2$, 1.2 mM NaH_2PO_4, 26.2 mM $NaHCO_3$, and 11 mM D-glucose in MilliQ water, adjusting the pH to 7.3-7.4. For chemical interferences testing, aCSF was enriched with 50 µM AP5, 10 µM NBQX, and 50 µM PTX. All the chemicals were purchased from Sigma Aldrich. Calibration curves were obtained according to the same procedure described for hydrogen peroxide

sensing and, in all the calibration curves, the error bars reported represent the standard deviation calculated on the measurements.

2.2.2 Results and discussion

2.2.2.1 Micro-sensors for the detection of hydrogen peroxide

As described in section 1.4, the biosensors function by measuring the oxidation current resulting from the reaction between *Rg*DAAO and D-serine, leading to the production of hydrogen peroxide in stoichiometric quantities. Consequently, I started the electrode's characterization by assessing its suitability as sensor for detecting H_2O_2.

The electrochemical cell utilized is schematically represented in *figure 17a. Figure 17b* illustrates an example of the resulting calibration curve for a platinum micro-cylinder electrode with length equal to around 1 mm, obtained according to the procedure described in section 2.2.1. Notably, the plot demonstrates a linear trend within the examined concentration range of 1 µM to 1 mM (R^2=0.99). For this sensor, a sensitivity equal to 0.4 mA/M was calculated. Considering the exposed surface, the specific sensitivity for this electrode was equal to 420 mA/Mcm^2. The surface was geometrically calculated, considering the exposed platinum micro-cylinder, without considering the roughness of the electrode and its contribution to the electrochemically active area. It is important to note that sensitivity varies with the length of the micro-cylinder. Therefore, I have chosen to provide sensitivity per unit of active surface. Electrodes of this type exhibit an average sensitivity of 285 ± 120 mA/Mcm^2. To determine the lowest detectable concentration, H_2O_2 concentrations ranging from 100 nM to 1 µM were also investigated. For a micro-cylinder electrode with length of around 1 mm, the lowest detectable concentration was found to be 700 nM. Nevertheless, also the linear range, and therefore the lowest detectable concentration, is influenced by the size of the platinum micro-cylinder.

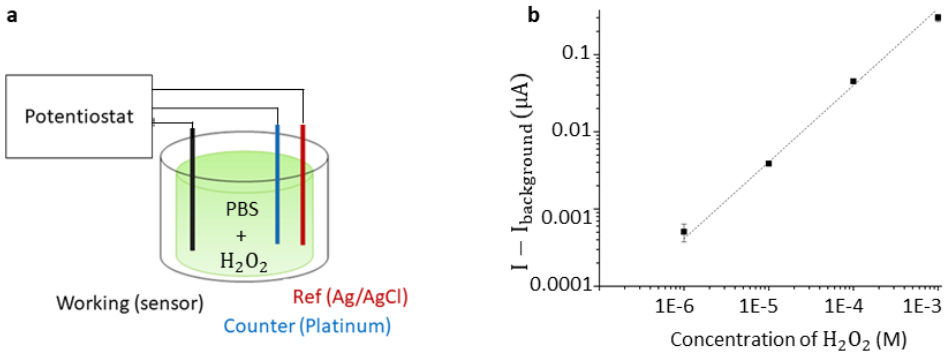

Figure 17. Hydrogen peroxide detection with micro-sensors.
a) 3-electrodes electrochemical setup used for detection of hydrogen peroxide. b) calibration curve for H_2O_2 sensing with a platinum microelectrode in PBS. The error bars reported represent standard deviation calculated on three measurements.

Institut Polytechnique de Paris
91120 Palaiseau, France

2.2.2.2 PPD electropolymerization

Selectivity is a critical determinant of sensor performance, as it dictates the sensor's ability to differentiate the signal of the target analyte from the background noise. In electrochemical sensors, the current generated at the electrode is directly proportional to the analyte concentration. However, potential interferences from other electrically active molecules must be addressed to ensure selectivity. In our case, substances like ascorbic acid, dopamine, and serotonin, which can undergo oxidation within the same voltage range as hydrogen peroxide, leading to false positive signals.

Permselective membranes are often employed as additional layers on the electrode surface. These thin polymer membranes can be deposited using techniques such as drop casting, dip coating, spin coating, or electrochemical polymerization, and they selectively exclude interfering substances based on their charge or size.[213] For instance, charge-based membranes such as Nafion and polyethersulfonic acid, and size-based membranes like phenylenediamine, polyaniline, and polypyrrole, serve this purpose.[214] Nafion, for example, used in the context of glucose sensing,[215] acts as a barrier to anions like ascorbic acid and uric acid through electrostatic interactions, hindering their diffusion to the sensor's surface, while allowing smaller and uncharged molecules like hydrogen peroxide to pass through. Another common approach is the electropolymerization of various compounds such as pyrrole, phenol, and phenylenediamine, that prevent the access of larger interfering compounds while allowing the analyte of interest to pass through.

I deposited a polymeric layer on the platinum electrodes through the electrochemical polymerization of PPD. The resulting membrane forms a reticular structure that effectively prevents nonspecific adsorption on the platinum surface. Based on size-exclusion principle, large molecules such as ascorbic acid or serotonin are hindered from diffusing towards the PPD layer on the platinum electrode, while smaller components like hydrogen peroxide can still traverse the polymeric barrier and oxidize on the platinum surface.

To create the PPD layer on the platinum wire, I followed the protocol described in section 2.2.1. *Figure 18a* displays the cyclic voltammograms obtained during PPD deposition for 5 CV cycles. In the first cycle, two peaks around 0.2 and 0.6 V vs Ag/AgCl indicate the oxidation of the two amino groups present in the molecular structure of PPD monomers. In subsequent cycles, these peaks disappear, and the anodic current progressively decreases, indicating the gradual deposition of a non-conductive layer of polymer on the platinum electrode.[76, 216] The deposition of PPD has been further confirmed via SEM image, as shown in *figure 18b.* In this panel, we clearly observe an area of the platinum wire where the polymer has been electropolymerized, surrounded by a matrix of needle-like structure, consistent with what reported in literature.[216]

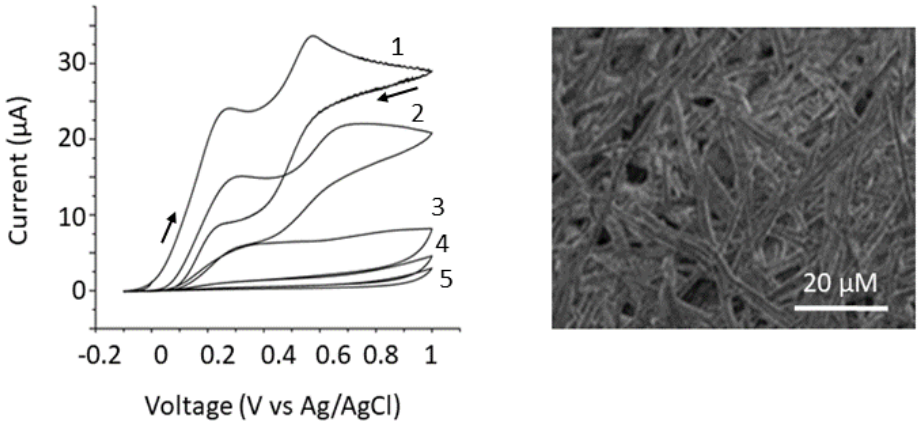

Figure 18. PPD deposition on micro-electrodes.
a) CV cycles during the electropolymerization of PPD on the platinum electrode. b) SEM image of a detail on the surface of a Pt-PPD micro-electrode.

The number of CV cycles utilized plays a role in determining the quantity of deposited PPD, which, in turn, significantly influences various performance characteristics of the biosensor. Specifically, a higher amount of PPD enhances the biosensor's capacity to reject interfering substances. However, thicker PPD layers can adversely impact the detection of hydrogen peroxide by impeding its diffusion towards the platinum surface.[76, 212] I investigated the impact of different numbers of CV cycles on the sensor's performance in rejecting interferences and potential variations in sensitivity towards hydrogen peroxide. In particular, I explored four scenarios corresponding to the deposition of PPD using 1, 3, 5, and 8 cycles. Micro cylinder electrodes of about 1 mm length were employed to measure the current values associated with the detection of 20 µM serotonin (5-HT) and 5 mM L-ascorbic acid before and after the deposition of varying amounts of PPD. By comparing the currents, the effects in terms of interference rejection can be assessed. The chosen concentrations have been selected based on the levels found in the brain.[217, 218]

The results of these tests are presented in *figures 19a* and *19b*. When PPD was deposited using only 1 CV cycle, the rejection of both serotonin and ascorbic acid was not complete. Specifically, serotonin exhibited a rejection of only 46%, while ascorbic acid showed a rejection of 82%. Further assessment was carried out after PPD deposition with 3, 5, and 8 CV cycles. As depicted in *figure 19a*, starting from 3 cycles, no detectable signal was observable upon the addition of 20 µM serotonin, indicating a 100% rejection of this interference. Similarly, *figure 19b* illustrates that for 3, 5, and 8 cycles, the rejection of interferences from ascorbic acid exceeded 99%, which is satisfactory.

Institut Polytechnique de Paris
91120 Palaiseau, France

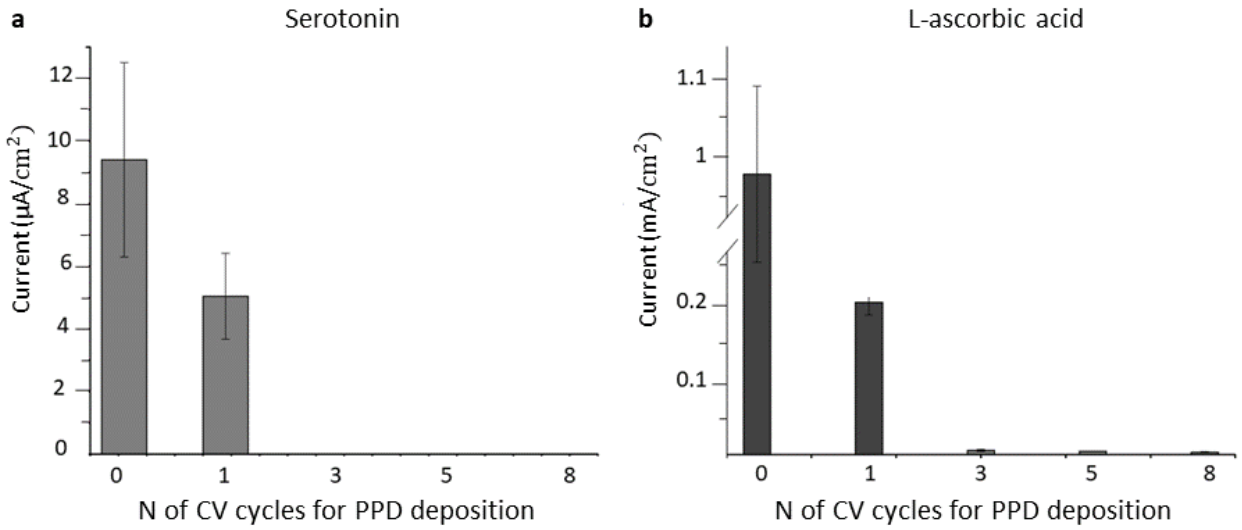

Figure 19. Impact of PPD on interference rejection in micro-electrodes.
a) Bar graph representing the specific current (µA/cm^2) recorded in a solution of PBS and 20 µM serotonin as a function of the number of CV cycles used to deposit PPD, b) bar graph representing the specific current (µA/cm^2) recorded in a solution of PBS and 5 mM of L-ascorbic acid as a function of the number of CV cycles used to deposit PPD. In both panels, the error bars reported represent standard deviation calculated on three measurements.

To confirm the previous tests, I also evaluated the sensitivity of the Pt-PPD electrode for detecting hydrogen peroxide within the concentration range of 1 µM to 1 mM, before and after depositing varying amounts of PPD.

Figure 20a displays bar graphs illustrating the percentage decrease in sensitivity of the electrodes towards H_2O_2 detection compared to the bare platinum micro-cylinder. When using only 1 cycle of CV to deposit PPD, the sensitivity towards hydrogen peroxide decreases "only" by 43%. However, as previously observed, this amount of PPD is inadequate for rejecting interfering molecules. Examining the bars in *figure 20a* , when using 3 or 5 cycles, the sensitivity decrement is 60% for 3 cycles and 62% for 5 cycles, aligning with previous reports in literature.[212] Therefore, I considered 3 or 5 cycles to be suitable for depositing an appropriate amount of PPD. Considering that there is no significant difference between choosing 3 or 5 cycles, I opted for 5 cycles to be coherent with previous works.[70, 71] The last bar in *figure 20a* corresponds to the use of 8 cycles for PPD deposition. In this case, the decrement in sensitivity towards hydrogen peroxide exceeds 70%, leading us to avoid employing this higher number of cycles. *Figure 20b* presents the superimposition of two calibration curves within the range of 1 µM and 1 mM of hydrogen peroxide in PBS, obtained with the same electrode shown in *figure 17b.* We observe that the red curve, representing the detection of H_2O_2 with a Pt-PPD electrode obtained using 5 CV cycles, is lower than the black curve (bare Pt electrode), indicating the aforementioned decrease in sensitivity. However, the linearity of the calibration curve is still maintained (R^2=0.99), and the detectable range is not compromised.

Institut Polytechnique de Paris
91120 Palaiseau, France

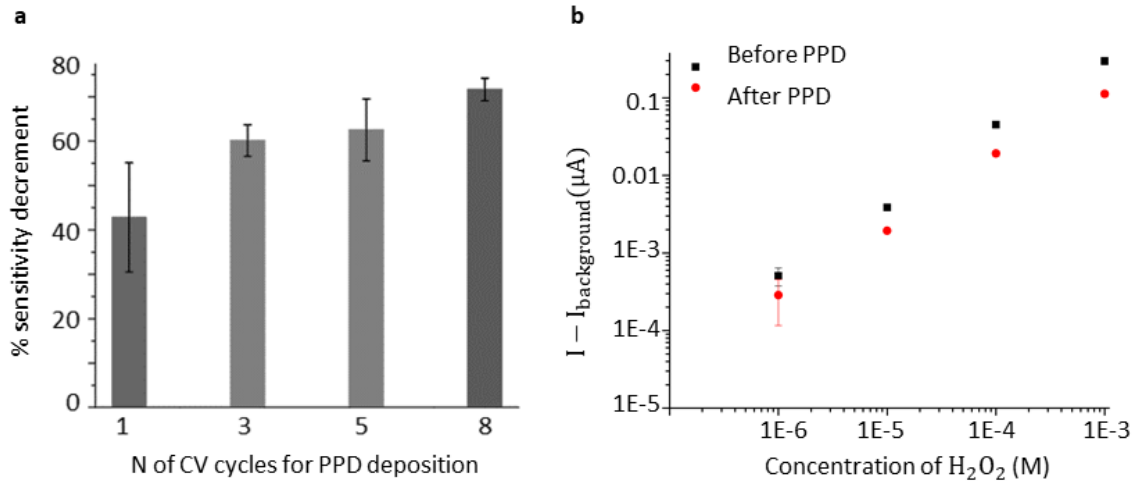

Figure 20. Impact of PPD deposition on sensitivity to hydrogen peroxide in micro-electrodes.
a) Bar graph representing the percentage decrease of the sensitivity to hydrogen peroxide as a function of the number of CV cycles used to deposit the PPD. The error bars reported represent standard deviation calculated on three measurements. b) Comparison of the micro-sensor calibration curve for the detection of hydrogen peroxide before (in black) and after (in red) the deposition of the PPD layer with 5 CV cycles. The error bars reported represent standard deviation calculated on three measurements.

2.2.2.3 Micro-sensors for the detection of D-serine

Protein immobilization was carried out and the protein activity was calculated (15.80 U/mg) following the procedure outlined in section 2.2.1. Further details can be found in the appendix section. Nevertheless, the catalytic characteristics of the free enzyme do not necessarily correspond to those of the enzyme once immobilized. Indeed, literature suggests that the chemical immobilization of an enzyme on a support can impact stability, activity, as well as the selectivity of the protein.[219, 220, 221] In particular, a study conducted by *Moussa et al.* using *Rg*DAAO-based D-serine microsensors, revealed that substrate affinity increases when transitioning from free to immobilized enzyme.[222]

To evaluate the performance of the biosensor, I tested its ability to detect increasing concentrations of D-serine in solution. Specifically, concentrations ranging from 1 µM to 10 mM D-serine in PBS were examined. The setup and protocol utilized are described in section 2.2.1. *Figure 21a* shows a calibration curve obtained according to the procedure described in section 2.2.1. This calibration curve represents the current-concentration relation obtained using a cylindrical electrode-based biosensor with a length of around 1 mm that exhibits good linearity (R^2=0.99) within the concentration range of 1 µM to 10 mM, with a sensitivity of 5.5 µA/M. Taking into account the surface of the sensor (1.2 mm length), the specific sensitivity is equal to 5.8 mA/Mcm^2. Also in this case, the surface was geometrically calculated, considering the exposed platinum micro-cylinder. As previously discussed in the context of hydrogen peroxide detection, the surface area and geometry of the biosensor impact its sensitivity. As depicted in *figure 21b*, sensitivity tends to increase with larger

size of the electrode. This can be attributed to the fact that larger electrodes offer a greater surface area for protein attachment, enabling more significant reactions with D-serine.

Nevertheless, electrodes size is not the only factor affecting the final sensitivity. In fact, the ability of these sensors to effectively detect D-amino acid concentrations is a complex and multifactorial phenomenon whose comprehension can be challenging. For instance, appropriate electropolymerization of the PPD on the platinum surface is crucial for successful protein immobilization as, during the crosslinking phase of the immobilization process, glutaraldehyde facilitates the crosslinking of the protein with the PPD layer underneath. Therefore, the cleaning process of the platinum wire with KOH and ethanol preceding the first functionalization step with PPD is of utmost importance, as neglecting it results in insufficient deposition of PPD.

The average specific sensitivity for this type of sensor was determined to be 5±2 mA/Mcm^2.The observed variations in measurement can be attributed to differences in the amount of protein attached to the sensor, possibly influenced also by the varying quantities of deposited PPD. To determine the detection range of this type of sensor, I investigated concentrations between 100 nM and 10 mM. For biosensors with a length of 1 mm, the lowest concentration in solution detected experimentally was determined to be 800 nM. However, the size of the electrode and the quantity of protein on it play a significant role. In general, it is needed to strike a balance as, opting for shorter sensors, means sacrificing potential sensitivity but prioritizing improved spatial resolution. For the subsequent applications, I used sensor's length equal to 1 mm.

Finally, during the course of characterization of the microsensors, it resulted evident that the oxygenation of the solution is fundamental. In fact, working without oxygenated solution usually results in less steep, less linear, and less reproducible calibration curves because DAAO require O_2 as a co-substrate to complete the catalytic cycle.

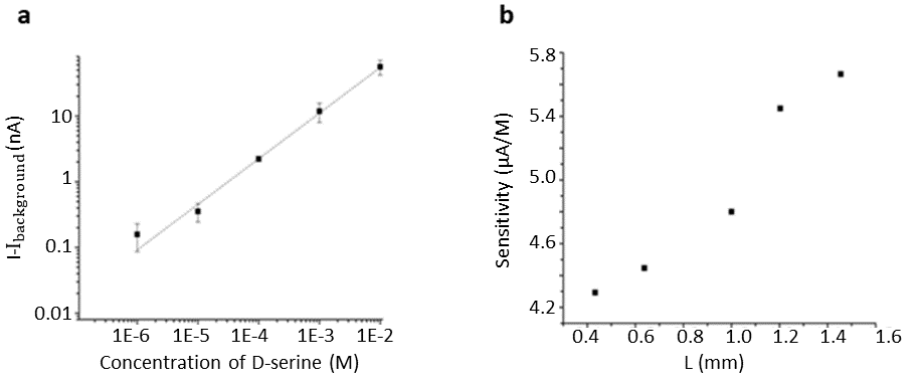

Figure 21. Characterization of the micro-sensors for D-serine detection.
a) Calibration curve of a 1 mm long micro-sensor for the detection of D-serine. The error bars reported represent standard deviation calculated on three measurements. b) Sensitivity of several micro-sensors (µA/M) as a function of the length of the sensor micro-cylinder.

Institut Polytechnique de Paris
91120 Palaiseau, France

Chemical interferences. Calibration curves were replicated using aCSF as electrolyte solution, as it is more appropriate than PBS for investigation on brain slices. *Figure 22a* shows two calibration curves for another sensor (length 1mm), one conducted in PBS (black curve) and the other in aCSF (red curve). Despite, for this specific sensor, a slight variation in the sensitivity is observable when transitioning from PBS to aCSF, D-serine is still detected in the concentration range 1 µM- 1mM.

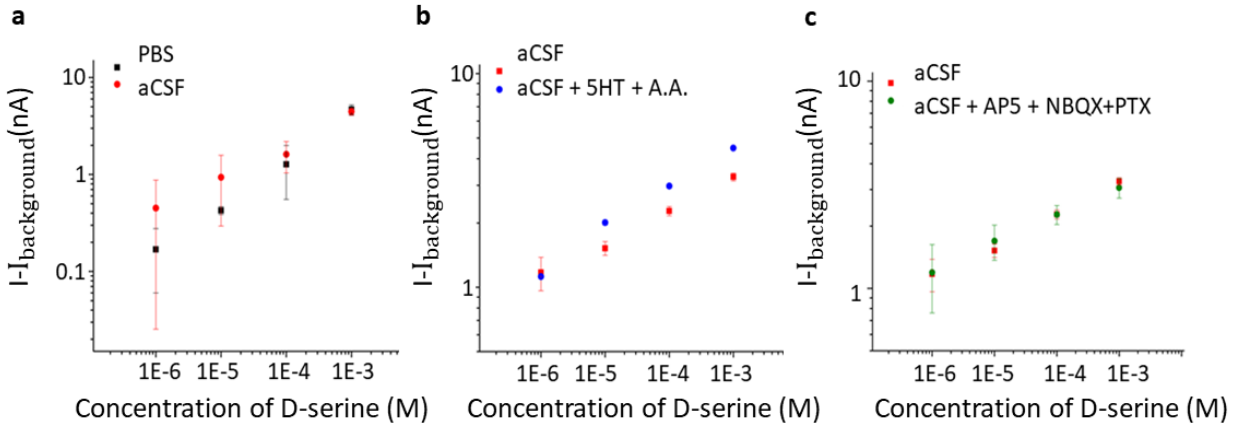

Figure 22. Calibration and interferences in D-serine detection.
a) Comparison of two calibration curves for D-serine detection using PBS (in black) and aCSF (in red) as supporting electrolyte. b) Comparison of a calibration curve for D-serine detection in aCSF (in red) and aCSF enriched with 20 µM serotonin and 5 mM L-ascorbic acid (in blue), c) Comparison of a calibration curve for D-serine detection in aCSF (in red) and aCSF enriched with 50 µM AP5, 10 µM NBQX, and 50 µM PTX. In all the panels, the error bars reported represent standard deviation calculated on three measurements.

Similarly, using another sensor (length around 1mm), the calibration in aCSF was repeated in the presence of the two main interfering molecules, serotonin and L-ascorbic acid. *Figure 22b* shows the calibration curve in aCSF (shown in red), and in aCSF enriched with 20 µM serotonin and 5 mM L-ascorbic acid (shown in blue) and the two curves are superimposable.

Furthermore, I wanted to determine whether the sensors are compatible with chemicals typically used in electrophysiological experiments. Specifically, I investigated the sensing of D-serine in aCSF in the presence of D-AP5 (50 µM), NBQX (10 µM), and PTX (50 µM), which are commonly used neuroreceptors antagonist. *Figure 22c* illustrates the overlapping of two calibration curves: one obtained in aCFS (red curve) and the other in aCSF enriched with the aforementioned chemicals (green curve). This finding confirms that my sensors can be used effectively in the presence of these blockers, thereby opening up possibilities for various experimental applications.

2.2.2.4 Micro-sensors for the detection of D-alanine

It is important to highlight that the fabricated sensor based on *Rg*DAAO is not only suitable for detecting D-serine but also other D-amino acids. Previous studies using the same type of sensor have shown that *Rg*DAAO exhibits a preference for D-alanine and D-serine as substrates.[222] Hence, we aimed to compare the sensing performance of the sensors towards the two D-amino acids.

Institut Polytechnique de Paris
91120 Palaiseau, France

The results of an example biosensor are presented in *figure 23.* The black curve displays a calibration curve obtained by adding increasing amounts of D-alanine to PBS, following the same protocol described earlier for the calibration for D-serine sensing. The sensor shows linearity between 1 µM and 1 mM (R^2=0.99). The sensitivity of this specific biosensor towards D-alanine within the linear range, was determined to be 32 µA/M. In the same figure, the curve in red represents the calibration curve for D-serine. The calibration curve for D-serine sensing also shows good linearity in the range between 1 µM and 1 mM (R^2=0.99).

In this case, the sensitivity of the biosensor for D-serine was determined to be 13 µA/M, which represents 58% decrease compared to the sensitivity for D-alanine. The average ratio, along the different concentrations, between the steady state current measured during D-alanine sensing and D-serine sensing is approximately 1.59. This finding aligns with previous studies reporting an average ratio of around 1.44 and describing that both free and immobilized *Rg*DAAO exhibit higher specific activity towards D-alanine compared to D-serine. While the disparity between the two becomes less pronounced when transitioning from free to immobilized *Rg*DAAO, it remains noticeable.[222]

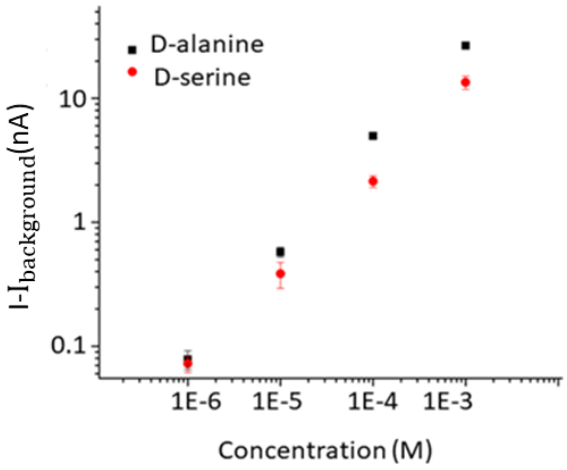

Figure 23. Micro-sensors characterization for D-amino acids sensing.
Comparison of two calibration curves of a micro-biosensor for the detection of D-alanine (in black) and D-serine (in red). The error bars reported represent standard deviation calculated on three measurements.

2.3 D-serine measurements on brain slices

2.3.1 Motivation

Following the characterization of the micro-sensors for detecting D-serine in solution, I focused on applying this technology for measurements on biological samples. As highlighted in section 1.1.3, D-serine plays a crucial role in various brain disorders, including epilepsy. This section of the manuscript will detail experiments conducted on biological samples utilizing my micro-sensors, aiming to explore the role of D-serine in the pathological context of epilepsy.

Institut Polytechnique de Paris
91120 Palaiseau, France

Epilepsy, a neurological disorder characterized by recurrent and unpredictable seizures, poses a significant burden on individuals and society alike. With an estimated 50 million people affected worldwide (2020),[223] the impact of epilepsy extends beyond the seizures themselves, impacting cognitive functions, quality of life, and mental health.[224, 225] Temporal lobe epilepsy (TLE) is the predominant form of drug-resistant epilepsy in adults[226] and therapeutic interventions are still inconclusive due to the unclear nature of its underlying process. TLE has been associated with cognitive impairment and unusual excitatory synaptic activity patterns in the hippocampus in both animal models and human subjects.[227]

Although epileptogenesis involves multifaceted pathways, emerging evidences point towards an association between epilepsy and the abnormal expression of NMDARs.[228, 229, 230, 231] NMDARs, indeed, are key players in long-term plasticity, learning, and memory, that are significantly altered in epileptic patients. Mutations within the subunits constituting NMDARs have been identified and associated to the pathogenesis of epilepsy.[232, 233, 234, 235] Furthermore, various forms of epilepsy have been correlated with alterations in the expression patterns of NMDARs.[236, 237, 238] Notably, an elevated expression of the GluN1 subunit has been observed in individuals with intractable TLE.[239] In addition, the modulation of NMDARs has demonstrated an anticonvulsive effect on different preclinical models of seizure and in patients with epilepsy.[240]

The central importance of D-Serine in synaptic circuits maintenance and dynamics has naturally question its role in brain disorders and particularly in epilepsy. Several observations have already been reported. For example, pharmacological inhibition of astroglial connexin-43 hemichannels protects against pilocarpine-induced seizures lowering extracellular D-Serine levels during convulsions.[241] Accordingly, pentylenetetrazole-induced epileptic seizures are decreased in $SR^{-/-}$ mice.[242] Morover, implications of D-Serine in epilepsy has been further evidenced in patients. For example, an anatomopathological analysis of 20 patients reported that D-Serine levels increase along with GluN1 expressions in intractable epilepsy.[243] However, the exact role played by D-serine in epilepsy, is still elusive. Indeed, *Klatte and colleagues* (2013) have shown that TLE induced by pilocarpine would be rather associated, in rats, with a reduction in the levels of D-Serine in the hippocampus, leading to the desaturation of the co-agonist binding site of synaptic and extrasynaptic NMDARs, causing a deficit in hippocampal long-term potentiation (LTP).[244] Not only application of D-Serine can restore LTP[245] but its administration also mitigates neuronal loss and astrogliosis associated to epileptogenesis in the pilocarpine model of TLE.[246]

Consequently, directing attention towards the D-serine-NMDARs system emerges as an approach for guiding pharmacological interventions. However, the current body of data about the

precise role of D-serine in epilepsy is controversial. Furthermore, most studies have focused on the latent or chronic phases but the role in the acute phase of status epilepticus has been ignored.

In this context, I have utilized the electrochemical enzymatic micro-electrodes I have developed in order to probe the levels of D-serine in a TLE model. This model utilized mouse hippocampal brain slices that underwent aberrant chemical stimulation through the addition of an epileptogenic mixture containing pilocarpine, mimicking the pathological state of epilepsy.
Because it has been reported that the identity of the co-agonist (glycine or D-Serine) of NMDARs varies between the hippocampal CA_1 and DG regions,[247] I have analyzed the impact of the epileptogenic stimulation on these two areas.

2.3.2 Materials and methods

Chemicals. Slicing aCSF (pH7.3-7.4) has the following composition: 3.5 mM KCl, 7 mM $MgSO_4$, 0.5 mM $CaCl_2$, 1.2 mM NaH_2PO_4, 26.2 mM $NaHCO_3$, 212 mM sucrose, 11 mM D-glucose, 1.3 mM L-ascorbic acid, and 2.4 mM Na-pyruvate in MilliQ water. Magnesium free (0 Mg) aCSF has the following composition: 124 mM NaCl, 3.5 mM KCl, 2.5 mM $CaCl_2$, 1.2 mM NaH_2PO_4, 26.2 mM $NaHCO_3$, and 11 mM D-glucose in water.
The epileptogenic medium (referred here as pilo-aCSF) was prepared by dissolving pilocarpine (10 µM, Tocris bioscience), and picrotoxin (100 µM) in 0 Mg aCSF. All the chemicals, unless specified, were purchased from Sigma Aldrich.

Instrumentation. *Figure 24a* illustrates the setup, highlighting its primary components. The setup comprised a micro-chamber to accommodate the brain slices, positioned on an anti-vibrational table, beneath an optical stereoscope (Stemi 2000, Zeiss), essential for precise sensor localization on the brain slices by mean of micro-manipulators. To maintain physiological conditions, a perfusion system with a peristaltic pump (Minipuls 3, Gilson) continuously supplied the recording chamber that contains the slice with oxygenated aCSF (2 ml/min), maintained at 30-32 °C, using a temperature controller (CL-100, Warner Instruments). In order to achieve stable positioning of the sensors in the experimental setup, I have constructed a specialized holder, following a protocol similar to the one outlined by *Papouin et al.*[248] Each holder was assembled using a glass Pasteur pipette, a connecting cable, and a heat-shrink tube. The construction process involved several steps. Initially, the tapered tip of the pipette was cut to enlarge its opening. Subsequently, the connecting cable was inserted into the pipette, allowing for the appropriate connector to protrude to insert the back pin. On the opposite side of the glass support, a cable of approximately 20 cm was left exposed to be connected to the potentiostat. To enhance the mechanical stability of the holder, sections of heat-shrink tube were

sealed around the structure. *Figures 25a* and *25 b* depict the complete holder structure (panel *a*) and the same structure with a biosensor connected (panel *b*). To ensure that this holder structure did not introduce noise or significantly increase resistance, I tested a cylinder electrode inserted into the holder for detection of H_2O_2 in PBS, and appropriate signals were successfully detected.

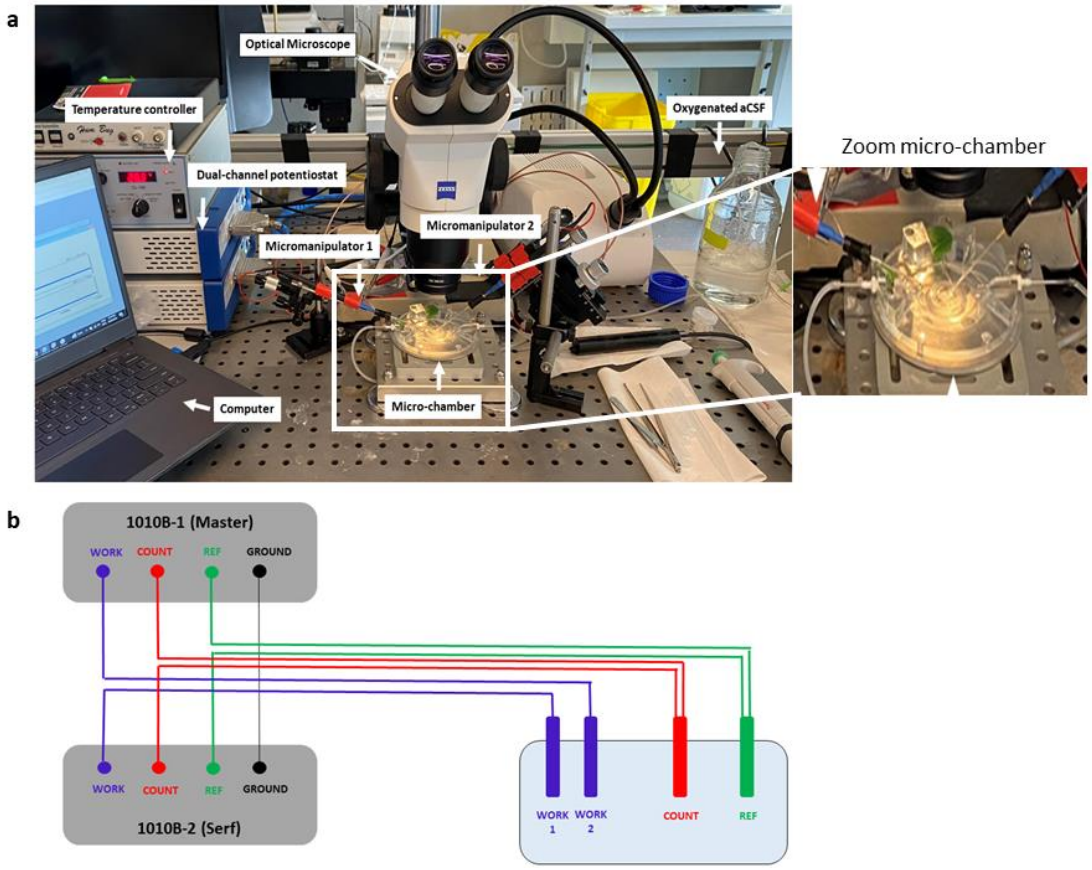

Figure 24. Setup for D-serine measurements on acute brain slices.
a) Picture of the setup used for the application of the biosensors. A central micro-culture chamber is placed below a microscope and two micromanipulators are placed laterally for positioning and fine movements of a sensor and a control electrode. b) Synchronization of two 1010B Gamry potentiostats: each potentiostat is connected to a working electrode (in blue) while they share common counter (red) and reference (green) electrodes.

During our experiment, we conducted simultaneous measurements with sensors and control electrodes. The control electrode, or null sensor, consisted of a microelectrode having the same geometry and PPD deposit of the micro-sensors, but not possessing a layer of immobilized DAAO, and therefore not able to detect D-serine. The control electrode measurement was needed in order to exclude from the final measured signal components that may have derived, for example, from hydrogen peroxide oxidation not associated with D-serine degradation. To allow the simultaneous measurements with sensor and control electrodes, a two-channels potentiostat was assembled through the cable synchronization of two Gamry single-channel potentiostats (1010B, Gamry Instruments). A common Ag/AgCl wire served as the reference electrode, while a Pt wire was utilized as the

common counter electrode. *Figure 24b* illustrates the schematic diagram of the connection between the bipotentiostats and the electrochemical cell, where counter electrode, reference electrode, and the ground connection are shared between the two systems. Here we refer to the potentiostats as Master and Serf. The Master potentiostats serves as the primary control for the experimental timing. The bias applied to the master electrode, which corresponds to the sensor electrode, can be varied as in single-channel configuration. On the other hand, the Serf potentiostat regulates the control electrode, maintaining the potential at 0.5 V vs Ag/AgCl.

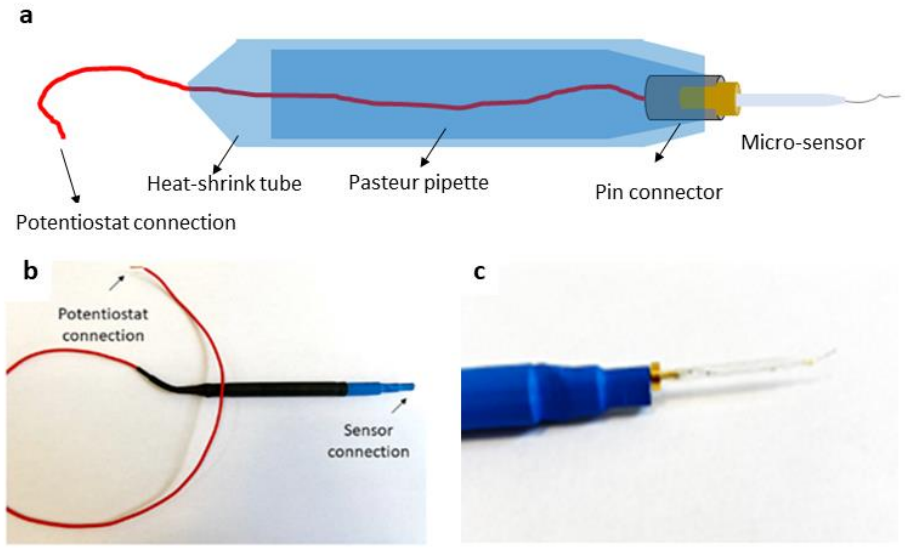

Figure 25. Picture of the micro-sensors holder.
a) Schematic of the holder structure. b)Picture of the holder, showing potentiostat and micro-sensor connections. b) Detail of the micro-sensor inserted in its holder.

Biological samples. 1.5-2 months-old males and females wild type (WT) and SR knock-out ($SR^{-/-}$) mice were used in this study. Animals were deeply anesthetized with isoflurane before decapitation. The brain was then quickly removed and coronal hippocampal slices (400 µm thickness) were cut using a 7000 smz vibratome (Campden Instruments, UK) in ice-cold slicing aCSF. The slices were allowed to recover for 30 min at 30°C and then were kept at room temperature in oxygenated aCSF until usage, between 1h30 minutes and 6 hours after brain extraction.

Calibration. Prior to evaluating D-serine levels, each sensor was calibrated. A voltage of 0.5 V vs Ag/AgCl was applied, utilizing the micromanipulator to precisely position the electrodes in contact with the slice, or immersing it in solution in the micro-chamber. For hydrogen peroxide sensing calibration, hydrogen peroxide was added to the aCSF solution, from 1 µM to 10 mM concentration. For each concentration, CA pulses of 0.5 V vs Ag/AgCl lasting 10 seconds were applied for three times. Likewise, for D-serine sensing characterization, increasing amounts of D-serine were introduced into the recording chamber.

D-serine measurement. Control and sensor electrodes were located in the hippocampal CA_1 or dentate gyrus (DG) regions (*figure 26a*), 150-200 µm apart. A voltage of 0.5 V vs Ag/AgCl was applied to both the control and sensing electrodes for a duration of 30 minutes. Following a 10-minutes period required for signal stabilization in 0 Mg aCSF, the convulsant pilo-aCSF was perfused, and variations in current levels were recorded for an additional 20 minutes. *Figure 26b* represents a diagram of the experimental protocol. The control micro-electrode, possessing same geometry and PPD coating as the sensor, exhibits sensitivity to hydrogen peroxide but remains insensitive to D-serine due to the absence of immobilized *Rg*DAAO enzyme, as described in section 2.2.1. Analyzing the signals from both electrodes provides insights into the sensor's signal component associated with variations in D-serine levels. The schematic in *figure 26c* summarizes the experiments conducted in these two regions, considering the two mouse models. Consequently, we define four conditions (CA_1-WT, CA_1-$SR^{-/-}$, DG-WT, and DG-$SR^{-/-}$) for which the results will be presented and compared. In the following sections, I will describe calibration tests conducted in order to confirm the suitability of my sensors for measurements on brain slices, to then proceed to the description of the on-slice measurements of D-serine.

Data analysis. To quantify the percentage variations in current, I utilized the software Origin (8.6, OriginLab). Detailed information about signal processing is presented in subsequent sections of the chapter. The resultant dataset underwent analysis for outlier identification using the software GraphPad Prism 8.0.2. Specifically, after a negative outcome from a normality test, outliers were categorized using the first and the third percentile definitions. To generate average time traces for both the sensor and blind electrodes, raw traces for each slice were averaged within a time interval extending from the moment of drug addition to the end of the recording, employing Origin software. Subsequent statistical analysis was conducted using GraphPad Prism. Comparisons between control and sensor electrodes were executed using the Wilcoxon matched-pairs signed-rank test.[249] Additionally, comparisons in increments of D-serine level between $SR^{-/-}$ and WT mice were performed using the unpaired non-parametric Mann-Whitney test.[250] Graphs were generated using GraphPad Prism software.

Institut Polytechnique de Paris
91120 Palaiseau, France

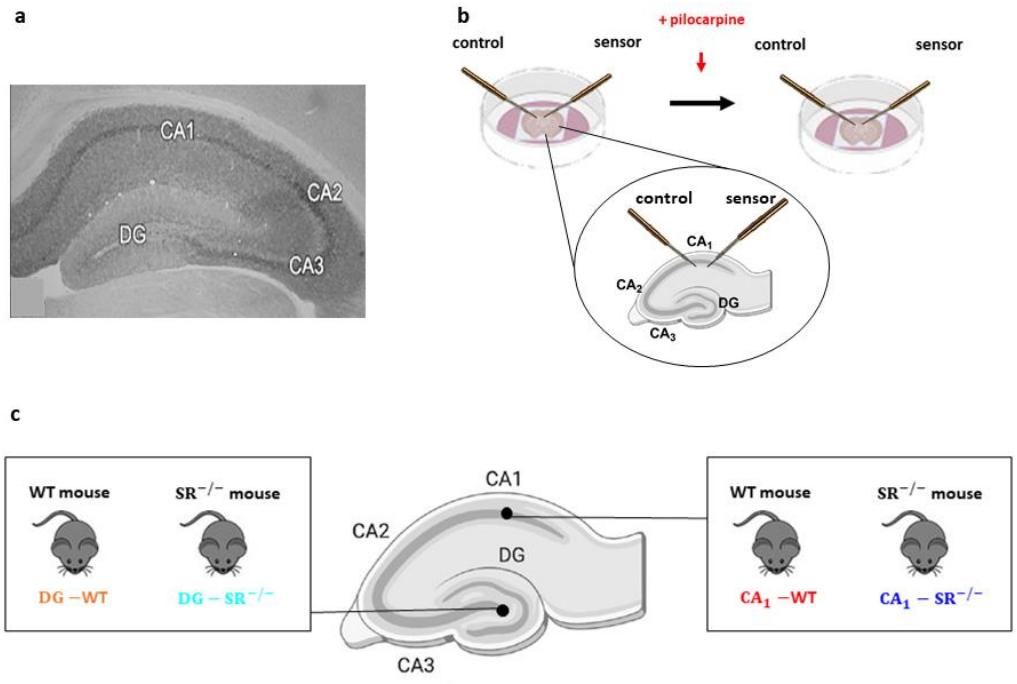

Figure 26. Experiments on mouse brain slices.
Representation of a mouse hippocampus slice, in which the sub-regions CA_1, CA_2, CA_3, and DG are visible. The picture is taken from *Choi and Lee*.[251] b) Schematic diagram of the experimental protocol: a control electrode and a sensor are located in the same hippocampal sub-regions and are used to measure variations of D-serine levels as a consequence of pilocarpine addition. c) Summary of the experiments conducted in the CA_1 and the DG, with WT and $SR^{-/-}$ mice.

2.3.3 Results and discussion

2.3.3.1 On-slice micro-sensors calibration

One important challenge when recording with sensors are potential contamination of the sensor's surface and subsequent impact on reliable sensing, when placing the electrode in close proximity or direct contact with brain tissue. Therefore, I conducted two sets of control experiments to assess the impact of electrode-slice physical contact on the sensitivity of a micro-sensor.

In the first set of experiments, I evaluated the impact of slice-sensor physical contact on sensitivity to hydrogen peroxide, as D-serine measurement with these DAAO-based sensors depends on the detection of H_2O_2 produced from the enzymatic reaction. A micro-cylinder electrode was calibrated by introducing increasing concentrations of H_2O_2 (ranging from 1 µM to 10 mM) in aCSF without the presence of the brain slice, according to the same procedure described in section 2.3.2. The resulting calibration curve, illustrated in black in *figure 27*, displays linearity across the entire tested concentration range (R^2=0.99) and the sensitivity to hydrogen peroxide was determined to be 1.6 mA/M.

Subsequently, I positioned the same sensor in contact with the slice. The sensor is kept tilted in a way then, when approaching the electrode to the slice, the full length of the shaft is in contact

Institut Polytechnique de Paris
91120 Palaiseau, France

with the tissue. The calibration curve depicted in red in *figure 27* illustrates data obtained in this new condition. Notably, the contact between the probe and the slice did not significantly impact the electrode's ability to detect hydrogen peroxide. The calibration curve maintained linearity (R^2=0.98), and the sensitivity (0.9 mA/M) remained comparable to typical values for this kind of probe.

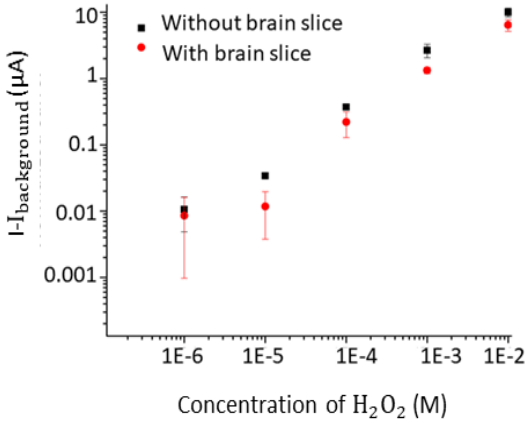

Figure 27. Hydrogen peroxide sensing calibration on slice.
Overlay of two calibration curves for H_2O_2 sensing obtained with the same microsensor without (black) and with (red) brain slice contact. The error bars reported represent standard deviation calculated on three measurements.

Given this favorable result, I proceeded to the second set of experiments to assess the performance of the sensors for measuring D-serine on the slices.

I aimed to determine whether the sensors could detect the basal concentration of D-serine, specifically the local levels released at the hippocampus. One of the sensors was immersed in the chamber containing a solution of oxygenated aCSF, maintaining a temperature of 30 °C and continuous perfusion. A brain slice was also located in the chamber. I conducted measurements of the electrode signal both at a distance of few millimeters from the slice and by making direct contact with the slice. *Figure 28a* presents 10 seconds of current recording acquired via CA at 0.5 V vs Ag/AgCl. Initially, the sensor was located few millimeters away from a WT mouse brain slice and, at the moment indicated by the red arrows, the sensor was swiftly brought in physical contact with the slice, with a speed of approximately tens of mm/s, while keeping the voltage at 0.5 V vs Ag/AgCl. An abrupt increment in the current is evident, attributable to the fact that, when the sensor is in contact with the slice, it is able to detect D-serine. To establish a negative control, I replicated this experiment with another sensor on a hippocampus slice from a $SR^{-/-}$ mouse, anticipated to exhibit little or no D-serine content. The current trend depicted in *figure 28b* reveals that, upon contacting the slice with the sensor, contrarily to what happened in the WT sample, there is a decrement in the recorded current. This phenomenon might arise from the sudden change in the system conductivity due to the contact between the electrode and the brain tissue. This pattern was consistently observed across multiple slices from $SR^{-/-}$ mice. Furthermore, a similar response was also observed when bringing a control electrode (without *Rg*DAAO, therefore not sensitive to D-serine) in contact with both $SR^{-/-}$ and WT

slices. An example of null sensor measurement on WT slice is reported in *figure 28c*. Note that, differently from what described in panels *a* and *b*, in this case the null sensor is kept in physical contact with the slice and detached at the instant indicated by the red arrow.

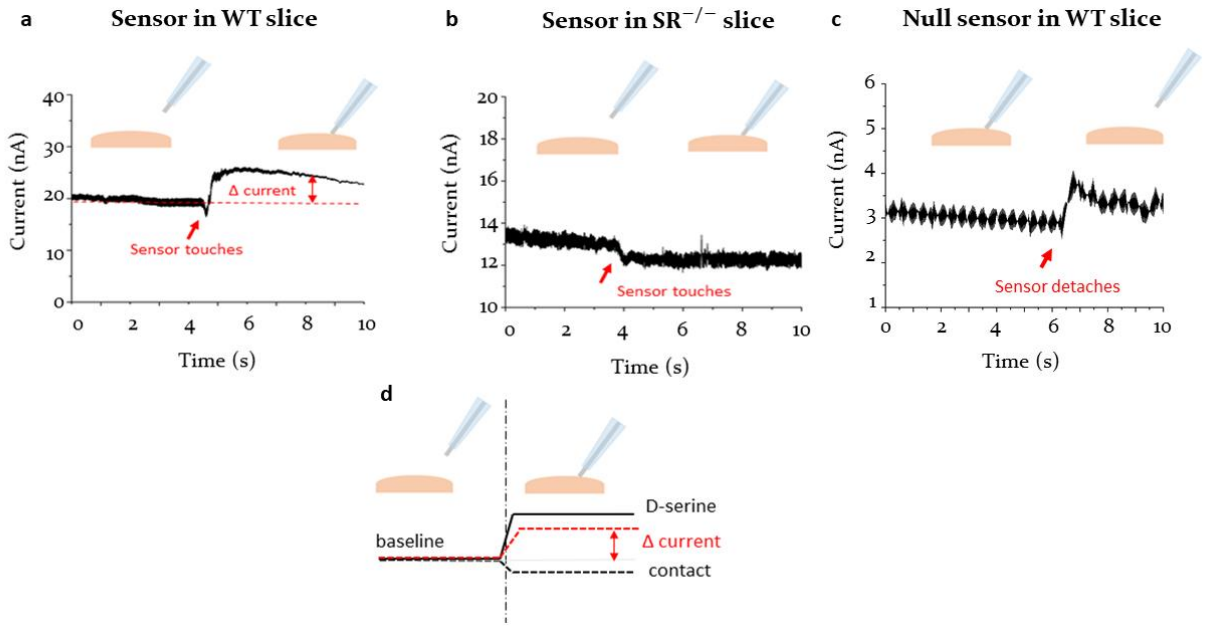

Figure 28. D-serine reading on brain slices.
a) Current trend recorded while touching a WT slice with a micro-sensor. b) Current trend recorded while touching a SR$^{-/-}$ slice with the same micro-sensor. c) current trend recorded while detaching a null sensor from a WT slice. d) Theoretical schematic representing the different possible contributions to the observed signal.

These observations led us to question the reliability of deriving the basal D-serine levels directly from these observed current variations (Δcurrent in panel *a*). As schematically illustrated in *figure 28d*, when bringing the sensor in contact with a WT slice, Δcurrent, schematically represented by the dotted line, may actually result from a combination of various current fluctuations, including the decrement due to the sudden contact between the sensor and the tissue (depicted by the black dotted line) and the increment attributed to D-serine detection (depicted by the black continuous line).

In this study, the primary interest is using these micro-sensors to monitor changes in D-serine levels resulting from chemical stimulation with pilocarpine. It is crucial therefore to determine whether, despite the influence of the contact between the slice and the sensor on the recorded signal, it remains possible to sense varying levels of D-serine. To address this, I conducted on-slice calibration for D-serine detection. Initially, the sensor was approached (length around 1.5 mm) to the slice (WT mouse) until they made contact, observing an increase in the recorded current. This value was taken as the background, and increasing amounts of D-serine have then been added to the recording chamber following the protocol outlined in section 2.3.2.

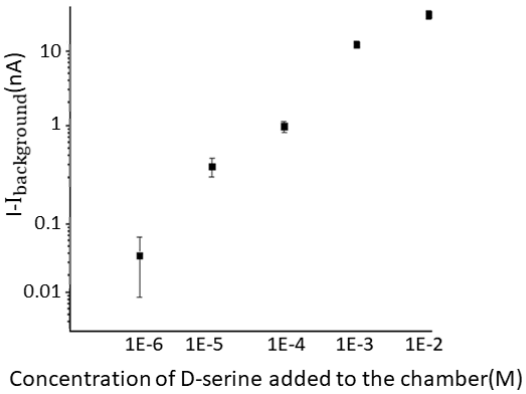

Figure 29. D-serine sensing calibration on slice.
The current values, for each concentration, have been corrected by subtraction of the background value corresponding to current recorded just after establishing the contact between the sensor and the slice. The error bars reported represent standard deviation calculated on three measurements.

The resulting calibration curve is depicted in *figure 29*. Remarkably, the sensor maintains its ability to detect D-serine within the concentration range of 1 μM to 10 mM, despite the contact with the brain slice. The calibration process gave a sensitivity value of 2.24 μA/M, aligning with the typical sensitivity values expected for biosensors of this kind. The similarity of this value to those obtained from calibration in solution (section 2.2.2.3) holds significant importance. In fact, before each measurement, sensor calibration is needed for interpretation of subsequent readings. Given that the presence of the slice does not introduce significant variations, we can opt to conduct the calibration in solution prior to the actual measurement. Subsequently, residual D-serine can be removed from the chamber through perfusion, before introducing the brain slice for the real experiment. To ensure effective removal of D-serine from the micro-chamber after the calibration and before experiments, the current was monitored while applying a 0.5 V vs Ag/AgCl pulse and it was observed to return to the baseline value after few minutes of perfusion.

2.3.3.2 Measurements on-slice in epileptic conditions

As previously illustrated, the objective of these experiments is the monitoring of D-serine levels within specific regions of the hippocampus, in order to elucidate their variation as a result of chemically-induced (pilocarpine-induced) epileptic condition. As described in section 2.3.2, during the 30 minutes of the experiment, a CA pulse of 0.5 V vs Ag/AgCl is applied, while keeping the sensor and the control electrode immersed in aCSF and in contact with the slice. *Figure 30a* illustrates the current transient recorded by a micro-sensors during the first 10 minutes of the recording in the CA_1 region of a slice from a WT mouse. A peak is visible, at the beginning of the measurement, when the voltage of 0.5 V vs Ag/AgCl is applied, and it is followed by an exponential decay. This behavior

persisted even when using control micro-electrodes or bare platinum wires on slices from both WT and $SR^{-/-}$ mice, as well as without presence of brain slice.

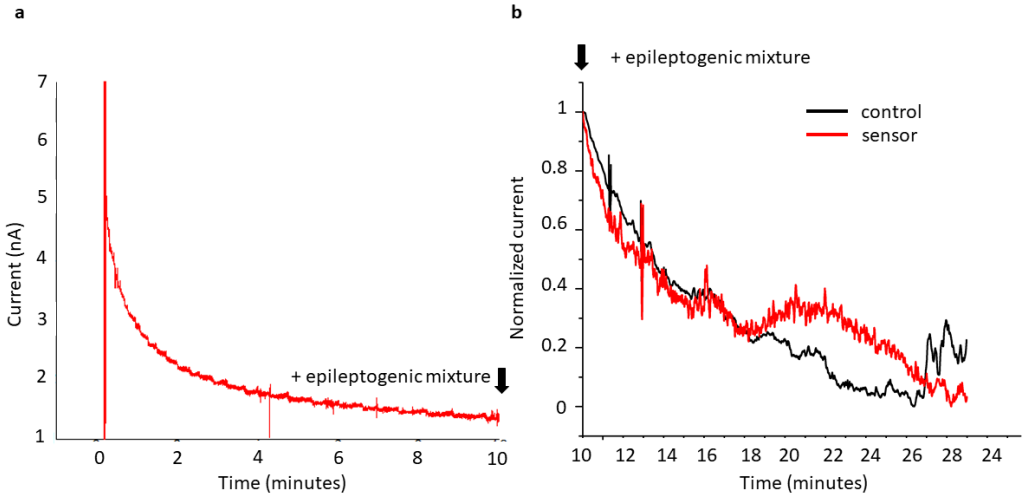

Figure 30. Current exponential trends on WT hippocampus brain slice.
a) Current exponential decay obtained applying a 0.5 V vs Ag/AgCl pulse for the duration of 10 minutes, before proconvulsant pilo-aCSF addition, using a sensor on a WT hippocampal slice. b) Comparison between the normalize current trends measured by sensor (red) and control (black) electrodes, after the epileptogenic mixture addition: the sensor curve presents an increment around 10 minutes after drug administration.

Following a 10-minutes period of signal stabilization, the epileptogenic pilocarpine mixture was introduced into the recording micro-chamber, at the instant denoted by the black arrow in *figures 31a* and *31b.* The two representations have to be considered as subsequent one to the other, as the time scale indicates. In the second image, current trends have been normalized to their maximum in order to highlight the increment of the current recorded by the sensor after pilocarpine addition, representing the variation in D-serine levels (red curve). The black curve in *figure 30b* illustrates the current recorded simultaneously with the control electrode.

The scenario may vary from slice to slice, nevertheless, despite the sensor's more pronounced increment, a slight current increase can also be observed with the control electrode after pilocarpine addition. This occurrence can be explained considering that the application of the epileptogenic mixture not only induces variations in D-serine levels. Notably, an increase in hydrogen peroxide levels can take place, influencing the overall recorded signal. Consequently, I quantified these variations for meaningful comparisons.

Institut Polytechnique de Paris
91120 Palaiseau, France

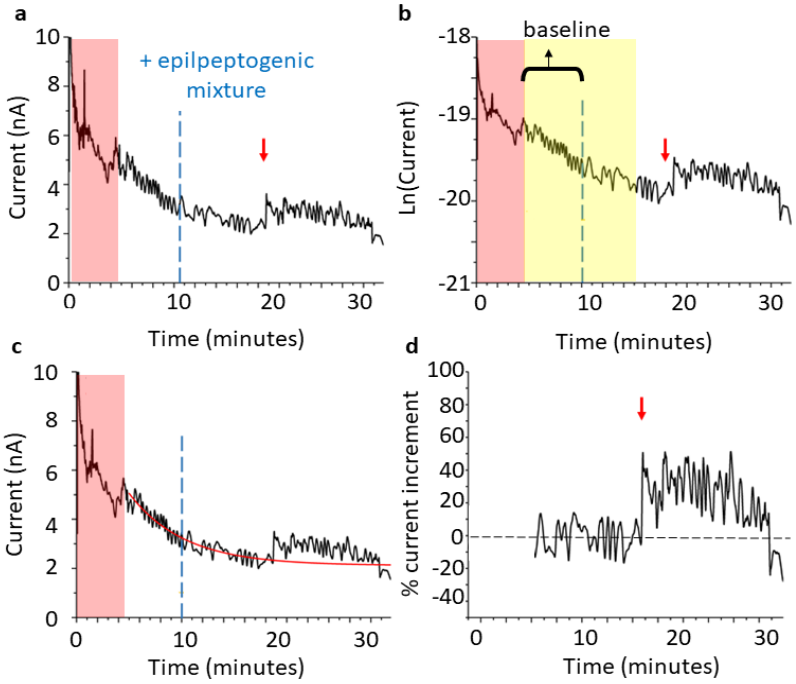

Figure 31. Data processing.
a) Current trend of a full 30 minutes' measurement with a sensor on a WT hippocampal slice in the CA_1 region: the first five minutes (red area) are associated with high variations of the signal and are not considered for analysis. The blue line represents the instant of pilo-aCSF addition, and the red arrows indicates the increment of the signal. b) Current trend represented in logarithmic form: the area in yellow is characterized by a linear trend, and the region of the signal used for constructing the baseline is indicated. c) Overlay of the experimental trend (black) and the exponential baseline (in red). d) Resulting trend showing the percentage current increment associated with the drug administration, with the red arrow indicating the increment of the recorded current.

To accomplish this, I analyzed both the control and the sensor signals. The first minutes of all the measurements, when operating with the sensor in contact with the slice, were characterized by a high level of noise, that disappeared after few minutes. Therefore, with the aim of identify a stable baseline, I decided to exclude the first 5 minutes of each measurement from the following analysis, indicated by the red areas in *figure 31*, that refers to a measurement conducted with one sensor in a WT slice in the CA_1. The current increment typically manifested itself no earlier than 5 minutes after the addition of the drug, both in control and sensor, as indicated by the red arrow in *figure 31a*. As observable *figure 31b*, where the current trend is plotted in its logarithmic form, the region of the curve in yellow is characterized by a constant slope, indicating the signal follows the pre-drug addition trend. I decided to use the first portion of the yellow region, being the 5 minutes before drug addition, for the construction of the baseline and fit the recorded data to a first order exponential function. The resultant curve was then utilized as the baseline, denoted by the red trend in *figure 31c*. Subtracting this baseline from the recorded signal until the conclusion of the measurement, resulted in the final trend depicted in *figure 31d.* The maximum increment was quantified in percentage terms for both the sensor (Δ_s%) and the control electrode (Δ_c%). For each slice, the difference (Δ_{s-c}%) was used to compared different slices and was associated with variations of D-serine content.

Institut Polytechnique de Paris
91120 Palaiseau, France

F*igure 32a* delineates, point by point, the outcomes associated with distinct slices for the CA_1 region, portrayed in red for the WT mice (CA_1-WT condition) and in blue for the $SR^{-/-}$ (CA_1-$SR^{-/-}$ condition). Each data point is plotted as a function of the control current variation Δ_c% and the sensor current variation Δ_s%. The two groups of data points exhibit closely aligned values for Δ_c% but divergent values for Δ_s%.

For both CA_1-WT and CA_1- $SR^{-/-}$ data corresponding to 12 slices were recorded (deriving from 5 mice for the WT, and from 4 mice from the $SR^{-/-}$). To refine the dataset by excluding non-significant observations, a Shapiro-Wilk normality test[252] was conducted, yielding a negative result. Subsequently, employing the first and third quartile definitions allowed the identification and exclusion of outliers, resulting in a final dataset comprising 12 slices for the WT and 11 slices for the $SR^{-/-}$ group. Additional details are provided in the appendix section (2.6). For each of the two conditions (CA_1-WT and CA_1- $SR^{-/-}$), the values of Δ_s% and Δ_c% were statistically compared via Wilcoxon matched-pairs signed rank test. In the WT slices, the test provided a significant p-value of 0.0005 ($p< 0.05$), confirming a difference in the values of Δ_s% and Δ_c%. On the other hand, the same test conducted in the $SR^{-/-}$ revealed a non-significant p-value equal to 0.3203, indicating that Δ_s% and Δ_c% have very similar values.

To compare D-serine increments in the CA_1 between WT and $SR^{-/-}$ mice, I computed the average time traces for sensor and control for each condition, starting from the moment of pilocarpine addition. In *figure 32b*, a comparison is drawn between the average CA_1 curves for the WT and $SR^{-/-}$ mice. The visual representation underscores that the curve associated with the sensor in WT slices (red continuous line) is consistently higher than that of the sensor in $SR^{-/-}$ (blue line). Pilo-aCSF induces an increase in the current at the D-Serine sensor reflecting a positive variation in the levels of D-Serine starting few mins (8±1 min) after the perfusion and lasting at least until the end of the recording. Most importantly, the average trend for the control electrode (red dotted line) on the WT slices, totally overlaps with the trend of the sensor in the $SR^{-/-}$ slices (blue line). This observation affirms the effectiveness of the control, thereby validating the robustness and reliability of my results. I next compared the Δ_{s-c}% values in the conditions CA_1-WT and CA_1-$SR^{-/-}$, as shown in *figure 32c*. The average value of Δ_{s-c}% for the WT condition was equal to 24.0±6.0%, while the one for $SR^{-/-}$ equals 1.7±0.8 %. Employing the unpaired non-parametrical Mann-Withney test,[250] I computed a p-value of 0.0002, indicative of statistical significance (p-value < 0.05). These results indicate that, in the CA_1 region of the hippocampus, the epileptic condition is associated with an increase in D-serine levels, which is not observed in $SR^{-/-}$ slices where there is no D-serine.

In order to quantify the increment in D-serine, for each of the WT slices the maximum current variation (nA) was extracted for both the sensor and the control microelectrodes. To account for slight

Institut Polytechnique de Paris
91120 Palaiseau, France

deviations in geometry between the electrodes the current variation was considered per unit of surface (specific current, nA/cm^2), computing geometrically the area of the full exposed micro-cylinder, without considering the electrode roughness. Subsequently, for each measurement, specific current variations of the control electrode were subtracted from those of the corresponding sensor. The resulting value was converted into local molar concentration, taking into the sensitivity obtained from pre-measurement calibration curves. The computed average values of the current variations were 56 ± 20 µM (mean ± sem). However, it is important to note that this value can only be regarded as an approximation of the real maximum D-serine levels. In fact, by subtracting specific current variations of the control from those of the sensor, we assume that their sensing capabilities, excluding D-serine, are identical. Nevertheless, despite the identical treatment and PPD deposition, the non-exact reproducibility of the PPD deposition process may introduce variations in sensitivities to H_2O_2.

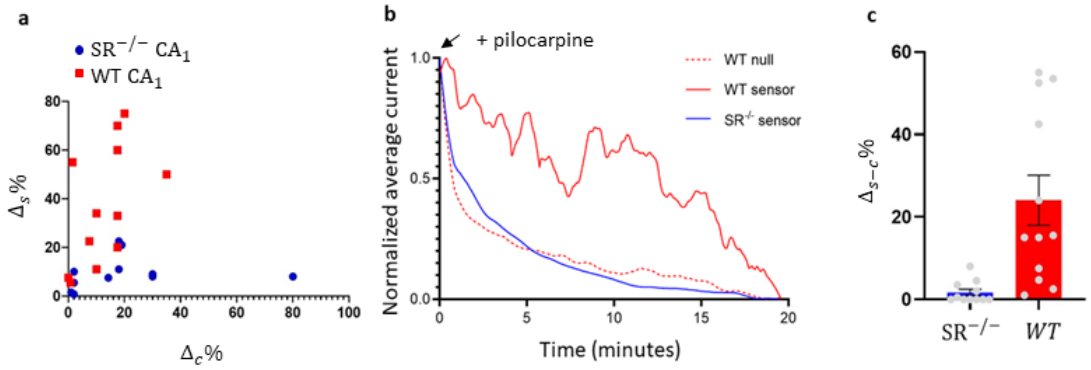

Figure 32. Results of the measurements in the CA$_1$ hippocampus region.
a) Representation of the results obtained from each slice, as a function of the percentage control current increment and the percentage sensor current increment for WT mice (red) and SR$^{-/-}$ mice (blue). b) Overlay of the average curve for sensor in the WT mice (continuous red), the control in the WT mice (dotted red), and the sensor in the SR$^{-/-}$ mice (continuous blue). c) Bar graph representing the mean and the sem values of the difference between the percentage current increment of the sensor and control electrode for WT mice (red) and SR$^{-/-}$ mice (blue).

Subsequently, I extended the investigation to another region of the hippocampus, the DG, employing the experimental procedure and data analysis method described for the CA$_1$ region. Original data set comprised measurements from 11 slices for the DG-WT condition (from 3 mice), and 12 slices from the DG-SR$^{-/-}$ one (from 3 mice). After outlier exclusion, the final data-set contained data corresponding to 10 slices for the WT mice, and 10 slices for the SR$^{-/-}$ ones (detailed information provided in section 2.6). *Figure 33a* illustrates data points corresponding to slices for the WT mice (orange) and the SR$^{-/-}$ mice (cyan). Notably, in this case, the two data groups overlap. To confirm the similarity between the Δ_s% and Δ_c% values in the two experimental conditions (DG-WT and DG-SR$^{-/-}$) statistical analysis via Wilcoxon matched-pairs signed-rank test was conducted, revealing non-significant p-values equal to 0.8457 for DG-WT condition, and to 0.3340 for DG-SR$^{-/-}$. *Figure* 33*b* displays the overlay of three distinct curves: the sensor for the WT mice (continuous orange line), the control for the WT mice (dotted orange line), and the sensor for the SR$^{-/-}$ mice (cyan line).

Interestingly, the three curves overlap with no discernible separation between the sensor and the control curve for the WT mice, as well as between the sensor curves for the WT and $SR^{-/-}$ mice. Similarly, *figure 33c* summarizes the comparison between the $\Delta_{s\text{-}c}$% in WT (2.1±1.0%) and $SR^{-/-}$ mice (0.2±0.1%). Statistical analysis, conducted using the unpaired non-parametrical Mann-Withney tests, yielded a non-significant values of 0.2206 (p-value > 0.05). These outcomes suggest that, unlike the CA_1 region, the DG is not characterized by an increment in D-serine content during pilocarpine induced epilepsy.

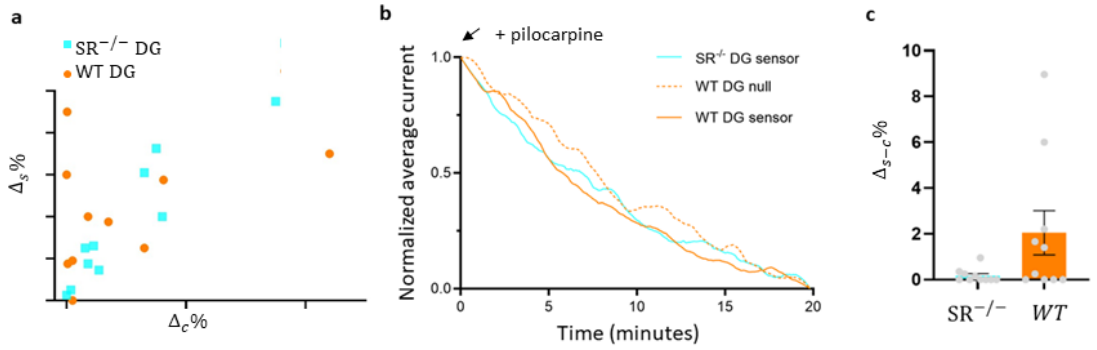

Figure 33. Results of the measurements in the DG hippocampus region.
a) Representation of the results obtained from each slice, as a function of the percentage control current increment and the percentage sensor current increment for WT mice (orange) and $SR^{-/-}$ mice (cyan). b) Overlay of the average curve for sensor in the WT mice (continuous orange), the control in the WT mice (dotted orange), and the sensor in the $SR^{-/-}$ mice (continuous cyan). c) Bar graphs representing the mean and the SEM values of the difference between the percentage current increment of the sensor and control electrode for WT mice (orange) and $SR^{-/-}$ mice (cyan).

The micro-sensors, used for the first time on brain slices, provided direct evidence that pilocarpine treatment induces an increment of D-serine release in WT mice CA_1 hippocampus region, where D-serine is the main co-agonist, differently from what observed in $SR^{-/-}$ mice. My results attain more significance when considered in conjunction with several additional experimental observations, that are not described in this thesis but that will be detailed in an upcoming publication, and that fully align with my observations.

Pilocarpine behaves as a cholinergic agonist and a non-selective muscarinic receptor ligand and it has long been recognized that one of the most important effects of aberrant activation of muscarinic receptors in the hippocampus and other forebrain regions is the potentiation of NMDAR-mediated synaptic transmission[253] but the underlying cellular mechanisms have been largely unknown. In this study, we reveal that pilocarpine increases excitatory synaptic transmission through the modulation of D-serine release. Previous studies have shown that cholinergic signaling controls the synaptic availability of D-serine in physiological conditions[254, 255, 256] but our study underscores the importance of this pathway in pathological conditions.

It is important to note that my results are in contrast with the findings by *Clasadonte et al.*,[257] showing the absence of any detectable changes in D-Serine levels in the hippocampus brain slices

using amperometric detection. These dissimilarities could be explained by the different mouse models used and the experimental approach employed for measuring D-serine levels on the slices. I fact, in their work, Clasadonte et al. used commercial D-serine biosensors to measure D-serine basal levels in slice derived from WT mice and from a mice model in which astrocytic D-serine level is reduced compared to WT. Morever, in their work, D-serine basal levels are determined according to a method similar to the one described in *section 2.3.3.1, figure 28.* In our work, instead, rather than measuring basal levels of D-serine, we detect their variation, as epileptic seizure is induced by pilocarpine on WT and $SR^{-/-}$hipocampus brain slices.

However, my observations confirm a previous study by *Walrave* and colleagues who have reported that pilocarpine-induced seizures is accompanied by an increase in D-serine microdialysate levels.[241] Remarkably, I have found that the observed D-serine increment was region-specific and restricted primarily to the hippocampal CA_1 region, and was not observed in the DG. This observation perfectly aligns with previous findings demonstrating that D-serine is the preferred co-agonist for GluN2A-NMDARs in the mature hippocampus.[247, 258] Furthermore, recent high resolution anatomical analysis of the hippocampal formation in the rat pilocarpine model of TLE revealed that cell loss and neuroinflammation was more pronounced in the CA_1 area and not observed to a similar extent in other regions of vulnerability like the hilus, DG or CA_3,[259] suggesting a selective vulnerability of CA_1 neurons most likely conferred by selective D-serine modulation.

My work not only establishes causality between pathological modulation of the cholinergic system and D-serine *via* NMDAR co-agonist supply, but also provides valuable insights for epilepsy. Thus, our study uncovers a potential target for early therapeutic intervention in epilepsy.

2.4 Conclusion

This chapter details the fabrication and characterization of micrometric electrochemical sensors starting from appropriately sized cylindrical micro-electrodes. The electrodes underwent a series of steps starting from cleaning and electropolymerization of a PPD layer to form a semipermeable membrane enhancing final sensor selectivity. The PPD membrane allowed optimal rejection of the major interfering molecules (serotonin and L-ascorbic acid), while maintaining good sensitivity to hydrogen peroxide in the concentration range 1 µM- 1mM. Subsequently, a layer of the D-serine degrading enzyme *Rg*DAAO was immobilized on the platinum-PPD structure for sensing purposes. Characterization in solution (PBS and aCSF) confirmed the sensor's suitability for detecting D-serine in a concentration range of 1 µM to 10 mM, with an average sensitivity of 5 ± 2 mA/Mcm^2. Notably, the performances of the biosensor are not impacted by the presence of chemicals typically used during

electrophysiology experiments, rendering them a versatile tool to use in combination with other techniques for brain samples analysis.

Similar micro-sensors based on DAAO for D-serine detection had been previously fabricated, with proof-of-concept experiments validating their potential for *in vivo* D-serine monitoring. In this work, these sensors have been used for the first time to measure D-serine variations in mouse hippocampus brain slices, focusing on chemically induced epileptic seizures, a model of TLE, in order to better understand the role of D-serine in the pathology.

Using these sensors, D-serine content variations were analyzed in hippocampus brain slices during pilocarpine-induced seizure, revealing an increase in D-serine content in the CA_1, where D-serine is the preferred co-agonist,[247] differently from what observed in the DG. These observations, combined with other aligning experiment evidences, shed light on the involvement of D-serine in TLE.

This use of electrochemical enzymatic biosensors on brain slices opens avenues for further investigation into the unclear role of D-serine in other pathological and physiological processes. Moreover, the sensor's capability to detect other D-amino acids, notably D-alanine, expands the range of potential applications of these sensors.

2.5 Appendix

Protein activity calculation.

To conduct the assay for determination of the enzymatic activity, I used a spectrophotometer to measure the variation of absorbance values at 440 nm for a period of 6 minutes, recording the value every minute. This allowed us to track the progressive coloration of the mixture. To calculate the enzyme activity (U/mL), we can utilize the *equation 3*:

$$\frac{U}{mL} = \frac{\Delta abs_{440nm}/\min * mL\ tot}{\varepsilon * l * mL\ DAAO} \qquad \textit{(eq. 3)}$$

Here, $\Delta abs_{440nm}/min$ (min^{-1}) represents the initial reaction rate, *mL tot* is the total volume of the mixture in the cuvette, ε is the molar extinction coefficient at 440 nm for orthodianisidine (13 mM^{-1} cm^{-1}), *l* is the optical path of the cuvette (cm), and *mL DAAO* is the volume of *Rg*DAAO in the mixture.[260]

Definition of outliers. According to the quantification process described in the result section, I calculated, for each experimental condition, the difference between the percentage variation of the sensor current and the control one (Δ_{s-c}%). The data-set obtained is represented in the following table.

Institut Polytechnique de Paris
91120 Palaiseau, France

Table1: Summary of the values $\Delta_{s\text{-}c}$% in the 4 experimental conditions referring to different slices. The values reported in red have been later defined identified as outliers.

$\Delta_{s\text{-}c}$% CA_1 $SR^{-/-}$ s-b	$\Delta_{s\text{-}c}$% CA_1 WT s-b	$\Delta_{s\text{-}c}$% DG $SR^{-/-}$ s-b	$\Delta_{s\text{-}c}$% DG WT s-b
14.00	24.00	0.00	6.00
0.00	1.00	0.00	8.96
3.50	15.50	0.00	1.66
0.50	53.00	3.00	1.40
0.00	42.50	0.00	0.00
0.00	2.70	0.15	2.20
4.50	53.50	0.25	0.00
8.00	7.50	0.00	10.70
0.00	15.00	0.00	0.00
0.00	15.00	0.35	0.25
0.00	55.00	0.95	0.00
2.00	4.70	2.50	

A normality test has been performed, using Prism software and it gave negative results. Therefore, outlier have been defined based on the first and third quartile. Having individuated and excluded outliers value, the following final data-set was obtained:

Table2: Summary of the values $\Delta_{s\text{-}c}$% in the 4 experimental conditions referring to different slices after identification of outliers.

$\Delta_{s\text{-}c}$% CA_1 $SR^{-/-}$ s-b	$\Delta_{s\text{-}c}$% CA_1 WT s-b	$\Delta_{s\text{-}c}$% DG $SR^{-/-}$ s-b	$\Delta_{s\text{-}c}$% DG WT s-b
0.00	24.00	0.00	6.00
3.50	1.00	0.00	8.96
0.50	15.50	0.00	1.66
0.00	53.00	0.00	1.40
0.00	42.50	0.15	0.00
4.50	2.70	0.25	2.20
8.00	53.50	0.00	0.00
0.00	7.50	0.00	0.00
0.00	15.00	0.35	0.25
0.00	15.00	0.95	0.00
2.00	55.00		
	4.70		

Institut Polytechnique de Paris
91120 Palaiseau, France

Chapter 3. SICM Imaging

3.1 Introduction

This section will describe the progression and utilization of the Scanning Ion Conductance Microscopy (SICM) technique for live-cell imaging. The discussion will encompass the entire process, starting with the fabrication of the scanning probes, and advancing to the initial efforts in SICM imaging. The first measurements on inorganic samples will be presented before progressing to the imaging of several cell line models, specifically including Madin-Darby Canine Kidney (MDCK) cells, PC12 cells, human podocytes, and Neuro-2a cells. Within this context, we will emphasize the necessity of optimizing several imaging parameters to achieve successful whole cell imaging. Additionally, we will explore the feasibility of acquiring high-resolution topographical maps of cell membranes, a crucial tool for enhancing the comprehension of the cellular state. With the ultimate goal of imaging living neurons, we will delineate the essential modifications required for the SICM setup to maintain the delicate physiological conditions of primary neurons. Furthermore, some examples of topographical mapping of neurons will be provided.

It is relevant to note that all the optimization and advancements in this technique will be discussed within the broader framework of a multifunctional analysis to conduct using dual-barrel probes. As a result, even though it was not obligatory solely for imaging, all SICM topographical measurements were executed using a two-barrels nanopipette.

3.2 Materials and methods

SICM probes fabrication. SICM probes are fabricated from quartz capillaries that were pulled employing a CO_2-based laser puller (P-2000, Sutter) to the desired tapered shape and dimension. For single-barrel nanopipettes (around 150 nm tip diameter), I used single-barrel capillaries (GQF120-90-10, World Precision Instruments) and applied a two-lines pulling program, with the following settings: HEAT= 410, FIL=3, VEL=30, DEL=180, PUL= --; HEAT=410, FIL=4, VEL=40, DEL=160, PUL=120. In the case of two-barrels nanopipettes (around 250 nm dual-barrel tip diameter), I utilized theta quartz capillaries (GQT120-90-7.5, World Precision Instruments) and executed the following pulling program: HEAT = 850, FIL = 5, VEL = 45, DEL = 180, PUL = 85. HEAT = 750, FIL = 5, VEL = 55, DEL = 160, and PUL = 110.

Culture of MDCK and PC12 cells. We received MDCK cells (00062106, Sigma Aldrich) as a generous donation from *Laboratoire d'Optique et Bioscience* (LOB) at *École Polytechnique*, France.

PC12 cells (ATCC-CRL-1721.1) were acquired from LGC Standards. Both cell types were cultured in Dulbecco's Modified Eagle Medium (DMEM) (Sigma-Aldrich), supplemented with 10% Fetal Bovine Serum (Gibco, Thermo Fisher Scientific) and 1% penicillin-streptomycin (Gibco, Thermo Fisher Scientific). The cells were incubated at 37°C in a 5% CO_2 environment within a humidified incubator and passaged when they reached confluence. The culture medium was replaced every 48 hours.

Culture of podocytes. Conditionally immortalized Human Podocytes (CiPodocytes),[261] originally obtained from M. Saleem, were kindly provided by LOB laboratory. CiPodocytes are cultured in Roswell Park Memorial Institute Medium (RPMI) (Gibco, Thermo Fisher Scientific), supplemented with 10 % Fetal Bovine Serum and 1% penicillin-streptomycin at 5% CO_2 and 33°C.

Culture of N2a cells. N2a cells (ATCC-CCL-131) were purchased from LGC Standards and were cultured in Eagle's Minimum Essential Medium (EMEM) (LGC Standards), supplemented with 10% Fetal Bovine Serum. Cells were incubated at 37°C in a 5% CO_2 environment within a humidified incubator and passaged when they reached confluence. The medium was changed twice per week.

Culture of neurons. Human derived iPSC neurons, originally obtained from F. Yates (SEPIA, CEA, France), were provided from the *Lumière, Matière et Interfaces* (LuMIn) laboratory at *ENS Paris-Saclay*, France. Cells were cultured on Geltrex-coated 18-mm coverslips in Neurobasal A medium, supplemented with 1% Glutamax, 1% penicillin-streptomycin, 0.2% ß-mercaptoethanol, 2% B-27, 10 ng/ml GDNF, 10 ng/ml BDNF, 1 µl/ml laminin, and 100 µM AMPc.

Sample preparation for SICM imaging. For MDCK, PC12, and podocytes, cells were seeded onto 35 mm diameter petri dishes (IbiTreat 80156, Ibidi) at a density of 10,000 cells/cm^2, one day before imaging experiments. Similar procedure was followed for seeding N2a cells, that were plated at a density of 500 cells/cm^2, at least three days before the SICM experiment, to allow the observation of single cells with elongated lateral processes. One hour before SICM experiments, cells were thoroughly washed with PBS (pH 7.4, 0.1 M) (Gibco, Thermo Fisher Scientific) and immersed in 800 ml of pure culture medium supplemented with 0.02 M N-2-hydroxyethylpiperazine N'-2-etahne sulfonic acid (HEPES) for pH control. The same solution was used to fill the pipette for imaging. Two chlorinated silver wires of 0.15 mm diameter (AG00-WR-000124, Goodfellow) were used as quasi-reference counter electrodes (QRCEs), one inside the pipette probe and the other immersed in the bulk solution. SICM imaging was performed at room temperature. Neurons were transported to

Laboratoire de Physique des Interfaces et des Couches Minces (LPICM), *École Polytechnique*, the day before the measurement. During imaging, neurons were immersed in their culture medium, while the probe channel was filled with PBS solution. Measurements were performed at a temperature of 32°C, 5% CO_2, and 95% humidity.

SICM setup. A custom-build SICM microscope was specifically designed for biological applications thus being assembled on an inverted optical microscope (DMi8, Leica Microsystems). Optical images were acquired through a 10× objective (HC PL Fluotar, 10x/0.3, Leica Mycrosystems) with a CCD camera (K3C, Leica Microsystems). The SICM probe was hold with an aluminum arm attached to a 3-axis nanopositioner (Nanocube, P-616, Physik Instrumente) with a 100 µm range per axis. The whole ensemble was mounted on three 1-axis linear stepper motors (M-112.2DG1, Physik Instrumente) to expand the positioning of probe to a 25 mm range in X, Y, and Z directions. The nanopositioner was controlled with an analog multi-channel controller (E-727, Physik Instrumente) and the stepper motor with a servo controller (C-863 Mercury, Physik Instrumente). Ionic currents were measured with a transimpedance amplifier (DLPCA-200, FEMTO). A lock-in amplifier (SR830, Stanford Research Systems) was used as sinewave generator to oscillate the probe in Z-direction and to extract the AC component of the ionic current. The probe positioning and SICM imaging was carried out in a LabVIEW environment using the WEC-SPM software, kindly provided by the WEIG group at the University of Warwick (UK). *Figure 34* shows a 3-dimensional schematic of the SICM setup, including the sample stage and the pipette positioning system.

For imaging of living neurons, the setup just described was implemented with the addition of a micro-culture chamber (DH-40iL, Warner Instruments). In order to be fixed on the stage of the microscope, a specific holder has been designed and 3D printed. Thermoresistive connectors on the micro-chamber allow the control of temperature, by mean of a temperature controller (TC-344C, Warner Instruments). In addition, specific perfusion inlets allow CO_2 and humidity control utilizing a CO_2 controller (0506.000, Pecon).

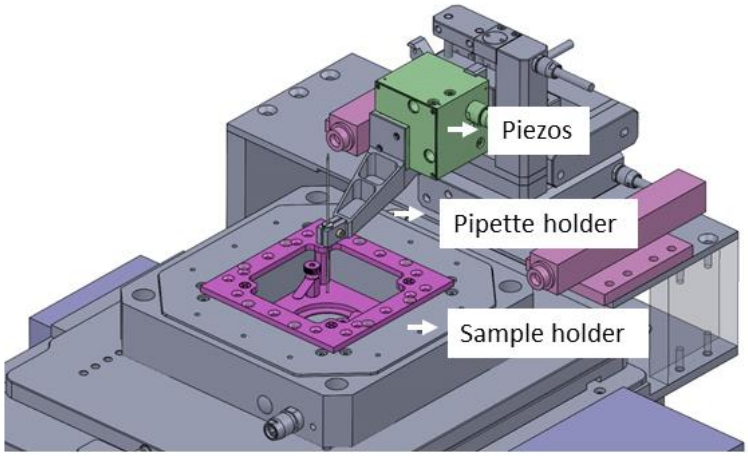

Figure 34. 3D view of the SICM setup.

SICM settings for imaging of silicon samples. Imaging of hard non-biological samples has been conducted in AC+ DC mode, using double-barrel probes. Approach curves have been obtained using an approach speed of 0.1 µm/s and setting an AC threshold equal to 2.2 pA, under an applied voltage of 0.1 V. During the approach, a vertical oscillation of 25 nm (peak-to-peak) was applied to the pipette and the frequency of the lock-in amplifier was set to 273.15 Hz for all the following measurements. Imaging of inorganic samples has been performed in constant distance imaging mode, mapping a 10 × 10 µm area, using a resolution of 25 × 25 pixels, and a lateral speed of 0.2 µm/s. For imaging, I used 0.1 M KCl (Emsure) in MilliQ water (18.2 MΩcm at 25 ℃). Additional imaging was carried out in PBS solution and complete DMEM, enriched with 10% Fetum Bovine Serum and 1% penicillin-streptomycin. Imaging measurements have been performed at room temperature.

SICM settings for imaging of MDCK cells Imaging of MDCK cells has been conducted in AC+ DC modality, in hopping mode, setting an AC setpoint equal to 2 pA. First topographical maps were obtained with hopping approach rate (h.a.r.) equal to 4 µm/s, hopping retract rate (h.r.r.) equal to 9 µm/s and lateral scan rate (l.s.r.) equal to 6 µm/s. In the subsequent speed optimization, the h.a.r. has been increased up to 20, 30, and 40 µm/s. The absolute distance to retract has been set equal to 15 µm and the hopping distance to 2 µm for all the scans. For insertion of the pipette in the cell body, the AC threshold was increased up to 100 pA.

SICM settings for imaging of the membrane of MDCK cells. For SICM imaging of the cell membrane surface, constant distance imaging mode was utilized, to image an area 2 × 2 µm large, with 100 nm lateral resolution (20 × 20 pixels). The AC threshold was set to a value of 1.2 pA and the probe was scanned laterally at a rate equal to 0.2 µm/s.

For Scanning Electron Microscopy (SEM) imaging of MDCK cells, they were initially cultured on 18-mm coverslips and subsequently fixed with a solution of 2% paraformaldehyde and 2% glutaraldehyde for a duration of 1 hour. Following fixation, the cells underwent multiple rinses with PBS. Subsequently, they were sequentially immersed for 15 minutes in 50%, 70%, and 90% ethanol. Following this step, the cells were subjected to a 5-minutes vacuum-drying process, and platinum sputtering was applied to their surface. SEM images were acquired with the voltage and current values set at 10 kV and 5 µA, respectively.

SICM settings for imaging of PC12 cells and human podocytes. PC12 cells have been mapped in hopping mode, setting an AC threshold equal to 2 pA. The h.a.r. was equal to 40 µm/s, while the h.r.r. and l.s.r. were respectively 30 µm/s and 25 µm/s. The absolute distance to retract was equal to 15 µm. Podocytes were also imaged in hopping mode, using h.a.r., h.r.r., and l.s.r. respectively equal to 20 µm/s, 80 µm/s, and 80 µm/s. The AC threshold was set to 2 pA, the absolute distance to retract was equal to 7 µm, and the hopping distance was 2 µm.

SICM settings for imaging of N2a cells. N2a cells have been mapped in hopping mode, with an AC setpoint equal to 2 pA. H.a.r., h.r.r. and l.s.r. were respectively 20 µm/s, 60 µm/s, and 55 µm/s. Absolute distance to retract was equal to 15 µm. During the resolution optimization, the hopping distances employed have been 2 µm, 1 µm, and 0.5 µm.

SICM settings for imaging of iPSCs Neurons. Human derived iPSC neurons have been imaged with 2 µm resolution, using hopping mode imaging mode. AC setpoint threshold was set to 5 pA, h.a.r., h.r.r., and l.s.r. were respectively equal to 10 µm/s, 20 µm/s, and 10 µm/s. Absolute distance to retract was equal to 15 µm, and the hopping distance used was 2 µm. For higher resolution imaging, hopping distance was modified to 1 µm.

3.3 Results and discussion

3.3.1 Fabrication of SICM nanopipettes

The laser pulling process involves controlled heating and stretching of a glass capillary, resulting in a finely crafted, sharp apex with a small aperture. The laser puller, whose picture is shown in *figure 35a*, utilizes a laser beam to precisely heat the glass, allowing a precise control over the dimensions and shape of the resulting pipette. The equipment includes a laser source and a pipette holder to secure the capillary alignment beneath the laser focal point. The laser beam raises the capillary's temperature until it softens, at which point a carefully controlled force is applied to separate the two ends, creating

the desired elongated apex. Users can fine-tune the pulling settings through a control panel ensuring precision and repeatability in the shape and size of the resulting nanopipettes. Between the parameters to be defined, the HEAT (0-999) specifies the output power of the laser and the FILAMENT (0-15) specifies the scanning pattern of the laser beam that is used to supply HEAT to the glass. The VELOCITY (0-255) refers to the speed at which the puller bar must be moving before the hard pull is executed, while the DELAY (0-255) controls the timing of the start of the hard pull relative to the deactivation of the laser. Finally, the PULL (0-255) is the force applied for the hard pull.

Different types of capillaries can be pulled, yielding to different types of nanopipettes geometries. For example, pulling from a single-barrel capillary yields a pair of single-barrel pipettes, as depicted in the SEM images, from front and bottom view, in *figures 36b* and *36c*. Tips opening in this case typically range between 100 and 150 nm. Alternatively, pulling a double-barreled or theta capillary results in a pair of identical two-barrels nanopipettes, as shown in SEM images of *figures 36d* and *36e*, with a double-barrel dimension of approximately 200 – 250 nm. Both the single and the double-barrel pipettes present a regular flat profile (observable in *36b* and *36d*) with homogeneously thick walls, fundamental to the successful utilization of the probes.

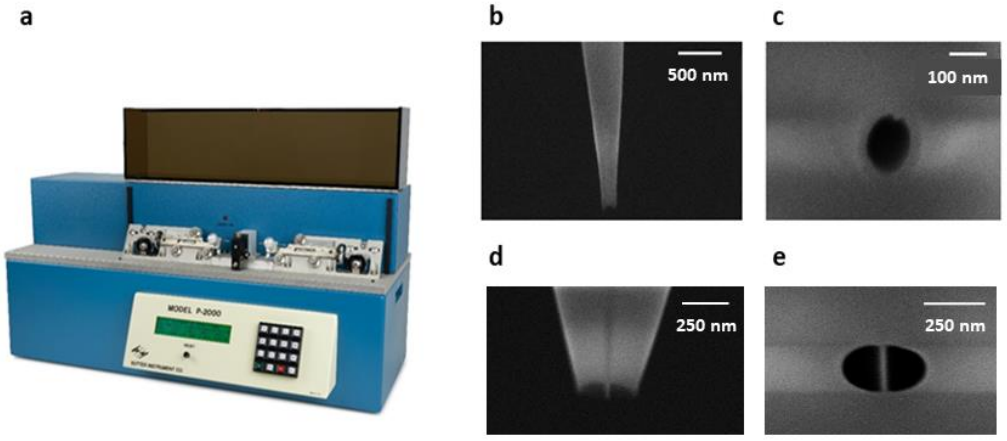

Figure 35. SICM probes fabrication.
a) Picture of the CO_2-based laser puller (Sutter, P-2000) used for the fabrication of our nanopipettes;[262] b) SEM picture of the front view of a single-barrel nanopipette; c) SEM picture of the bottom view of the tip opening of a single-barrel nanopipette; d) SEM image of the front view of the tip of a two-barrels nanopipette; e) SEM picture of the bottom view of tip opening of a two-barrel nanopipette.

Precisely controlling the size and shape of the tip opening is critical when using these pipettes for SICM imaging. Smaller opening enhance resolution by reducing spatial constraints, enabling the detection of finer details and smaller structures. However, it is essential to strike a balance, as excessively small openings can pose challenges for the functionalization to operate (see chapter 4). Therefore, considerable effort has been dedicated to achieving a size that balances our requirements while maintaining good repeatability.

Institut Polytechnique de Paris
91120 Palaiseau, France

3.3.2 SICM imaging of reference substrate

While conducting SICM imaging under non-physiological conditions, a solution of KCl 0.1 M is typically employed. However, when working with living cells, the choice of an appropriate imaging medium becomes more intricate. The selected solution must not only be suitable for imaging purposes but also support the maintenance of the conditions that keep the cell viable and functional, closely mimicking the cell's natural state. In this context, the suitability of two primary physiological solutions, PBS and DMEM, was examined.

In *figure 36a*, two approach curves are depicted, acquired using twin pipettes that were identically positioned on a silicon-patterned sample, illustrated in *figure 36b*. The approach curve for KCl (in red) exhibits a lower bulk value than the one for PBS (in blue) due to the lower ionic strength of the KCl solution compared to PBS solution, but the two curves look equally stable. To visually illustrate the possibility to conduct SICM imaging in PBS, *figure 36c* presents an example in which a selected area measuring 10 × 10 µm (25 × 25 pixels) is imaged using the constant distance imaging mode. The topographical map generated reveals a geometry consistent with the known dimensions and shape of the silicon sample.

The maintenance of a stable bulk current is crucial for achieving effective feedback in experiments. This stability resulted particularly critical when assessing the suitability of culture medium as solution for SICM imaging. DMEM is a common medium utilized for many cell lines and is typically supplemented with serum components to enhance cell growth and viability. However, it is reported that when employing complex culture media such as complete DMEM for imaging, caution must be exercised to prevent pipette clogging caused by macromolecular species present in solution.[263] This issue is confirmed in *figure 36d*, which presents a brief representation of the measured bulk i_{DC} over a 10-minutes period, with data recorded every 2 minutes. The graph illustrates a gradual decrease in the bulk i_{DC} over time. Consequently, a new test was conducted using pure DMEM without the inclusion of serum components. This serum-deprived solution was found to provide a stable i_{DC}, effectively addressing the challenges previously encountered. Subsequently, this solution was utilized to create a topographical map of a patterned silicon sample using the constant distance mode, as depicted in *figure 36e*.

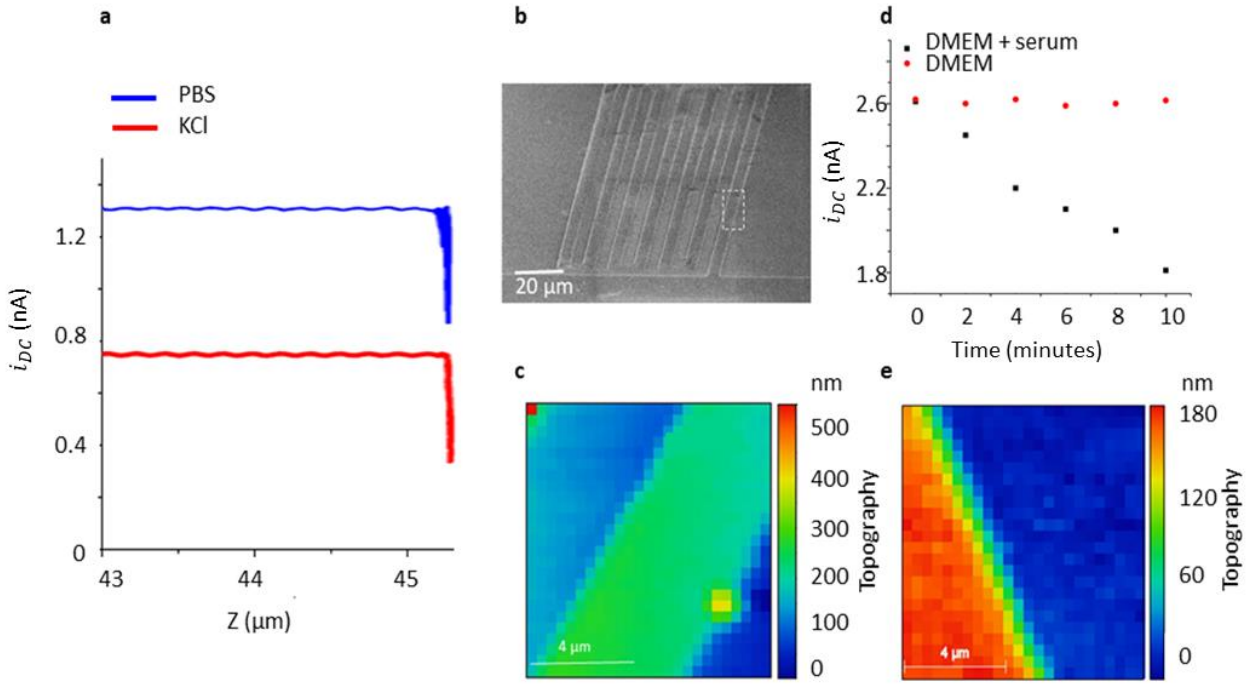

Figure 36. SICM imaging of reference samples in physiological conditions.
a) DC signals during approach curve in PBS (blue) and in KCl (red) conducted with two identical pipettes, b) SEM image of a silicon patterned sample: the area surrounded by the dotted line is the one mapped in SICM, c) SICM topographical map of the silicon sample using PBS as imaging solution, d) $\boldsymbol{i_{DC}}$ over time in complete DMEM culture medium (in black) and DMEM without serum components (in red), e) SICM topographical map of silicon sample using DMEM deprived of serum components as imaging solution.

3.3.3 SICM imaging of living cells

To initiate the imaging of living cells, we opted to start with relatively simple cellular models that are easy to culture and exhibit strong adhesion properties. Therefore, our initial subjects for imaging were MDCK cells, PC12 cells, and human podocytes.

Before the imaging process, these cells were cultured and seeded onto petri dishes (section 3.2). The culture duration and the seeding density were carefully optimized to ensure robust adhesion of individual cells. This choice of isolated cells was deliberate, as it facilitates the visualization of cell topography. Adequate adherence prevents any unintended disturbances in the measurements arising from potential contact between loosely attached samples and the probe. It is worth emphasizing that prior to SICM imaging, the cells underwent thorough rinsing with PBS to eliminate any residual serum components, which could potentially obstruct the pipette and disrupt the feedback loop. The original complete medium was subsequently replaced with pure DMEM, in accordance with the findings outlined in the preceding section. Additionally, the medium was supplemented with 20 mM HEPES to ensure pH control during the imaging process, as it was conducted under atmospheric CO_2 conditions.

The optimization of scanning parameters was conducted to tailor SICM imaging for living cells. Given the considerable height of cellular structures relative to the tip size, in the range of 5 to 10 µm, the most suitable imaging mode is hopping mode. In this context, a parameter that requires particular attention is the retraction distance initiating each of the hopping steps. In fact, having mentioned the significant thickness of the cellular body, the consequence of not sufficiently retracting the probe is the risk to laterally hit the cell surface during the displacement of the probe horizontally. For this reason, an absolute retracting distance of 10 µm to 15 µm has always been used. Even if for each pixel the pipette is retracted of a certain distance with respect to the last position. This precaution is taken because of the unknown steepness of the lateral borders of the cell. *Figure 37a* shows an SICM topographical map obtained after scanning a spindle-like MDCK cell, using a lateral resolution of 2 µm and an AC threshold equal to 2 pA. Comparing the SICM map with the optical image represented in *figure 37b*, we can appreciate that the distinctive shape of a similar cell is reproduced.

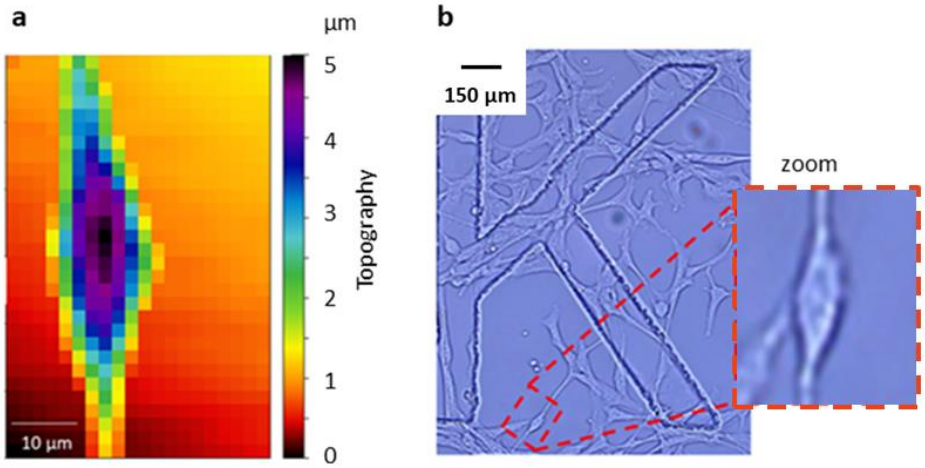

Figure 37. SICM imaging of MDCK cells.
a) SICM topographical map of a spindle-like MDCK cell obtained in hopping mode, using a hopping distance of 2 µm; b) optical image of a similar cell (inset showing the zoomed area containing the cell).

When optimizing scanning parameters in AC+DC mode, it has to be considered that the feedback mechanism maintains the AC current (i_{AC}) at a specific setpoint. Choosing this value is important because it must be above the AC noise level but kept as low as possible to prevent unintended probe-cell contact. As explain in section 1.3.2, the feedback mechanism changes the vertical (z-direction) position of the nanopipette to maintain a constant i_{AC} equal to a user-selected threshold. As seen in the explanatory AC approach curve, the i_{AC} is negligible when the pipette is far from the sample surface but rises sharply as it approaches the surface. The closer the pipette gets to the surface, the higher the i_{AC} becomes. Therefore, selecting a higher i_{AC} threshold has the following consequences. First, it makes the system less susceptible to background noise since it operates well above the noise level. Second, it brings the probe much closer to the surface, requiring careful operation to avoid collisions with the sample. Examining *figure 38*, we can observe a notable distinction in the behavior

Institut Polytechnique de Paris
91120 Palaiseau, France

of the approach curves depicted. The red curves, respectively DC and AC in *figures 38a* and *38b*, are generated by approaching a probe to an inorganic silicon surface in DMEM medium. The subsequent curves, in blue in *figures 38c* and *38d*, illustrate the case of an approach on a cell body obtained with another pipette also in DMEM medium. The discrepancy in the steepness between the curves is evident, with the curves for the cell bodies being notably less steep compared to those on the silicon surface. Both of these approach curves were obtained by setting the AC threshold to a specific value equal to 6 pA, and using an approach rate of 0.1 µm/s. In addition, it is worth noting that when attempting to map cellular structures with such an AC threshold value, I encountered challenges, including highly unstable current readings and cell bodies detaching from the underlying support.

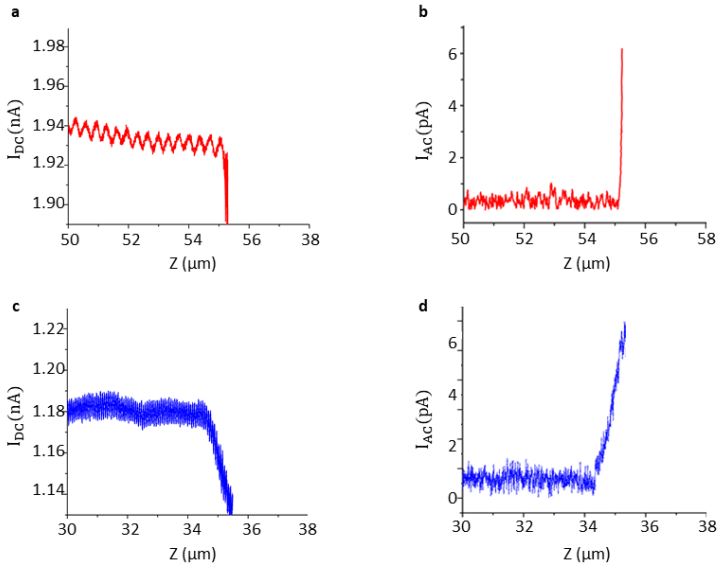

Figure 38. Approach cure on reference samples and cell body.
a) DC approach curve on a silicon surface; b) AC approach curve on a silicon surface; c) DC approach curve on a cell body; d) AC approach curve on a cell body.

Given the soft nature of biological materials, we can bear in mind that glass pipettes, similar to those utilized in this investigation, find extensive use in electrophysiological studies there they serve to pierce membrane of living cells. Consequently, I contemplate whether the distinct behavior observed in these recordings can be attributed to contact-related issues or inadvertent insertion of the nanopipette into the cell body.

To further explore this concept, I conducted the following experiment. I mapped a pair of MDCK cells using hopping mode, employing a hopping distance of 2 µm, resulting in the topographical map shown in *figure 39a*. After completing the scan, the micropositioner of the SICM setup was used to position the probe at a specific location, marked by the red dot and arrow in the figure. Here I initiated a new approach by increasing the AC threshold to 100 pA, allowing the probe to come very close to the surface, and maintaining an approach rate of 0.1 µm/s to prevent unintentional damage to the probe structure. *Figures 39b* and *39c* display the resulting approach

Institut Polytechnique de Paris
91120 Palaiseau, France

curves, representing DC and AC, respectively. In both plots, we can observe a distinct change in current: a decrease for DC and an increase for AC. The changes in current are observable between a specific starting z value (green arrow in *40b* and *40c*) and a final one (blue arrow *40b* and *40c*). Notably, the difference between these two values of z matches the thickness of the cell at the specific location where we are probing, suggesting that during the approach, we may be traversing through the cell body's thickness.

Indeed, some examples reported in literature have used SICM probes for controlled insertion into cellular bodies. Researchers have tried to elucidate the complex current patterns resulting from these experiments and several interpretations have been proposed, describing how the measured current varies during the insertion of the pipette in the cell body.[264, 265] Nevertheless, explanations can be challenging and variable in different scenarios. In general, it is suggested that during the approach, an initial decrease in the i_{DC} and an increase in the i_{AC} is observed, signifying the detection of the cellular membrane by the pipette. This is illustrated in *figures 39b* and *39c* with the green arrows. Initially, the behavior aligns with the standard SICM approach curves, but it diverges when the pipettes pushes on the membrane's surface, indicated by the yellow area in the two plots.[264] As the cell membrane is penetrated, there is a continuous decrease of the DC current, as observable in *figure 39b.* The substrate is detected as a sudden change in DC and AC currents, at the point marked in *figures 39b* and *39c* with a blue arrow.[265] This is visible in the final decrease/increase of the DC/AC trends, marked by the blue arrows.

The potential use of SICM probes for controlled penetration of living cells opens up possibilities for intracellular analysis applications. However, this work is primarily focused on cellular imaging and therefore establishing the appropriate AC threshold for topography mapping. In order to avoid any chance of contact or probe insertion into the cell during imaging, I opted to use relatively low AC threshold values, which proved effective for cell imaging.

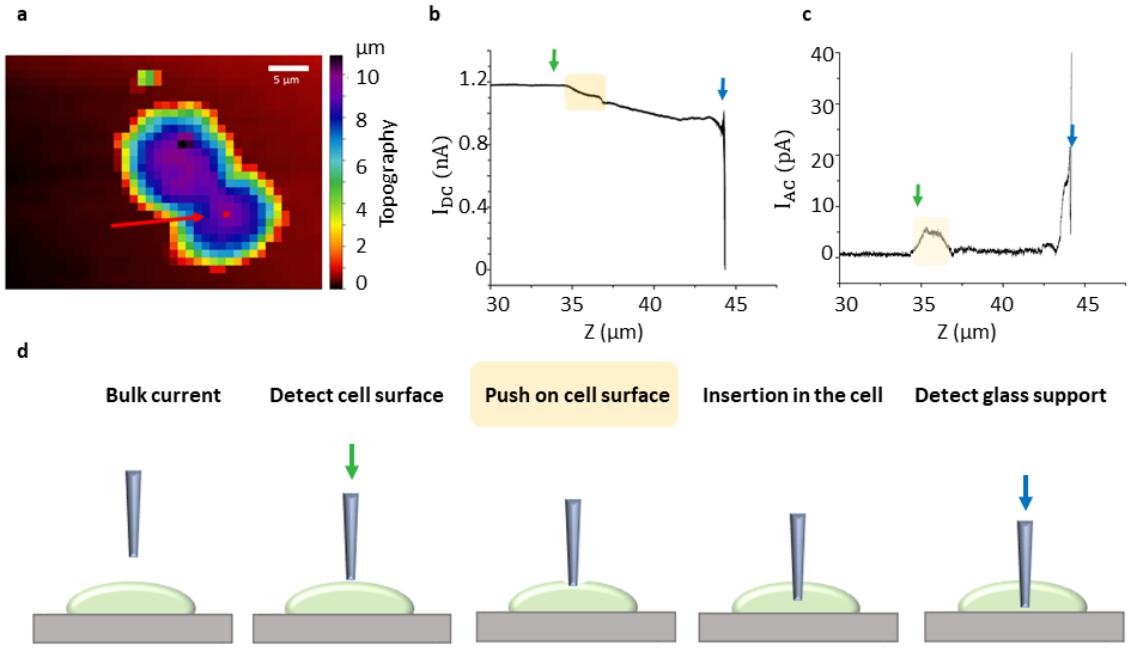

Figure 39. Insertion of a SICM probe in a cell.
a) Topographical SICM map of a couple of MDCK cells, obtained in hopping mode, with a hopping distance of 2 µm, b) $\boldsymbol{i_{DC}}$ trend during the insertion of the pipette in the cell body, c) $\boldsymbol{i_{AC}}$ trend during the insertion of the pipette in the cell body. d) Summary of the subsequent steps during the insertion of a nanoprobe in a cell body.

In reference to the topographical map depicted in *figure 37*, it is noteworthy that the acquisition time for this image was 31 minutes. Over the course of such an extended duration, the shape of the cell may evolve. Therefore, it is critical to adapt the settings to reduce the scanning time. Furthermore, the ability to obtain topographical maps in shorter times can be highly beneficial, especially when mapping groups of cells or larger cells. In this context, *figure 40a* summarizes several tests conducted on a single MDCK cell, demonstrating that h.a.r. of up to 20, 30, and 40 µm/s can be used, resulting in scanning durations of 20 × 25 pixels' area of 6, 4, and 3 minutes, respectively. These adjustments do not yield significant differences in the resulting topography and do not harm the probe. Moreover, the capability to scan the probe at much higher speeds (40 µm/s) allowed us to map an area of 60 × 80 µm containing three adjacent PC12 cells with a resolution of 2 µm in just 8 minutes, as depicted in *figure 40b*. Furthermore, *figure 40c* provides another example illustrating how the use of a high scanning speed enables the acquisition of topographical maps of larger cells, such as the podocyte depicted here, within a 100 × 100 µm area and a resolution per pixel of 2 µm, in a reasonable amount of time (19 minutes).

Institut Polytechnique de Paris
91120 Palaiseau, France

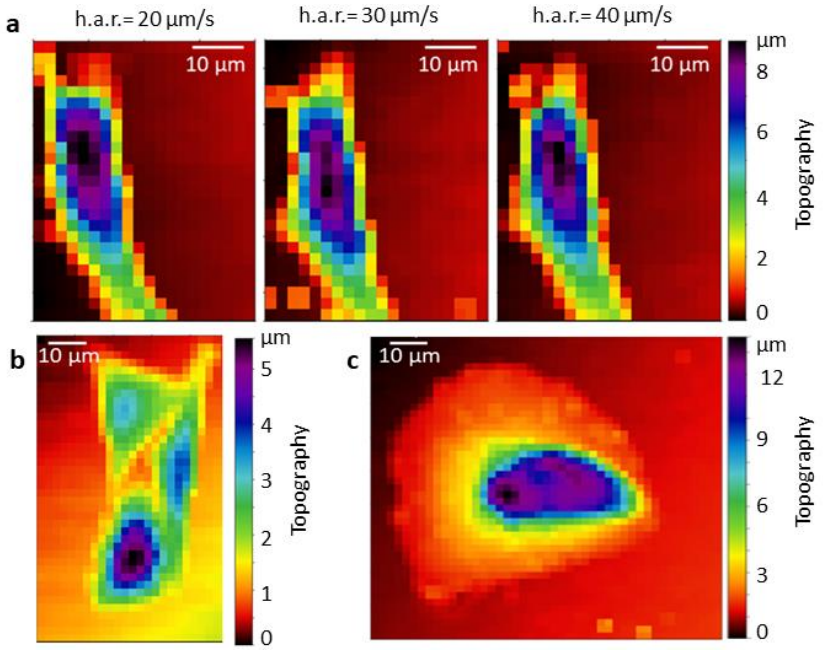

Figure 40. Optimization of SICM scanning speed.
a) Subsequent topographical map of a single MDCK cells, using h.a.r. equal to 20 µm/s, 30 µm/s, and 40 µm/s; b) SICM topographical map of a group of three PC12 cells; c) SICM topographical map of a podocyte.

However, the ultimate objective is to map primary neurons, which possess axons and dendrites that may not be visible at the resolution employed thus far. Instead of directly transitioning to imaging primary cells, which would introduce additional complexities and require modifications to the setup, as we will discuss later, it was chosen to utilize mouse neuroblastoma N2a cells as an alternative cellular model. N2a cells exhibit elongated lateral filaments similar to neural branches, rendering them well-suited for training in imaging of intricate features. Furthermore, due to the slender nature of these structures, N2a cells serve as an ideal model for enhancing spatial resolution for the imaging purposes.

In *figure 41a*, an optical image of N2a cells on a petri dish is presented before undergoing an imaging experiment. The dotted line demarcates the region that has been mapped, zoomed in the inset, and *figure 41b* shows the topographical map of a 60 × 40 µm area representing a single N2a cell, where thin lateral processes are discernible. To optimize imaging resolution, a series of subsequent maps were acquired, as summarized in *figure 41c*.

By focusing on a specific segment of a cell (20 × 24 µm), representing the connection between the cellular body and a lateral process, three maps were generated utilizing a hopping approach rate of 20 µm/s and selecting hopping distances of 2 µm, 1 µm, and 0.5 µm. As the resolution increases, finer details become more precisely defined at the expense of scanning duration. Notably, the scanning time varied from 2 minutes, for the low-resolution image, to 28 minutes, for the map with the highest resolution. Therefore, depending on the specific needs and the size of the area to observe, a compromise between scanning speed and spatial resolution needs to be chosen.

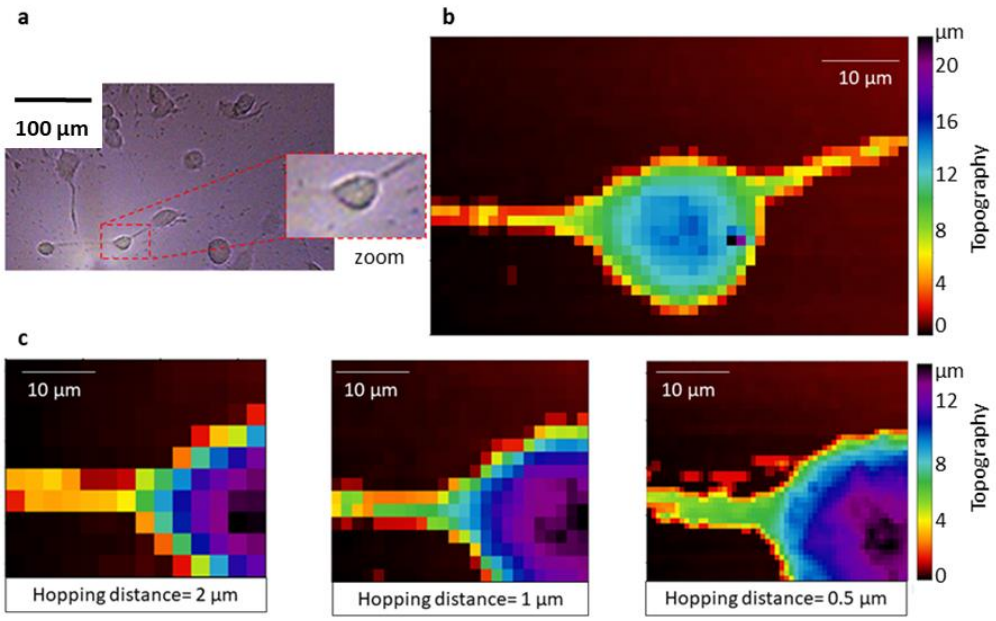

Figure 41. SICM imaging of N2a cells.
a) Optical image of cultured N2a cells: the area surrounded by the dotted line has been used for SICM imaging, b) SICM topographical map (60 × 40 µm) of a single N2a cell with 1 µm lateral resolution, c) SICM topographical map of a portion (20 × 25 µm) of the same N2a cell with increasing lateral resolution of respectively 2, 1 and 0.5 µm.

3.3.4 Imaging of cellular membrane

The cell membrane is a biological layer separating the intracellular environment from the extracellular one. It is a fluidic structure composed by a lipid bilayer, consisting of two phospholipidic layers with cholesterol spread in between. It also contains protein components, with a fundamental role in transmembrane transport and interaction with the cell surrounding environment. The semipermeable membrane controls the passage of different substances inside and outside of the cell and also plays an important role in cell adhesion.[266] It is a dynamic and multifunctional structure that undergoes shape modifications and movements, as a result of physiological events, and its characterization is therefore of greater interest. The observation of membrane topography can be done via SICM, due to the non-contact nature of the technique, that may prevent disruption of its delicate features.[181, 172]

In this case, it is necessary to obtain high resolution topographical information (hundreds of nm) about the cell surface topography, while still using double-barreled probes (tip opening 200 – 300 nm), to be able to combine imaging with local analysis through the second functionalized barrel. As observed until this point, the lateral resolution when imaging in hopping mode is given by the hopping distance set by the user and the opening size of the pipette. In order to increase the resolution, it was decided to avoid hopping and use the constant distance imaging mode for mapping small areas (micrometric areas), observing the local topography of the membrane with more data points in the map, increasing the resolution of pixels. More in detail, a first low-resolution scan in hopping mode

was performed to spatially locate the full cell and individuate flat areas on it, where high resolution constant distance imaging was performed. In these areas, in fact, the risk of lateral collision between the tip and tall structures from the cell is minimal. This change of imaging mode is possible as it is featured in the WEC-SPM software employed.

Figure 42a represents a SICM topographical map of an MDCK cell: the white square on top of the cellular body represents a 2 × 2 µm area, selected for constant distance imaging with 100 nm lateral resolution (20 × 20 pixels), shown in *figure 42b*. The probe was scanned laterally with a rate of 0.2 µm/s and the duration of the scan was 14 minutes. The resulting map reveals a surface topography characterized by variations in thickness, presenting depressions and swellings that may represent actual roughness on the cell surface. Consequently, a second constant distance scan was conducted on the same area immediately afterwards, employing the same image settings, to determine whether a similar surface topography was observed. Upon examining the topographical map in *figure 42c*, it also reveals a rough surface, with irregularities of sizes comparable to those in *figure 42b*. Nevertheless, differences in their shape and distribution are visible and could likely be attributed to the dynamic nature of the cell, which undergoes morphological changes.

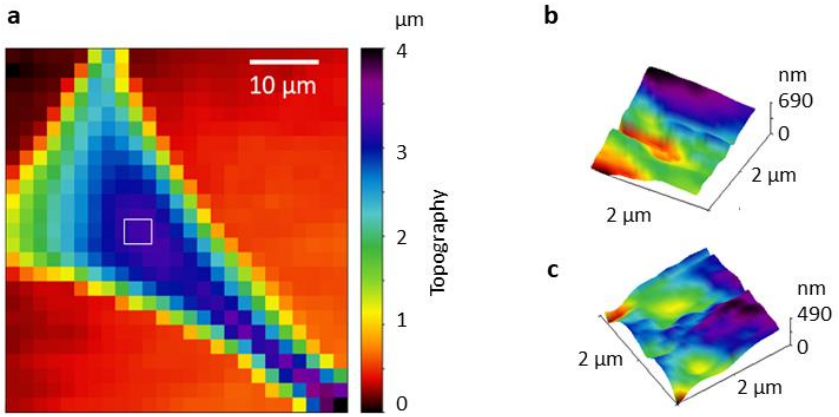

Figure 42. SICM imaging of the cell membrane of MDCK cells.
a) Topographical map of the whole cell morphology of a MDCK cell, b) first topographical map in constant distance of the cell surface; c) second topographical map of the cell surface.

To address any doubts and confirm the existence of real topographical features, a series of tests was conducted, as depicted in *figure 43*. Initially, a 2 × 2 µm area of the coverslips supporting the cells was mapped, using the same imaging mode and settings employed to generated the topographical maps in *figures 42b* and *42c*. This was done to demonstrate that the surface roughness observed in this case is smaller, thus attributing what was previously mapped to the cell itself. As shown in *figure 43a*, the roughness is indeed one order of magnitude smaller, validating the previous findings. Furthermore, to validate the topographical maps obtained through SICM, it was chosen to fix MDCK cells and examine their surface using SEM. *Figure 43b* displays a complete MDCK cell, with a specific focus on a portion of the cell body (indicated by the white arrow) in *figure 43c*. In this SEM

image, representing an area of dimensions similar to those in the SICM topographical maps, we can observe both larger and smaller depression on the cell surface, marked by the red and blue arrows. When comparing the SEM and SICM representations, it suggests that we are likely detecting these topographical features. It is important to note that while the fixation process can slightly alter the appearance of the cellular surface due to membrane shrinkage, it does not entail a complete modification of its topography.[267]

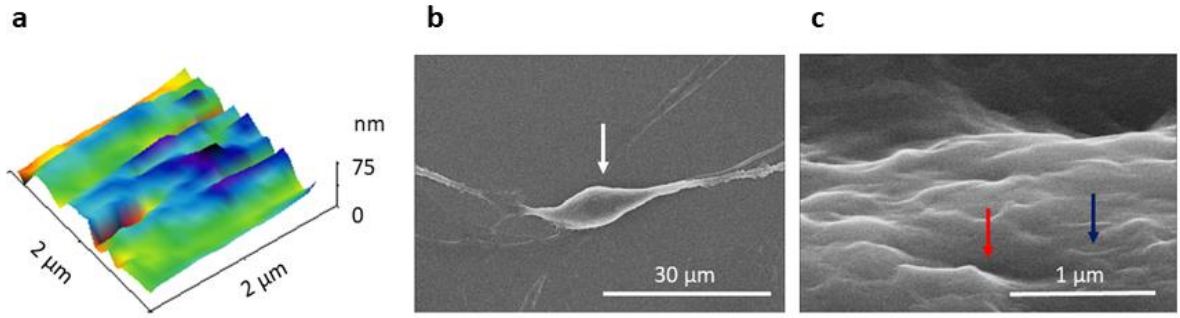

Figure 43. Tests for the validation of SICM imaging of cell membrane.
a) SICM topographical map of a 2 × 2 µm area on the plastic support of the sample, b) SEM image of a full fixed MDCK cell; c) SEM image of a detail of the MDCK cell surface.

To ultimately validate this observation and attempt to provide an explanation for the topographical differences between f*igures 42b* and *42c*, I conducted SICM imaging of fixed MDCK cells, to map a cellular surface with increased rigidity and therefore less varying morphology. The imaging solution employed was DMEM, deprived of serum components but supplemented with 20 mM HEPES. HEPES is added to non-fixed cells in order to keep the pH of the imaging solution constant and equal to the physiological one, to prevent affecting cellular growth during the imaging process. While fixed cells do not necessitate a constant pH, HEPES was included to maintain consistency with previous measurements.

Figure 44 presents a sequence of three consecutive topographical maps generated by scanning the same 3 × 3 µm area atop a fixed MDCK, with a resolution of 30 × 30 pixels. The duration of each scan was 30 minutes. Notably, across these successive maps, the same primary depressions and swellings on the cell surface remain clearly visible. Consequently, we can confirm that we have the capacity to accurately depict cell membrane features and that the system does not have a significant spatial drifting in the duration of this experiments.

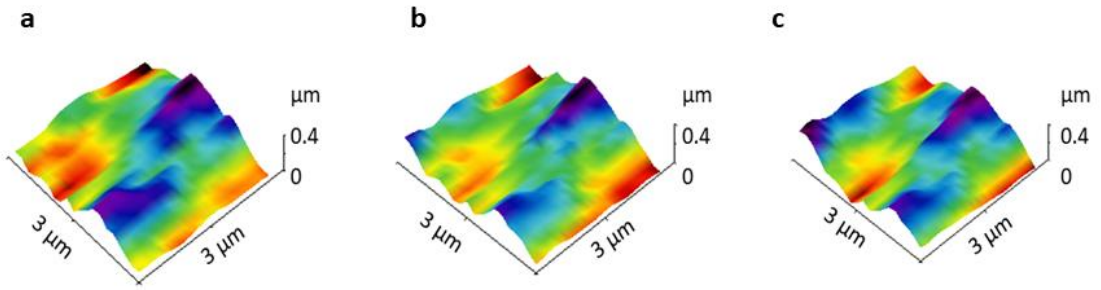

Figure 44. SICM imaging of the surface of fixed MDCK cells.
a) First constant distance image of the cell surface; b) second constant distance image of the cell surface; c) third constant distance image of the cell surface.

With the ability to accurately map cell membrane details, I aimed to increase scanning speed. To achieve this, an area of 2 × 2 µm on a cell body was selected and a series of tests was conducted, as depicted in *figure 45*. The same area was mapped in constant distance mode, gradually increasing the lateral scan rate from 0.1 µm/s to 2 µm/s. In the first three scans, as seen in *figures 45a* to *45c*, corresponding to lateral scan rates of 0.1 µm/s (scan duration of 14 minutes), 0.2 µm/s (7 minutes), and 0.3 µm/s (4 minutes), the same topography is consistently observed. However, as the scanning speed increases to 0.5 µm/s (3 minutes), 0.7 µm/s (2 minutes), and 1 µm/s (90 seconds) (*figure 45d*, *45e*, and *45f*) a variation in the cell body's surface features becomes apparent. This variation becomes even more pronounced when the lateral rates reach 1.5 µm/s (56 seconds) and 2 µm/s (42 seconds), as illustrated in *figures 45g* and *45h*. To address whether the changes in surface topography were due to actual cell movement or artifacts of the imaging process, I conducted another scan of the same area immediately after the 2 µm/s scan, using lateral scan rate of 0.1 µm/s. *Figure 45i* displays the resulting map, which closely resembles the topography observed in the first three scans. This suggests that scanning at higher speeds poses a risk of affecting the imaging process, maybe due to vibrations and fluctuations associated with the rapid lateral movement, leading to inaccurate data acquisition. Additionally, scanning at high speeds might result in insufficient time for the probe to adequately interact with the cell membrane, resulting in incomplete or distorted measurements. Further investigation may be conducted in order to see whether changing the feedback setting would improve the outcomes of rapid scanning.

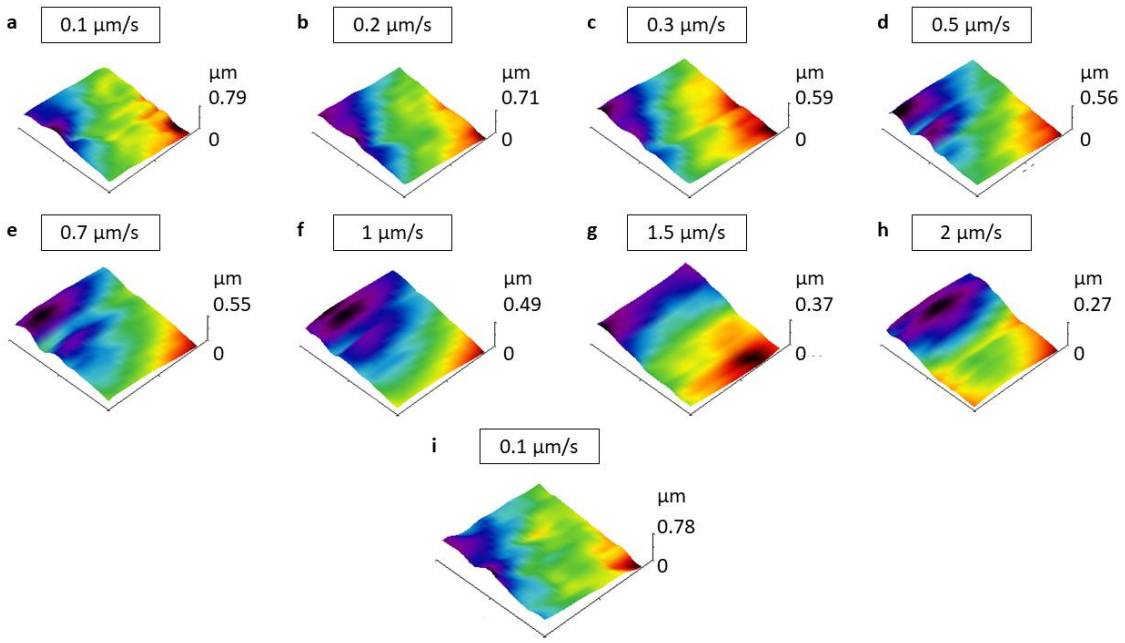

Figure 45. Impact of the lateral scan rate on the topography of the cell membrane.
From a) to h) SICM topographical map of the same 2 × 2 µm area obtained with lateral scan speed of 0.1 µm/s, 0.2 µm/s, 0. 3 µm/s, 0.5 µm/s, 0.7 µm/s, 1 µm/s, 1.5 µm/s, 2 µm/s. i) Topographical map of the same area using, again, a lateral scan speed of 0.1 µm/s

3.3.5 Adaptation of the SICM setup for imaging of neurons

In this study and in most of the literature, SICM imaging, even when combined with functional analysis, is conducted outside the controlled environment of the incubator, with some remarkable exceptions.[268, 269] This practice exposes cells to conditions quite distinct from their culture environment, which can significantly impact their behavior. Notably, when cells are handled outside the incubator, they face challenges such as lower CO_2 levels, reduced humidity, and low temperatures. These drastic environmental changes can lead to cellular stress and even cell death within a short period, which makes long SICM acquisition impossible.

While working with robust cell lines that are less sensitive to temperature variations, I have primarily focused on controlling the pH of the imaging solution. Since the bicarbonate buffer in the culture medium does not maintain adequate pH at low CO_2 levels outside the incubator, this issue was addressed by adding HEPES to the culture medium during imaging. This adjustment has allowed us to work with the same cells for extended periods of time.

However, the goal is to use the SICM platform for imaging and functional analysis on primary neurons. Given the fragility of these samples, it is essential to maintain their physiological state for as long as possible. Operating in a stable and controllable environment would enable us to conduct more extensive and meaningful measurements. Therefore, modifications of the SICM setup were made to control key physiological parameters that can influence cellular behavior. To create a controlled environment, a culture dish microincubator has been integrated onto the stage of the

microscope (*figure 46*). Additionally, a special adaptor was designed and 3D printed to ensure the stable positioning of the microincubator within the existing setup. The microincubator can be used in open configuration mode (*figure 46a*), as a culture dish whose temperature can be controlled through a metallic plate positioned on the chamber. In alternative, the microincubator is equipped with a special lid, allowing to work in closed configuration mode, to perform not only temperature but also CO_2 control (*figure 46b*).

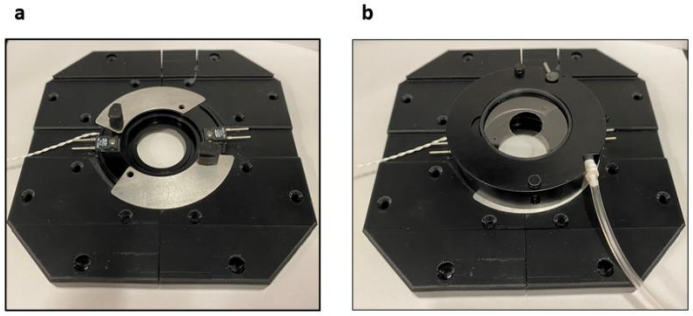

Figure 46. Culture dish micro-incubator.
In a) open configuration, and b) closed configuration.

When operating in open configuration, the micro dish incubator allows control of the temperature by means of thermoresistive elements and specific connectors. *Figure 47a* shows an image of a petri dish located in the micro-chamber and connected to the cables for temperature control. In order to start testing the performances of SICM imaging in a controlled environment, I started right from questioning about the stability of the current signals when operating at a temperature of 32°C, several degrees higher than the usual 19°C of the room.

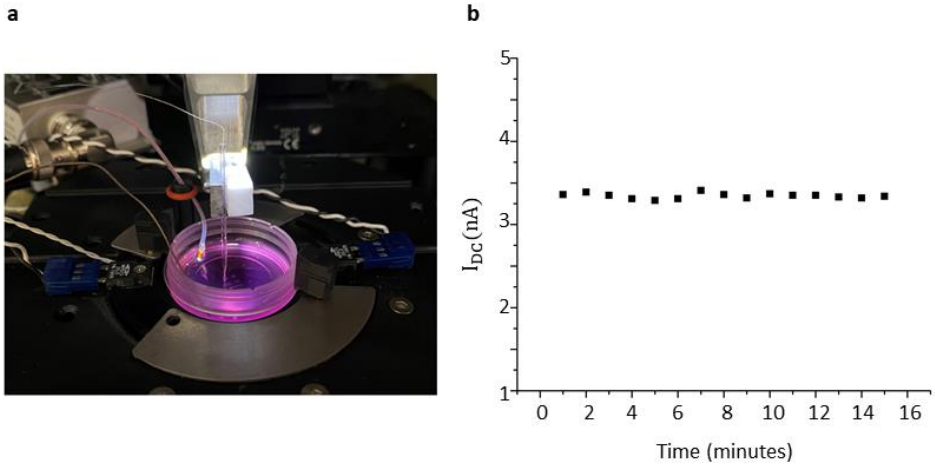

Figure 47. SICM signal stability during temperature control.
a) Picture representing a petri dish located in the microincubator in open configuration, on the SICM stage; b) bulk $\boldsymbol{i_{DC}}$ over time, data recorded every 60 seconds.

Figure 47b represents a test performed keeping a probe immersed in the warm bath, while applying a DC bias of 0.1V, and recording the i_{DC} bulk current values for 15 times every 60 seconds. As we can observe, the values of the i_{DC} are the typical for this kind of probe while imaging in DMEM

Institut Polytechnique de Paris
91120 Palaiseau, France

culture medium and the oscillations of the DC signal are negligible (less than 1.5% of the starting value), and do not get worsen as a result of the higher temperature at which we operate.

After having made sure that the increment of the temperature does not impact the stability of the recorded signals, I tested the adapted platform for imaging of MDCK cells. *Figure 48a* represents the optical micrograph of two MDCK cells and, mapped using DMEM enriched with HEPES as electrolyte. In particular, the area underlined in white is the cell portion chosen for topographical observation. *Figure 48b* shows the corresponding topographical map obtained while imaging at a controlled temperature of 32°C a 50 × 50 µm area, in hopping mode, setting hopping distance of 2 µm and a hopping approach rate of 20 µm/s.

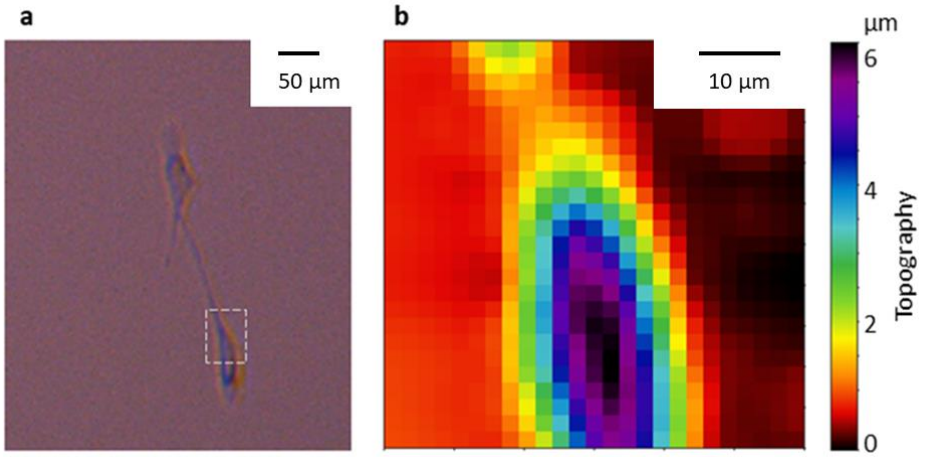

Figure 48. SICM imaging of MDCK cells during temperature control.
a) Optical micrograph of a couple of MDCK cells. In white the area mapped in SICM; b) topographical SICM map of the portion of MDCK cell.

When operating in close configuration, the microdish incubator not only allows the control of the temperature but also of the CO_2 and humidity level, thanks to the presence of a special lid, that allows to define a controlled closed environment, and a special connector, indicated by the white arrow in *figure 49a*, through which 5% of CO_2 is flown into the chamber. The CO_2 – air mixture, before entering the chamber, is humidified into a dedicated container and the flow fed into the imaging space is therefore at 95% of humidity. As previously observed for the temperature control, *figure 49b* represents a test performed keeping a probe immersed in the imaging solution while the temperature and the CO_2 control were performed and applying a constant bias of 0.1 V and measuring the i_{DC}. As we can observe, i_{DC} values remain constant during an observation period of 15 minutes (variations less than 1.7%).

Institut Polytechnique de Paris
91120 Palaiseau, France

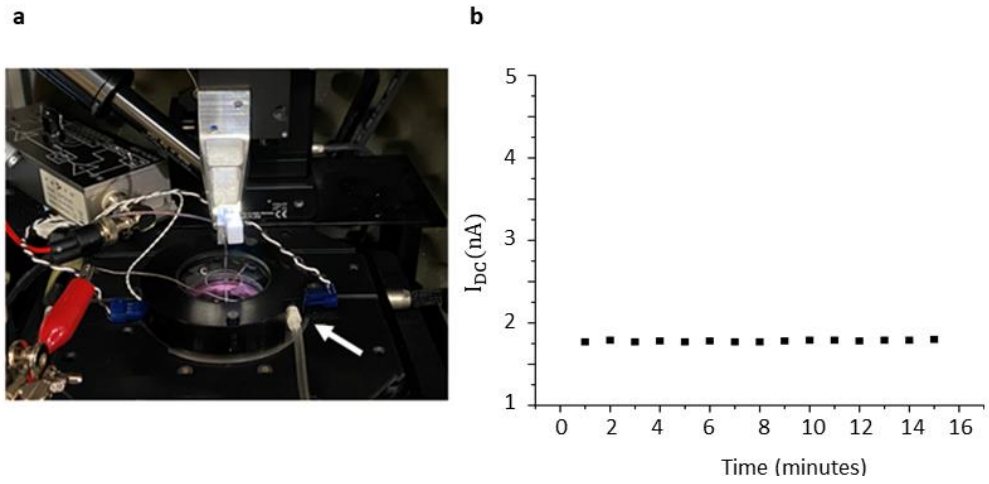

Figure 49. SICM signal stability during temperature, humidity, and CO_2 control.
a) Picture representing a petri dish located in the microincubator in closed configuration, on the SICM stage; b) bulk $\boldsymbol{i_{DC}}$ over time, data recorded every 60 seconds.

Therefore, I decided to test the setup with the microdish in closed configuration for imaging of MDCK cells. In this case, cells have been imaged in DMEM culture medium but, being able to control an appropriate CO_2 level, the addition of HEPES was not necessary anymore. *Figure 50a* represents the optical micrograph of some MDCK cells and the area underlined in white is the portion of the sample whose topographical map in shown in *figure 50b*. The map was obtained scanning a 70 × 40 µm area, in hopping mode, setting hopping distance of 2 µm and a hopping approach rate of 20 µm/s.

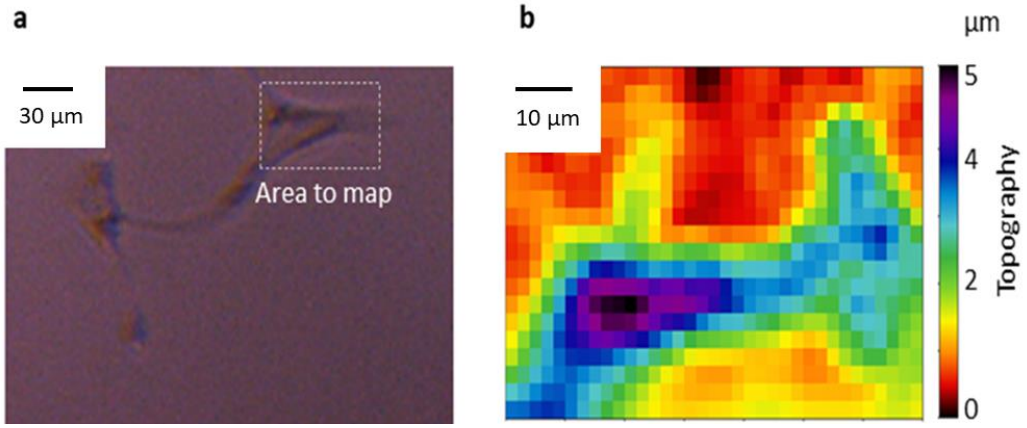

Figure 50. SIMC imaging of MDCK cells during temperature, humidity, and CO_2 control.
a) Optical micrograph of a couple of MDCK cells. The white inset surrounds the area mapped in SICM; b) topographical SICM map of the portion of MDCK cell.

In order to better understand whether the new modifications of the setup introduce any deviation from the standard SICM imaging process, a series of tests has been conducted. As imaging sample, a glass patterned surface has been used instead of the cells observed until this point. This choice was done to exclude variations in the morphology or movements of the cell that could have been misleading for the interpretation of results.

Figure 51 represents a series of approaches conducted in different conditions. Starting from *figure 51a*, that corresponds to SICM imaging without control of temperature or CO_2, we can observe an i_{AC} approach curve in which the surface of the sample is detected at z equal to around 31 µm. Moving to the subsequent condition, that corresponds to temperature fixed at 32 °C (*figure 51b*), it was observed (*figure 51d*) that, by increasing the temperature, the i_{DC} also increased consistently until a moment when it stabilizes, once the temperature has reached an equilibrium. However, no significant increment was observed in the i_{AC} but, importantly, the surface is sensed at z equal to around 19 µm. This is explained taking into account possible expansion of plastic or metallic components of the setup, as a result of the temperature increment. The same z-distance of approach is also observable in *figure 51c*, representing the condition of temperature, CO_2, and humidity control, where the newly inserted control of CO_2 and humidity does not seem to introduce further deviations.

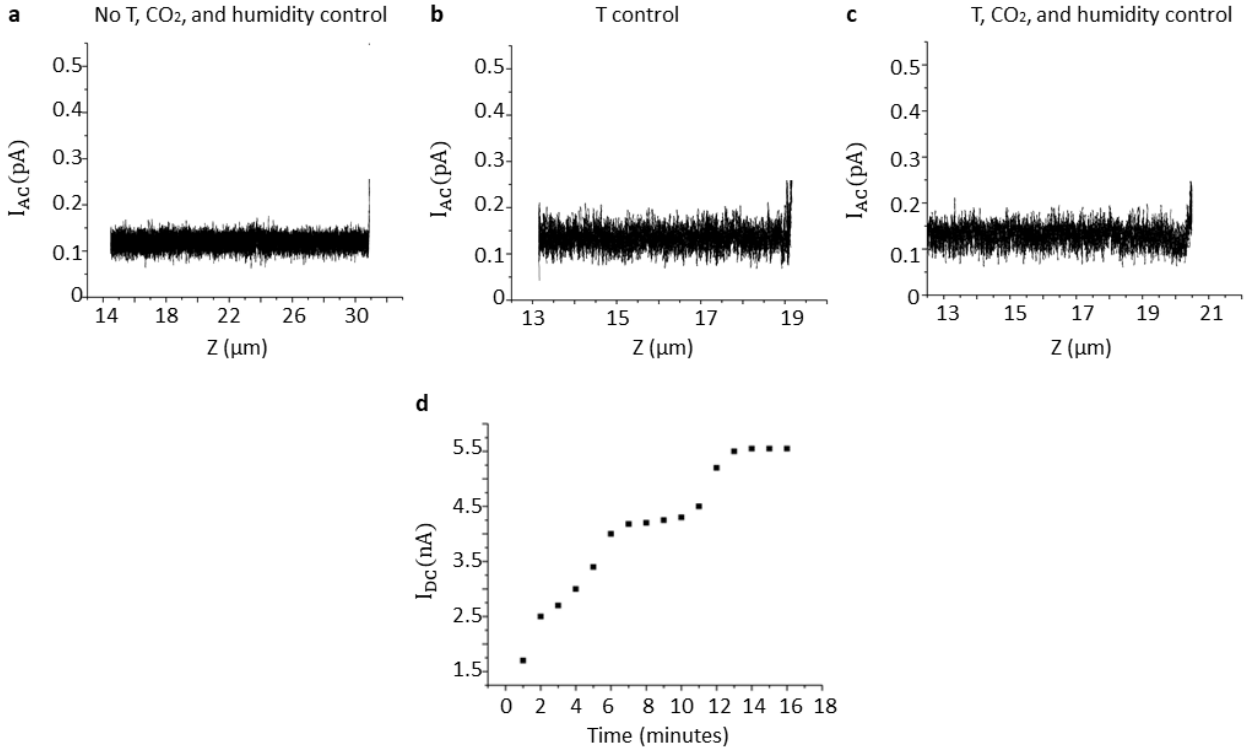

Figure 51. Impact of the controlled environment on approach curves.
a) AC current during an approach curve on a silicon substrate in standard condition (no controls); b) AC current during an approach curve on a glass substrate during temperature control; c) AC current during an approach curve on a glass substrate during temperature, CO_2, and humidity control. d) Increment of the DC current, recorded for 15 minutes after starting the temperature control.

Figure 52 represents a series of topographical maps of a 30 × 30 µm area, imaged in hopping mode with a resolution of 2 µm. Moving from *figure* 52*a*, to 52*b*, and finally to *52c*, that correspond respectively to the conditions of SICM without T and CO_2 control (*a*), only temperature control (*b*), and temperature, CO_2, and humidity control (*c*), we can observe that the topographical maps show a progressive drift through the top left. This can also be explained as a result of progressive expansion of the materials of the setup, resulting in a physical shift of the position of the area of interest. Being

Institut Polytechnique de Paris
91120 Palaiseau, France

aware of the presence of the drift, adjusting the position of the probe with respect to the sample underneath, will allow us to interrogate precise location of interest, when probing the concentration of D-serine in living neurons. Moreover, the map reported in panels *b* and *c*, present grain-like features, possibly associated with a noisier signal, caused by the increment of the temperature, also observable in the AC current trends of figures *51b* and *c*. These features may be avoided setting higher value of the AC setpoint during the SICM scan.

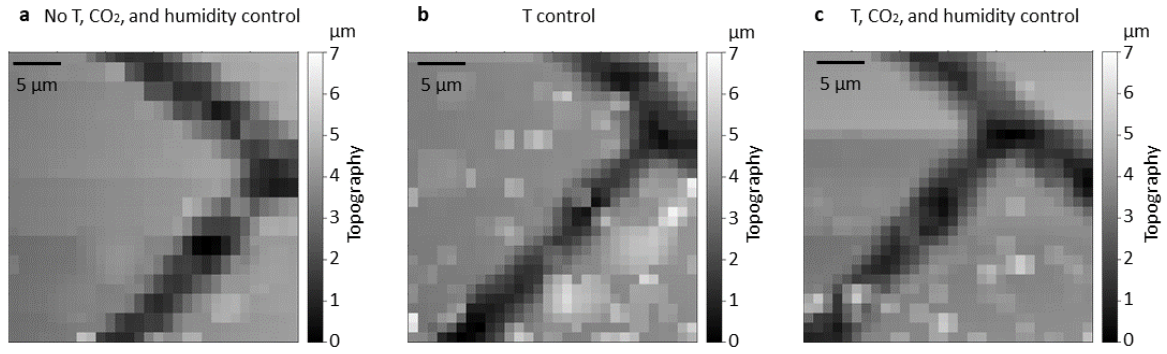

Figure 52. Impact of controlled environment on topography.
a) Topographical map of an inorganic sample without T, CO_2 and humidity control; b) topographical map of inorganic sample during temperature control; c) topographical map of inorganic sample during temperature, CO_2, and humidity control.

3.3.6 SICM imaging of living neurons

Once all the modifications of the setup were applied, I carried out SICM imaging of neurons. In particular, I conducted the first tests on human-induced pluripotent stem cells (iPSC) derived neurons obtained by our collaborators at CEA (generous gift of *Frank Yates*).

To ensure maintaining of physiological conditions during imaging, measurements were carried out at a temperature of 32 °C, 5% CO_2, and 95 % humidity, taking advantage of the previously described setup adaptations. By performing measurements at a controlled temperature and CO_2 level, potential distortions in experimental data resulting from changes in environmental conditions were minimized, ensuring more accurate and reliable results.

As shown previously in section 3.3.1, the use of complex media as an imaging electrolyte may pose challenges during experiments. This was confirmed when attempting to employ the original culture medium of neurons for SICM imaging. The i_{DC} trend displayed in *figure 53a*, while the pipette was approaching the sample in bulk solution, showed a gradual reduction in current amplitude, indicating a progressively intensifying clogging of the tip opening. This phenomenon was repeatedly observed in numerous pipettes. After several minutes of immersion, the current signal was no longer suitable for implementing functional feedback, and the pipette crashed onto the sample upon proximity. The corresponding i_{AC} trend is shown in *figure 53b.*

Institut Polytechnique de Paris
91120 Palaiseau, France

To avoid clogging without compromising the viability of the cells, it was decided to replace only the medium contained in the pipette with PBS. *Figures 53c* and *53d* illustrate i_{DC} and i_{AC} trends during an approach under these new conditions, which demonstrate increased stability of the current during the approach phase and facilitated more accurate topographical measurements. The approach described, involving the use of two different solutions inside the pipette and in the bath, while effective for the current needs, is not in line with the common practice in SICM. For future application, a simpler medium that can be used during imaging will have to be considered.

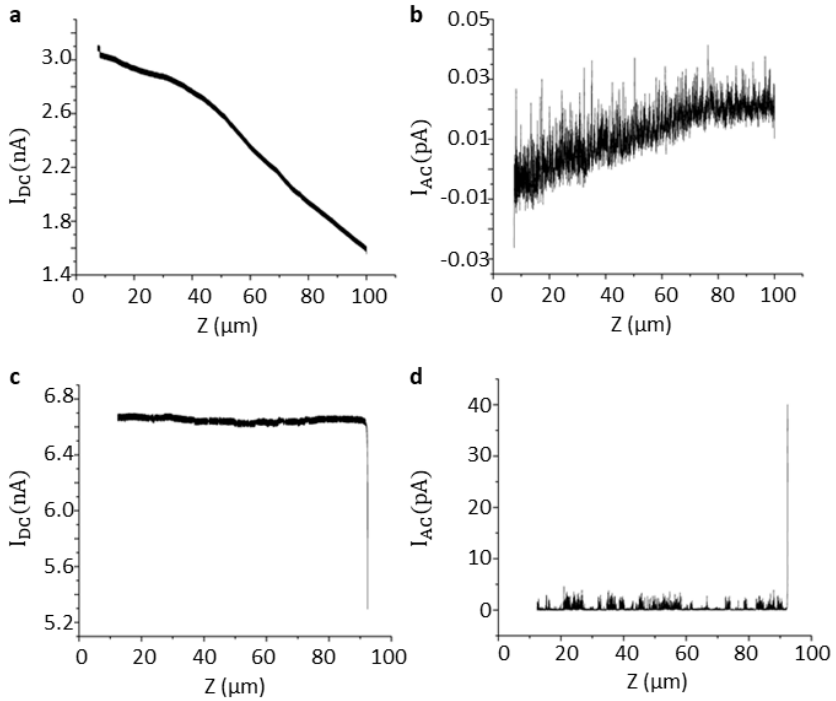

Figure 53. Approach curves during SICM imaging of living neurons.
a) DC current during an approach obtained with the pipette filled with the culture medium; b) AC current during the same approach obtained with the pipette filled with the culture medium; c) DC current during an approach obtained with the pipette filled with PBS; d) AC current during the same approach obtained with the pipette filled with PBS.

This has made it possible to obtain the first topographical SICM images of human derived iPSC neurons, as observable below in *figure 54*. The initial imaging attempts were conducted using the hopping mode with a hopping distance of 2 µm. Although this setting does not allow for high resolution imaging of the entire cell, it was still appropriate to first test the feasibility of whole cell imaging and subsequently move to higher resolution imaging of interesting selected areas. In this regard, an optical micrograph of a group of neurons subjected to SICM topographical mapping was acquired. Moving from left to right on the optical image we can first observed the SICM topographical map of the neuron underlined in yellow, where the curvature of the lateral processes, indicated by arrow 1, well matches what observable from the optics. Similarly, the cell reported in the green panel, presents several lateral extensions (arrows 2) and a pronounced protuberance (arrow 3), and all

Institut Polytechnique de Paris
91120 Palaiseau, France

elements can be found back in the resulting SICM graph. The cell contoured by the purple square has finally also been mapped with SICM, where it appears clear the presence of a central body and lateral processes (arrows 4 and 5). Indeed, if we look more in detail at the top right process of the last described cell, we can observe, in the blue square, a bifurcation. As we may be interested in observing such small details, an attempt to image this kind of delicate structure has been made, as can be seen in the blue panel on the top right. In order to be able to properly detect the presence of dendritic details, the resolution has been increased by employing hopping distance of 1 µm and the resulting topographical SICM map appears much more detailed. Notably, the topographical maps here presented have been acquired in more than 7 hours, confirming the stability of our imaging process.

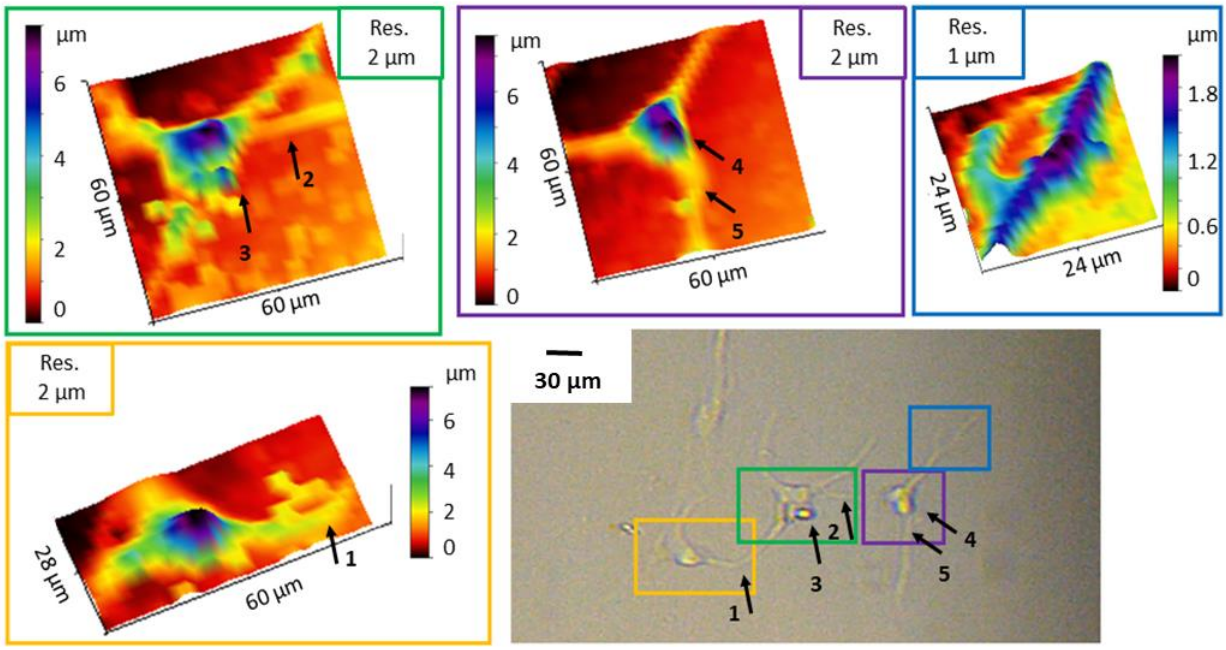

Figure 54. SICM imaging of human derived iPSC neurons.
On the bottom right, an optical micrograph representing a group of three neurons. Each of the neurons is underlined in a different color, and the corresponding SICM topographical map can be found in the color-associated frame. Black arrows indicate details of the cellular structure that can be found represented both in the optical and in the SICM representations.

3.4 Conclusion

In this chapter of the thesis, we have outlined the adaptation and refinement of the SICM imaging technique, aiming at high-resolution topographical measurements of living cells.

I began by identifying the most suitable imaging solution for biological samples analysis under physiological conditions to ensure a consistent and stable imaging process. Subsequently, I advanced imaging capabilities by learning how to image living cells, commencing with cell-line models such as MDCK cells, PC12 cells, podocytes, and N2a cells. Through optimizations in scanning settings, I adapted the scanning speed and spatial resolution to our needs, thereby demonstrating the feasibility of the SICM setup for high-resolution imaging of cellular membrane

Institut Polytechnique de Paris
91120 Palaiseau, France

details in constant distance mode. With the ultimate objective of analyzing living neurons, I introduced modifications to the microscope setup that enabled real-time control of temperature, CO_2, and humidity during the imaging process. As a result of these enhancements, I successfully obtained the first topographical map of human-derived iPSC neurons, providing insights into whole cell morphology, highlighting some of the lateral processes details, and paving the way to the multifunctional imaging platform. Indeed, it is worth noting that all the imaging measurements described in this chapter were conducted using a two-barreled nanopipette with a two-barrel opening diameter ranging from 200 to 300 nm. The dimensions of the tip opening present a physical constraint in terms of the achievable lateral resolution. It is important to emphasize that employing smaller pipettes may yield even better resolutions. However, it is important to understand this imaging effort in the context of the future applications. In the next chapter, we will delve into the challenge of functionalizing the second barrel, which is dedicated to sensing interesting biological molecules, such as D-serine.

As mentioned in the introductory chapter, obtaining analytical information regarding the concentration levels of D-serine at the single-cell level is of paramount importance for unravelling unresolved mechanisms in which this molecule is involved. My approach exploits the potent analytical capabilities of a miniaturized nanosensor, coupled with the impressive spatial resolution achievable through SICM. As demonstrated, in fact, we have the potential to achieve high resolutions, enabling the interrogation of individual synapses, by combining different imaging modes. In the future, whole-cell topographical maps as those presented in this chapter will serve as guides for the precise and controlled placement of the sensor, integrated with the imaging probe itself, in areas of interest such as synapses. Furthermore, the ability to rapidly acquire consecutive topographical maps of intriguing areas will allow to monitor morphological changes, for example at the synaptic or cellular membrane level, and correlate them with chemical events that can be detected using the other barrel of the probe.

With this foundation, the subsequent chapter will explore the probe functionalization that has been undertaken to create the appropriate nanosensor in the other barrel of the probe.

Chapter 4. Nanosensors for D-serine detection

4.1 Introduction

This chapter will focus on the efforts undertaken to miniaturize micro-sensors into nanosensors and integrate them into glass nanopipettes, to be employed as probes for the Scanning Ion Conductance Microscopy technique.

The subsequent sections will detail the progressive fabrication of the nanoprobes, starting from the construction of nanoelectrodes embedded within the pulled pipette. This process will extend to the electrochemical platinization of the nanoelectrodes, followed by their functionalization for sensing purposes. Notably, this will involve the deposition of a perm-selective PPD layer to enhance sensor selectivity and the subsequent immobilization of *Rg*DAAO, mirroring the approach employed for micrometric sensors seen in chapter 2.

Being the ultimate objective the combination of imaging and sensing capabilities within the same probe, the decision to tackle the two functionalities separately is made to simplify the first steps of the fabrication. Consequently, in this study, the results will be presented in the majority of cases employing dual-barrel nanoprobes, the intended final configuration, as well as single-barrel nanopipettes. The latter served as preliminary model to assess the potential of the sensors, being regarded both as promising initial outcomes for the eventual dual-functionality platform and as effective standalone tools within the broader context of nanosensing.

4.2 Materials and Methods

Single-barrel and dual-barrel nanopipettes were fabricated through a laser pulling process, following the procedures and utilizing the instrumentation outlined in Chapter 3. The same type of probes was also utilized for imaging purposes.

Carbon nanoelectrodes fabrication and characterization. To construct the nanoelectrodes embedded in the nanopipette, the pyrolysis of butane was employed. *Figure 55a* displays a schematic of the carbon filling process for a single-barrel nanopipette. Specifically, butane gas was flown into the nanobarrel designated for the nanoelectrodes. Following a protocol very similar to that described by *Takahashi et al.*,[132] a butane flame was applied to the pipette tip for a duration of 20 seconds. During the procedure, the tapered end of the pipette was placed inside a quartz capillary coaxially aligned, introducing a flow of argon at a flow rate of 0.1 litre/minute. This step was taken to protect against both the oxidation of the carbon layer and the deformation of the capillary caused by elevated

Institut Polytechnique de Paris
91120 Palaiseau, France

temperatures. Additionally, this method served to prevent the closure of the pipette aperture due to the softening of the quartz pipette walls.[132] For double-barrel probes, during the carbon-filling process, the barrel dedicated to imaging was back-sealed with adhesive paste to keep it unmodified (*figure 55b*). *Figure 55c* reports a picture of the setup utilized for the carbon filling procedure. The electrochemical characterization of the nanoelectrodes was conducted through CV within a solution containing 5 mM $Ru(NH_3)_6Cl_3$, along with 10 mM KCl, 18 mM Na_2HPO_4, and 7 mM NaH_2PO_4 as the supporting electrolyte. All the chemicals were purchased from Sigma Aldrich. CV was executed using a two-electrodes setup and a HEKA potentiostat (PG618, HEKA) and the voltage was swept from 0 to 0.8 V at 50 mV/s with respect to the Ag/AgCl counter-reference electrode.[133] SEM images were acquired with the voltage and current values set at 2 kV and 5 µA, respectively.

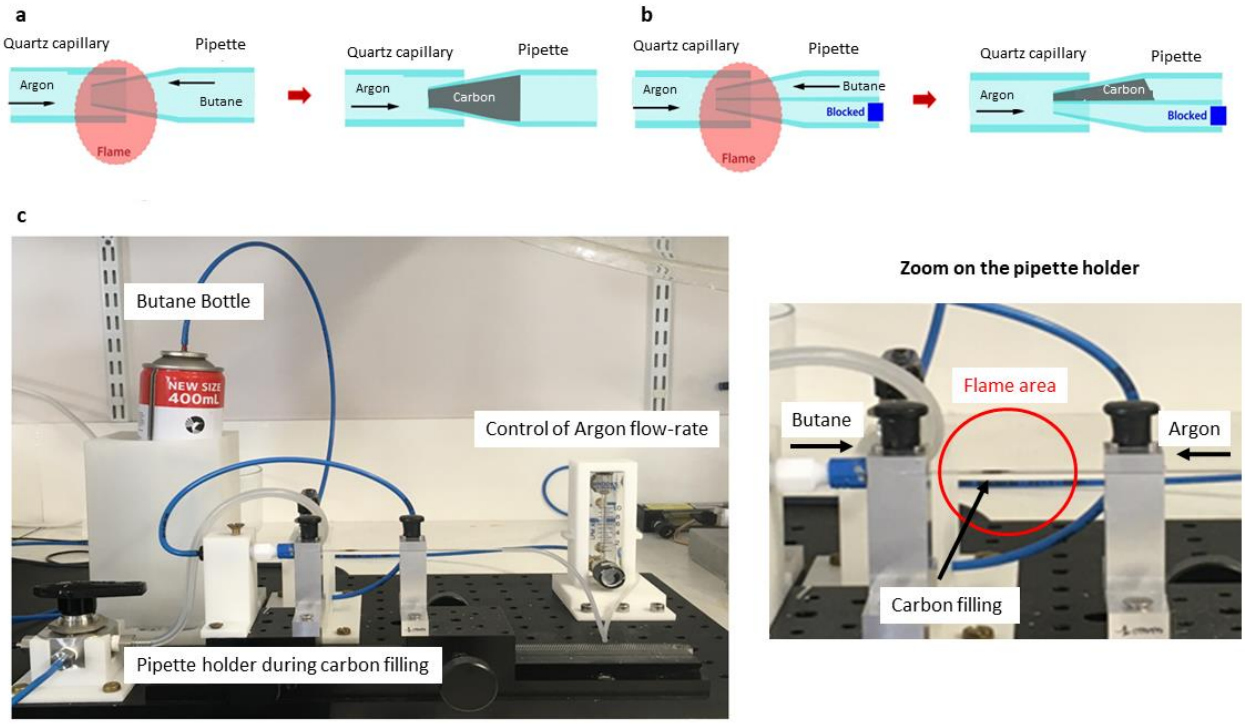

Figure 55. Carbon nanoelectrodes fabrication.
a) Schematic representation of the pyrolytic carbon filling setup for a single barrel pipette: while butane gas is blown from the back of the nanopipette, a flow of argon is passed into a coaxially aligned capillary. In the meantime, a flame is used for butane pyrolysis, creating a layer of pyrolytic carbon inside the nanopipette; b) schematic representation of the pyrolytic carbon filling setup for a single barrel pipette; c) Picture of the pyrolytic carbon-filling setup used during this thesis. The inset show the details of the pipette positioning area.

Platinum electrodeposition and characterization. The platinum electrodeposition was carried out by varying the voltage between 0 and -0.8 V vs Ag/AgCl reference electrode, in a solution containing 2 mM H_2PtCl_6 in 0.1 M HCl, employing a scan rate of 200 mV/s.[133] The choice of the number of cycles in the CV played a crucial role in determining the dimensions of the resulting platinum deposit and was varied between 2 and 10 cycles based on the desired final geometry. To characterize the platinized nanoelectrodes, I followed the same electrochemical method and conditions previously

employed for the carbon nanoelectrodes. SEM images were obtained with the voltage and current values set at 30 kV and 20 µA, respectively.

MDCK cells were cultured on 35 mm Petri Dishes (IbiTreat 80156, Ibidi), following the procedures outlined in section 3.2. The imaging barrel of the nanopipette was filled with DMEM culture medium supplemented with 20 mM HEPES. SICM imaging was conducted in hopping mode, featuring a hopping approach rate of 20 µm/s, hopping retract rate of 40 µm/s, and lateral scan rate of 35 µm/s. During each hopping step the probe was retracted by 18 µm and laterally shifted by 2 µm. Utilizing the AC+DC mode, the AC setpoint was set at 2.2 pA. During the approach, a vertical oscillation of 25 nm (peak-to-peak) was applied to the pipette and the lock-in amplifier frequency was set to 273.15 Hz.

Platinized nanopipettes as hydrogen peroxide sensors. Platinized nanopipettes were assessed as sensors for detecting hydrogen peroxide, employing CA.[70] The pipettes were immersed in PBS enriched with increasing concentrations of H_2O_2 (Sigma Aldrich), from 500 nM to 10 mM and, for each concentration, CA pulses lasting 10 seconds were repeated 3 times. The PBS contained 137 mM NaCl, 2.7 mM KCl, 10 mM Na_2HPO_4, and 1.8 mM KH_2PO_4 in MilliQ water. All the chemicals were purchased from Sigma Aldrich. In order to obtain the calibration curve, for each concentration analyzed, the three current values recorded during the last 2 seconds of the CA pulses were averaged. The resulting mean value was then corrected by subtracting the average background value, recorded in PBS, and the values of $I\text{-}I_{background}$ were then plotted. The error bars reported in the calibration curves represent standard deviation calculated on three measurements.

PPD deposition and characterization. To apply a semi-permeable polymeric layer onto the platinized nanopipettes, electrodes were positioned in a two-electrodes cell containing 100 mM PPD (Sigma Aldrich) in 0.01 M PBS at pH 7.4. The voltage was swept between -0.1 and 1 V vs Ag/AgCl at 100 mV/s for 5 cycles.[71] Electrochemical characterization of the nanopipettes was conducted both before and after PPD deposition, following the protocol outlined for carbon and platinum nanopipettes characterization. Similarly, calibration curves for hydrogen peroxide sensing were established in accordance with the procedures detailed for the platinized nanopipettes. The assessment of interference rejection was carried out using the same electrochemical setup. Similarly to the process followed for micro-sensors, to quantify the rejection of interferences, each PPD deposition condition (N=1, 3, or 5) was evaluated with a different nano-electrode, showing similar geometry upon SEM observation. The probes were immersed in PBS enriched with 20 µM serotonin (Sigma Aldrich) and 5 mM L-ascorbic acid (Sigma Aldrich), applying 0.5 V vs Ag/AgCl CA pulses lasting 10 seconds. Each measurement was repeated three times. For each of the electrodes, the average

current during the last 2 seconds of the CA recording was calculated for the bare platinum electrode, and taken as a reference, after subtraction of a background value recorded in PBS. After the deposition of PPD, the same average value was calculated again and the percentile decrement with respect to the reference current was evaluated. Similarly, for evaluating the decrement in the sensitivity to hydrogen peroxide, a calibration curve was obtained for each bare electrode and the sensitivity was computed and taken as a reference. To obtain the calibration curve for hydrogen peroxide sensing, the same procedure described for the platinized nanopipettes was followed. After the deposition of PPD, according to the different CV cycles number, the calibration curve was repeated and the new sensitivity was computed. The percentile decrement was computed with respect to the reference values.

Protein immobilization and cleaning of the SICM barrel. The protein immobilization on the platinized nanopipette was achieved by dipping the pipette four times into the protein solution for 30 seconds each time, allowing it to dry for 4 minutes. Subsequently, the pipette was placed in a desiccator saturated with vapors of glutaraldehyde (Sigma Aldrich) for *Rg*DAAO-PPD crosslinking for a duration of 15 minutes. Before usage, the pipette was immersed in PBS for 20 minutes.For double-barrel nanopipettes, the evaluation of the current flowing in the imaging barrel was conducted by immersing the probe in PBS. A voltage of 0.1 V vs Ag/AgCl was applied to the pipette electrode and the resulting current was measured. To prevent clogging of the imaging barrel, a 6 bars flow of argon was connected to the back of the nanopipette during both the immersion of the probe in *Rg*DAAO and the subsequent drying time.[270] To ensure their integrity between fabrication and usage, nanosensors were stored at -20°C in a sealed box. Before being employed for sensing purposes, the nanopipettes were immersed in PBS for 20 minutes to ensure the rehydration of the PPD-*Rg*DAAO layer.

Characterization of the nanosensors for D-serine and D-alanine sensing. Detection of D-amino acids was conducted using the potentiostat, maintaining the 2-electrodes configuration described for the carbon characterization and platinum deposition and characterization. CA pulses of 10 seconds were applied while immersing the pipette in oxygen saturated aCSF solution enriched with increasing concentrations of D-serine or D-alanine (Sigma Aldrich), ranging from 500 nM to 10 mM. Each measurement was repeated 3 times.

4.3 Results and discussion

4.3.1 Carbon nanoelectrodes fabrication and characterization

In the initial stage of the pipettes' functionalization, a carbon nanoelectrode is created within the nanopipette. An inherent advantage of carbon nanopipette-based electrodes lies in their elevated mechanical resilience compared to metal wire-based electrodes, which are more susceptible to deformation. Furthermore, the dimensions of this type of electrodes can be minutely tailored, depending on the aperture size of the glass nanopipettes, facilitating precise measurements within compact and restricted spaces. Additionally, carbon nanopipettes are open to functionalization, enabling their utilization in exceptionally specific sensing applications, as we will see in following sections of this chapter.

During the carbon filling process, the argon flow rate is a critical factor. In fact, an insufficient flow-rate could lead to carbon deposit outside the probe channel, while excessive rate might hinder butane from reaching the tip of the pipette, resulting in a recessed carbon nanoelectrodes. The optimal balance is therefore important for the success of the process and an optimization has been necessary in order to determine the suitable argon flow-rate for functionalization of nanopipettes like those here described. In *figure 56a* an optical microscope image of a single-barrel nanopipette immediately after the process of carbon filling is illustrated. To assess their electrochemical behavior, the carbon-based nanoelectrodes were subjected to characterization via CV, as described in the experimental section, using an experimental setup as the one schematically represented in *figure 56b*. The redox-active molecule $Ru(NH_3)_6Cl_3$ was chosen because it is commonly used as a model outer-sphere redox mediator for electrochemical studies and its use provides a suitable method for characterizing the electrochemical behavior of working electrodes. *Figure 56c*, the resulting voltammogram illustrates an abrupt escalation in reduction current as the voltage surpasses -0.25 V vs Ag/AgCl. The substantial augmentation of the current as more molecules are reduced is indicative of the electrochemical activity of the electrode. For these very small electrodes, a maximum current, I_L, is then reached and maintained constant at potentials where current is limited by diffusion.

To establish a correlation between the current I_L and the geometric properties of the electrode, I employed the subsequent diffusion equation, tailored for disk-shaped electrodes, which has been previously employed for analogous nanoscale electrochemical probes.[133]

$$I_L = 4.64\, r\, n\, F\, C\, D \qquad \textit{(eq. 4)}$$

Here, r [cm] denotes the radius of the electrode, n signifies the number of electrons involved in the redox process, F [C/mol] is the Faraday constant, C [mol/cm^3] is the bulk concentration of the analyte, and D [cm^2/s] is the diffusion coefficient of the analyte. Although *equation 4* was originally

Institut Polytechnique de Paris
91120 Palaiseau, France

applied in the context of nanopipettes for which R_g, defined as the ratio between the total radius of the tip and the one of the electrochemically active area, was set equal to 1.5, it was considered the most appropriate to approximate this case. Based on the acquired values of limiting current and utilizing this equation, the resultant dimensions of the nanoelectrodes corresponded with expectations derived from SEM imagery.

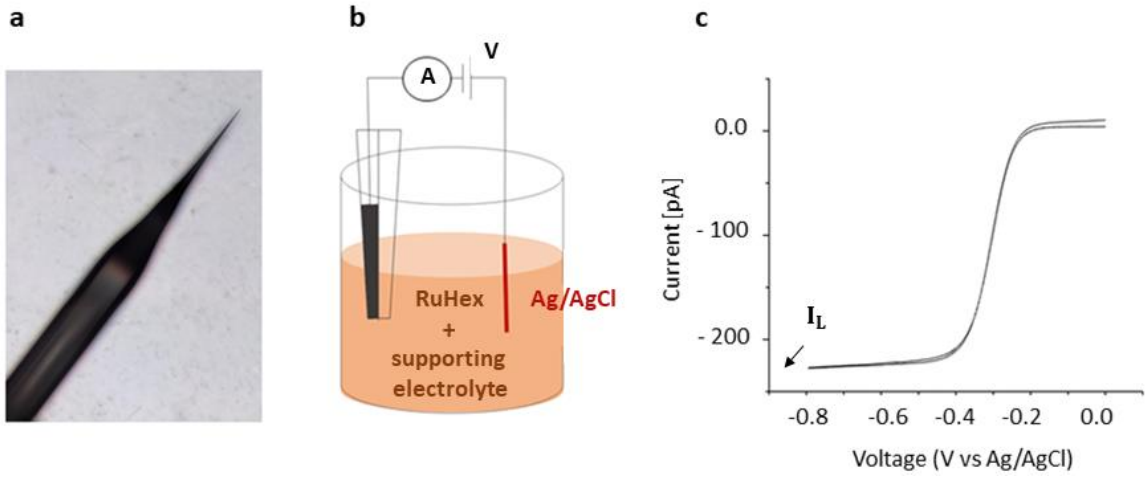

Figure 56. Carbon nanoelectrodes characterization.
a) Optical microscope image of a single-barrel nanopipette just after carbon filling; b) schematic of the two-electrodes setup used for electrochemical characterization of the carbon nanoelectrodes; c) resulting voltammogram at 50 mV/s for a single-barrel carbon nanoelectrodes, obtained via CV in a solution containing 5 mM $Ru(NH_3)_6Cl_3$ along with 10 mM KCl, 18 mM Na_2HPO_4, and 7 mM NaH_2PO_4 as the supporting electrolyte.

Double-barrel nanopipettes can also serve as a means for producing carbon-filled structures. In this approach, one of the barrels can be utilized to generate carbon nanoelectrodes, intended for employment in electrochemical analysis or sensing. Meanwhile, the other barrel remains unoccupied and can be used for alternative functions following appropriate functionalization or for enabling feedback-based positional control in SICM imaging.

The procedure for constructing double-barrel carbon filled nanopipettes adheres to the same methodology previously outlined. However, in this case, one of the barrels is sealed off using adhesive paste. Butane is then introduced solely into the sensing barrel, leaving the other one empty. *Figures 57a, 57b,* and *57c* represent respectively an optical microscope image of a double barrel nanopipette just after carbon filling, and two SEM images of lateral and top view of a carbon-filled nanopipette tip. Observing the SEM images, the ability to keep the carbon nanoelectrodes confined in one of the two barrels is confirmed. In fact, invasion of the second channel, as well as external coating of the probe would result in the impossibility of conducting independent measurements from the two channels. Furthermore, double-barrel carbon-filled nanopipettes were subjected to electrochemical characterization via CV, following the same procedure of single-barrel ones. An example of resulting voltammogram can be found in *figure 57d*, where we can observe a similar trend to the one for single barrel pipettes. Also in this case, there were no significant discrepancies

observable between the final size of the functionalized pipettes observed in SEM and the one derived from the value of I_L.

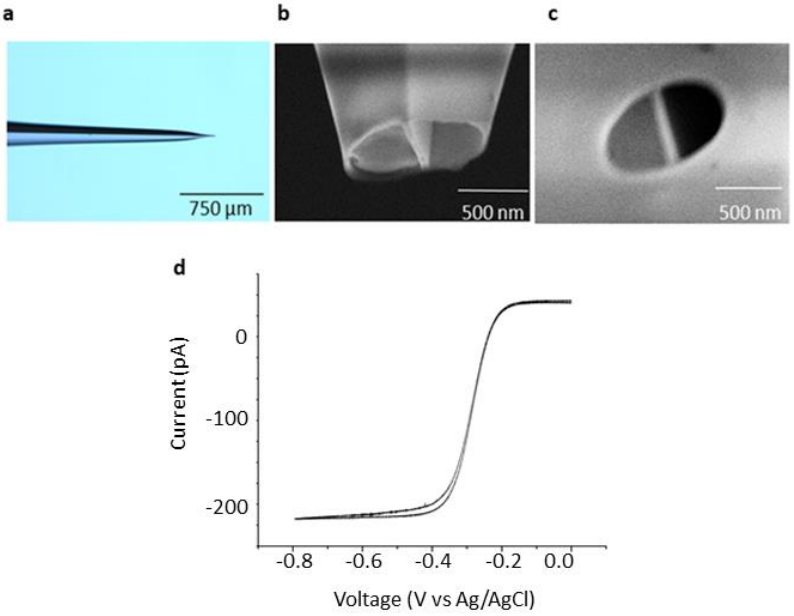

Figure 57. Electrochemical characterization of carbon-filled double-barrel nanopipettes.
a) Optical microscope image of a double-barrel nanopipette after carbon-filling; b) SEM image of a nanopipette lateral view after carbon filling; c) SEM image of a nanopipette top view after carbon filling; d) electrochemical characterization of a carbon-filled double-barrel nanopipette obtained via CV at 50 mV/s in a solution containing 5 mM $Ru(NH_3)_6Cl_3$ along with 10 mM KCl, 18 mM Na_2HPO_4, and 7 mM NaH_2PO_4 as the supporting electrolyte.

4.3.2 Platinum deposition and characterization

Platinum deposition is a common approach for enhancing the electrocatalytic properties of carbon electrodes, since platinum creates an electrocatalytic interface that reduces the overpotential of, for example, oxygen reduction and hydrogen peroxide reduction/oxidation.[133] Therefore, platinized carbon-filled nanopipettes have a wide range of applications in the field of electrochemistry and biosensing, due to their small size and increased sensitivity. They have been used for NTs detection in brain tissues[133] and for determination of reactive oxygen species at single cell level.[271, 272] In this specific context, I functionalized carbon-filled nanopipettes through CV to create an electrodeposited layer of platinum. The amount of platinum was controlled by the number of CV cycles.

When employing single-barrel pipettes, I varied the number of CV cycles (N) from N=2, to N=5, and to N=10, yielding a corresponding increase in the size of the platinum deposit. This evolution is effectively portrayed in *figures 58a, 58b, and 58c*. Indeed, it is worth highlighting that the application of a 2-cycles protocol typically results in platinum deposits that remain largely contained within the tip aperture, as demonstrated in *figure 58a.* On the other hand, opting for a higher number of CV cycles (N=5) induces the formation of a platinum deposit that extends beyond the glass structure, resembling a spherical particle with an approximate diameter of 500 nm, as depicted in

Institut Polytechnique de Paris
91120 Palaiseau, France

figure 58b. Lastly, adopting a 10-cycles protocol produces a platinum deposit that can reasonably be approximated to a sphere with a diameter of around 1 µm. In the context of sensing application, a larger platinum deposit presents the advantage of an expanded catalytic surface, thereby leading to significant larger currents. However, this augmentation comes at the cost of sensor spatial resolution and the mechanical stability of the final structure, critical aspects to take into account for future applications.

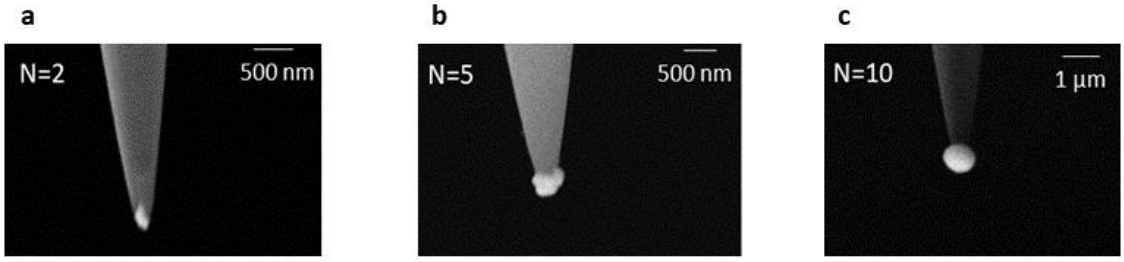

Figure 58. Platinum deposition on single-barrel nanopipettes.
Platinized nanopipette obtained with a) N=2 CV cycles, b) N=5 CV cycles, c) N=10 CV cycles.

The process of platinum deposition can also be executed using two-barrel nanopipettes. In this case, it is of paramount importance to ensure that the platinum deposit remains confined within the sensing barrel to prevent obstruction of the adjacent barrel, as demonstrated in *figure 59a*. An excessive platinum deposit might result in the partial blocking of the neighboring barrel, as illustrated in *figure 59b*, which can impact the feedback mechanism of SICM. Additionally, when the pipette is near the sample at distances on the order of hundreds of nanometers, there is risk of a protruding platinum structure to fracture or partially detach. Conversely, having a recessed platinum deposit, as in the scenario of *figure 59c*, can introduce diffusion-related challenges for the analytes to be measured within the barrel. Therefore, also in this case, the determination of the effect of the number of CV cycles during electrodeposition is of importance to ensure suitable probe for imaging and sensing.

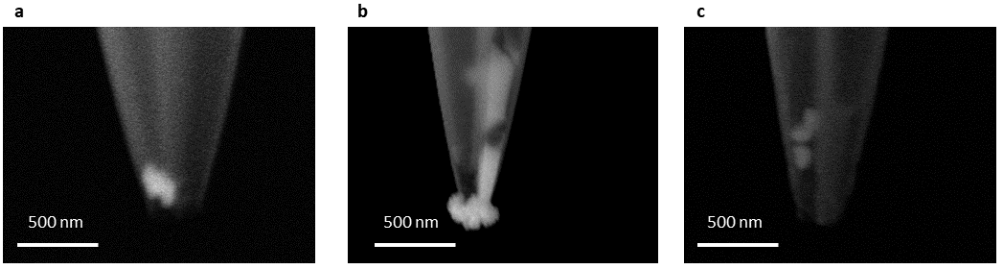

Figure 59. Platinum deposition on double-barrel nanopipettes.
a) SEM image of a platinized double-barrel nanopipette with the good size of platinum deposit; b) SEM image of a platinized double-barrel nanopipette with too big size of the platinum deposit; c) SEM image of a platinized double-barrel nanopipette with recessed platinum deposit.

When establishing the optimal count of CV cycles for the process of electrodeposition, a critical factor to take into account is the underlying carbon. The initial dimensions and structure of the carbon

Institut Polytechnique de Paris
91120 Palaiseau, France

electrode have an impact and influences the optimal number of CV cycles. Indeed, starting with a carbon electrode that spans to the terminus of the glass nanopipette, a specific count of CV cycles could lead to a platinum deposit that protrudes beyond the walls of the sensing barrel. Conversely, in cases where the starting carbon nanoelectrodes is recessed to a significant degree, the same number of CV cycles might yield a platinum deposit that remains recessed within the confines of the glass aperture. In order to establish a standardized protocol for platinum electrodeposition, I took advantage of the electrochemical evaluation of the carbon nanoelectrodes described in section 4.2, before engaging in the platinum deposition process. This preliminary step was essential to ensure that the carbon material was not excessively recessed or protruding. Starting from a carbon geometry contained in the glass pipette but not too recessed, achieving a suitable platinum deposit, not protruding from the glass nanopipette, could be accomplished with just 2 CV cycles.

For the purpose of characterizing the platinized nanoelectrodes, I adhered to the same electrochemical characterization procedure that was previously employed for the carbon nanoelectrodes. Similar voltammogram shapes have been observed using both single and double-barrel platinized nanopipettes. In the case of a double-barrel nanopipette, as the one depicted in the SEM image of *figure 60a*, the resultant cyclic voltammogram is presented in *figure 60b.* The reduction current displays a marked increase, followed by a more modest elevation current at more negative voltages. This contrast to the behavior depicted in *figure 57d* can be attributed to increased catalytic activity towards oxygen reduction.

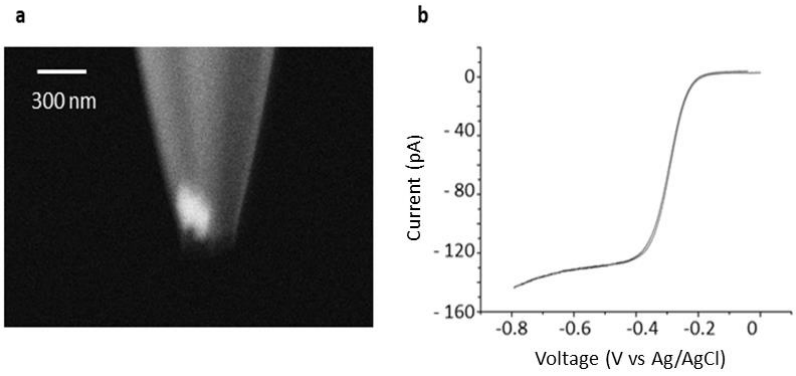

Figure 60. Electrochemical characterization of platinized carbon nanopipettes.
a) SEM image of a double-barrel platinized nanopipette. b) electrochemical characterization of a platinized double-barrel nanopipette obtained via CV in a solution containing 5 mM $Ru(NH_3)_6Cl_3$ along with 10 mM KCl, 18 mM Na_2HPO_4, and 7 mM NaH_2PO_4 as the supporting electrolyte.

As discussed earlier, ensuring that the presence of a platinum deposit in the sensing barrel does not disrupt the SICM imaging process is of utmost significance. To evaluate this aspect, I employed a platinized double-barrel nanopipette, depicted in the SEM image of *figure 61a*, for conducting SICM topographical mapping of a MDCK cell, according to the methodologies described in the experimental section. The resulting topographical maps of a MDCK cell, which are presented in

Institut Polytechnique de Paris
91120 Palaiseau, France

figures 61b and *61c*, in both 2D and 3D representations, respectively demonstrate successful execution of imaging using the platinized double-barrel nanopipette, confirming that the appropriately sized and shaped platinum deposit does not impede the SICM imaging process.

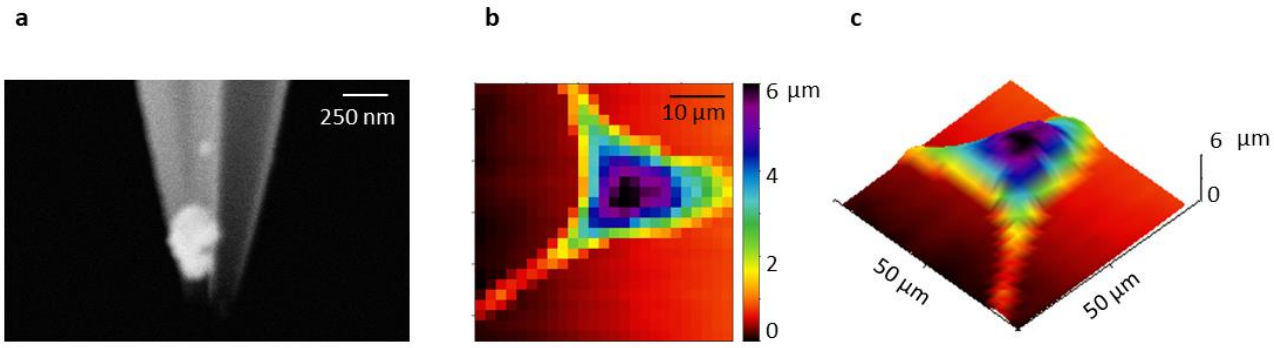

Figure 61. SICM imaging of MDCK cells with double-barrel platinized nanopipettes.
a) SEM image of a platinized double-barrel nanopipette: the left barrel is carbon-filled and functionalized with a platinum deposit visible in light gray and white, respectively, while the right barrel is left empty for imaging purposes; SICM topographical map of a 50 × 50 µm area containing a MDCK cell in b) 2D and c) 3D representation.

4.3.3 Platinized nanopipettes as hydrogen peroxide sensors

As observed in the context of platinum wire-based biosensors in chapter 2, the logical progression toward constructing the nano-biosensor for D-serine involves an initial assessment of the capabilities exhibited by the platinized nanopipettes when employed as sensors to detect hydrogen peroxide. This evaluation is motivated by the principle previously presented, wherein the detection of the D-amino acid through *Rg*DAAO depends on an indirect mechanism of detection of hydrogen peroxide, a by-product resulting from the interaction between enzyme and target analyte.

Calibration curves were obtained according to the protocol described in section 4.2. The results from these tests clearly highlighted how the shape and the size of the platinum deposit significantly affect the performance of the hydrogen peroxide detection probe. In more detail, *figure 62* displays a series of SEM images of platinized nanopipettes (panels *a-c*) where the size of the platinum deposit varies. Specifically, *figure 62a* shows a platinized nanopipette characterized by a platinum deposit grown inside of the sensing barrel, but not enough to reach the apex of it. *Figure 62b* shows a platinized nanopipette with platinum staying within the glass structure of the probe, with an approximate size of 150 nm (diameter of the platinum deposit). Meanwhile, in *figure 62c*, the platinum deposit has grown outside of the barrel, forming a small deposit resembling a sphere about 840 nm in diameter. Moving on to *figures 62d, 62e*, and *62f*, calibration curves resulting from hydrogen peroxide sensing for the pipettes featured respectively in *figures 62a*, *62b*, and *62c*, are presented. Notably, in *figure 62d*, the sensor starts detecting at concentrations equal to 50 µM and the curve's linear range spans from this point to 10 mM (R^2 =0.98). Shifting to the platinum deposit configuration shown in *figure 62b*, extends the sensor's linear range in the calibration curve, covering

Institut Polytechnique de Paris
91120 Palaiseau, France

from 10 µM to 10 mM (R^2=0.97), as seen in the *figure 62e*. This larger detection range can be attributed to the larger active surface area of the sensor exposed to the analyte for detection. Lastly, further expanding the sensor's geometry as in *figure 62c*, leads to a wider linear range of detection visible in the curve of figure *62f*, now ranging from 1 µM to 10 mM (R^2=0.97).

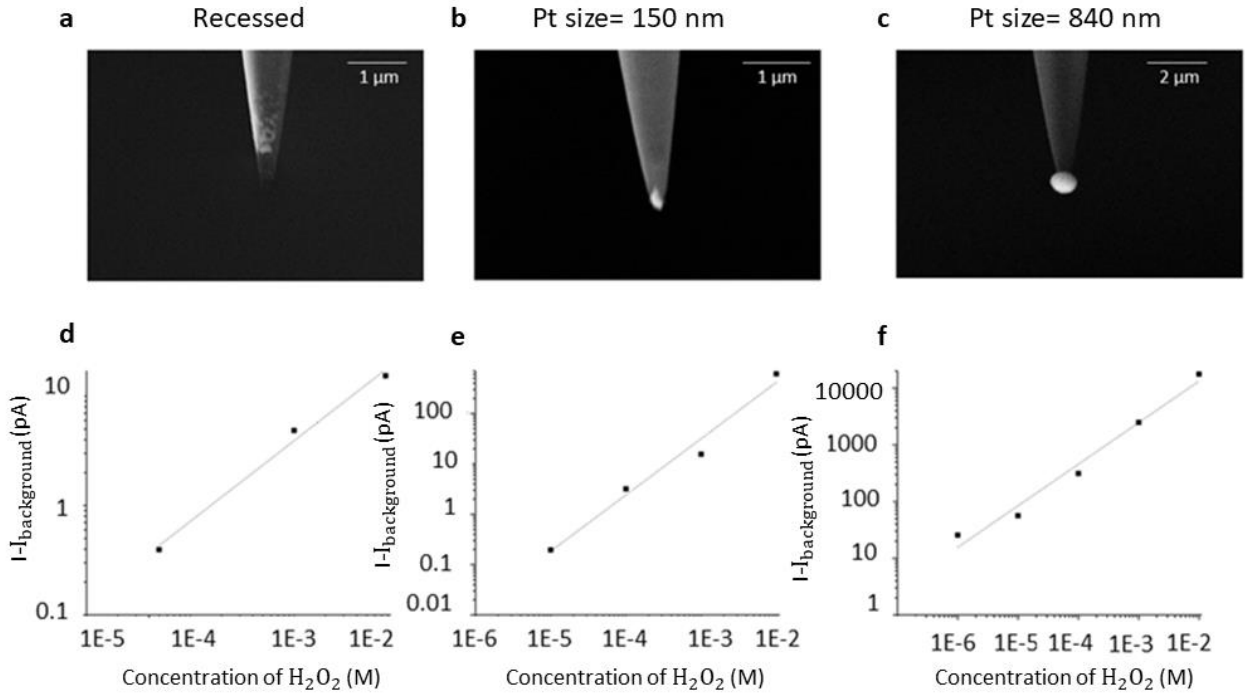

Figure 62. Platinized single-barrel nanopipettes as sensors for hydrogen peroxide detection.
a, b, c) SEM images of three pipettes having different geometries of the platinum deposit. d, e, f) calibration curves for hydrogen peroxide detection of the pipettes represented in panels a, b, and c, respectively.

Utilizing the identical methodology employed for evaluating single-barrel platinized nanopipettes, I proceeded to assess the sensing capabilities of the dual-barrel probes. Once again, a discernible relationship emerged, illustrating the impact of platinum deposit dimensions and geometrical arrangement on the sensing performances.

In *figure 63*, we present three distinct instances (panels *a-c*) featuring platinized dual-barreled nanopipettes, each marked by notable variations in dimensions and the geometry of the platinum deposit. Considering *figure 63a*, where the platinum deposit is strongly recessed, we can see that this geometric characteristic hamper effective hydrogen detection until concentration exceeds 100 µM (R^2=0.99), as highlighted in *figure 63d*. Contrastingly, the SEM image in *figure 63b* captures an optimal scenario wherein the platinum deposit has grown within the sensing barrel, extending to its very tip, with an approximate size of 210 nm. This configuration achieves substantial exposure while remaining confined within the glass structure, thus precluding the risk of contaminating the neighboring imaging barrel. As evident in *figure 63e*, the larger platinum surface area exposed in this arrangement improves the detection range, enabling the sensing of concentrations from as low as 10 µM (R^2=0.97). Lastly, *figure 63c* exemplifies a configuration wherein the platinum deposit extends

Institut Polytechnique de Paris
91120 Palaiseau, France

beyond the sensing barrel, forming a spherical structure that occludes the opening of the adjacent imaging barrel, with an approximate diameter of 760 nm. This arrangement, offering an exceedingly extensive active surface area, enables the detection of hydrogen peroxide concentrations as minute as 1 µM (R^2=0.99), however this configuration renders this third probe unusable for simultaneous SICM imaging capabilities.

Nonetheless, it's crucial to emphasize that, while characterizing these probes as hydrogen peroxide sensors is interesting, the detection ranges established do not necessarily correspond to the detection ranges for D-serine detection. Despite this, these ranges provide valuable insights into the functionality of this type of sensors.

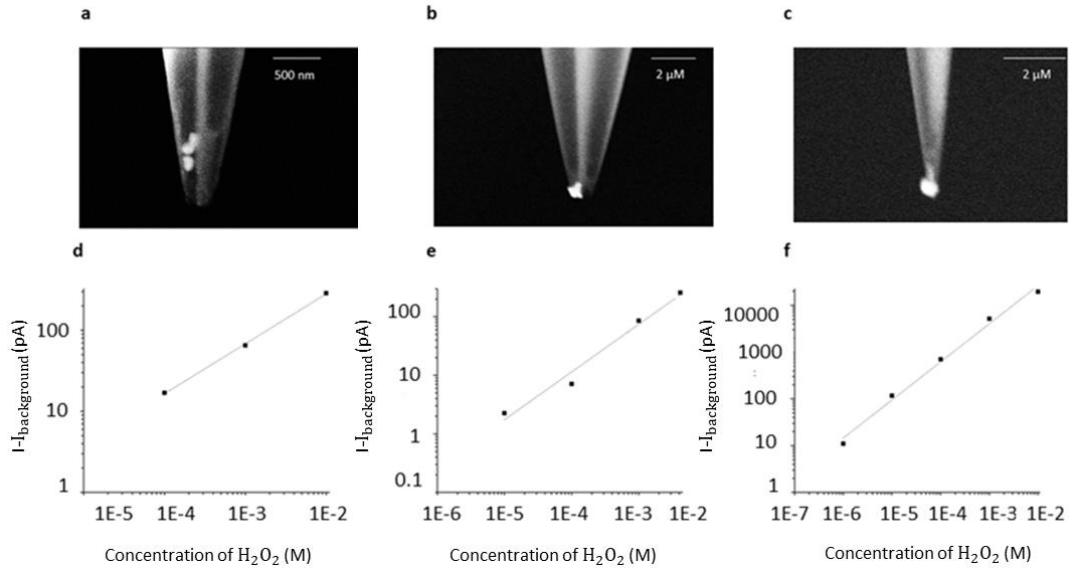

Figure 63. Platinized double-barrel nanopipettes as sensors for hydrogen peroxide detection.
a, b, c) SEM images of three pipettes having different geometries of the platinum deposit. d, e, f) calibration curves for hydrogen peroxide detection of the pipettes represented in panels a, b, and c, respectively

4.3.4 PPD deposition and characterization

As observed in the context of platinum wire-based biosensors, it is imperative to mitigate the influence of electrochemically active molecules such as ascorbic acid or mono-amines present in the cerebral environment, since they may interfere with the sensing signals. Therefore, in order to downscale the functionalization procedure carried out for the previously described micro-sensors (chapter 2), the semipermeable PPD coating was adapted to the nanopipettes' structure, according to the methods described in the experimental section, making use of the electrochemical setup described in the schematic of *figure 64a. Figure 64b* shows a series of consecutive CVs during the PPD electropolymerization on the platinized nanopipette. The resulting trend is equivalent to the one previously described for platinum wire-based microelectrodes: the current rises during the first cycle at around 0.6 V vs Ag/AgCl and decreases during the subsequent cycles, due to a progressive deposition of an insulating layer that screens faradaic processes.

Institut Polytechnique de Paris
91120 Palaiseau, France

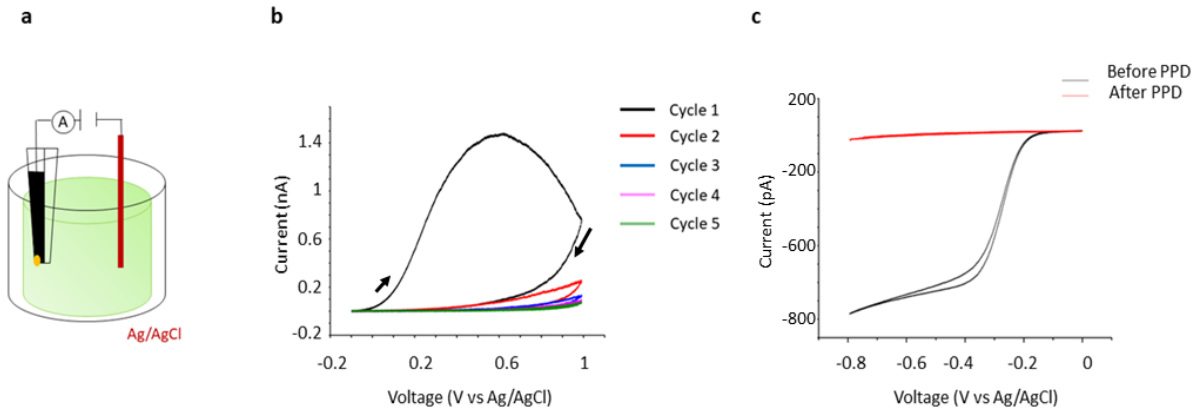

Figure 64. PPD deposition on nanoelectrodes.

a) Schematic of the electrochemical setup for PPD electropolymerization and deposition on platinized nanopipettes. b) CVs resulting from the PPD electropolymerization of a dual-barrel platinized nanopipette. c) comparison between the reduction of RuHex on a dual-barrel nanopipette before (black curve) and after (red curve) the deposition of the PPD layer.

Characterizing the electrodeposited layer of PPD via SEM, as in chapter 2, was not possible due to the small sizes at stake. Therefore, another type of analysis had to be taken into account. In order to confirm the PPD layer deposition was successful, I compared the results of electrochemical characterization in $Ru(NH_3)_6Cl_3$ before and after the PPD coating, as done for bare electrodes (section 4.3.1). The resulting trend, before PPD deposition, is represented from the black curve in f*igure 64c*. The same protocol has then been repeated for the platinum-PPD pipette and the resulting voltammogram is represented by the red curve in *figure 64c*. The low currents of the red curve can be explained as the polymeric layer shields the platinum, hindering the faradaic reaction with the ruthenium hexamine to take place.[71]

It is important to remember that, for the final application, the barrel devoted to imaging needs to remain empty to avoid any interference with the SICM feedback. SEM observations revealed the absence of a thick visible layer of PPD covering the imaging barrel but, additionally, the value of current through the imaging barrel, immersed in PBS, was also evaluated. Current values similar to those obtained with bare double-barrel nanopipettes were registered, confirming that the PPD layer does not impede the ionic flux in the imaging barrel.

Previously, in chapter 2, the suitable number of CV cycles for platinum wire-based biosensors was investigated, by allowing them to reject interfering species while retaining sensitivity to low concentration of hydrogen peroxide. Since the nanoelectrodes have a different geometry compared to those previously reported in literature [71, 70, 149] and in previous chapters of this manuscript, I needed to confirm that five cycles were appropriate and would not completely block the diffusion of hydrogen peroxide towards the platinum. *Figure 65a* displays, in black, the calibration curve of a platinized nanopipette for detection of hydrogen peroxide, having linear range from 10 µM to 1 mM (R^2=0.99)

Institut Polytechnique de Paris
91120 Palaiseau, France

and a sensitivity of 0.46 µA/M. In blue, the calibration curve for the same probe, after PPD deposition obtained with 5 CV cycles, is also represented. In this second case, even if the linear range is not affected (R^2=0.99), the sensitivity of the Pt-PPD nanopipette is equal to 0.049 µA/M, corresponding to a drop of the sensitivity towards hydrogen peroxide of 90%. This is probably due to the thickness of the PPD layer that strongly impedes the diffusion of the peroxide in solution towards the platinum, resulting in lower oxidation current measured at the electrode compared to the case of the bare platinum electrode. This effect is comparable with previous literature reported about platinum wire based biosensors.[71] *Figure 65b* shows, in black, the calibration curve for another probe, for which the range of linearity is between 10 µM and 1 mM (R^2=0.99) and the sensitivity is equal to 3.27 µA/M. Observing the comparison between calibration curves before and after the PPD electropolymerization obtained with 3 cycles of CV, shown in red, we can observe that also in this case the linear range is not impacted (R^2=0.99), and the sensitivity of the new Pt-PPD sensor becomes 1.13 µA/M. Therefore, in this case, we have a loss in sensitivity towards hydrogen peroxide equal to 65%. Finally, the number of CV cycles during the PPD electropolymerization was further decreased, reducing it to a single cycle. *Figure 65c* shows the calibration curve for a third probe, whose linear range also goes from 10 µM to 1 mM (R^2=0.99) and whose sensitivity is equal to 6.35 µA/M. The green curve represents the calibration curve after the addition of the PPD layer, obtained with one CV cycle. In this instance, the linearity range is not affected by the introduction of the semipermeable membrane (R^2=0.99) while the sensitivity of the sensor decreases of around 50 % (3.3 µA/M – 48%). These recent tests indicate that to keep strong sensitivity to hydrogen peroxide after applying the PPD layer, it is advisable to minimize the PPD thickness. This means using as few CV cycles as possible to apply the PPD. However, before confirming that a single CV cycle is sufficient, I verified that it forms a suitable PPD layer to effectively block the interfering substances. *Figures 65d, 65e,* and *65f* represent a summary of a series of tests conducted in order to assess the capability of different number of CV cycles to reject interferences. We can observe that 1 cycle (*figure 65f)* results in a 69% serotonin and 13% ascorbic acid rejection. Instead, if we use 3 cycles (*figure 65e*), 100 % of serotonin, and 65% of ascorbic acid interferences are avoided, while increasing the number of cycles to 5 (*figure 65d*), rejection reach a level of 100% for both. Therefore, considering that is fundamental to maintain a compromise between interference rejection and sensitivity to hydrogen peroxide, a number of 5 cycles of CV for PPD deposition has been considered suitable. Even if it may seem a remarkable loss in terms of sensitivity for hydrogen peroxide detection, the oxidation current can still be easily detected, therefore this result can be considered satisfactory.

Institut Polytechnique de Paris
91120 Palaiseau, France

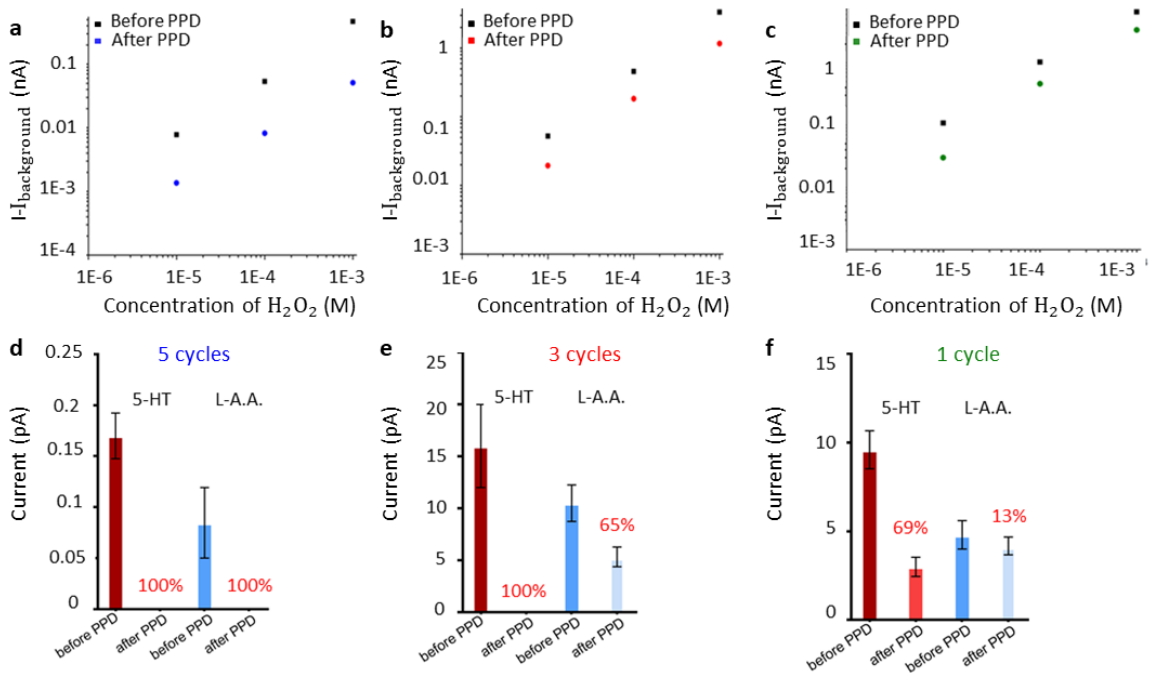

Figure 65. Comparison of nanopipettes' sensing performances towards hydrogen peroxide and interference before and after the PPD layer deposition.
Sensitivity to hydrogen peroxide before and after PPD deposition obtained with a) 5 CV cycles, b) 3 CV cycles, and c) 1 CV cycle, respectively. Rejection of interferences before and after PPD deposition obtained with d) 5 CV cycles, e) 3 CV cycles, and f) 1 CV cycle.

4.3.5 Cleaning of SICM barrel in dual-barrel nanopipettes

The immobilization of the protein on the platinized nanopipettes takes place by dipping the nanoprobes in a solution of the enzyme, as described in the section 4.2, similarly to the procedure for micro-sensors (chapter 2). Nevertheless, when working on the functionalization of double-barrel nanopipettes via enzyme immobilization, also in this case, we need to avoid contaminating the second barrel during the protein immobilization. In fact, any trace of the protein blocking the hole of the imaging barrel, would compromise the SICM feedback.

In fact, after standard protein immobilization procedure, dual-barrel probes were observed in SEM and, referring to their top view, the tip opening appeared block by a thick layer, in correspondence of the imaging barrel. The imaging barrels of the same probes were also tested via SICM, measuring the ionic current in PBS when a bias of 0.1 V vs Ag/AgCl was applied, and no current was measurable, confirming the clogging of the imaging barrel.

Therefore, different strategies have been tested in order to keep the imaging barrel free during the *Rg*DAAO immobilization process. In order to test a suitable cleaning procedure, it was decided to use just-pulled dual-barrel nanopipettes. One of the possibilities is that the blocking of the barrels happens because, during the pipette dipping in the *Rg*DAAO, the solution enters the barrel and subsequently dries blocking the barrel. Nevertheless, it was unclear whether the clogging is due to

the drying process, or to the crosslinking of the protein matrix. Therefore, I wanted to understand if the 4 minutes drying is enough to clog the tip's opening.

Figure 66 shows a schematic summary of the tests performed: a group of pipette, indicated with A, was dipped in *Rg*DAAO, according to the immersion-drying times previously described, immersed in PBS for 20 minutes, to be as much as possible consistent with the biosensor fabrication procedure, and then observed in SEM and SICM for testing the current. The group B, instead, was immersed in *Rg*DAAO, subjected to glutaraldehyde crosslinking, rehydrate in PBS and then tested for SICM current observation and SEM imaging. As we can observe from the reported SEM images, representing one example pipette for each of the two groups, the tip's opening of both pipettes show the presence of a layer blocking the barrels' hole. The current measurement in SICM also confirmed the clogging of the pipettes. Therefore, it was concluded that the dipping and drying step of the immobilization process are enough to provoke a blockage. This step of the functionalization was subjected to optimization.

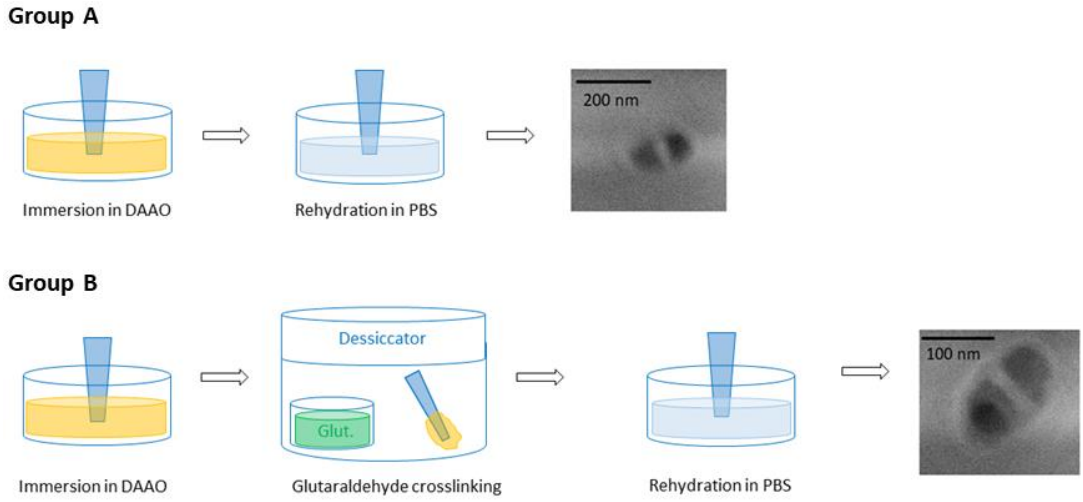

Figure 66. Approaches for cleaning the imaging barrel.
Procedure group A: probes are subjected to immersion in *Rg*DAAO, rehydration in PBS, and then they are tested. Procedure group B: probes are subjected to immersion in *Rg*DAAO, glutaraldehyde crosslinking, rehydration in PBS, and then they are tested. For each of the two groups, an example SEM image of the resulting pipette aperture is reported.

At first, it was thought to connect the back part of the probe to a flow of argon (6 bars) immediately after every immersion of the probe in *Rg*DAAO, in order to push out of the barrel the residual amount of protein in it. *Figure 67* shows some examples of probes whose tip openings have been observed in SEM after having tested this method. It can be observed that for the smallest pipettes as those in *figures 67a* and *67b* (285 and 340 nm double-barrel size, respectively), the opening was found closed. For bigger probes' aperture, as the one in *figure 67c* (650 nm double-barrel size), the top view of the probes shows areas partially free. In fact, having bigger probes will provoke easier entrance of the protein per capillarity, but also easier release of that. Nevertheless, using larger probes is not a valid

Institut Polytechnique de Paris
91120 Palaiseau, France

alternative since, decreasing the size of the tip opening leads to a loss in sensitivity during SICM imaging.

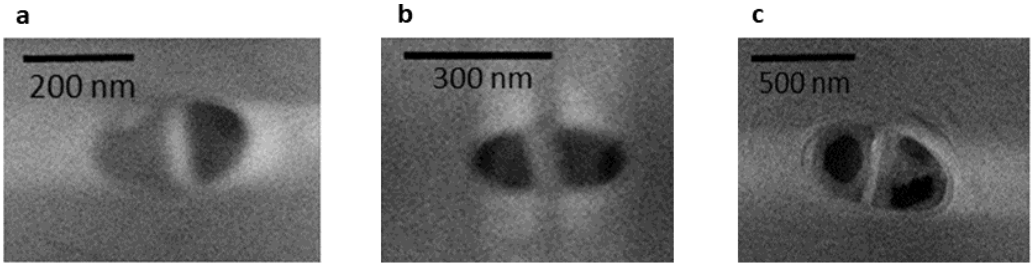

Figure 67. Attempts for cleaning of the imaging barrel.
SEM images of several double-barrel nanopipettes, characterized by different opening size, after cleaning of the imaging barrel, post *Rg*DAAO immobilization procedure. Opening size of the nanopipettes are a) 285 nm, b) 340 nm, and c)650 nm.

Therefore, to prevent the infiltration of the protein, a flow of argon was blown also during the immersion of the pipette in *Rg*DAAO, and during the drying time. Different pressure values have been tested, starting from 3 bars up to 6 bars, being the latter the one that proved to be appropriate to successfully preserve the imaging barrels during the immobilization procedure. *Figure 68a* represents an SEM picture of an example pipettes used to test this last approach: we can observe it looks clean in correspondence of the tip opening, still having a size lower than 500 nm. In addition, measuring of ionic current, revealed values of current typical of probes of this size. In order to confirm that the blockage does not happen even if the neighboring barrel is fully functionalized, SICM currents were recorded for fully functionalized dual-barrel pipettes, showing current values typical for nanopipettes of this size. This confirmed that the last procedure described is appropriate to maintain the imaging barrel free while functionalizing the sensing one. *Figure 68b* shows the SEM picture of the tip opening of a functionalized barrel, where the barrel devoted to imaging looks clean.

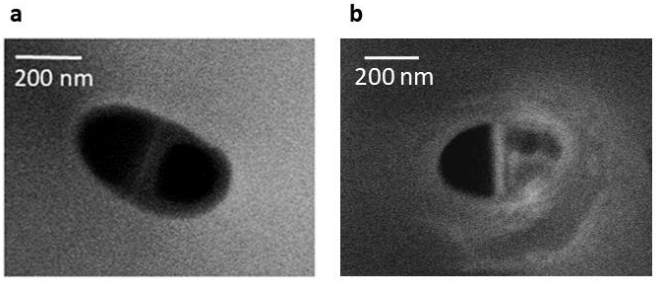

Figure 68. Successful cleaning of the imaging barrel.
SEM pictures of two example nanopipettes after *Rg*DAAO immobilization. The tip opening is clean for a) the two barrels of a non-functionalized nanopipette and b) the imaging barrel of a platinum-functionalized nanopipette.

Institut Polytechnique de Paris
91120 Palaiseau, France

4.3.6 Characterization and performances of nanosensors for D-serine and D-alanine detection

Assessing the capability of these small probes to detect D-amino acids and evaluating whether nanometric geometry affects sensitivity was a priority. To address this, I opted to work on a simplified version of the nanosensors wherein nanoelectrodes were constructed in a single-barrel pipette.

As delineated in section 4.3.2, the utilization of varying numbers of CV cycles during electrodeposition introduces distinct geometries in the resulting platinum deposit. Two models were employed, each representing a different geometry of this deposit. The type 1 geometry, illustrate schematically in *figure 69a* and its corresponding SEM image, depicts the platinum deposit as approximating a sphere with an average diameter computed as 500 ± 225 nm, based on 10 samples. In contrast, the type 2 geometry, presented schematically in *figure 69b* and its SEM representation, confines the Pt deposit within the nanopipette body, aligning more closely with the anticipated geometry for use in dual-barrel probes. In this application, the nanopipette opening measures 150 nm, though this dimension can be adjusted according to the laser-pulling settings. Both the two models have been tested for the detection of D-serine and D-alanine according to the procedures described in section 4.2.

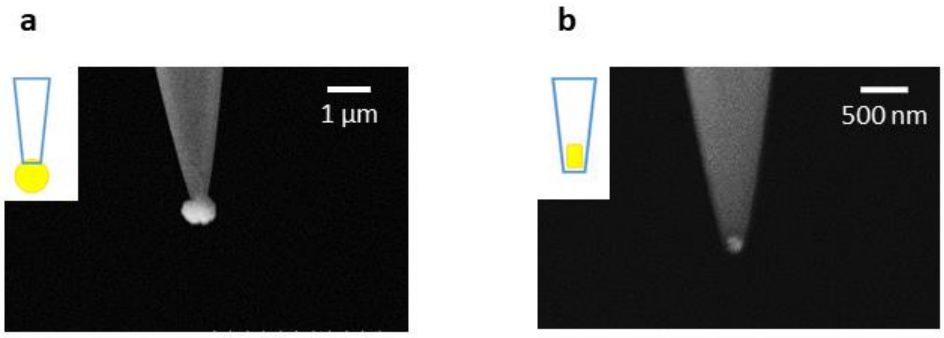

Figure 69. Two models used for D-serine sensing evaluation.
a) Pt deposit protrudes outside of the glass body, resembling a sphere. b) Pt deposit is confined in the body of the glass nanopipette.

The resulting calibration curve for the sensing of D-serine, for an example probe of the first type, are shown in *figure 70a.* This specific probe has a sensitivity of 4.09 nA/M. Nevertheless, the variability between the sensitivity values of the spherical probes is very high, as shown by *figure 70b*, and can vary of several orders of magnitude, being the smallest detected values equal to 0.29 nA/M and the biggest to 175 nA/M. Spherical probes are able to detect between the concentrations of 1 µM and 10 mM, as seen in the example of *figure 70a* (R^2=0.95). Nonetheless, also on this regard, lowest and highest concentration detected can vary of one order of magnitude around these values. (example: 10 µM – 1mM)

Institut Polytechnique de Paris
91120 Palaiseau, France

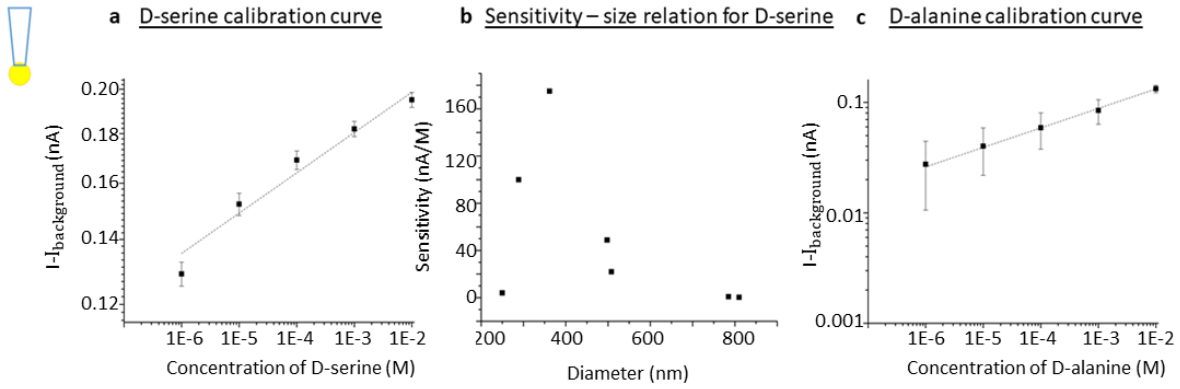

Figure 70. Characterization of the sensing performances of geometry type 1.
a) Calibration curve for the detection of D-serine. The error bars reported represent standard deviation calculated on three measurements. b) sensitivity-size relation for a group of probes of type 1 when sensing D-serine. The error bars reported represent standard deviation calculated on three measurements. c) Calibration curve for the detection of D-alanine.

The variability observed among different nanoprobes may be attributed to various factors. Firstly, environmental conditions, such as the pH and the temperature of the solution, can impact sensor performance.[70] While efforts were made to control the pH of the buffer solution, measurements were not conducted at a controlled temperature, introducing a potential factor affecting results consistency. Nevertheless, care was taken to ensure consistent oxygenation of the aCSF solution, fundamental to obtain reliable results, as emphasized in Chapter 2. Secondly, as previously noted, minor variations in the probe's geometry can influence the sensor's final sensitivity. In this context, one crucial parameter is the active surface of the sensor, affected by the surface area of the platinum deposit. While deriving the deposit's approximate diameter from SEM images is feasible, this method significantly underestimates the effective surface. The platinum deposit's surface, in fact, exhibits irregularities and roughness, enhancing the actual surface area. Literature examples have already illustrated strategies aimed at increasing surface area to improve nanosensor sensitivity.[136] Moreover, in the realm of platinum wire-based micro-sensors for D-serine detection, studies have explored how altering the roughness of the platinum electrode surface influences sensors performance. Increased roughness has been associated with heightened sensitivity and improved limits of detection.[148] While this may favor the functionality of the electrodes, confidence in uniform roughness across all probes is uncertain. Additionally, different configuration of the platinum aspect may lead to varied deposition of the PPD layer, impacting sensitivity to H_2O_2 and the extent of protein crosslinking to the Pt-PPD structure. Considering these factors, the unpredictable size-sensitivity relationship observed when trying to represent sensitivity as a function of the approximate sphere diameter (*figure 70b*) can be attributed to these diverse considerations, highlighting the absence of a monotonic relation between the two entities. Similarly, conducting a comparison with other cylinder or disk-shaped sensors designed for D-serine detection, such as previously reported micro-sensors,[70, 71, 149] proves

Institut Polytechnique de Paris
91120 Palaiseau, France

challenging due to the inability to provide area specific sensitivity value. It is crucial to note, however, that in comparison to the smallest D-serine sensors produced thus far,[149] the sensors here described are 20 times smaller in size, while still maintaining a commendable sensitivity to detect D-serine within a biological relevant range.

Geometry of type 1 has also been tested for detection of D-alanine, as already done for micro-sensors. *Figure 70c* represents an example of calibration curve for an electrode type 1presenting a sensitivity equal to 8.69 nA/M and with a linear range spanning from 1 µM to 10 mM (R^2=0.99). Inter-sample variability also in this case is accentuated, varying between 0.2 nA/M and 8.69 nA/M. As also seen in Chapter 2, the sensitivity of *Rg*DAAO towards D-alanine appears higher than the one for D-serine, as visible comparing this last example with the one of *figure 70a.* Nevertheless, taking into account all the considerations about how little variations of the geometry affect the final sensor performance, it should not be surprising finding similar sensitivities values, in average, between D-serine and D-alanine. Also in this case, the detection range of 1 µM to 10 mM, even if not appropriate to detect D-alanine in the brain in physiological conditions, known to be lower than the concentration of D-serine, is still relevant considering the levels of D-alanine in other tissues.[273]

Having seen the results for the detection of the D-amino acids using nanoelectrode geometries of the first type, I then moved to the second type of geometry, and repeated the same calibration tests. Two examples of resulting calibration curves are given in *figures 71a* and *71b*. D-serine is detected between the concentrations of 1 µM and 100 µM (R^2 = 0.90) in the first case, while between 100 µM and 10 mM (R^2 = 0.98) in the second one. In these instances, the detection ranges are narrow compared to the geometry type 1, and this could be explained in terms of smaller surface area of the sensor. Sensitivities are respectively equal to 28 nA/M and 1 nA/M respectively, therefore, also for this type of geometry, values of sensitivity resulted highly variable. Even if in this case we may think that the variability related to the size is not as impacting, since the size of the nanoelectrodes is related to the opening of the tip, that is relatively constant, is also true that the deposit of the platinum inside the barrels is not exactly identical in terms of recession or porosity. This results in differences that can still impact the final performances. In this case, smaller dimensions are at stake, therefore making even more critical differences that can result in a lack of suitable sensitivity.

I then tested the same type of geometry for the detection of D-alanine, shown in *figure 71c*. The sensitivity of 26 nA/M was evaluated, with linear range spanning between 1 µM and 1 mM (R^2=0.98). Sensitivities had a wide variability between 0.4 and 26 nA/M. In this context, the values of sensitivity towards D-alanine are very close (slightly higher) to the one for D-serine, and considering the inter-probes variability, we consider that this makes sense, because of the multiple aspects impacting the final sensor's sensitivity, included the active surface. It is important to point

Institut Polytechnique de Paris
91120 Palaiseau, France

out that in the case of geometry type 2, the success rate for D-serine sensing can be estimated to be around 43%, differently from the case of geometry type 1, for which it was equal to 65%. Therefore, the smaller sensor active area, as well as the geometrical characteristics, sometimes resulting in a recessed platinum deposit that may impact the diffusion profile of the analyte, have to be taken into account when considering to apply these sensors in real contexts, as small deviation from ideality may result into an impossibility to correctly sense the molecule of interest.

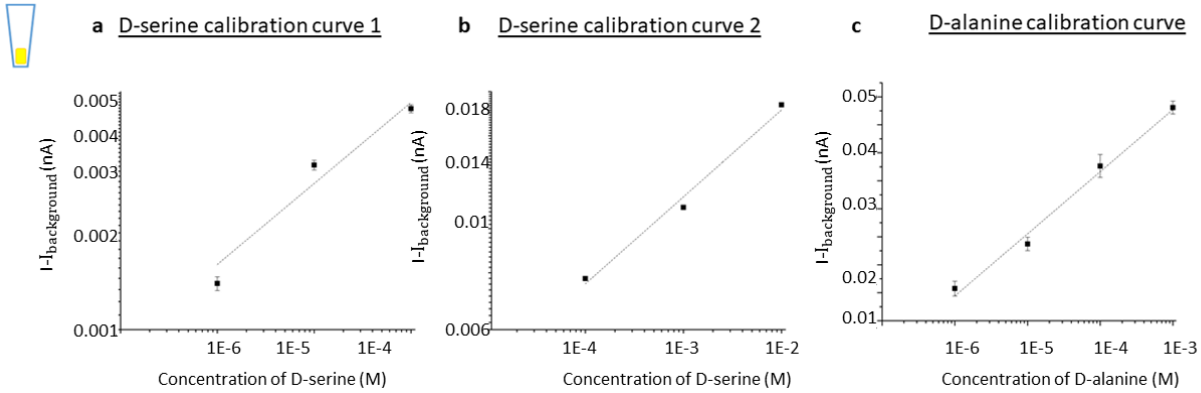

Figure 71. Characterization of the sensing performances of geometry type 2.
a) First example of calibration curve for the detection of D-serine. b) Second example of calibration curve for the detection of D-serine. c) Calibration curve for the detection of D-alanine. In all the panels, the error bars reported represent standard deviation calculated on three measurements.

4.3.7 Potentialities and possible applications

When examining sensors based on the geometry type 1, it can be affirmed that I have constructed the smallest existing sensors for the detection of D-serine. While these sensors may not yet be compatible with SICM, they can be easily integrated into a micromanipulator – a tool commonly employed in various biological experiments. Similar to the application of micro-sensors, this type of electrode can be strategically placed near areas of interest, in tissue or cell cultures, ensuring a much higher spatial resolution compared to wire-based sensors.

However, it is important to prevent the platinum deposit from detaching when in contact with brain tissue. SEM observations have already revealed that these probes are susceptible to detachment and may lose platinum when subjected to intense mechanical shaking or impacts on the tip.
When envisioning the use of these sensors in the presence of real biological samples rather than in solution, concerns may arise about the potential biofouling of the electrode. Contaminants pose a significant threat, potentially fouling the nanoelectrodes surface and compromising experimental outcomes.[274]

Nevertheless, the ability to locally probe D-serine at the single-cell level opens up new possibilities and ideally provides the capability to address unanswered questions regarding how this molecule regulates various physiological and pathological processes. Moreover, the ability to also

Institut Polytechnique de Paris
91120 Palaiseau, France

sense D-alanine extends the tool's applicability beyond the neuroscience domain, making it suitable for other areas of biological research.

Transitioning to in-barrel nanosensors, the observation that sensing is feasible for this geometry is of utmost importance. This principle paves the way for integrating such nanosensor technology into double- or multi-barrel pipettes. This integration allows for fine positioning of the tip in the area of interest, enhancing spatial resolution to the level of SICM, and provides the opportunity to use neighboring empty barrels for local chemical delivery.

It is crucial to emphasize that the construction approach used for the D-amino acid sensor can be extended to the enzymatic detection of other biological targets, rendering it a highly versatile tool. Envisioning the use of multi-barrel probes capable of detecting multiple analytes through different functionalization of various barrels adds further potential to this versatile platform.

4.4 Conclusion

In this chapter, we have detailed the efforts invested in the fabrication and functionalization of nanosensors designed for the detection of D-serine. The fabrication process of nanoelectrodes has been outlined, commencing with the construction and platinum deposition on carbon nanoelectrodes within a glass nanopipette barrel. Subsequently, the downscaling of the protein attachment process, previously employed for larger micro-sensors, has been elucidated. Challenges inherent in the transition from the micro- to the nano- world have been underscored, and strategies for overcoming these challenges have been described.

During the nanosensor characterization phase, I confronted numerous challenges arising from the intricate fabrication steps introduced thus far. These steps exhibit complexity and can fail to ensure high reproducibility, particularly given the minute geometries involved. Indeed, previous reports have already highlighted the susceptibility of these delicate electrodes to geometric alterations, such as those induced by minimal incorrect handling and electrostatic discharge, potentially leading to inefficiencies during testing.[274] Moreover, the construction of platinum nanoelectrodes within dual-barrel pipettes adds another layer of complexity, making the procedure susceptible to even minor errors.

It is important to point out that, when dealing with this class of sensors, a clear understanding of the active area's geometry is crucial for comprehensive result interpretation. The transition to nanoelectrodes significantly heightens complexity compared to macroelectrodes or microelectrodes, as the size-dependency effects remain inadequately understood within classical electrochemical theory at very small dimensions. In the nanoelectrodes domain, in fact, slight deviations from anticipated geometries can exert a substantial influence on electrochemical behavior, necessitating a

Institut Polytechnique de Paris
91120 Palaiseau, France

meticulous examination of electrode geometry for accurate result interpretation.Therefore, the characterization has been carried out taking into account two different geometry types. The characterization of one-barrel nanosensors in two distinct geometries has been presented, unveiling the novel capability of D-serine and D-alanine sensing with nanosensors for the first time. In light of this, we can confidently assert that I have successfully designed and fabricated the smallest existing sensor for D-serine detection, demonstrating its successful utilization in detecting D-serine in solution. While these findings represent significant progress, further investigations are imperative to assess the performances of these sensors in real biological contexts and to explore the potential integration with SPM techniques. Despite these considerations, these results can be viewed as preliminary outcomes, laying the foundation for the development of a multi-functional, high-resolution platform. Such a platform holds the potential to serve as a unique tool for researchers across diverse biological fields.

Institut Polytechnique de Paris
91120 Palaiseau, France

Chapter 5. Conclusions and future perspectives

The investigation presented in my thesis stems from the need to elucidate the function of D-serine in the regulation of NMDA receptors under both physiological and pathological conditions. D-serine, together with glycine, serves as co-agonist essential for the activation of NMDARs. The multifaceted role and operational mechanism of D-serine in physiological conditions still present numerous unresolved aspects, such as the mechanisms of action of its transport, whose preferred direction of operation remains not understood. Furthermore, NMDARs and their regulatory component D-serine, play a role in various pathological conditions and neurological disorders, lacking effective treatment options.

In order to explore and comprehend many of these phenomena, the application of an appropriate technique capable of sensitively and selectively probing D-serine with high temporal and spatial resolution is needed. Over the past decades, one of the most extensively employed tools to achieve this objective has been the utilization of electrochemical biosensors, owing to their heightened sensitivity, user-friendliness, and potential for miniaturization. The latter characteristic proves essential when targeting investigations in small regions, such as synaptic terminals, where the release of D-serine occurs. Electrochemical biosensors have demonstrated superiority over more conventional techniques for D-serine detection, including microdialysis approaches and chromatography techniques, as they enable real-time and localized detection of the analyte under investigation. Specifically, the detection of non-electroactive NTs like D-serine relies on the utilization of enzymes as recognition elements. DAAO is an enzyme that specifically reacts with D-amino acids, such as D-serine. When DAAO degrades D-serine, it produces stoichiometric amounts of hydrogen peroxide, whose oxidation can be detected at a biased platinum electrode of the electrochemical sensor.

This thesis is situated within the framework of D-serine sensing through electrochemical enzymatic-based biosensors. Specifically, I drew inspiration from previous models of electrochemical biosensors that utilized wire-based platinum ultra-micro-electrodes (25 μm in diameter) onto which a layer of the enzyme *Rg*DAAO was applied for sensing purposes.[70, 71] The efficacy of this sensor type had already been validated through proof-of-concept experiments for *in vivo* measurements of D-serine levels. Furthermore, numerous studies had demonstrated that modifications in physical characteristics such as geometry, size, or roughness of these sensors lead to variations in sensor's performance and sensitivity. Motivated by the success of these findings, I opted to replicate one of these sensors and subsequently employed them for the first time in an *in vitro* on-slice analysis of D-serine levels in the pathological condition of epilepsy.

Institut Polytechnique de Paris
91120 Palaiseau, France

When dealing with micro-sensors, the thorough characterization of sensor performance is important for the accurate interpretation of results. Despite not introducing significant deviations from the fabrication process outlined in the literature, a meticulous analysis of all fabrication steps was essential to optimize the final sensor's performance. Of particular significance is the application of PPD semipermeable membrane, designed to reject interferences originating from other electroactive molecules abundant in the brain. Excessive amounts of PPD can lead to reduced sensitivity to hydrogen peroxide and an extended response time of the sensor, rendering it unsuitable for detecting D-serine levels. Therefore, the optimization of the electropolymerization protocol is crucial to achieve a well-balanced rejection of interferences and sensitivity to H_2O_2. Once ensuring appropriate sensitivity and a suitable detection range, I proceeded with the utilization of the micro-sensors.
I employed mouse hippocampal brain slices for the measurements, utilizing electrochemical sensors to monitor how the levels of D-serine change during an epileptic seizure induced by chemical stimulation of the slices. Specifically, an increase in D-serine content associated with the seizure was observed in the CA_1 region of the hippocampus. In contrast, such an increment was not observed in the DG area.

In future applications of these sensors on brain slices, a deeper investigation into the impact of the physical contact between the slice and the sample on sensitivity and calibration curves will be needed for precise quantification of the variations of D-serine levels.

Encouraged by the positive outcomes achieved, I directed the efforts towards the second part of this thesis. This section delves into a more technical aspect, involving the creation of a novel electrochemical enzymatic-based sensor designed for D-serine detection. By employing 25 μm wire-based sensors, we can focus on the investigation of single cells or cluster of cells. However, given the synaptic context in which D-serine functions, it is of paramount interest to probe the molecule's levels at synaptic terminals or membrane nanodomains for precise tracking of NT release. Consequently, with the objective of improving spatial resolution, it was decided to develop nano-biosensors tailored for the detection of D-serine.

Transitioning to the use of nanosensors not only presents technical challenges but also introduces difficulties in precisely positioning the nanosensor within the region of interest for investigation. To address these challenges, the development of an electrochemical D-serine nanosensor embedded in the probe of a SICM was proposed. SICM is a well-established SPM technique that operates in a liquid environment and employs a glass nanopipette as a scanning probe to reconstruct the topography of samples. The non-contact nature of the feedback mechanism renders this technique particularly suitable for investigating soft biological samples in their physiological environment.

In this work, I employed a specialized type of SICM probe with a divided tip opening, creating two separate channels. One of these channels is dedicated to imaging living neurons, while the other is functionalized for the construction of a D-serine nanosensor. The ability to allocate distinct channels for different functionalities enables the simultaneous application of imaging and sensing on in vitro cultures of neurons. SICM imaging not only facilitates the acquisition of high spatial resolution topographical maps but also serves as a navigation system, allowing precise positioning of the sensor at desired locations on the cell surface and control of the sensor-sample distance.

In developing the dual-functionality probes, I initially focused on separately refining the two functionalities, always with the ultimate goal of their simultaneous operation in mind. The optimization of the SICM imaging process for visualizing living cells, particularly neurons, involved multiple steps. A crucial consideration was the selection of a suitable imaging solution, necessitating to satisfy physiological condition requirements. However, the use of complex culture media as imaging solutions posed challenges, notably progressive clogging of the tip opening. The definition of appropriate imaging settings was then conducted to control the distance between the sample and the probe. Addressing soft samples like cells with conductive membranes required careful analysis to prevent unintended contact or penetration of the cell by the probe. To mitigate these risks, a precise definition of the feedback setpoint was undertaken. While not the primary focus of this thesis, the capability to control the probe's insertion into the cell body offers potential for other applications, enabling monitoring of the pipette's insertion depth into the cell. Various imaging modalities were explored, allowing for whole-cell topography and detailed analysis of cell membrane features, achieving lateral resolution down to 100 nm. Finally, the setup was optimized to enable imaging of living neurons in their physiological conditions, encompassing parameters such as temperature, humidity and CO_2 levels. These modifications will facilitate prolonged topographical acquisition providing valuable insights into cell movements and morphological changes over time.

For the sensing aspect, a process of miniaturization of the micro-sensors was followed. The first step of the process was the construction of carbon nanoelectrodes within the sensing barrel itself, creating a compact and mechanically resistant structure. This approach is alternative to the use of very thin wire that are susceptible to folding or movements when immersed in a solution, requiring subsequent steps to enhance their mechanical rigidity. The size of the nanoelectrodes is determined by the pulling process of the tip and can be tuned accordingly. While smaller sensors could theoretically be produced, this would introduce higher challenges during the functionalization process and would result in a decreased active surface, potentially compromising sensitivity. However, smaller probes offer higher spatial resolution, prompting further investigation to reduce the size. Given the inherent inertness of carbon, a layer of platinum was electrodeposited onto the electrode

surface to enhance catalytic properties and ensure the detection of hydrogen peroxide oxidation. A particular challenge has involved the study of sensitivity patterns to H_2O_2 in relation to the size of the platinum deposit. Generally, increasing the size of platinum deposit improved sensing performance. However, substantial variability was observed, likely explained by differences in platinum surface area due to surface roughness, not reproducible between different samples. Additionally, variations in the outcomes of the platinum deposition were attributed to the incomplete reproducibility of the preceding fabrication step, the carbon filling procedure. Indeed, different levels of recession of the carbon nanoelectrodes in the glass structure of the nanopipette could lead to different final exposure of the platinum surface, influencing catalytic performance. Therefore, a well-defined geometry of the carbon would be beneficial. Several studies, recognizing the importance of having a well-defined geometry for meaningful interpretation of results, have employed focus ion beam (FIB) milling. This technique enabled the accurate definition of nanopipette-based nanoelectrodes with size ranging between 50 nm and 350 nm, and based on different metals such as gold, platinum, silver, and copper, starting from both single and double-barreled capillaries.[275] Similarly, hybrid SICM/SECM probes with opening tip sizes of 200-250 nm have been prepared using FIB milling to expose gold nanoelectrodes[276] or define the geometry of carbon ring electrodes, as well as carbon/platinum disk electrodes with different opening sizes (200 – 1000 nm).[277]

In this case, the application of platinized nanopipette-based nanoelectrodes would necessitate calibration prior to experimentation to accurately quantify the level of H_2O_2. These probes, in their single-barrel form, can be employed in conjunction with a micro-manipulator for localized analysis, such as at the single-cell level. Single-barrel probes with a similar electrode structure but smaller size (tip opening between 5 and 200 nm) have already been utilized to monitor oxygen consumption inside and outside a brain slice. Additionally, they have been inserted into single cells to perform intracellular electrochemical measurements.[133] When combined with SICM, these probes offer expanded possibilities, leveraging their sensing capabilities with the position control provided by the SPM technique. Double-barreled carbon-platinum nanopipettes have, for example, been utilized for simultaneous mapping and sensing of H_2O_2 at single nanoparticle level.[278] As a result, numerous applications for both single and double-barrel platinum nanoelectrodes could be envisioned, aiming to detect hydrogen peroxide at the single-cell level, given its recognized importance as signaling molecule.[279]

The subsequent step in the construction of the nanosensor involved the deposition of a p-PPD layer on the platinized electrode. Similarly to the micro-sensors, I explored an appropriate protocol for depositing a polymer layer capable of fully rejecting interferences. However, in the case of nanosensors, achieving complete interference rejection is correlated with 90% reduction in sensitivity

to H_2O_2 compared to the platinum surface prior to PPD deposition. This decrement in sensitivity poses challenges in the final detection of hydrogen peroxide resulting from D-serine degradation, potentially leading to an inadequate detection range for the NT.

A potential approach to address this challenge could involve not only controlling the number of applied CV cycles but also varying the concentration of PPD in the solution. This strategy may offer a finer control over the amount of deposited polymer and, consequently, the permeability of the membrane. In a study conducted on platinum microelectrodes, it was shown that by maintaining the same number of PPD cycles and adjusting the concentration of the PPD solution, the desired rejection of interferences could be achieved.[76]

An alternative solution to the aforementioned problem could involve exploring a different isoform of PPD. Existing literature includes numerous studies aimed at investigating the suitability of p-, o-, and m- PPD isoforms on various electrode materials including palladium[280] and carbon fibers.[281] However, as the underlying substrate material[282] and its geometry and size[283] may influence the characteristics of the deposited polymeric layer, additional studies have been conducted to assess the performance of the three PPD isoforms when deposited on platinum cylinder electrodes. In a particular study, researchers utilized the same electropolymerization protocol for o-PPD, m-PPD, and p-PPD, resulting in different final permeability to hydrogen peroxide and ascorbic acid (AA), the latter serving as a reference for evaluating interference blockage. All three isoforms exhibited very high and similar permeability to hydrogen peroxide, with a slight advantage (3%) observed for m-PPD. Therefore, the determination of the most suitable compound was based on the assessment of the lowest permeability to AA, which was found to be concentration-dependent. Specifically, for concentrations below 200 µM, m-PPD was the optimal isoform, while for higher concentrations, such as those found in the brain (up to 0.5 mM[218]), o-PPD was the best option.[284] Exploring the substitution of the isoform used in this study for the o-isoform may potentially require fewer layers of PPD for effective interference blocking, resulting in a reduced decrement in sensitivity to hydrogen peroxide. Furthermore, for the deposition of the PPD layer, I opted for an approach based on CV to replicate prior works.[149] However, it is also feasible to apply the PPD layer through constant potential amperometry.[70] The superiority of one method over the other remains a subject of debate, and various studies suggest the equivalence between the two approaches.[76] Hence, for this thesis, the CV method was chosen due to its significantly shorter deposition time. However, it is known that PPD layers applied via CV are characterized by larger pores in the resulting membranes,[76] leading to higher permeability values.[284] The application of the constant potential method may be explored to evaluate

whether its superior interferences rejection capability allows for blocking interferences with a smaller amount of PPD, potentially facilitating H_2O_2 sensing.

Exploring alternative polymers is another avenue that can be considered, although some researchers have previously encountered challenges in finding alternatives to o-PPD for creating semipermeable membranes on Pt microelectrodes. The use of polyaniline (PANI), for instance, has been reported to create a semipermeable membrane on microcylinder platinum electrodes for enzymatic electrochemical detection, specifically employing GOx to detect glucose. However, while the resulting membrane showed improved rejection of ascorbic acid, it also exhibited reduced permeability to hydrogen peroxide, subsequently lowering sensitivity to glucose.[285]

Following the application of the PPD layer, enzyme immobilization was carried out using vapors of glutaraldehyde to crosslink the *Rg*DAAO enzyme to the Pt-PPD structure. The sensing performance of the sensors for D-serine strongly depends on the geometry of the platinum deposit, influencing both sensitivity and detection range. Similar to the observations in H_2O_2 sensing, significant variability was noted among nanosensors with similar geometries observed in SEM. As mentioned earlier, careful optimization of the fabrication procedure to enhance geometry reproducibility may assist in minimizing these differences. However, both the immobilization process and testing can be influenced by environmental conditions such as temperature or pH. Rigorous control of the temperature during the calibration phase, for example, may offer insights into potential sources of this lack of reproducibility.

The challenges associated with the diversity in shape and size among different probes are compounded by a further issue related to the fragility of such probes, which can be easily damaged. Various sources of damage for nanopipette-based platinum micro- and nanoelectrodes have been previously reported, including electrostatic discharge damage caused by the contact of the probe with non-grounded objects or the operator itself. This contact can lead to substantial modifications of the glass and platinum surfaces.[274] This may have resulted in additional modifications to the electrodes' appearance and damage, contributing to the difficulties and complexity of testing and preparing such nanoprobes. To simplify the preparation process of these probes, one-barrel model nanopipettes were employed.

In an effort to gain further insights into the relationship between geometry and the performance of the final D-serine nanosensor, I analyzed two types of platinum structures. The first structure comprised a platinum deposit resembling a spherical structure protruding outside of the imaging barrel. The resulting detection range for D-serine, as well as sensitivity, proved to be suitable for biological applications. However, it was observed that increasing the size of the platinum deposit led to mechanical instability of the protruding structure, which was lost in some cases after

manipulation. Therefore, a more detailed analysis is necessary to determine the optimal size that balances good mechanical stability with excellent sensitivity.

This type of sensor, as previously observed in the case of H_2O_2, could be employed in conjunction with a micromanipulator and an optical microscope to determine local levels of D-serine. However, such an application would require careful consideration when approaching the sensor to the surface of cells or tissue. It is necessary to investigate the needed distance between the sample and the probe to acquire information about the local production of D-serine. Operating at very small distances between the two carries the risk of contact, which may result in damage to the platinum element or its enzyme layer. Additionally, the risk of surface fouling when working in proximity of a biological sample should be further investigated.

Various strategies have been reported to reduce the risk of biofouling when working with microelectrodes and nanoelectrodes, primarily centered on the use of additional porous membranes to shield the sensor surface from contamination. Protection of platinum microelectrodes has been achieved using hydrogels[286] or silicon nanopore membranes.[287] CFMEs, on the other hand, have been successfully shielded from biofouling risks by integrating Nafion[288] or Nafion-PPD[289] membranes. Moreover, a previous study employing cylinder microsensors for the detection of D-serine utilized a Nafion membrane to enhance the mechanical rigidity of the sensor when inserted into brain tissue. This approach demonstrated no decrement in sensitivity towards D-serine due to the application of the Nafion membrane.[70]

Transitioning to a different platinum geometry contained in the glass channel yields distinct outcomes in the characterization of the D-serine sensing. A decrease in sensitivity, variation of the detection range, and significant variability between samples were observed. However, this geometry is the most suitable for application of single-barrel probes, as it offers a more compact and stable structure. It is also advantageous for double-barrel probes, facilitating integrated sensing and SICM functionalities. The exposed size of the nanoelectrodes clearly impacts the sensor's performance, with larger electrodes providing higher surface for enzyme immobilization. This impact was further demonstrated when functionalizing probes that, due to a fabrication error, presented a thin layer of carbon deposited on the external surface of the probe, on which platinum deposit had grown in the form of separated but still connected islands. In this case, functionalization with *Rg*DAAO resulted in a sensor with improved sensitivity and detection ranges. However, attempting to replicate this approach, as well as increasing the opening size of the tip and consequently the diameter of the nanoelectrodes, has the drawback of decreased final spatial resolution. Therefore, further investigation is necessary to understand the reasons behind the poor sensitivity and explore possible solutions.

Institut Polytechnique de Paris
91120 Palaiseau, France

Firstly, it is important to note that the exact amount of protein immobilized on the surface of the Pt-PPD nanostructure is not known. For micro-wire based D-serine disk nanosensors like those presented, previous studies have reported approximately 25 μg of immobilized enzyme, corresponding to a total protein activity of 2 U.[71, 149] In this case, given the small geometries involved, it is possible that we have lower amounts of protein attached to the sensor, which need to be carefully evaluated. Additionally, the process of enzyme immobilization can impact the catalytic performances of enzymes, affecting both stability and activity. Common methods for determining the activity of free *Rg*DAAO are based on measuring H_2O_2 production using various assays, such as the o-DNS method used in this thesis. However, these methods are not always suitable for determining the activity of immobilized enzymes. A previous study using a micro-disk based biosensor for D-serine reported the determination of the activity of immobilized *Rg*DAAO through continuous measurements of the rate of current change associated with the production of hydrogen peroxide, along with simulations.[222] Although this study associates the method of immobilization with increased affinity of *Rg*DAAO towards D-serine in its immobilized form, it is also acknowledged that other studies have reported a decrease in activity as a result of immobilization.[220]

Furthermore, the future use of dual-barrel nanoelectrodes for sensing purposes may face an additional challenge related to the potential for the neighboring barrel to partially impede the effective diffusion of the molecule of interest on the sensor's surface. Therefore, it becomes even more crucial to explore new strategies aimed at enhancing the sensing signal.

In this study I immobilized the enzyme *Rg*DAAO through chemical crosslinking with the PPD layer using vapors of glutaraldehyde. However, while this method results in a highly stable enzymatic layer, PPD is not the sole technique for immobilization. Other techniques such as adsorption and entrapment in polymeric membranes allow for very high enzyme loading.[290] Alternatively, examples exist of enzyme immobilization occurring simultaneously with the electropolymerization of an o-PPD membrane. For instance, GOx was immobilized on platinum nanoparticles by mixing it in the PPD solution.[291] Similarly, GOx was immobilized on disk platinum electrodes using the same procedure to achieve a very thin layer characterized by high enzyme load.[292] Testing this approach alone or in combination with the crosslinking method could be a way to increase the amount of immobilized protein and enhance sensing performances. Alternatively, entirely different approaches should be considered for the development of nanopipette-based sensors for D-serine that can be integrated with the SICM technique. For example, a different method was employed for the creation of an electrochemical enzymatic (GOx) pipette-based nanosensor for glucose detection. In this work, the enzyme was covalently immobilized on the inner walls of the pipette's tip, which had been previously subjected to surface modification with poly-L-lysine. The sensor operates based on the

variation of the current at the pipette tip when the enzyme detects glucose, producing hydrogen peroxide as a reaction byproduct. The pipette is filled with a redox mediator to enhance signal reading.[211] All these strategies should be viewed as alternatives to the considerations previously mentioned regarding the optimization of the PPD layer characteristics.

When assessing the selectivity of the sensors, whether in their micro- or nano- versions, it is important to note that *Rg*DAAO enzymes in solution preferentially oxidize neutral D-amino acids. When immobilized, their activity towards acidic amino acids also increases. Micro-sensors for D-serine detection based on *Rg*DAAO have been scrutinized in various studies to analyze their sensitivity towards different D-amino acids, with D-serine and D-alanine reported as preferential substrates.[222] Negligible or no signal was detected for other D-amino acids present in the brain.[70, 222] Although the sensitivity of the sensors to D-alanine needs consideration in experiment interpretation, the levels of D-alanine in the brain are typically much lower than those of D-serine.[293] This dual functionality can be viewed as a strength of the sensors, allowing their application in various biological contexts.

As observed with micro-sensors, the presence of the PPD layer does not eliminate the potential for false positive signals arising from other sources of hydrogen peroxide production. Therefore, it becomes necessary to consider the use of control or blind nanoelectrodes. Consequently, optimizing the sensor geometry becomes even more essential to achieve a reproducible structure for accurate quantification of the measured quantities.

Excluding techniques such as chromatography-based methods or microdialysis, whose drawbacks have been extensively explored in comparison to micro- and nano-electrochemical biosensors, the latter prove to be highly potent tools for exploring the brain also when compared to other broadly used techniques. Among the array of tools employed by neuroscientists, super-resolution fluorescence microscopies have emerged as the preferred imaging modalities for investigating living neurons and their synapses at the nanoscale, both in health and disease. Super-resolution methods have unveiled dynamic processes influencing the structure of neurons, synapses, and their interactions with other brain cells, all heavily influenced by neuronal activity levels. Conversely, these nanoscale morphological changes play a crucial role in facilitating functional synaptic plasticity and cognition. The significance of these morphological features lies in their abilities to shape the extracellular space, creating a physical connection for the diffusion-mediated transport of neuroactive substances. While SR techniques hold promise in advancing brain sciences, they encounter limitations in their compatibility with analytical methods, such as neuromodulator concentration measurement.

Institut Polytechnique de Paris
91120 Palaiseau, France

Therefore, the development of such a device, capable of measuring concentrations of D-serine with precise spatial resolution in synaptic and extra-synaptic nanodomains, will significantly enhance the understanding of its role. The potency of these tools lies in their versatility, allowing them to be employed in conjunction with other techniques for a more comprehensive understanding of various mechanisms. For instance, to monitor neural activity while simultaneously mapping morphology and co-agonist concentration, this technique can be integrated with the patch clamp technique, facilitating the correlation of changes in network activity with levels of D-serine release. Additionally, the morphological alterations of synapses induced by synaptic plasticity can be investigated using SICM imaging, with a subsequent correlation to local co-agonist concentrations. The ability to locally probe D-serine, especially when combined with pharmacological treatment, will also contribute to unraveling elusive mechanisms associated with the uptake and release of the neurotransmitter from neurons.

While these electrochemical enzymatic biosensors for D-serine detection showcase their suitability in cellular studies, it is essential to acknowledge the emergence of innovative and complementary methods, bringing unique advantages and perspectives. Emerging methods such as genetically encoded biosensors, for example, offer innovative approaches providing valuable insights into cellular dynamics. Electrochemical nanosensors represent a potent tool for quantitative cellular analysis, excelling in applications that demand precise measurements of analyte concentrations. They do not need extensive sample preparation, and their localized nature facilitates focused investigations into a specific region of interest, making them particularly suitable for subcellular analysis. On the other hand, genetically encoded biosensors offer unique advantages by eliminating the need for the complex sensor engineering. These biosensors are based on genetically modified cells to express proteins that respond to specific analytes, making them ideal for studies involving an ensemble of cells rather than localized analysis. They excel in capturing the collective behavior of cell populations, enabling *in vivo* imaging, and are particularly beneficial for investigations into complex cellular interactions and signaling pathways. Ultimately, the choice between my approach and alternative ones depends on the specific goal of the study, while integrating different approaches enhances the versatility and depth of the studies

The utilization of multi-barrel pipettes, to combine imaging and sensing with other approaches, for example, other neurotransmitter sensing or local chemical delivery, can be envisaged. My probes have been thought to be in the future extendable to the utilization of quad-barrels for the integration of a delivery barrel and another functionalized barrel for the enzymatic sensing of glycine, to create a powerful tool for better understanding the complex and dynamic crosstalk between the two co-agonists. In addition, this type of double-barrel sensor has to be considered as a prototype

scaffold that can be modified with the addition of alternative enzymes for the detection of other types of analytes.

All in all, the study presented in this PhD work constitutes a starting point for the development of a multimodal tool for imaging and neurotransmitter sensing. Taking advantage of the current emerging developments in tip engineering, this tool can be easily adapted for applications in other fields of biology, where it has the potential to bring about significant improvements and advancements.

Institut Polytechnique de Paris
91120 Palaiseau, France

Résumé en français

Le cerveau est composé de milliards de neurones qui communiquent entre eux au niveau des synapses, où les neurotransmetteurs libérés du neurone présynaptique agissent sur les cellules effectrices. Les récepteurs du glutamate N-méthyl-D-aspartate (NMDA) sont essentiels à la physiologie cérébrale, et leur dysfonctionnement est souvent lié à des conditions pathologiques. L'activation des récepteurs NMDA nécessite un co-agoniste, tel que la glycine ou la D-sérine. Bien que le rôle de la D-sérine ait été découvert il y a deux décennies, les conditions régissant sa disponibilité synaptique et sa fonction relative à la glycine demeurent mal comprises.

Cette thèse vise à élucider la fonction de la D-sérine dans la régulation des récepteurs NMDA en conditions physiologiques et pathologiques. Pour cela, une technique analytique a été développée, permettant de mesurer en temps réel et avec une haute résolution la concentration locale de D-sérine dans les nanodomaines synaptiques et extrasynaptiques.

Au cours des dernières décennies, les biocapteurs électrochimiques sont devenus un outil précieux pour ces mesures, grâce à leur sensibilité, leur facilité d'utilisation et leur potentiel de miniaturisation. Cette dernière caractéristique est cruciale pour cibler de petites régions, telles que les terminaisons synaptiques, où la D-sérine est libérée. Les biocapteurs électrochimiques surpassent les techniques conventionnelles, comme la microdialyse et la chromatographie, en permettant une détection en temps réel et localisée. La détection des neurotransmetteurs non électroactifs, comme la D-sérine, repose sur l'utilisation d'enzymes comme éléments de reconnaissance. La D-aminoacides oxydase (DAAO) est une enzyme qui réagit spécifiquement avec les acides aminés D, tels que la D-sérine, produisant du peroxyde d'hydrogène, détectable par oxydation sur une électrode de platine polarisée. Ainsi, des micro et nanocapteurs électrochimiques basés sur la DAAO ont été développés.

La première partie de ce travail se concentre sur la fabrication et la caractérisation de capteurs électrochimiques micrométriques. Inspirés de modèles antérieurs utilisant des microélectrodes de platine (25 µm de diamètre) couverts de DAAO, ces capteurs ont été reproduits et utilisés pour analyser in vitro les niveaux de D-sérine en condition d'épilepsie. Leur utilisation pour surveiller les niveaux locaux de D-sérine dans des tranches d'hippocampe vivant en phase aiguë dans des expériences physiologiques est décrite, rapportant que la libération de D-sérine augmente dans des conditions chimiques proconvulsives imitant l'épilepsie.

En utilisant des capteurs de 25 µm, il est possible d'étudier des cellules individuelles ou des groupes de cellules. Toutefois, pour sonder les niveaux de D-sérine au niveau des terminaisons synaptiques,

Institut Polytechnique de Paris
91120 Palaiseau, France

une résolution spatiale plus fine est nécessaire. C'est pourquoi des nanobiocapteurs adaptés à cette détection ont été développés.

La deuxième partie de ce travail présente des nanocapteurs électrochimiques à base de DAAO intégrés dans des nanosondes en verre pour la microscopie de conductance ionique à balayage (SICM). Cette sonde comporte une nanopipette divisée en deux canaux: l'un pour le capteur à base de DAAO et l'autre pour la cartographie topographique SICM. La SICM est une technique de microscopie à sonde locale qui, grâce à une nanopipette en verre, reconstruit la topographie des échantillons dans un environnement liquide, idéale pour les échantillons biologiques mous. Lors du développement des sondes à double fonction, l'amélioration séparée des deux fonctions a été privilégiée tout en gardant à l'esprit leur utilisation simultanée. La double fonctionnalité permet l'application simultanée de l'imagerie et de la détection sur des cultures in vitro de neurones. L'imagerie SICM non seulement fournit des cartes topographiques à haute résolution, mais sert aussi de système de navigation, positionnant précisément le capteur sur la surface cellulaire.

La plateforme à double fonction qui en résulte deviendra un outil analytique puissant, combinant la détection locale de la D-sérine avec l'acquisition d'informations topographiques locales.

Institut Polytechnique de Paris
91120 Palaiseau, France

Bibliography

1. Tozzi, A. Information processing in the CNS: a supramolecular chemistry? *Cogn. Neurodyn.* **9**, 463–477 (2015).
2. Eccles, J. C. The Synapse: From Electrical to Chemical Transmission. *Annu. Rev. Neurosci.* **5**, 325–339 (1982).
3. Pereda, A. E. Electrical synapses and their functional interactions with chemical synapses. *Nat. Rev. Neurosci.* **15**, 250–263 (2014).
4. Martini, F. H. *Anatomy & Physiology*. (Rex Bookstore, 2005).
5. Jahn, R. & Sudhof, T. C. Synaptic Vesicles and Exocytosis. *Annu. Rev. Neurosci.* **17**, 219–246 (1994).
6. Snyder, S. H. A Life of Neurotransmitters. *Annu. Rev. Pharmacol. Toxicol.* **57**, 1–11 (2017).
7. Taoufik, E., Kouroupi, G., Zygogianni, O. & Matsas, R. Synaptic dysfunction in neurodegenerative and neurodevelopmental diseases: an overview of induced pluripotent stem-cell-based disease models. *Open Biol.* **8**, 180138 (2018).
8. Willard, S. S. & Koochekpour, S. Glutamate, Glutamate Receptors, and Downstream Signaling Pathways. *Int. J. Biol. Sci.* **9**, 948–959 (2013).
9. Rousseaux, C. G. A Review of Glutamate Receptors I: Current Understanding of Their Biology. *J. Toxicol. Pathol.* **21**, 25–51 (2008).
10. Mayer, M. L. Structure and mechanism of glutamate receptor ion channel assembly, activation and modulation. *Curr. Opin. Neurobiol.* **21**, 283–290 (2011).
11. Nakanishi, S. *et al.* Glutamate receptors: brain function and signal transduction. *Brain Res. Rev.* **26**, 230–235 (1998).
12. García-Gaytán, A. C., Hernández-Abrego, A., Díaz-Muñoz, M. & Méndez, I. Glutamatergic system components as potential biomarkers and therapeutic targets in cancer in non-neural organs. *Front. Endocrinol.* **13**, 1029210 (2022).
13. Foutz, A. S., Champagnat, J. & Denavit-Saubié, M. Involvement of N-methyl-d-aspartate (NMDA) receptors in respiratory rhythmogenesis. *Brain Res.* **500**, 199–208 (1989).
14. Paoletti, P., Bellone, C. & Zhou, Q. NMDA receptor subunit diversity: impact on receptor properties, synaptic plasticity and disease. *Nat. Rev. Neurosci.* **14**, 383–400 (2013).
15. Scatton, B. The NMDA receptor complex. *Fundam. Clin. Pharmacol.* **7**, 389–400 (1993).
16. Mony, L., Zhu, S., Carvalho, S. & Paoletti, P. Molecular basis of positive allosteric modulation of GluN2B NMDA receptors by polyamines. *EMBO J.* **30**, 3134–3146 (2011).
17. Hansen, K. B., Yi, F., Perszyk, R. E., Menniti, F. S. & Traynelis, S. F. NMDA Receptors in the Central Nervous System, *NMDA Receptors.* **1677**, 1–80 (2017)
18. Flores-Soto, M. E. *et al.* Structure and function of NMDA-type glutamate receptor subunits. *Neurol. Engl. Ed.* **27**, 301–310 (2012).
19. Pérez-Otaño, I., Larsen, R. S. & Wesseling, J. F. Emerging roles of GluN3-containing NMDA receptors in the CNS. *Nat. Rev. Neurosci.* **17**, 623–635 (2016).
20. Henson, M. A., Roberts, A. C., Pérez-Otaño, I. & Philpot, B. D. Influence of the NR3A subunit on NMDA receptor functions. *Prog. Neurobiol.* **91**, 23–37 (2010).
21. Benarroch, E. E. NMDA receptors: Recent insights and clinical correlations. *Neurology* **76**, 1750–1757 (2011).
22. Johnson, J. W. & Ascher, P. Glycine potentiates the NMDA response in cultured mouse brain neurons. *Nature* **325**, 529–531 (1987).
23. Kleckner, N. W. & Dingledine, R. Requirement for Glycine in Activation of NMDA-Receptors Expressed in *Xenopus* Oocytes. *Science* **241**, 835–837 (1988).
24. Friedman, M. Chemistry, Nutrition, and Microbiology of D -Amino Acids. *J. Agric. Food Chem.* **47**, 3457–3479 (1999).

Institut Polytechnique de Paris
91120 Palaiseau, France

25. Hashimoto, A. *et al.* The presence of free D-serine in rat brain. *FEBS Lett.* **296**, 33–36 (1992).
26. Mothet, J.-P. *et al.* Glutamate receptor activation triggers a calcium-dependent and SNARE protein-dependent release of the gliotransmitter D-serine. *Proc. Natl. Acad. Sci.* **102**, 5606–5611 (2005).
27. Schell, M. J., Molliver, M. E. & Snyder, S. H. D-serine, an endogenous synaptic modulator: localization to astrocytes and glutamate-stimulated release. *Proc. Natl. Acad. Sci.* **92**, 3948–3952 (1995).
28. Mothet, J.-P. *et al.* D -Serine is an endogenous ligand for the glycine site of the *N* -methyl- D -aspartate receptor. *Proc. Natl. Acad. Sci.* **97**, 4926–4931 (2000).
29. Wolosker, H., Blackshaw, S. & Snyder, S. H. Serine racemase: A glial enzyme synthesizing D -serine to regulate glutamate- *N* -methyl- D -aspartate neurotransmission. *Proc. Natl. Acad. Sci.* **96**, 13409–13414 (1999).
30. Sacchi, S., Rabattoni, V., Miceli, M. & Pollegioni, L. Yin and Yang in Post-Translational Modifications of Human D-Amino Acid Oxidase. *Front. Mol. Biosci.* **8**, 684934 (2021).
31. Papouin, T. *et al.* Synaptic and Extrasynaptic NMDA Receptors Are Gated by Different Endogenous Coagonists. *Cell* **150**, 633–646 (2012).
32. J. A. Kemp., P., T. KinetiC Study of the InteraCtions Between the Glutamate and Glycine Recognition Sites on the N-Methyl-D-aspartic Acid Receptor Complex. *olecular Pharmacology*, **46**, 1191-1196 (1994).
33. Mothet, J., Le Bail, M. & Billard, J. Time and space profiling of NMDA receptor co-agonist functions. *J. Neurochem.* **135**, 210–225 (2015).
34. Kartvelishvily, E., Shleper, M., Balan, L., Dumin, E. & Wolosker, H. Neuron-derived D-Serine Release Provides a Novel Means to Activate N-Methyl-D-aspartate Receptors. *J. Biol. Chem.* **281**, 14151–14162 (2006).
35. Wolosker, H. & Radzishevsky, I. The serine shuttle between glia and neurons: implications for neurotransmission and neurodegeneration. *Biochem. Soc. Trans.* **41**, 1546–1550 (2013).
36. Horn, M. R. V., Sild, M. & Ruthazer, E. S. D-serine as a gliotransmitter and its roles in brain development and disease. *Front. Cell. Neurosci.* **7,** (2013).
37. Puyal, J., Martineau, M., Mothet, J., Nicolas, M. & Raymond, J. Changes in D -serine levels and localization during postnatal development of the rat vestibular nuclei. *J. Comp. Neurol.* **497**, 610–621 (2006).
38. Krishnan, K. S. & Billups, B. ASC Transporters Mediate D-Serine Transport into Astrocytes Adjacent to Synapses in the Mouse Brain. *Biomolecules* **13**, 819 (2023).
39. Kim, P. M. *et al.* Serine racemase: Activation by glutamate neurotransmission via glutamate receptor interacting protein and mediation of neuronal migration. *Proc. Natl. Acad. Sci.* **102**, 2105–2110 (2005).
40. Fujii, K. *et al.* Serine racemase binds to PICK1: potential relevance to schizophrenia. *Mol. Psychiatry* **11**, 150–157 (2006).
41. Martineau, M. *et al.* Storage and Uptake of d-Serine into Astrocytic Synaptic-Like Vesicles Specify Gliotransmission. *J. Neurosci.* **33**, 3413–3423 (2013).
42. Mikou, A. *et al.* Asc-1 Transporter (SLC7A10): Homology Models And Molecular Dynamics Insights Into The First Steps Of The Transport Mechanism. *Sci. Rep.* **10**, 3731 (2020).
43. Rosenberg, D. *et al.* Neuronal d-Serine and Glycine Release Via the Asc-1 Transporter Regulates NMDA Receptor-Dependent Synaptic Activity. *J. Neurosci.* **33**, 3533–3544 (2013).
44. Sason, H. *et al.* Asc-1 Transporter Regulation of Synaptic Activity via the Tonic Release of d-Serine in the Forebrain. *Cereb. Cortex* **27**, 1573-1587 (2016).
45. Ribeiro, C. S., Reis, M., Panizzutti, R., De Miranda, J. & Wolosker, H. Glial transport of the neuromodulator d-serine. *Brain Res.* **929**, 202–209 (2002).

Institut Polytechnique de Paris
91120 Palaiseau, France

46. Martineau, M., Baux, G. & Mothet, J.-P. d-Serine signalling in the brain: friend and foe. *Trends Neurosci.* **29**, 481–491 (2006).
47. Mothet, J. P. *et al.* A critical role for the glial-derived neuromodulator D -serine in the age-related deficits of cellular mechanisms of learning and memory. *Aging Cell* **5**, 267–274 (2006).
48. Panatier, A. *et al.* Glia-Derived d-Serine Controls NMDA Receptor Activity and Synaptic Memory. *Cell* **125**, 775–784 (2006).
49. Souza, I. N. D. O., Roychaudhuri, R., De Belleroche, J. & Mothet, J.-P. d-Amino acids: new clinical pathways for brain diseases. *Trends Mol. Med.* **29**, 1014–1028 (2023).
50. Weatherly, C. A. *et al.* D -Amino Acid Levels in Perfused Mouse Brain Tissue and Blood: A Comparative Study. *ACS Chem. Neurosci.* **8**, 1251–1261 (2017).
51. Dong, M. W. *Modern HPLC for Practicing Scientists*. (Wiley, 2006).
52. Kumar, D. *et al.* A Comprehensive Review on Analytical Method Development using RP-HPLC and Recent Advances in Pharmaceutical Applications. *J. Res. Appl. Sci. Biotechnol.* **2**, 53–60 (2023).
53. Matsui, T. *et al.* Functional Comparison of D -Serine and Glycine in Rodents: The Effect on Cloned NMDA Receptors and the Extracellular Concentration. *J. Neurochem.* **65**, 454–458 (1995).
54. Hamase, K. *et al.* Regional distribution and postnatal changes of d-amino acids in rat brain. *Biochim. Biophys. Acta BBA - Gen. Subj.* **1334**, 214–222 (1997).
55. Bartle, K. D. & Myers, P. History of gas chromatography. *TrAC Trends Anal. Chem.* **21**, 547–557 (2002).
56. Goodnough, D. B., Lutz, M. P. & Wood, P. L. Rapid and sensitive procedure for the separation and quantitation of d- and l-serine in rat brain using gas chromatography-mass spectrometry. *J. Chromatogr. B. Biomed. Sci. App.* **667**, 223–232 (1995).
57. Harstad, R. K., Johnson, A. C., Weisenberger, M. M. & Bowser, M. T. Capillary Electrophoresis. *Anal. Chem.* **88**, 299–319 (2016).
58. Zhao, S., Yuan, H. & Xiao, D. Detection of d-Serine in rat brain by capillary electrophoresis with laser induced fluorescence detection. *J. Chromatogr. B* **822**, 334–338 (2005).
59. Urban, P. L. Quantitative mass spectrometry: an overview. *Philos. Trans. R. Soc. Math. Phys. Eng. Sci.* **374**, 20150382 (2016).
60. Kinoshita, K., Jingu, S. & Yamaguchi, J. A surrogate analyte method to determine d-serine in mouse brain using liquid chromatography–tandem mass spectrometry. *Anal. Biochem.* **432**, 124–130 (2013).
61. Karakawa, S. *et al.* Simultaneous analysis of d-alanine, d-aspartic acid, and d-serine using chiral high-performance liquid chromatography-tandem mass spectrometry and its application to the rat plasma and tissues. *J. Pharm. Biomed. Anal.* **115**, 123–129 (2015).
62. Li, X., McCullum, C., Zhao, S., Hu, H. & Liu, Y.-M. D -Serine Uptake and Release in PC-12 Cells Measured by Chiral Microchip Electrophoresis-Mass Spectrometry. *ACS Chem. Neurosci.* **6**, 582–587 (2015).
63. Ungerstedt, U. Microdialysis—principles and applications for studies in animals and man. *J. Intern. Med.* **230**, 365–373 (1991).
64. Ciriacks, C. M. & Bowser, M. T. Monitoring D -Serine Dynamics in the Rat Brain Using Online Microdialysis-Capillary Electrophoresis. *Anal. Chem.* **76**, 6582–6587 (2004).
65. Ciriacks Klinker, C. & Bowser, M. T. 4-Fluoro-7-nitro-2,1,3-benzoxadiazole as a Fluorogenic Labeling Reagent for the in Vivo Analysis of Amino Acid Neurotransmitters Using Online Microdialysis−Capillary Electrophoresis. *Anal. Chem.* **79**, 8747–8754 (2007).
66. O'Brien, K. B., Esguerra, M., Klug, C. T., Miller, R. F. & Bowser, M. T. A high-throughput on-line microdialysis-capillary assay for D -serine. *Electrophoresis* **24**, 1227–1235 (2003).

Institut Polytechnique de Paris
91120 Palaiseau, France

67. Schell, M. J., Brady Jr., R. O., Molliver, M. E. & Snyder, S. H. d-Serine as a Neuromodulator: Regional and Developmental Localizations in Rat Brain Glia Resemble NMDA Receptors. *J. Neurosci.* **17**, 1604–1615 (1997).
68. Bergersen, L. H. *et al.* Immunogold Detection of L-glutamate and D-serine in Small Synaptic-Like Microvesicles in Adult Hippocampal Astrocytes. *Cereb. Cortex* **22**, 1690–1697 (2012).
69. Vongsouthi, V. *et al.* A Rationally and Computationally Designed Fluorescent Biosensor for D -Serine. *ACS Sens.* **6**, 4193–4205 (2021).
70. Pernot, P. *et al.* Characterization of a Yeast D -Amino Acid Oxidase Microbiosensor for D -Serine Detection in the Central Nervous System. *Anal. Chem.* **80**, 1589–1597 (2008).
71. Polcari, D. *et al.* Disk-Shaped Amperometric Enzymatic Biosensor for in Vivo Detection of D -serine. *Anal. Chem.* **86**, 3501–3507 (2014).
72. Di Pietrantonio, F. *et al.* A Shear horizontal surface acoustic wave biosensor for a rapid and specific detection of d-serine. *Sens. Actuators B Chem.* **226**, 1–6 (2016).
73. Thevenot, D. R., Tóth, K., Durst, R. A. & Wilson, G. S. Electrochemical Biosensors: Recommended Definitions and Classification. *Pure Appl. Chem.* **71**, 2333–2348 (1999).
74. Karunakaran, C., Rajkumar, R. & Bhargava, K. Introduction to Biosensors. in *Biosensors and Bioelectronics* 1–68 (Elsevier, 2015).
75. Turner, A. P. F. Biosensors: sense and sensibility. *Chem. Soc. Rev.* **42**, 3184 (2013).
76. Soldatkina, O. V. *et al.* Improvement of amperometric transducer selectivity using nanosized phenylenediamine films. *Nanoscale Res. Lett.* **12**, 594 (2017).
77. Perumal, V. & Hashim, U. Advances in biosensors: Principle, architecture and applications. *J. Appl. Biomed.* **12**, 1–15 (2014).
78. Wilson, G. S. & Hu, Y. Enzyme-Based Biosensors for in Vivo Measurements. *Chem. Rev.* **100**, 2693–2704 (2000).
79. Gizeli, E. & Lowe, C. R. Immunosensors. *Curr. Opin. Biotechnol.* **7**, 66–71 (1996).
80. Bora, U. Nucleic Acid Based Biosensors for Clinical Applications. *Biosens. J.* **02**, (2013).
81. Liu, Q. *et al.* Cell-Based Biosensors and Their Application in Biomedicine. *Chem. Rev.* **114**, 6423–6461 (2014).
82. Romanholo, P. V. V. *et al.* Biomimetic electrochemical sensors: New horizons and challenges in biosensing applications. *Biosens. Bioelectron.* **185**, 113242 (2021).
83. Song, S., Wang, L., Li, J., Fan, C. & Zhao, J. Aptamer-based biosensors. *TrAC Trends Anal. Chem.* **27**, 108–117 (2008).
84. Greenwald, E. C., Mehta, S. & Zhang, J. Genetically Encoded Fluorescent Biosensors Illuminate the Spatiotemporal Regulation of Signaling Networks. *Chem. Rev.* **118**, 11707–11794 (2018).
85. Wu, Z., Lin, D. & Li, Y. Pushing the frontiers: tools for monitoring neurotransmitters and neuromodulators. *Nat. Rev. Neurosci.* **23**, 257–274 (2022).
86. Ronkainen, N. J., Halsall, H. B. & Heineman, W. R. Electrochemical biosensors. *Chem. Soc. Rev.* **39**, 1747 (2010).
87. Heller, A. Amperometric biosensors. *Curr. Opin. Biotechnol.* **7**, 50–54 (1996).
88. Ding, J. & Qin, W. Recent advances in potentiometric biosensors. *TrAC Trends Anal. Chem.* **124**, 115803 (2020).
89. Dzyadevych, S. & Jaffrezic-Renault, N. Conductometric biosensors, *Biological Identification*, 153–193 (Elsevier 2014).
90. Borisov, S. M. & Wolfbeis, O. S. Optical Biosensors. *Chem. Rev.* **108**, 423–461 (2008).
91. Damborský, P., Švitel, J. & Katrlík, J. Optical biosensors. *Essays Biochem.* **60**, 91–100 (2016).
92. Pohanka, M. The Piezoelectric Biosensors: Principles and Applications, a Review. *Int. J. Electrochem. Sci.* **12**, 496–506 (2017).

Institut Polytechnique de Paris
91120 Palaiseau, France

93. Thakur, M. S. & Ragavan, K. V. Biosensors in food processing. *J. Food Sci. Technol.* **50**, 625–641 (2013).
94. Terry, L. A., White, S. F. & Tigwell, L. J. The Application of Biosensors to Fresh Produce and the Wider Food Industry. *J. Agric. Food Chem.* **53**, 1309–1316 (2005).
95. Mello, L. D. & Kubota, L. T. Review of the use of biosensors as analytical tools in the food and drink industries. *Food Chem.* **77**, 237–256 (2002).
96. Griesche, C. & Baeumner, A. J. Biosensors to support sustainable agriculture and food safety. *TrAC Trends Anal. Chem.* **128**, 115906 (2020).
97. Rogers, K. Biosensors for environmental applications. *Biosens. Bioelectron.* **10**, 533–541 (1995).
98. Velasco-Garcia, M. N. & Mottram, T. Biosensor Technology addressing Agricultural Problems. *Biosyst. Eng.* **84**, 1–12 (2003).
99. Nikoleli, G.-P. *et al.* Biosensors for Security and Bioterrorism : Definitions, History, Types of Agents, New Trends and Applications. *Biosensors for Security and Bioterrorism Applications*, 1–13 (Springer International Publishing, Cham, 2016).
100. Clark, L. C., Wolf, R., Granger, D. & Taylor, Z. Continuous Recording of Blood Oxygen Tensions by Polarography. *J. Appl. Physiol.* **6**, 189–193 (1953).
101. Kaplan, S., Matthews, E. C., Schwab, L. & Clark, L. C. Oxygen availability to the brain during inflow occlusion of the heart in normotherapia and hypothermia. *J. Thorac. Surg.* **32**, 576–582 (1956).
102. Clark, L. C., Kaplan, S., Matthews, E. C., Edwards, P. K. & Helmsworth, J. A. Monitor and control of blood oxygen tension and pH during total body perfusion. *J. Thorac. Surg.* **36**, 488–496 (1958).
103. Clark, L. C. & Lyons, C. Electrode systems for continuous monitoring in cardiovascular surgery. *Ann. N. Y. Acad. Sci.* **102**, 29–45 (1962).
104. Narwal, V. *et al.* Cholesterol biosensors: A review. *Steroids* **143**, 6–17 (2019).
105. Jayanthi, V. S. P. K. S. A., Das, A. B. & Saxena, U. Recent advances in biosensor development for the detection of cancer biomarkers. *Biosens. Bioelectron.* **91**, 15–23 (2017).
106. Huang, H., Bai, W., Dong, C., Guo, R. & Liu, Z. An ultrasensitive electrochemical DNA biosensor based on graphene/Au nanorod/polythionine for human papillomavirus DNA detection. *Biosens. Bioelectron.* **68**, 442–446 (2015).
107. Nascimento, H. P. O. *et al.* An impedimetric biosensor for detection of dengue serotype at picomolar concentration based on gold nanoparticles-polyaniline hybrid composites. *Colloids Surf. B Biointerfaces* **86**, 414–419 (2011).
108. Liu, C. *et al.* An electrochemical DNA biosensor for the detection of Mycobacterium tuberculosis, based on signal amplification of graphene and a gold nanoparticle–polyaniline nanocomposite. *The Analyst* **139**, 5460–5465 (2014).
109. Afonso, A. S. *et al.* A promising bioelectrode based on gene of Mycobacterium leprae immobilized onto poly(4-aminophenol). *J. Appl. Polym. Sci.* **118**, 2921–2928 (2010).
110. Dash, S. K., Sharma, M., Khare, S. & Kumar, A. Omp85 genosensor for detection of human brain bacterial meningitis. *Biotechnol. Lett.* **35**, 929–935 (2013).
111. Ajami, S. & Teimouri, F. Features and application of wearable biosensors in medical care. *J. Res. Med. Sci.* **20**, 1208 (2015).
112. Sardini, E. & Serpelloni, M. Instrumented wearable belt for wireless health monitoring. *Procedia Eng.* **5**, 580–583 (2010).
113. Yu, D., Blankert, B., Viré, J. & Kauffmann, J. Biosensors in Drug Discovery and Drug Analysis. *Anal. Lett.* **38**, 1687–1701 (2005).
114. Banerjee, S., McCracken, S., Hossain, M. F. & Slaughter, G. Electrochemical Detection of Neurotransmitters. *Biosensors* **10**, 101 (2020).

Institut Polytechnique de Paris
91120 Palaiseau, France

115. Fredj, Z., Singh, B., Bahri, M., Qin, P. & Sawan, M. Enzymatic Electrochemical Biosensors for Neurotransmitters Detection: Recent Achievements and Trends. *Chemosensors* **11**, 388 (2023).
116. Chandra, S., Siraj, S. & Wong, D. K. Y. Recent Advances in Biosensing for Neurotransmitters and Disease Biomarkers using Microelectrodes. *ChemElectroChem* **4**, 822–833 (2017).
117. Soleymani, J. Advanced materials for optical sensing and biosensing of neurotransmitters. *TrAC Trends Anal. Chem.* **72**, 27–44 (2015).
118. Liu, R. *et al.* Recent trends in carbon-based microelectrodes as electrochemical sensors for neurotransmitter detection: A review. *TrAC Trends Anal. Chem.* **148**, 116541 (2022).
119. Moon, J.-M., Thapliyal, N., Hussain, K. K., Goyal, R. N. & Shim, Y.-B. Conducting polymer-based electrochemical biosensors for neurotransmitters: A review. *Biosens. Bioelectron.* **102**, 540–552 (2018).
120. Deng, Y., Wang, W., Ma, C. & Li, Z. Fabrication of an Electrochemical Biosensor Array for Simultaneous Detection of L-Glutamate and Acetylcholine. *J. Biomed. Nanotechnol.* **9**, 1378–1382 (2013).
121. Li, Y.-T. *et al.* Receptor-Mediated Field Effect Transistor Biosensor for Real-Time Monitoring of Glutamate Release from Primary Hippocampal Neurons. *Anal. Chem.* **91**, 8229–8236 (2019).
122. Durairaj, S., Sidhureddy, B., Cirone, J. & Chen, A. Nanomaterials-Based Electrochemical Sensors for In Vitro and In Vivo Analyses of Neurotransmitters. *Appl. Sci.* **8**, 1504 (2018).
123. Robinson, D. L., Venton, B. J., Heien, M. L. A. V. & Wightman, R. M. Detecting Subsecond Dopamine Release with Fast-Scan Cyclic Voltammetry in Vivo. *Clin. Chem.* **49**, 1763–1773 (2003).
124. Venton, B. J. & Cao, Q. Fundamentals of fast-scan cyclic voltammetry for dopamine detection. *The Analyst* **145**, 1158–1168 (2020).
125. Puthongkham, P. & Venton, B. J. Recent advances in fast-scan cyclic voltammetry. *The Analyst* **145**, 1087–1102 (2020).
126. Scoggin, J. L. *et al.* An enzyme-based electrochemical biosensor probe with sensitivity to detect astrocytic versus glioma uptake of glutamate in real time in vitro. *Biosens. Bioelectron.* **126**, 751–757 (2019).
127. Yang, C. *et al.* An electrochemical biosensor for sensitive detection of nicotine-induced dopamine secreted by PC12 cells. *J. Electroanal. Chem.* **832**, 217–224 (2019).
128. Clausmeyer, J. & Schuhmann, W. Nanoelectrodes: Applications in electrocatalysis, single-cell analysis and high-resolution electrochemical imaging. *TrAC Trends Anal. Chem.* **79**, 46–59 (2016).
129. Zhang, X., Zhang, W., Zhou, X. & Ogorevc, B. Fabrication, Characterization, and Potential Application of Carbon Fiber Cone Nanometer-Size Electrodes. *Anal. Chem.* **68**, 3338–3343 (1996).
130. Cheng, H., Huang, W., Chen, R., Wang, Z. & Cheng, J. Carbon fiber nanoelectrodes applied to microchip electrophoresis amperometric detection of neurotransmitter dopamine in rat pheochromocytoma (PC12) cells. *Electrophoresis* **28**, 1579–1586 (2007).
131. Li, Y. *et al.* Nanoelectrode for Amperometric Monitoring of Individual Vesicular Exocytosis Inside Single Synapses. *Angew. Chem. Int. Ed.* **53**, 12456–12460 (2014).
132. Takahashi, Y. *et al.* Multifunctional Nanoprobes for Nanoscale Chemical Imaging and Localized Chemical Delivery at Surfaces and Interfaces. *Angew. Chem. Int. Ed.* **50**, 9638–9642 (2011).
133. Actis, P. *et al.* Electrochemical Nanoprobes for Single-Cell Analysis. *ACS Nano* **8**, 875–884 (2014).
134. Rees, H. R., Anderson, S. E., Privman, E., Bau, H. H. & Venton, B. J. Carbon Nanopipette Electrodes for Dopamine Detection in *Drosophila*. *Anal. Chem.* **87**, 3849–3855 (2015).

Institut Polytechnique de Paris
91120 Palaiseau, France

135. Boo, H. *et al.* Electrochemical Nanoneedle Biosensor Based on Multiwall Carbon Nanotube. *Anal. Chem.* **78**, 617–620 (2006).
136. Cao, Q., Shao, Z., Hensley, D. & Venton, B. J. Carbon nanospike coated nanoelectrodes for measurements of neurotransmitters. *Faraday Discuss.* **233**, 303–314 (2022).
137. Xu, J., Tao, J., Su, L., Wang, J. & Jiao, T. A Critical Review of Carbon Quantum Dots: From Synthesis toward Applications in Electrochemical Biosensors for the Determination of a Depression-Related Neurotransmitter. *Materials* **14**, 3987 (2021).
138. Mann, F., Herrmann, N., Meyer, D. & Kruss, S. Tuning Selectivity of Fluorescent Carbon Nanotube-Based Neurotransmitter Sensors. *Sensors* **17**, 1521 (2017).
139. Sun, F. *et al.* A Genetically Encoded Fluorescent Sensor Enables Rapid and Specific Detection of Dopamine in Flies, Fish, and Mice. *Cell* **174**, 481-496.e19 (2018).
140. Petersen, E. D. *et al.* Bioluminescent Genetically Encoded Glutamate Indicators for Molecular Imaging of Neuronal Activity. *ACS Synth. Biol.* **12**, 2301–2309 (2023).
141. Deuschle, K. *et al.* Rapid Metabolism of Glucose Detected with FRET Glucose Nanosensors in Epidermal Cells and Intact Roots of *Arabidopsis* RNA-Silencing Mutants. *Plant Cell* **18**, 2314–2325 (2006).
142. Zhang, W. H. *et al.* Monitoring hippocampal glycine with the computationally designed optical sensor GlyFS. *Nat. Chem. Biol.* **14**, 861–869 (2018).
143. Borden, P. M. *et al.* A Fast Genetically Encoded Fluorescent Sensor for Faithful in Vivo Acetylcholine Detection in Mice, Fish, Worms and Flies. *BioRxiv. 2020-2022 (2020).*
144. Mohd Zain, Z., Ab Ghani, S. & O'Neill, R. D. Amperometric microbiosensor as an alternative tool for investigation of d-serine in brain. *Amino Acids* **43**, 1887–1894 (2012).
145. Bibi, S. Fabrication and use of D-serine biosensors for characterising D-serine signalling in rat brain, Ph.D. Dissertation, University of Warwick, Coventry, UK (2010).
146. Vasylieva, N. *et al.* Covalent enzyme immobilization by poly(ethylene glycol) diglycidyl ether (PEGDE) for microelectrode biosensor preparation. *Biosens. Bioelectron.* **26**, 3993–4000 (2011).
147. Polcari, D., Perry, S. C., Pollegioni, L., Geissler, M. & Mauzeroll, J. Localized Detection of D -Serine by using an Enzymatic Amperometric Biosensor and Scanning Electrochemical Microscopy. *ChemElectroChem* **4**, 920–926 (2017).
148. Perry, S. C., Gateman, S. M., Sifakis, J., Pollegioni, L. & Mauzeroll, J. Enhancement of the Enzymatic Biosensor Response through Targeted Electrode Surface Roughness. *J. Electrochem. Soc.* **165**, G3074–G3079 (2018).
149. Moussa, S. *et al.* Editors' Choice—A Miniaturized Enzymatic Biosensor for Detection of Sensory-Evoked D-serine Release in the Brain. *J. Electrochem. Soc.* **168**, 025502 (2021).
150. Campos-Beltrán, D., Konradsson-Geuken, Å., Quintero, J. & Marshall, L. Amperometric Self-Referencing Ceramic Based Microelectrode Arrays for D-Serine Detection. *Biosensors* **8**, 20 (2018).
151. Draghiciu, L. *et al.* Interdigitated biosensor for D-serine detection, using gold nano-particles, *2019 International Semiconductor Conference (CAS)* 263–266 (IEEE, Sinaia, Romania, 2019).
152. Jaiswal, S., Singh, R., Singh, K., Fatma, S. & Prasad, B. B. Enantioselective analysis of D- and l- Serine on a layer-by-layer imprinted electrochemical sensor. *Biosens. Bioelectron.* **124–125**, 176–183 (2019).
153. Staiano, M. *et al.* D-Serine-Dehydratase from Saccaromyces cerevisiae: A Pyridoxal 5'-phosphate-Dependent Enzyme for Advanced Biotech Applications. *Protein Pept. Lett.* **19**, 592–595 (2012).
154. Binnig, G. & Rohrer, H. Scanning tunneling microscopy. *Surf. Sci.* **126**, 236–244 (1983).
155. Baro, A. M., Miranda, R. & Carrascosa, J. L. Application to biology and technology of the scanning tunneling microscope operated in air at ambient pressure. *IBM J. Res. Dev.* **30**, 380–386 (1986).

Institut Polytechnique de Paris
91120 Palaiseau, France

156. Binnig, G., Quate, C. F. & Gerber, Ch. Atomic Force Microscope. *Phys. Rev. Lett.* **56**, 930–933 (1986).
157. Friedbacher, G. & Fuchs, H. Classification of Scanning Probe Microscopies. *Pure Appl. Chem.* **71**, 1337–1357 (1999).
158. Sarid, D. & Elings, V. Review of scanning force microscopy. *J. Vac. Sci. Technol. B Microelectron. Nanometer Struct. Process. Meas. Phenom.* **9**, 431–437 (1991).
159. Pohl, D. W. Scanning Near-field Optical Microscopy (SNOM). *Advances in Optical and Electron Microscopy*. **12,** 243–312 (Elsevier, 1991).
160. Williams, C. C. & Wickramasinghe, H. K. Scanning thermal profiler. *Microelectron. Eng.* **5**, 509–513 (1986).
161. Matey, J. R. & Blanc, J. Scanning capacitance microscopy. *J. Appl. Phys.* **57**, 1437–1444 (1985).
162. Amemiya, S., Bard, A. J., Fan, F.-R. F., Mirkin, M. V. & Unwin, P. R. Scanning Electrochemical Microscopy. *Annu. Rev. Anal. Chem.* **1**, 95–131 (2008).
163. Bian, K. *et al.* Scanning probe microscopy. *Nat. Rev. Methods Primer* **1**, 36 (2021).
164. Chen, X. *et al.* Principles and Applications of Liquid-Environment Atomic Force Microscopy. *Adv. Mater. Interfaces* **9**, 2201864 (2022).
165. Lamontagne, C.-A., Cuerrier, C. M. & Grandbois, M. AFM as a tool to probe and manipulate cellular processes. *Pflüg. Arch. - Eur. J. Physiol.* **456**, 61–70 (2008).
166. Müller, D. J., Janovjak, H., Lehto, T., Kuerschner, L. & Anderson, K. Observing structure, function and assembly of single proteins by AFM. *Prog. Biophys. Mol. Biol.* **79**, 1–43 (2002).
167. Vinckier, A. & Semenza, G. Measuring elasticity of biological materials by atomic force microscopy. *FEBS Lett.* **430**, 12–16 (1998).
168. Hansma, P. K., Drake, B., Marti, O., Gould, S. A. C. & Prater, C. B. The scanning ion-conductance microscope. *Science* 641–643 (1989).
169. Nitz, H., Kamp, J. & Fuchs, H. A combined scanning ion-conductance and shear-force microscope. **1**, 187–2001 (1998).
170. Chen, C.-C., Zhou, Y. & Baker, L. A. Scanning Ion Conductance Microscopy. *Annu. Rev. Anal. Chem.* **5**, 207–228 (2012).
171. Rheinlaender, J., Geisse, N. A., Proksch, R. & Schäffer, T. E. Comparison of Scanning Ion Conductance Microscopy with Atomic Force Microscopy for Cell Imaging. *Langmuir* **27**, 697–704 (2011).
172. Seifert, J., Rheinlaender, J., Novak, P., Korchev, Y. E. & Schäffer, T. E. Comparison of Atomic Force Microscopy and Scanning Ion Conductance Microscopy for Live Cell Imaging. *Langmuir* **31**, 6807–6813 (2015).
173. Ushiki, T., Iwata, F., Nakajima, M. & Mizutani, Y. Comparison of Scanning Ion-Conductance Microscopy with Scanning Electron Microscopy for Imaging the Surface Topography of Cells and Tissues. *Scanning Ion Conductance Microscopy*. **3**, 187–204 (Springer International Publishing, Cham, 2021).
174. Kirk, S. E., Skepper, J. N. & Donald, A. M. Application of environmental scanning electron microscopy to determine biological surface structure. *J. Microsc.* **233**, 205–224 (2009).
175. Shevchuk, A. I. *et al.* Simultaneous Measurement of Ca2 and Cellular Dynamics: Combined Scanning Ion Conductance and Optical Microscopy to Study Contracting Cardiac Myocytes. *Biophys. J.* **81**, 1759–1764 (2001).
176. Pastré, D., Iwamoto, H., Liu, J., Szabo, G. & Shao, Z. Characterization of AC mode scanning ion-conductance microscopy. *Ultramicroscopy* **90**, 13–19 (2001).
177. McKelvey, K., Perry, D., Byers, J. C., Colburn, A. W. & Unwin, P. R. Bias Modulated Scanning Ion Conductance Microscopy. *Anal. Chem.* **86**, 3639–3646 (2014).
178. Novak, P. *et al.* Nanoscale live-cell imaging using hopping probe ion conductance microscopy. *Nat. Methods* **6**, 279–281 (2009).

Institut Polytechnique de Paris
91120 Palaiseau, France

179. Takahashi, Y. *et al.* Topographic imaging of convoluted surface of live cells by scanning ion conductance microscopy in a standing approach mode. *Phys. Chem. Chem. Phys.* **12**, 10012 (2010).
180. Korchev, Y. E., Bashford, C. L., Milovanovic, M., Vodyanoy, I. & Lab, M. J. Scanning Ion Conductance Microscopy of Living Cells. *Biophys. J.* **73**, 653–658 (1997).
181. Korchev, Y. E. *et al.* Specialized scanning ion-conductance microscope for imaging of living cells. *J. Microsc.* **188**, 17–23 (1997).
182. Mann, S. A., Hoffmann, G., Hengstenberg, A., Schuhmann, W. & Dietzel, I. D. Pulse-mode scanning ion conductance microscopy—a method to investigate cultured hippocampal cells. *J. Neurosci. Methods* **116**, 113–117 (2002).
183. Happel, P. & Dietzel, I. D. Backstep scanning ion conductance microscopy as a tool for long term investigation of single living cells. *J. Nanobiotechnology* **7**, 7 (2009).
184. Gesper, A. *et al.* Long-term, long-distance recording of a living migrating neuron by scanning ion conductance microscopy. *Scanning* **37**, 226–231 (2015).
185. Yang, X. *et al.* Investigation of morphological and functional changes during neuronal differentiation of PC12 cells by combined Hopping Probe Ion Conductance Microscopy and patch-clamp technique. *Ultramicroscopy* **111**, 1417–1422 (2011).
186. Tanaka, A. *et al.* Time-lapse imaging of morphological changes in a single neuron during the early stages of apoptosis using scanning ion conductance microscopy. *J. Struct. Biol.* **191**, 32–38 (2015).
187. Shevchuk, A. *et al.* Angular Approach Scanning Ion Conductance Microscopy. *Biophys. J.* **110**, 2252–2265 (2016).
188. Wong Su, S., Chieng, A., Parres-Gold, J., Chang, M. & Wang, Y. Real-time determination of aggregated alpha-synuclein induced membrane disruption at neuroblastoma cells using scanning ion conductance microscopy. *Faraday Discuss.* **210**, 131–143 (2018).
189. Sánchez, D. *et al.* Localized and non-contact mechanical stimulation of dorsal root ganglion sensory neurons using scanning ion conductance microscopy. *J. Neurosci. Methods* **159**, 26–34 (2007).
190. Pellegrino, M., Orsini, P. & De Gregorio, F. Use of scanning ion conductance microscopy to guide and redirect neuronal growth cones. *Neurosci. Res.* **64**, 290–296 (2009).
191. Pellegrino, M. *et al.* Weak hydrostatic forces in far-scanning ion conductance microscopy used to guide neuronal growth cones. *Neurosci. Res.* **69**, 234–240 (2011).
192. Rheinlaender, J. & Schäffer, T. E. Mapping the mechanical stiffness of live cells with the scanning ion conductance microscope. *Soft Matter* **9**, 3230 (2013).
193. Clarke, R. W. *et al.* Low Stress Ion Conductance Microscopy of Sub-Cellular Stiffness. *Soft Matter* **12**, 7953–7958 (2016).
194. Sánchez, D. *et al.* Noncontact Measurement of the Local Mechanical Properties of Living Cells Using Pressure Applied via a Pipette. *Biophys. J.* **95**, 3017–3027 (2008).
195. Kolmogorov, V. S. *et al.* Scanning Ion-Conductance Microscopy for Studying β-Amyloid Aggregate Formation on Living Cell Surface. *Analytical Chemistry* **95**, 15943-15949 (2023).
196. Kolmogorov, V. *et al.* Scanning Ion-Conductance Microscopy for Studying Mechanical Properties of Neuronal Cells during Local Delivery of Glutamate. *Cells* **12**, 2428 (2023).
197. Actis, P. Sampling from Single Cells. *Small Methods* **2**, 1700300 (2018).
198. Bruckbauer, A. *et al.* Nanopipette Delivery of Individual Molecules to Cellular Compartments for Single-Molecule Fluorescence Tracking. *Biophys. J.* **93**, 3120–3131 (2007).
199. Page, A., Kang, M., Armitstead, A., Perry, D. & Unwin, P. R. Quantitative Visualization of Molecular Delivery and Uptake at Living Cells with Self-Referencing Scanning Ion Conductance Microscopy-Scanning Electrochemical Microscopy. *Anal. Chem.* **89**, 3021–3028 (2017).

Institut Polytechnique de Paris
91120 Palaiseau, France

200. Korchev, Y. E., Negulyaev, Y. A., Edwards, C. R. W., Vodyanoy, I. & Lab, M. J. Functional localization of single active ion channels on the surface of a living cell. *Nat. Cell Biol.* **2**, 616–619 (2000).
201. Korchev, Y. E. *et al.* Hybrid Scanning Ion Conductance and Scanning Near-Field Optical Microscopy for the Study of Living Cells. *Biophys. J.* **78**, 2675–2679 (2000).
202. Vitol, E. A. *et al. In Situ* Intracellular Spectroscopy with Surface Enhanced Raman Spectroscopy (SERS)-Enabled Nanopipettes. *ACS Nano* **3**, 3529–3536 (2009).
203. Dubkov, S. *et al.* Single-Cell Analysis with Silver-Coated Pipette by Combined SERS and SICM. *Cells* **12**, 2521 (2023).
204. Page, A. *et al.* Fast Nanoscale Surface Charge Mapping with Pulsed-Potential Scanning Ion Conductance Microscopy. *Anal. Chem.* **88**, 10854–10859 (2016).
205. Takami, T. *et al.* Development of Dual Ion-selective Electrodes in Double-Barrel Glass Pipette at One Micrometer for Simultaneous Measurement of Sodium and Potassium Ions. *E-J. Surf. Sci. Nanotechnol.* **21**, 17–23 (2022).
206. Zhang, Y. *et al.* High-resolution label-free 3D mapping of extracellular pH of single living cells. *Nat. Commun.* **10**, 5610 (2019).
207. Guo, J. *et al.* Dynamic single-cell intracellular pH sensing using a SERS-active nanopipette. *The Analyst* **145**, 4852–4859 (2020).
208. Song, J. *et al.* Ultrasmall Nanopipette: Toward Continuous Monitoring of Redox Metabolism at Subcellular Level. *Angew. Chem. Int. Ed.* **57**, 13226–13230 (2018).
209. Fu, Y., Tokuhisa, H. & Baker, L. A. Nanopore DNA sensors based on dendrimer-modified nanopipettes. *Chem. Commun.* **32,** 4877-4879 (2009).
210. Zhang, Y. *et al.* Spearhead Nanometric Field-Effect Transistor Sensors for Single-Cell Analysis. *ACS Nano* **10**, 3214–3221 (2016).
211. Nascimento, R. A. S. *et al.* Single Cell "Glucose Nanosensor" Verifies Elevated Glucose Levels in Individual Cancer Cells. *Nano Lett.* **16**, 1194–1200 (2016).
212. Polcari, D. *et al.* Disk-Shaped Amperometric Enzymatic Biosensor for in Vivo Detection of D -serine. *Anal. Chem.* **86**, 3501–3507 (2014).
213. Bucur, B., Purcarea, C., Andreescu, S. & Vasilescu, A. Addressing the Selectivity of Enzyme Biosensors: Solutions and Perspectives. *Sensors* **21**, 3038 (2021).
214. Kulkarni, T. & Slaughter, G. Application of Semipermeable Membranes in Glucose Biosensing. *Membranes* **6**, 55 (2016).
215. Olejnik, A., Karczewski, J., Dołęga, A., Siuzdak, K. & Grochowska, K. Novel approach to interference analysis of glucose sensing materials coated with Nafion. *Bioelectrochemistry* **135**, 107575 (2020).
216. Cot, A. *et al.* Electrosynthesis and characterization of polymer films on silicon substrates for applications in micromanipulation. *Synth. Met.* **162**, 2370–2378 (2012).
217. Fernstrom, J. D. & Wurtman, R. J. Brain Serotonin Content: Physiological Dependence on Plasma Tryptophan Levels. *Science* **173**, 149–152 (1971).
218. Miele, M. & Fillenz, M. In vivo determination of extracellular brain ascorbate. *J. Neurosci. Methods* **70**, 15–19 (1996).
219. Meridor, D. & Gedanken, A. Enhanced activity of immobilized pepsin nanoparticles coated on solid substrates compared to free pepsin. *Enzyme Microb. Technol.* **67**, 67–76 (2014).
220. Bolivar, J. M., Schelch, S., Mayr, T. & Nidetzky, B. Mesoporous Silica Materials Labeled for Optical Oxygen Sensing and Their Application to Development of a Silica-Supported Oxidoreductase Biocatalyst. *ACS Catal.* **5**, 5984–5993 (2015).
221. Bolivar, J. M. & Nidetzky, B. On the relationship between structure and catalytic effectiveness in solid surface-immobilized enzymes: Advances in methodology and the quest for a single-molecule perspective. *Biochim. Biophys. Acta BBA - Proteins Proteomics* **1868**, 140333 (2020).

Institut Polytechnique de Paris
91120 Palaiseau, France

222. Moussa, S., Chhin, D., Pollegioni, L. & Mauzeroll, J. Quantitative measurements of free and immobilized RgDAAO Michaelis-Menten constant using an electrochemical assay reveal the impact of covalent cross-linking on substrate specificity. *Anal. Bioanal. Chem.* **413**, 6793–6802 (2021).
223. Ghosh, S. *et al.* Pharmacological and Therapeutic Approaches in the Treatment of Epilepsy. *Biomedicines* **9**, 470 (2021).
224. Thijs, R. D., Surges, R., O'Brien, T. J. & Sander, J. W. Epilepsy in adults. *The Lancet* **393**, 689–701 (2019).
225. Guerrini, R. Epilepsy in children. *The Lancet* **367**, 499–524 (2006).
226. Avoli, M. *et al.* Ligand-gated mechanisms leading to ictogenesis in focal epileptic disorders. *Neurobiol. Dis.* **180**, 106097 (2023).
227. Bod, R. *et al.* Synaptic alterations and neuronal firing in human epileptic neocortical excitatory networks. *Front. Synaptic Neurosci.* **15**, 1233569 (2023).
228. Dubey, V. *et al.* Differential glutamate receptor expression and function in the hippocampus, anterior temporal lobe and neocortex in a pilocarpine model of temporal lobe epilepsy. *Exp. Neurol.* **347**, 113916 (2022).
229. Marwick, K. F. M., Hansen, K. B., Skehel, P. A., Hardingham, G. E. & Wyllie, D. J. A. Functional assessment of triheteromeric NMDA receptors containing a human variant associated with epilepsy. *J. Physiol.* **597**, 1691–1704 (2019).
230. Punnakkal, P. & Dominic, D. NMDA Receptor GluN2 Subtypes Control Epileptiform Events in the Hippocampus. *NeuroMolecular Med.* **20**, 90–96 (2018).
231. Banerjee, J. *et al.* Enhanced endogenous activation of NMDA receptors in pyramidal neurons of hippocampal tissues from patients with mesial temporal lobe epilepsy: A mechanism of hyper excitation. *Epilepsy Res.* **117**, 11–16 (2015).
232. Ragnarsson, L. *et al. GRIN1* variants associated with neurodevelopmental disorders reveal channel gating pathomechanisms. *Epilepsia* **64**, 3377–3388 (2023).
233. Li, J. *et al.* De novo *GRIN* variants in NMDA receptor M2 channel pore-forming loop are associated with neurological diseases. *Hum. Mutat.* **40**, 2393–2413 (2019).
234. Li, D. *et al.* GRIN2D Recurrent De Novo Dominant Mutation Causes a Severe Epileptic Encephalopathy Treatable with NMDA Receptor Channel Blockers. *Am. J. Hum. Genet.* **99**, 802–816 (2016).
235. Burnashev, N. & Szepetowski, P. NMDA receptor subunit mutations in neurodevelopmental disorders. *Curr. Opin. Pharmacol.* **20**, 73–82 (2015).
236. Elmasri, M. *et al.* Common synaptic phenotypes arising from diverse mutations in the human NMDA receptor subunit GluN2A. *Commun. Biol.* **5**, 174 (2022).
237. Vieira, M. *et al.* A frameshift variant of GluN2A identified in an epilepsy patient results in NMDA receptor mistargeting. *J. Neurosci.* **44**, 4 (2023)
238. Beesley, S., Sullenberger, T., Lee, C. & Kumar, S. S. GluN3 subunit expression correlates with increased vulnerability of hippocampus and entorhinal cortex to neurodegeneration in a model of temporal lobe epilepsy. *J. Neurophysiol.* **127**, 1496–1510 (2022).
239. Parsons, M. P. & Raymond, L. A. Extrasynaptic NMDA Receptor Involvement in Central Nervous System Disorders. *Neuron* **82**, 279–293 (2014).
240. Sivakumar, S., Ghasemi, M. & Schachter, S. C. Targeting NMDA Receptor Complex in Management of Epilepsy. *Pharmaceuticals* **15**, 1297 (2022).
241. Walrave, L. *et al.* I nhibition of astroglial connexin43 hemichannels with TAT - G ap19 exerts anticonvulsant effects in rodents. *Glia* **66**, 1788–1804 (2018).
242. Harai, T. *et al.* Decreased susceptibility to seizures induced by pentylenetetrazole in serine racemase knockout mice. *Epilepsy Res.* **102**, 180–187 (2012).
243. Zhang, X., Lu, L., Weihong, L., Lichao, S. & Li, C. D-serine and nmda receptor 1 expression in patients with intractable epilepsy. *Turk. Neurosurg.* **31**, 76-82 (2020)

Institut Polytechnique de Paris
91120 Palaiseau, France

244. Klatte, K. *et al.* Impaired D-Serine-Mediated Cotransmission Mediates Cognitive Dysfunction in Epilepsy. *J. Neurosci.* **33**, 13066–13080 (2013).
245. Postnikova, T. Y. *et al.* Impairments of Long-Term Synaptic Plasticity in the Hippocampus of Young Rats during the Latent Phase of the Lithium-Pilocarpine Model of Temporal Lobe Epilepsy. *Int. J. Mol. Sci.* **22**, 13355 (2021).
246. Beesley, S. *et al.* D-serine mitigates cell loss associated with temporal lobe epilepsy. *Nat. Commun.* **11**, 4966 (2020).
247. Le Bail, M. *et al.* Identity of the NMDA receptor coagonist is synapse specific and developmentally regulated in the hippocampus. *Proc. Natl. Acad. Sci.* **112**, (2015).
248. Papouin, T. & Haydon, P. D-serine Measurements in Brain Slices or Other Tissue Explants. *BIO-Protoc.* **8**, (2018).
249. MacFarland, T. W. & Yates, J. M. Wilcoxon Matched-Pairs Signed-Ranks Test. *Introduction to Nonparametric Statistics for the Biological Sciences Using R*, 133–175 (Springer International Publishing, Cham, 2016).
250. Mann-Whitney Test. *SpringerReference* (Springer-Verlag, Berlin/Heidelberg, 2011).
251. Choi, H.-S. & Lee, C.-H. Time-course changes of hippocalcin expression in the mouse hippocampus following pilocarpine-induced status epilepticus. *J. Vet. Sci.* **17**, 137 (2016).
252. Mishra, P. *et al.* Descriptive statistics and normality tests for statistical data. *Ann. Card. Anaesth.* **22**, 67 (2019).
253. Marino, M. J., Rouse, S. T., Levey, A. I., Potter, L. T. & Conn, P. J. Activation of the genetically defined m1 muscarinic receptor potentiates *N* -methyl- D -aspartate (NMDA) receptor currents in hippocampal pyramidal cells. *Proc. Natl. Acad. Sci.* **95**, 11465–11470 (1998).
254. Papouin, T., Dunphy, J. M., Tolman, M., Dineley, K. T. & Haydon, P. G. Septal Cholinergic Neuromodulation Tunes the Astrocyte-Dependent Gating of Hippocampal NMDA Receptors to Wakefulness. *Neuron* **94**, 840-854.e7 (2017).
255. Takata, N. *et al.* Astrocyte Calcium Signaling Transforms Cholinergic Modulation to Cortical Plasticity *In Vivo*. *J. Neurosci.* **31**, 18155–18165 (2011).
256. Ma, W. *et al.* Astrocytic α4-containing nAChR signaling in the hippocampus governs the formation of temporal association memory. *Cell Rep.* **42**, 112674 (2023).
257. Clasadonte, J., Dong, J., Hines, D. J. & Haydon, P. G. Astrocyte control of synaptic NMDA receptors contributes to the progressive development of temporal lobe epilepsy. *Proc. Natl. Acad. Sci.* **110**, 17540–17545 (2013).
258. Ferreira, J. S. *et al.* Co-agonists differentially tune GluN2B-NMDA receptor trafficking at hippocampal synapses. *eLife* **6**, e25492 (2017).
259. Beesley, S. *et al.* D-serine mitigates cell loss associated with temporal lobe epilepsy. *Nat. Commun.* **11**, 4966 (2020).
260. Rosini, E., Caldinelli, L. & Piubelli, L. Assays of D-Amino Acid Oxidase Activity. *Front. Mol. Biosci.* **4**, 102 (2018).
261. Saleem, M. A. *et al.* A Conditionally Immortalized Human Podocyte Cell Line Demonstrating Nephrin and Podocin Expression. *J. Am. Soc. Nephrol.* **13**, 630–638 (2002).
262. Sutter Instrument. P-2000 Laser-Based Micropipette Puller System Operation Manual. (2020).
263. Zhu, C., Huang, K., Siepser, N. P. & Baker, L. A. Scanning Ion Conductance Microscopy. *Chem. Rev.* **121**, 11726–11768 (2021).
264. Pan, R. *et al.* Resistive-Pulse Sensing Inside Single Living Cells. *J. Am. Chem. Soc.* **142**, 5778–5784 (2020).
265. Simonis, M. *et al.* MoNa – A Cost-Efficient, Portable System for the Nanoinjection of Living Cells. *Sci. Rep.* **9**, 5480 (2019).

Institut Polytechnique de Paris
91120 Palaiseau, France

266. Gatenby, R. A. The Role of Cell Membrane Information Reception, Processing, and Communication in the Structure and Function of Multicellular Tissue. *Int. J. Mol. Sci.* **20**, 3609 (2019).
267. Kim, S.-O., Kim, J., Okajima, T. & Cho, N.-J. Mechanical properties of paraformaldehyde-treated individual cells investigated by atomic force microscopy and scanning ion conductance microscopy. *Nano Converg.* **4**, 5 (2017).
268. Leitao, S. M. *et al.* Time-Resolved Scanning Ion Conductance Microscopy for Three-Dimensional Tracking of Nanoscale Cell Surface Dynamics. *ACS Nano* **15**, 17613–17622 (2021).
269. Zhukov, A., Richards, O., Ostanin, V., Korchev, Y. & Klenerman, D. A hybrid scanning mode for fast scanning ion conductance microscopy (SICM) imaging. *Ultramicroscopy* **121**, 1–7 (2012).
270. Shao, Y. & Mirkin, M. V. Voltammetry at Micropipet Electrodes. *Anal. Chem.* **70**, 3155–3161 (1998).
271. Wang, Y. *et al.* Nanoelectrodes for determination of reactive oxygen and nitrogen species inside murine macrophages. *Proc. Natl. Acad. Sci.* **109**, 11534–11539 (2012).
272. Wang, N. *et al.* Self-Referenced Nanopipette for Electrochemical Analysis of Hydrogen Peroxide in the Nucleus of a Single Living Cell. *Anal. Chem.* **93**, 10744–10749 (2021).
273. Ota, N., Rubakhin, S. S. & Sweedler, J. V. d-Alanine in the islets of Langerhans of rat pancreas. *Biochem. Biophys. Res. Commun.* **447**, 328–333 (2014).
274. Nioradze, N. *et al.* Origins of Nanoscale Damage to Glass-Sealed Platinum Electrodes with Submicrometer and Nanometer Size. *Anal. Chem.* **85**, 6198–6202 (2013).
275. Hao, R. & Zhang, B. Nanopipette-Based Electroplated Nanoelectrodes. *Anal. Chem.* **88**, 614–620 (2016).
276. Comstock, D. J., Elam, J. W., Pellin, M. J. & Hersam, M. C. Integrated Ultramicroelectrode−Nanopipet Probe for Concurrent Scanning Electrochemical Microscopy and Scanning Ion Conductance Microscopy. *Anal. Chem.* **82**, 1270–1276 (2010).
277. Thakar, R., Weber, A. E., Morris, C. A. & Baker, L. A. Multifunctional carbon nanoelectrodes fabricated by focused ion beam milling. *The Analyst* **138**, 5973 (2013).
278. O'Connell, M. A., Lewis, J. R. & Wain, A. J. Electrochemical imaging of hydrogen peroxide generation at individual gold nanoparticles. *Chem. Commun.* **51**, 10314–10317 (2015).
279. Veal, E. A., Day, A. M. & Morgan, B. A. Hydrogen Peroxide Sensing and Signaling. *Mol. Cell* **26**, 1–14 (2007).
280. Dai, Y.-Q., Zhou, D.-M. & Shiu, K.-K. Permeability and permselectivity of polyphenylenediamine films synthesized at a palladium disk electrode. *Electrochimica Acta* **52**, 297–303 (2006).
281. Schuvailo, O. M., Soldatkin, O. O., Lefebvre, A., Cespuglio, R. & Soldatkin, A. P. Highly selective microbiosensors for in vivo measurement of glucose, lactate and glutamate. *Anal. Chim. Acta* **573–574**, 110–116 (2006).
282. O'Neill, R. D., Chang, S.-C., Lowry, J. P. & McNeil, C. J. Comparisons of platinum, gold, palladium and glassy carbon as electrode materials in the design of biosensors for glutamate. *Biosens. Bioelectron.* **19**, 1521–1528 (2004).
283. McMahon, C. P., Killoran, S. J., Kirwan, S. M. & O'Neill, R. D. The selectivity of electrosynthesised polymer membranes depends on the electrode dimensions: implications for biosensor applications. *Chem. Commun.* **2128** (2004).
284. Killoran, S. J. & O'Neill, R. D. Characterization of permselective coatings electrosynthesized on Pt–Ir from the three phenylenediamine isomers for biosensor applications. *Electrochimica Acta* **53**, 7303–7312 (2008).
285. Craig, J. D. & O'Neill, R. D. Comparison of simple aromatic amines for electrosynthesis of permselective polymers in biosensor fabrication. *The Analyst* **128**, 905 (2003).

Institut Polytechnique de Paris
91120 Palaiseau, France

286. Piper, A., Alston, B. M., Adams, D. J. & Mount, A. R. Functionalised microscale nanoband edge electrode (MNEE) arrays: the systematic quantitative study of hydrogels grown on nanoelectrode biosensor arrays for enhanced sensing in biological media. *Faraday Discuss.* **210**, 201–217 (2018).
287. Zhou, P., Yao, L. & Su, B. Fabrication, Characterization, and Analytical Application of Silica Nanopore Array-Modified Platinum Electrode. *ACS Appl. Mater. Interfaces* **12**, 4143–4149 (2020).
288. Brazell, M. P. *et al.* Electrocoating carbon fiber microelectrodes with Nafion improves selectivity for electroactive neurotransmitters. *J. Neurosci. Methods* **22**, 167–172 (1987).
289. Demuru, S. & Deligianni, H. Surface PEDOT:Nafion Coatings for Enhanced Dopamine, Serotonin and Adenosine Sensing. *J. Electrochem. Soc.* **164**, G129–G138 (2017).
290. Cen, Y., Liu, Y., Xue, Y. & Zheng, Y. Immobilization of Enzymes in/on Membranes and their Applications. *Adv. Synth. Catal.* **361**, 5500–5515 (2019).
291. Turkmen, E., Bas, S. Z., Gulce, H. & Yildiz, S. Glucose biosensor based on immobilization of glucose oxidase in electropolymerized poly(o-phenylenediamine) film on platinum nanoparticles-polyvinylferrocenium modified electrode. *Electrochimica Acta* **123**, 93–102 (2014).
292. Garjonyte, R. & Malinauskas, A. Amperometric glucose biosensor based on glucose oxidase immobilized in poly(o-phenylenediamine) layer. *Sens. Actuators B Chem.* **56**, 85–92 (1999).
293. Hamase, K., Konno, R., Morikawa, A. & Zaitsu, K. Sensitive Determination of D-Amino Acids in Mammals and the Effect of D-Amino-Acid Oxidase Activity on Their Amounts. *Biol. Pharm. Bull.* **28**, 1578–1584 (2005).

Institut Polytechnique de Paris
91120 Palaiseau, France

ECOLE DOCTORALE

Titre : Une plateforme multimodale d'imagerie et d'analyse basée sur des nanopipettes pour l'exploration de la communication cérébrale

Mots clés : Récepteurs NMDA, D-sérine, microscopie de conductance ionique à balayage, capteurs électrochimiques

Le cerveau est composé de milliards de neurones qui communiquent entre eux au niveau des synapses, où les neurotransmetteurs libérés du neurone présynaptique vont agir sur les cellules effectrices. Les récepteurs du glutamate N-méthyl-D-aspartate (NMDA) sont essentiels à la physiologie du cerveau et leur dysfonctionnement est systématiquement lié à des conditions pathologiques. L'activation des récepteurs NMDAR canoniques nécessite un co-agoniste, tel que la glycine ou la D-sérine. Bien que le rôle de la D-sérine ait été découvert il y a deux décennies, les conditions régissant la disponibilité synaptique relative et la fonction de la glycine et de la D-sérine au niveau des synapses restent insaisissables. Ce travail de doctorat aborde les questions relatives à la D-sérine en développant une technique analytique permettant d'obtenir des informations en temps réel et à haute résolution sur la concentration locale de D-sérine dans les nanodomaines synaptiques et extrasynaptiques. Des micro et nanocapteurs électrochimiques basés sur l'enzyme D-aminoacides oxydase (DAAO) sont développés. La première partie du travail se concentre sur la fabrication et la caractérisation de capteurs électrochimiques micrométriques. En outre, nous décrivons leur utilisation pour surveiller les niveaux locaux de D-sérine dans des tranches d'hippocampe vivant en phase aiguë dans des expériences physiologiques, rapportant que la libération de D-sérine augmente dans des conditions chimiques proconvulsives imitant l'épilepsie. La deuxième partie présente des nanocapteurs électrochimiques à base de DAAO intégrés dans des nanosondes en verre pour la microscopie de conductance ionique à balayage (SICM). Cette sonde comporte une nanopipette divisée en deux canaux : l'un contient une nano-version du capteur à base de DAAO et l'autre sert à la cartographie topographique SICM. La plateforme à double fonction qui en résulte servira à terme d'outil analytique puissant, combinant la détection locale de la D-sérine et l'acquisition d'informations topographiques locales.

Title: A multimodal nanopipette-based imaging and analytical platform for exploring brain communication

Keywords: NMDA receptors, D-serine, Scanning Ion Conductance Microscopy, electrochemical sensors

The brain is composed of billions of neurons that communicate through trillions of synapses, with neurotransmitters being transferred from sender neurons to effector cells. N-methyl-D-aspartate (NMDA) glutamate receptors are crucial for brain physiology and their malfunction is consistently linked with pathological conditions. Activation of canonical NMDARs require a co-agonist, such as glycine or D-serine. Despite the two-decades-old discovery of D-serine's role, the conditions governing the relative synaptic availability and function of glycine and D-serine at synapses remain elusive. This PhD work addresses questions about D-serine by developing an analytical technique for high-resolution, real-time information on local D-serine concentration at synaptic and extrasynaptic nanodomains. Micro- and nano- electrochemical biosensors based on the enzyme D-amino acids oxidase (DAAO) are developed. The first part of the work focuses on fabricating and characterizing micrometric electrochemical sensors. Moreover, we describe their use to monitor local D-serine levels in acute living hippocampal slices in physiological experiments, reporting that D-serine release increases under chemically proconvulsive conditions mimicking epilepsy. The second part introduces electrochemical DAAO-based nano-sensors embedded in Scanning Ion Conductance Microscopy (SICM) glass nanoprobes. This probe features a nanopipette divided into two channels: one housing a nano-version of the DAAO-based sensor and the other serving for SICM topographical mapping. The resulting double-functionality platform will ultimately serve as a powerful analytical tool, combining local D-serine sensing with the acquisition of local topographical information.